

Investigating noise radiation from jets by acoustic analogy

Thesis submitted for the degree of

Doctor of Philosophy

at the University of Leicester

by

Danilo Di Stefano



UNIVERSITY OF
LEICESTER

Department of Engineering

University of Leicester

2018

Investigating noise radiation from jets by acoustic analogy

by

Danilo Di Stefano

Abstract

The aerodynamic noise radiating from an unsteady flow can be extracted by acoustic analogy from time-resolved Computational Fluid Dynamic (CFD) simulations. For this purpose, two Ffowcs Williams and Hawkings (FW-H) solvers are developed, based on an advanced time formulation (AFW-H) and on a convective formulation (CFW-H). The methods are coded in Python and embedded in Antares, a CFD post-processor of wide access and usability for the scientific community, developed by Cerfacs, France. The new FW-H solvers are tested on a hierarchy of noise sources of increasing complexity. The radiating field from elementary acoustic sources is considered first, progressing then to single-stream and dual-stream jets. The tests on monopoles, dipoles, and quadrupoles show good predictions of pressure fluctuation time-history and directivity against reference analytical results. CFD results obtained at Cerfacs by Large Eddy Simulation and at the University of Leicester by Detached Eddy Simulation provide the input to the acoustic analogy to estimate the noise radiation from jets. The jet noise predictions are compared against acoustic results obtained numerically by the elsA software (ONERA, France) and against sound measurements taken at the Von Karman Institute for Fluid Dynamics, Belgium. The tool is then used to assess dual-stream under-expanded jet noise in a configuration by Airbus SAS, at flow conditions that differ from the ones explored in previous aeroacoustic literature. Flight effects on jet noise are tested by applying the CFW-H tool to a single-stream under-expanded jet in-flight. The acoustic predictions for both static and in-flight jets are found in good agreement with reference predictions and with measurements, building confidence in using the new FW-H solvers to extract the aerodynamic noise generated by unsteady shock-containing jets.

Acknowledgements

The dissemination of these results has received funding from the European Union Seventh Framework Programme FP7/2007-2013 under grant agreement no. 317142. This research used the ALICE High Performance Computing Facility at the University of Leicester. The graphical post-processing of the results was supported by licenses originally purchased with EPSRC support on grant GR/N23745/01. This research also used digitised experimental and numerical data kindly provided by Alessandro Mancini, University of Leicester, Carlos Pérez-Arroyo and Guillaume Puigt, Cerfacs, France, and by Daniel Guariglia and Christophe Schram, Von Karman Institute for Fluid Dynamics, Brussels.

A PhD is a long marathon made of daily tiny steps toward a final goal. In this long journey, I have been supported by many people and I walked side by side with most of them, even if for a short period. Now I have come to the finish and I would like to thank all the people involved in this adventure.

First of all, I am immeasurably grateful to my family, Pietro, Simonetta, and David for the support through the first 32 years of my life. They were fundamental for my personal growth and they supported me during both my life and my academic career.

A special mention to the great scientist and twice Nobel prize Marie Skłodowska Curie, who inspired the research grant funding the AeroTraNet2 project and my PhD, and who represents a model for every researcher in the world for her priceless contribution to science.

A very special gratitude goes out to the University of Leicester team, that is composed by: my supervisor Dr. Aldo Rona, who coordinated the AeroTraNet2 project and supported me through the whole PhD with his expertise in fluid dynamics and aeroacoustics; Dr. Edward Hall, project manager of the AeroTraNet2 project who represented a sensible friend beside being a great co-worker; my colleague Alessandro Mancini, PhD student at Leicester, who shared the whole experience with me.

My sincere thanks also goes to Emeritus Professor Christopher L. Morfey, Visiting Professor at the University of Leicester, as the second reader of this thesis, and I am gratefully indebted to him for his very valuable comments. He was also my

mentor, together with my supervisor, helping me through the acoustic analogy theory understanding and development with his expertise in aeroacoustics.

I would like to mention all the AeroTraNet2 fellows, Tobias, Lior, Carlos, Francisco, Daniel, Elena, Carina, Ilaria, Moshin, Sheryas, and also the supervisors in the project. They all helped making this adventure very productive but also contributed to establish a friendly atmosphere through the project network.

A warm greeting to my Leicester friends from all over the globe, who contributed to make this experience very pleasing and interesting, also by the mutual sharing of our different cultural baggage and background. A particular mention to Matteo, who was a wingman, a friend and a confident and to Cristina and Massimo, who were two important reference points during my stay in Leicester. And then Jerome, Maurizio, Sophie, Sara, Francesca, Micol, Hannah, Federica, Tomas, Emanuela, Claudia, the South American team with Christian, Johanna, Manolo, Isabel, Fiore, Mariel, and the swing team.

A special hug to all my Italian mates, living in Rome or somewhere else in Europe, who visited me in Leicester, or supported me through Skype talks during the tough moments, especially Alessandro, Paolo, Raffaele, Arianna, Tania, Micaela, Aurora, and Ilaria.

I am also grateful to the University of Leicester staff member Michelle Pryce, for her unfailing support and assistance on administrative or logistic matters.

Thanks to all the special people I met during these long four years who contributed to turn this PhD into a wonderful experience.

Contents

List of Symbols	vii
1 Introduction	1
1.1 Overview and objectives	1
1.2 Computational AeroAcoustics of supersonic jets	4
1.3 Noise from dual-stream coaxial jets	9
1.4 Acoustic source non-compactness in jets	16
1.5 Approach to modelling jet noise	19
1.6 Thesis outline	20
2 Methodology	22
2.1 Aeroacoustic techniques	22
2.1.1 Direct computation of sound	24
2.1.2 Hybrid methods	26
2.1.2.1 Acoustic analogy	27
2.1.2.2 The Kirchhoff formulation	34
2.1.2.3 Viscous/acoustic split	35
2.1.2.4 Theory of vortex sound	36
2.2 FW-H acoustic analogy theory	37
2.2.1 The porous FW-H formulation	42
2.2.1.1 Effect of neglecting the FW-H volume integral con- tribution	44
2.2.2 Advanced time vs retarded time approach	47
2.2.3 Casalino advanced time approach (AFW-H)	49
2.2.4 Convective acoustic analogy (CFW-H)	51

2.3	Implementation in Antares	54
2.3.1	Parallel MPI implementation	58
2.4	CFD dataset	59
2.4.1	DES by Cosmic	60
2.4.2	LES by elsA	61
2.4.3	FW-H surface placement in the CFD domain	62
3	Advanced-time FW-H acoustic analogy code validation	64
3.1	Predicting noise radiated from elementary sources	65
3.1.1	Monopole	67
3.1.2	Dipole	71
3.1.3	Longitudinal quadrupole	76
3.1.4	Lateral quadrupole	81
3.2	Numerical error sources in the AFW-H tool	88
3.2.1	Lateral quadrupole proximity to the FW-H surface corner	89
3.2.2	Dipole proximity to the FW-H surface corner	91
3.3	Chapter 3 summary	93
4	Application to stationary jets	95
4.1	Single jet noise predictions	97
4.1.1	Subsonic fully expanded isothermal jet	97
4.1.2	Supersonic under-expanded cold jet	104
4.2	Dual-stream jet noise	112
4.2.1	Far-field radiation	116
4.2.2	Near-field radiation	127
4.2.3	Jet acoustic source compactness	129
4.3	Chapter 4 summary	139
5	Noise radiation in a uniformly moving medium	141
5.1	Noise radiation from elementary sources in a uniform flow	142
5.1.1	Monopole acoustic source in a uniform flow	142
5.1.2	Dipole acoustic source in a uniform flow	147
5.2	Forward flight effects on BroadBand Shock Associated Noise	153
5.2.1	Far-field noise radiation from an under-expanded jet in flight	154

6	Conclusions	162
6.1	Key contributions	162
6.2	Implications of the main results	163
6.3	Future perspectives	166
	Appendices	168
A	AeroTraNet2	169
B	Convective FW-H derivation	173
C	FW-H integral solution	180
D	New CFW-H tool validation for stationary test cases	191
	References	195

List of Symbols

Roman symbols

A	Surface dilation factor
A_p, A_s	Primary and secondary flow nozzle exit area
B_j	CFD mesh block
D	Nozzle diameter
D_{eq}	Equivalent nozzle diameter
$\mathcal{F}(\mathbf{x}, t) = 0$	Equation defining the FW-H/integration surface
f	Frequency
$G()$	Green's function
$H()$	Heaviside function
h	Secondary nozzle annulus
I	Acoustic intensity
J	Jacobian of the transformation $\mathbf{y}-\boldsymbol{\eta}$
k	Wave number
L_{ij}	Momentum source
M	Source Mach number
$\hat{\mathbf{n}}, \hat{n}_i$	FW-H/integration surface outward-pointing unit-normal vector
$o^{(i)}$	i^{th} Observer
P	Acoustic power
p	Pressure
P_{ij}, τ_{ij}	Compressive and viscous stress tensor
Q_i	Mass source
\mathbf{R}, R_i	Source-observer acoustic distance in a uniformly convected flow
\mathbf{R}^*, R_i^*	Scaling factor with distance source-observer in a uniformly convected flow

\mathbf{r}, r_i	Source-observer geometric distance
Re	Reynolds number based on the jet exit velocity
$s^{(i)}$	i^{th} point source
$S_j, \Delta S_k$	FW-H surface discrete face and discrete element
Str	Strouhal number
T	Temperature
t	Observer time frame
t_{adv}	Advanced time
T_{ij}	Lighthill stress tensor
\mathbf{u}, u_i	Local fluid velocity
\mathbf{v}, v_i	Local FW-H surface velocity
\mathcal{V}_s	Source region
\mathbf{x}, x_i	Observer vector position
x_d	Primary-to-secondary nozzle exit distance
\mathbf{y}, y_i	Source vector position

Greek symbols

Δt	Observer time resolution
$\Delta \tau$	Source time resolution
$\delta()$	Dirac delta function
δ_{ij}	Kronecker delta
$\boldsymbol{\eta}, \eta_i$	Lagrangian coordinate moving with the FW-H surface
θ	Radiation angle from the jet axis
λ	Wavelength
μ	Dynamic viscosity
ϕ	Azimuth
Φ_{conv}	Variable to check the convergence of the acoustic simulation
ρ	Density
σ_e	Nozzle lip - single stream jet
τ	Source time frame
τ_e	Emission time \equiv retarded time (τ_{ret})
τ_0	Initial simulation time
τ_f	Final simulation time

$[\dots]_{\tau_e}$	Evaluation at emission time τ_e
ω	Angular frequency
∇	Gradient operator
\square^2	Linear wave operator
Subscripts	
0	Undisturbed uniform medium value
e	Nozzle exit section value
j	Fully-expanded
L	Loading
n	Projection in the normal direction
p	Primary flow
Q	Quadrupole
R	Projection in the radiation direction for a uniformly convected medium
r	Projection in the radiation direction for a stationary medium
s	Secondary flow
T	Thickness
t	Total quantity
Superscripts	
\cdot	Source time derivative
$\hat{}$	Unit vector
\prime	Acoustic fluctuation respect to the undisturbed medium
c	Convective form
Abbreviations	
AFW-H	Advanced time Ffowcs Williams and Hawkings
BBSAN	BroadBand Shock-Associated Noise
BPR	ByPass Ratio
CAA	Computational AeroAcoustics
CFD	Computational Fluid Dynamics
CFW-H	Convective Ffowcs Williams and Hawkings
CNPR	Core Nozzle Pressure Ratio
DNS	Direct Numerical Simulation

ER	Experienced Researcher
ESR	Early Stage Researcher
FNPR	Fan Nozzle Pressure Ratio
FW-H	Ffowcs Williams and Hawkings
ILES	Implicit Large Eddy Simulation
IVP	Inverted Velocity Profile
KFW-H	Kirchhoff Ffowcs Williams and Hawkings
LEE	Linear Euler Equation
LES	Large Eddy Simulation
LHS	Left-Hand Side
LIE	Linearized Inhomogeneous Euler
MPI	Message Passing Interface
NPR	Nozzle Pressure Ratio
NVP	Normal Velocity Profile
PSD	Power Spectral Density
RANS	Reynolds Averaged Navier-Stokes
RHS	Right-Hand Side
SCN	Shock-Cell Noise

Chapter 1

Introduction

1.1 Overview and objectives

The main objective of this research consists in developing an aeroacoustic tool of wide access and usability that allows the prediction of the noise radiation from unsteady flows both in the near-field and in the far-field. The new aeroacoustic tool is designed to be run either as a post-processor on a stored set of data, or embedded in a Computational Fluid Dynamic (CFD) software. Specifically, starting from the unsteady flow field prediction on a control surface, the tool aims to produce reliable noise estimations for under-expanded single-stream and dual-stream jets, towards cabin noise predictions. A dual-flux test case proposed by Airbus SAS, which is introduced in Appendix A and investigated in Section 4.2, represents a new application with flow conditions that differ from the ones explored in the previous aeroacoustic literature. Moreover, the convective acoustic analogy implementation described in Section 2.2.4 is applied to a single-stream under-expanded jet in flight in Chapter 5, for which no equivalent application is available in the literature.

Aeroacoustics is a compelling discipline that stems from the pioneering work of Sir James Lighthill [1, 2] on sound generated aerodynamically. The ensuing work on the modelling and control of jet noise from aircraft enabled the growth of air transport operations with acceptable levels of airport noise. In 2015, aviation supported 63 million jobs worldwide and underpinned \$ 2.7 trillion of Gross Domestic Product [3]. Such achievement of high economic, environmental, and societal impact was reached through an arduous research path, as reported by Tam [4].

The physics of jet noise radiation is extremely complex. Many elements interact with each other, generating complex dependencies that make it extremely difficult to disentangle and isolate the effect of each physical parameter. Jet noise modelling is closely linked to turbulence, which is another complex discipline that is far from being a closed subject.

Many analytical and numerical jet noise models have been tested and appraised over the past decades. However, there is still no large consensus among aeroacousticians on the most efficient modelling approach [5], especially for predicting supersonic jet noise, where broadband shock-associated noise is involved. This makes aeroacoustics a very interesting field, in which many researchers work to pursue a model that correctly reproduces the physics of the problem, given the restrictions imposed by the current technology and computing facilities.

The increasingly restrictive limits imposed by the International Civil Aviation Organization (ICAO) in terms of noise emission, both towards the ground and the cabin (ICAO Annex 16 Chapter 4), constitute a main driver for further reducing jet noise emissions from aircraft engines. The introduction of turbofan engined aircraft provided a significant reduction in noise pollution. The increase in the bypass ratio (BPR) between the secondary and the primary flow has given further noise reductions over the last half century. By increasing the air inflow to the engine, the same thrust can be produced with a lower jet exit velocity, which implies a reduction in the noise emission, the latter being proportional to a high power of the jet exit velocity [1, 6, 7]. Further increases in turbofan diameter are becoming difficult to integrate in the conventional underwing configuration and other techniques need to be investigated.

During the last half century, many solutions have been developed and tested to decrease noise radiation levels from turbofan engines, both towards the ground and towards the cabin, including mass injection [8], and the alteration of the nozzle shape [9] through vortex generators [10] or chevrons [11]. The use of acoustic liners is also very common, both on the engine and over the cabin fuselage, but this acts on the transmission path without reducing the noise level at source. Even though some of these solutions were shown to represent a good compromise between noise reduction and both thrust and efficiency losses, there is still not a general noise reduction technique that is independent of the aircraft configuration and that acts

effectively for reducing both low and high frequency jet noise components on modern turbofan engines.

Therefore, it is of interest to investigate jet noise radiation from modern wide-body civil aircraft, which operate high-bypass ratio turbofan engines with a fixed area nozzle. The annular nozzle from the bypass flux can operate ideally expanded only at one point of the flight envelope. The bypass jet is therefore typically under-expanded, causing unwanted shock-associated noise, which is more prominent in the passenger cabin, given today's more composite airframe fuselage materials. This prompts the pursuit of prediction techniques for the sound pressure at monitoring positions corresponding to the airframe fuselage alongside the jet, in order to evaluate the noise transmission from the engine to the fuselage.

The major accomplishment pursued during this PhD is the ability to extract engineering estimates of far-field as well as of near-field jet noise (Section 1.4), both in the static and in the in-flight configuration, given time-dependent descriptions of the flow, for which a common database format is defined, applicable to numerical, experimental, and analytical jet flow descriptions. For this purpose the author implemented two Ffowcs Williams and Hawkings acoustic analogy formulations in the Antares software [12], a post-processing package of wide access and usability for the scientific community that is developed and maintained by the Centre Européen de Recherche et de Formation Avancée en Calcul Scientifique (Cerfacs).

This research was undertaken within the context of the AeroTraNet2 (AERONautical TRAIning NETwork in Aerodynamic Noise from Wide-body Civil Aircraft) project [13]. The aim of the wider AeroTraNet2 project was to build a physics-based model for idealised dual-stream jets and to obtain predictions of the radiating acoustic pressure field from under-expanded single/dual-stream jets that match experimental data. Such predictions can then be used to investigate the physical mechanisms generating the noise.

1.2 Computational AeroAcoustics of supersonic jets

A comprehensive review of the advances in jet noise research since Lighthill [1] has been published by Tam [4] in 1998 and most recently by Viswanathan [14] in 2009. The physics of jet noise, for both subsonic and supersonic flows, has been described by Mancini [15] and Pérez [16], who were Early Stage Researchers in the AeroTraNet2 project. A special focus on supersonic jets and their shock-associated noise is given by Tam [17], who provides a clear classification of the main noise components. In this section, a brief introduction to supersonic jet noise is given, followed by a discussion on the issues pertaining to Computational AeroAcoustics (CAA) jet noise simulations.

In a jet, the driving parameter of the flow is the Nozzle Pressure Ratio (NPR). This is defined as the ratio between the jet total pressure p_t and the ambient pressure p_0 :

$$\text{NPR} = \frac{p_t}{p_0}. \quad (1.1)$$

This parameter and the nozzle exit pressure p_e determines whether the jet is fully expanded or otherwise. For supercritical nozzles, just one operating condition exists for which the jet is perfectly expanded and the fluid inside the nozzle expands to the external pressure p_0 at the nozzle exit section, satisfying $p_e = p_0$. All other conditions generate a system of shock-cells within the jet that produces a significant contribution to the overall radiated sound, referred to as Shock-Cell Noise (SCN).

A perfectly expanded supersonic jet requires a convergent-divergent nozzle, long enough to allow the flow to be accelerated to the fully expanded jet Mach number M_j and the ambient pressure p_0 to be reached at the nozzle exit. In most wide-body transport aircraft applications, this nozzle configuration would imply an unacceptable increase in the engine weight and consequent fuel consumption. The current solution is to use convergent nozzles even for supersonic flows, by generating under-expanded configurations, represented schematically in Figure 1.2(b). The degree of off-design operation \mathcal{O} depends on the difference between the local exit pressure of the flow, p_e , and the ambient pressure p_0 . Following Miller and Morris [18], \mathcal{O} is proportional to the difference between the squares of the fully expanded jet Mach number M_j , and

the nozzle exit Mach number M_e and it can be expressed as:

$$\Theta = \sqrt{|M_j^2 - M_e^2|} = \sqrt{|M_j^2 - 1|}, \quad (1.2)$$

where $M_e = 1$ is used for a supersonic under-expanded jet ($M_j > 1$) issuing from a convergent choked nozzle, according to simple 1D theory.

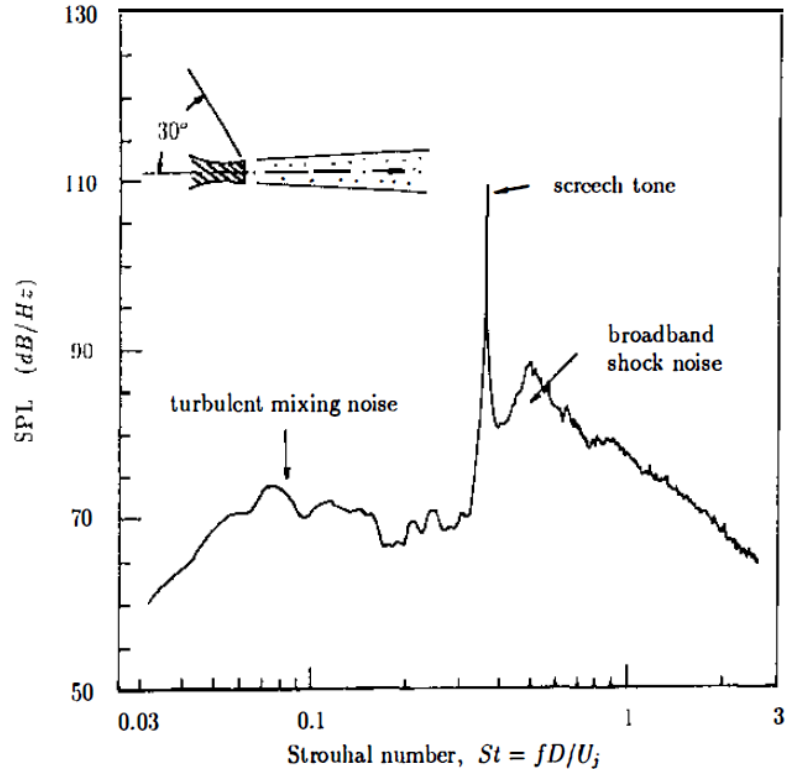


Figure 1.1: Typical far-field supersonic jet noise spectrum in the upstream direction, 150° from the jet axis (Seiner *et al.* [19]).

As described by Tam [17], supersonic jet noise is characterized by three main components, which are turbulent mixing noise, BroadBand Shock-Associated Noise (BBSAN), and screech tone. The last two components are generated by a shock-cell system in incorrectly expanded jets and constitute the SCN contribution. Figure 1.1 reports a typical jet noise spectrum in which the three contributions are clearly visible. The highest peak is the screech tone, while the weaker broadband noise peaks to the left (lower frequencies) and to the right (higher frequencies) of the screech tone are, respectively, the turbulent mixing noise (typical of all jet flows), and the BBSAN. As shown in Figure 1.1, the non-dimensional Strouhal number is typically used in place of the frequency f on the horizontal axis. Herein, the Strouhal number

is defined as $Str = (fD_e)/U_e$, where f is the frequency in Hertz, while D_e and U_e are respectively the nozzle exit diameter and velocity.

Both the fine and the large scales of turbulence in the flow are responsible for the generation of the turbulent mixing noise component [4], which is mainly directed downstream at an angle between 45° and 60° from the jet axis [17]. At polar angles higher than 60° , a weaker contribution is given predominantly by the fine scales of turbulence [20], of higher wave number. These scales, due to their unsteady and incoherent nature, generate a broadband noise that does not show a strongly directional radiation pattern. However, the mean flow refraction [21] effect, by causing the waves to deviate towards right angles from the jet axis, is responsible for the generation of a “cone of silence” at the downstream angles, where the fine-scale turbulence contribution is extremely weak [4].

The dominant component of turbulent mixing noise in the downstream direction is emitted by the large-scale (lower wave number) turbulent structures [17], which can be modelled by a superposition of instability wave modes of the mean flow [22]. In high speed jets, where the convection speed of the structures can reach supersonic values, the large-scale turbulence radiates noise mainly through the Mach wave radiation, described by Tam [4]. The contribution of these coherent structures is a broad peak in the noise spectrum with a preferred directivity towards small downstream angles, due to turbulent eddies convecting downstream in the jet shear-layer. Tam *et al.* [23] found empirical self-similar spectra, for both fine and large-scale contributions, confirming the existence of these two turbulent mixing noise components.

The other two jet noise components are mainly generated by the interaction between the shock-cell system and the shear-layer, where vortical structures are convected downstream. The BBSAN component is spread across the frequency domain and it is predominant in the upstream direction. The peak Strouhal number depends on the radiation direction and several weaker peaks are usually observed [17] to the right of the screech tone.

On the other hand, the screech component is an intense tonal noise contribution that was first observed by Powell [24], who proposed a model to predict both the directivity and the frequency of the screech fundamental tone and of its harmonics. Improvements on the model by Powell were proposed by Tam *et al.* [25] and by

Panda [26]. The main emission of the screech noise is in the upstream direction and several harmonics of the screech tone are usually observed, with different directivity patterns.

An important characteristic of a jet in screech is the oscillation of the jet, which can be either axisymmetric and toroidal, or helical and flapping [17]. Important contributions were made by Manning and Lele [27], and Suzuki and Lele [28] who introduced the concept of shock-leakage. Norum [29] stressed the effect of the nozzle lip thickness σ_e on the screech noise intensity, as σ_e influences the feedback loop responsible for the screech tonal component that appears in the acoustic radiation. However, despite the increasing number of studies on screech noise, the flow and geometric conditions that determine the onset of this tonal noise component are still not completely clear.

Figure 1.2 shows the two possible configurations for an incorrectly expanded jet which generate the BBSAN and the screech noise components described above. The over-expansion (Figure 1.2(a)) can occur with convergent-divergent nozzle and it causes the flow at the nozzle exit to have a pressure lower than the ambient value (Figure 1.2(c)). The exit Mach number M_e is supersonic and the velocity difference between the airflow at the nozzle exit plane, and the surrounding quiescent air, creates a streamwise growing shear-layer forming at the nozzle lip. The over-expanded air flow from the nozzle exit plane recompresses, due to the higher ambient pressure, through a shock-cone. The oblique shock from the nozzle lip first converges onto the nozzle axis where it recompresses the flow, then reflects as an expansion wave at the shear-layer, expanding the jet. This process repeats as a sequence of compressions and expansions.

The inflected velocity profile of the shear-layer is receptive to disturbances that convectively amplify, developing into large-scale instabilities. The resulting shear-layer motion makes the shock-cell structure inside it unsteady. Shock-shear layer interaction results in screech noise being emitted to the surroundings.

The under-expansion configuration (Figure 1.2(b)) has different initial conditions, with the flow at the convergent nozzle exit section having a pressure higher than the ambient value and a sonic Mach number M_e (Figure 1.2(d)). Therefore, the flow initially expands through expansion waves that are reflected as shocks at the

shear-layer. The flow then develops similarly to the over-expanded case.

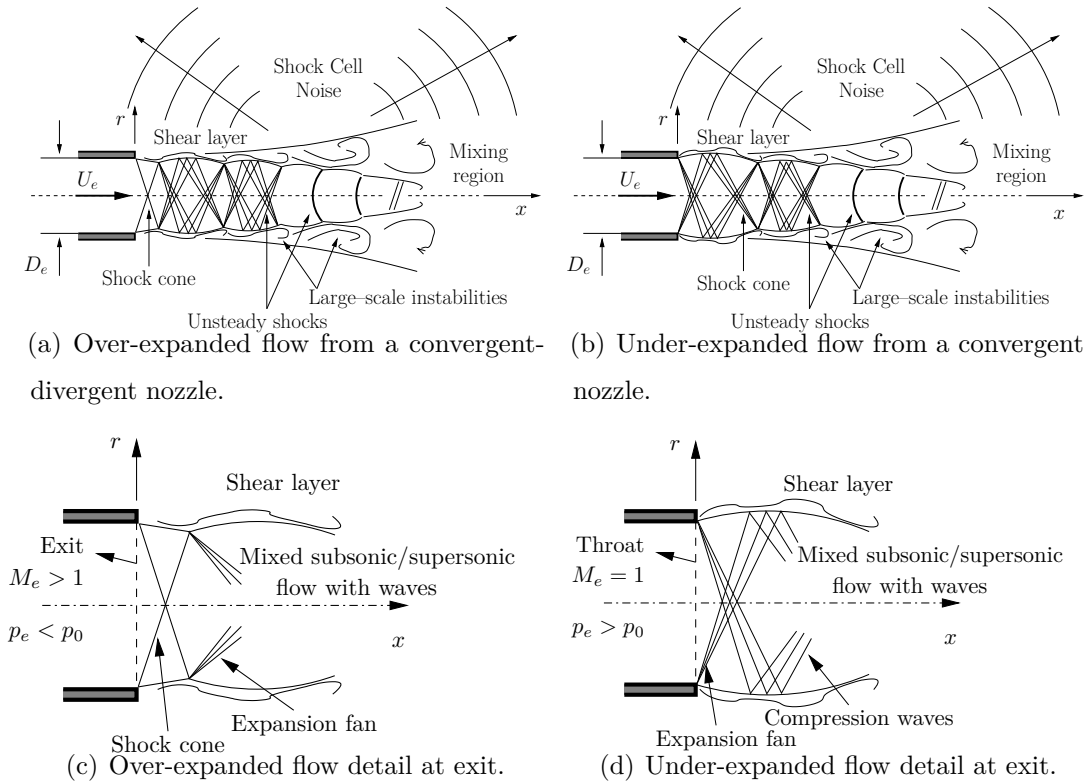


Figure 1.2: Noise radiation in a turbulent jet flow, with the presence of shocks.

The complexity of the physical phenomena driving the jet noise generation and propagation, represented schematically in Figure 1.2, makes a jet aeroacoustic simulation a complex and challenging process. An overview of the requirements for a successful aeroacoustic simulation is given by Tam [30] and Roe [31]. The most important difference between standard aerodynamic problems and aeroacoustic applications lies in the time-dependent nature of the noise generation phenomenon, which requires well resolved time-dependent simulations, as well as the storing of a time history of the flow prediction.

The large spectral bandwidth of the disturbances is another important factor. This dictates the spatial resolution requirements of the discretization [30]. Specifically, the shortest wavelength (highest frequency) of the sound waves determines this constraint. The amplitude of the velocity fluctuations associated with the sound radiation are usually several orders of magnitude smaller than the amplitude of the turbulent velocity fluctuations from the mean flow. This is due to the fact that only a small fraction of the turbulent energy is converted to acoustic energy [1] and it

represents another challenge for aeroacoustic simulations.

The domain size and accuracy requirements are also more stringent compared to other aerodynamic simulations. This increases further the computational cost of an aeroacoustic simulation. The sound waves propagate a long distance compared to aerodynamic disturbances and the computed solution needs to be accurate throughout the entire domain. Good dispersive and dissipative characteristics of the numerical scheme are therefore critical [30].

The presence of non-linearities, such as shocks, in the flow complicates the modelling further. Tailored boundary conditions are required to prevent the generation of reflection phenomena at the boundary of the computational domain, which can otherwise contaminate the noise field with spurious numerical waves.

Consequently, an aeroacoustic simulation presents different peculiarities compared to standard CFD problems, thus requiring the use of tailored numerical techniques, in order to build a model that can simulate and reproduce the main physical features of a heterogeneous flow phenomenon. Some of the complexity of an aeroacoustic simulation can be circumvented by adopting a hybrid approach. This consists in performing two separate simulations, one for the unsteady flow field prediction and one for the noise radiation. One-step simulations and hybrid approaches are introduced in Section 1.5 and discussed in Sections 2.1 and 2.2 in the next chapter.

1.3 Noise from dual-stream coaxial jets

One of the goals of this research is to capture the main features of the noise radiation from a dual-stream jet configuration presented in Appendix A by the use of a numerical implementation of the Ffowcs Williams and Hawkings acoustic analogy. The methodology is discussed in the next chapter, while in this section, a literature review of the noise radiation from dual-stream jets is given.

Most wide-body civil aircraft use turbofans. These engines are characterised by an internal core primary flow and a coaxial secondary flow. The primary flow undergoes the Brayton-Joule, or jet-engine, cycle and expands through a primary nozzle. The secondary flow compresses through a fan, by-passes the engine core, and expands through a nozzle coaxial to the primary flow.

According to the operating conditions, which are related to the specific engine and air transport operation types, the dual-stream outflow assumes different configurations. If both the internal and the coaxial flows are perfectly expanded, the local pressure at the nozzle exit equates the ambient pressure, for both secondary and primary flow, that is $p_p = p_0$ and $p_s = p_0$, where subscripts p and s stand for primary and secondary flow respectively. This ideal condition is not easily satisfied and the engine usually operates with at least one of the two flows not perfectly expanded.

In a dual-stream jet, there are two characteristic pressure ratios, *i.e.* the Core Nozzle Pressure ratio (CNPR), which relates to the core flow, and the Fan Nozzle Pressure Ratio (FNPR), for the secondary flow. CNPR and FNPR are obtained, from Equation 1.1, by substituting p_t with p_{tp} for the primary flow, and with p_{ts} for the secondary flow.

By varying these two parameters, different dual-nozzle set point operations are obtained, in which the two flows can be subsonic and/or supersonic. According to the velocity ratio between secondary and primary flow, a Normal Velocity Profile (NVP) $U_s/U_p < 1$ or an Inverted Velocity Profile (IVP) $U_s/U_p > 1$ is obtained. With a NVP, the jet is characterised by a higher inner velocity, while with an IVP, the secondary flow is faster. Both profile types are studied in the literature [32, 33].

As far as noise radiation is concerned, the same noise components described for a single jet in Section 1.2 can be observed in a dual-stream jet. If both streams are subsonic, turbulent mixing noise is the most important noise contribution, while with a supersonic imperfectly expanded jet, the Shock-Cell Noise contribution becomes dominant, especially towards the upstream direction and at right angles to the jet.

Additional complexities arise in the noise generation process, making the physical mechanisms responsible for sound production rather challenging to be reproduced, both numerically and experimentally. A comprehensive and general model is still far from being achieved for dual-stream jet noise generation and radiation and various approximate models are available (Chapter 2). This makes the dual-stream jet noise a very prominent topic in the aircraft noise research portfolio.

One of the main difference relative to a single-stream jet is that a shock-cell system can be formed in the primary stream and/or in the secondary stream. If the primary flow is incorrectly expanded and the outer flow fully expanded, the noise

generation process is similar to that of a single-stream jet in which the secondary stream acts as a co-flow [34], generating refraction effects that are negligible in the normal direction only [18] (see Chapter 5 for flight effects on under-expanded jets).

With an IVP from an incorrectly expanded supersonic secondary stream, as sketched in Figure 1.3(b), the secondary flow and the shock-cell system within it are bounded by the two shear-layers, one generated by the velocity discontinuity between the two flows (inner shear-layer), and the other arising from the difference between the outer jet and the ambient velocity (outer shear-layer). In this case, the shocks within the outer flow interact with both shear-layers, generating noise contributions with different characteristics in terms of frequency content and directivity. In Section 4.2, the noise radiation from a dual-stream jet of this type is investigated.

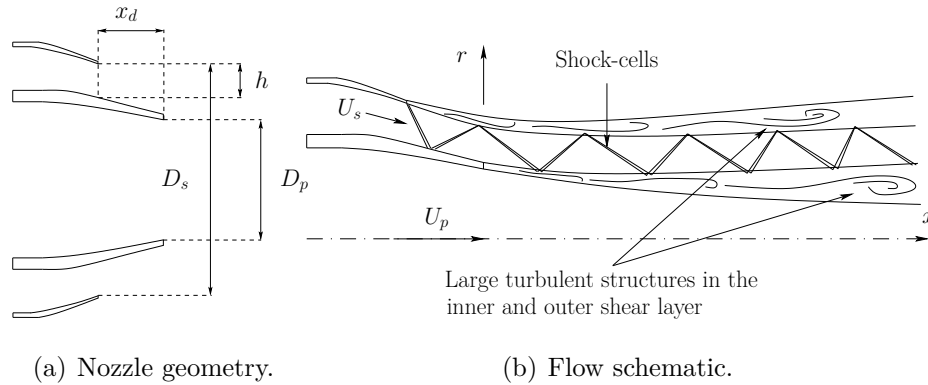


Figure 1.3: Nozzle geometry with recessed outer nozzle and flow schematic of a dual-stream jet, with shock-cells in the secondary flow ($M_{js} > 1$, $M_{jp} < 1$) interacting with turbulent structures convected both in the inner and in the outer shear-layer.

Tanna *et al.* [32] conducted extensive noise measurements on dual-stream jets, focusing on IVPs. They considered four main parameters: the primary and the secondary total temperatures, T_{tp} and T_{ts} , and pressure ratios, CNPR and FNPR, which they referred to as T_{tp} , T_{tf} , ξ_p , and ξ_f .

By comparing the results with an equivalent single jet, defined as having the same nozzle exit area, mass flow rate, and thrust, they investigated the conditions at which the coaxial jet is quieter, or noisier, compared to the single-stream case. A condition for minimum noise [35] was found by varying the CNPR and keeping the other parameters constant. When the shock-cell system is developed in the secondary flow, for low subsonic core flow Mach numbers, several regularly spaced shock-cells can be detected by flow visualization (Schlieren). By increasing the

CNPR above the critical value, the flow undergoes drastic changes and the shock-cell system is significantly reduced, preserving only one or two shock-cells close to the nozzle exit. These changes affect the SCN contribution, resulting in a minimum noise radiation condition with a slightly supersonic primary stream (for both IVP and NVP cases) [35].

The physical explanation for this minimum noise condition is given by Tam & Tanna [35] by analysing a simplified model, in which shear-layers are replaced by vortex sheets. SCN is mainly generated by the interaction between the convected large-scale turbulent structures in the shear-layer and the quasi-periodic shock-cell system. As the latter is essentially absent for slightly supercritical conditions in the inner flow, this interaction and consequently the SCN radiation is significantly weakened.

The shock-cell system in the secondary flow is supported by the two shear-layers surrounding it, which reflect shocks and expansion waves. The reflections bounce back into the secondary flow and are “trapped” within it. If the primary flow is subsonic, its core pressure field is continuous and smoothly varying, so that incident positive characteristics from the outer flow are reflected as negative characteristics at the primary flow boundary. The reflected waves are just slightly weaker than the incident ones. In the supersonic regime, the core flow allows discontinuities to propagate within it and the reflection process is far less efficient, so that the shocks and expansion waves become very weak after a few reflections.

Tam & Tanna proposed an analytical model to predict the peak frequency in the noise spectra and the noise intensity scaling for the SCN radiation, from both single-stream [36] and IVP dual-stream jets [37]. They developed the theoretical model by Harper Bourne and Fisher [38], who obtained simple analytical formulae relating the frequency of the spectral peaks to the direction of radiation.

The BBSAN component is generated by the interaction between the shock-cell system and the turbulent structures convected downstream in the jet shear-layer. Therefore, the peak frequencies of the spectrum mainly depend on the convective velocity of these vortical structures, on the shock-cell spacing, and on the direction of radiation [18]. The intensity of the BBSAN is dictated by geometrical factors, such as the jet diameter and the observer location, as well as by flow properties, such

as the fully expanded jet velocity and the off-design factor \mathcal{O} (Equation 1.2) [18].

As for a single-stream jet, the noise radiation is dominated by turbulent mixing noise when the jet is fully expanded. In order to investigate this noise component in coaxial jets, Dahl & Morris [33] developed a numerical model able to predict the mean flow properties of supersonic coaxial jets, with a NVP or an IVP. Mean flow properties are then used to determine turbulent mixing noise, through an extension of the instability wave theory [39] to coaxial jets. Even for incorrectly expanded jets, the noise radiation from instability waves with supersonic phase speed is the most efficient noise radiation mechanism at low angles from the jet axis [33, 40].

As far as NVP coaxial jets are concerned, Dahl & Morris [33] found that the instability waves in the inner shear-layer are the dominant turbulent mixing noise source, for low velocity ratios $U_s/U_p < 0.5$, and they are characterised by higher peak Strouhal numbers in the noise spectra, compared to the outer shear-layer component. For $U_s/U_p > 0.5$, the outer shear-layer becomes the main contributor to mixing noise. For IVP coaxial jets, the turbulent mixing noise component radiating to the acoustic far-field can be reduced by increasing the initial spreading rate of the outer shear-layer, which reduces the maximum amplitude of the instability waves [33].

Despite the potential noise reduction given by the IVP concept compared to a NVP, and the numerous investigations in the literature, a commercial engine with an IVP has not been built to date, due to the drawbacks in terms of weight and complexity [34]. Focusing on NVP dual-stream jets, Viswanathan [34] conducted a parametric experimental study to determine the effect, on both mixing and shock-associated noise, of a number of fundamental parameters: CNPR, FNPR, primary and secondary jet total temperatures, velocity ratio, forward flight, and nozzle geometry. The aim of this effort was to contribute to the understanding of a complex phenomenon, for which a model that is generally accepted and recognised within the research community is far from being achieved.

Viswanathan confirmed the strong dependence of the noise radiation features on the presence of a shock-cell system in the primary, secondary, or in both flows. He identified three main noise source regions: the inner shear-layer, the outer shear-layer, and the fully merged jet [34]. A strong shock-associated noise component radiating downstream is found to be generated for supersonic Mach numbers $M_{js} > 1$ in the

secondary flow [34], which is not affected by changes in the primary Mach number M_{jp} .

The primary jet temperature and secondary-to-primary velocity ratio, influencing turbulent mixing noise levels, are found to have minor effects on SCN [34]. Mixing noise increases as the primary flow is heated up, while the influence of the velocity ratio is dependant on the frequency range, as well as on the direction considered. The low and mid frequency noise contributions are believed to be generated by the fully merged jet, farther downstream than the primary nozzle exit plane. These contributions are amplified by an increase in the mixed jet velocity. The outer shear-layer is responsible for the high frequency noise components [34].

Forward flight effects are beneficial in terms of mixing noise reduction, while an amplification of the spectrum peaks from SCN follows an increase in flight speed, especially for the downstream radiation [34]. The nozzle geometry has a significant effect on the noise radiation from coaxial jets. Besides having different exit areas, the primary and secondary nozzles can be staggered, so that the outer nozzle exit section is located upstream from the inner one, as in Figure 1.3(a). The ratio of the distance between the nozzle exit sections x_d and the annulus height h is referred to as the recess ratio [34] and, together with the secondary-to-primary area ratio, is a fundamental geometrical parameter influencing dual-stream jet noise.

Focusing on the supersonic secondary jet and subsonic primary jet configuration of Figure 1.3(b), typical of current turbofan engines, two sets of interaction between the shock-cell system and the shear-layers occur. The shock-cell structure in the fan stream is confined between two shear-layers, both characterised by turbulent structures convected downstream and generating BBSAN, from the interaction with the shocks.

Two BBSAN components can therefore be identified [18, 41]. The first one behaves as in supersonic single-stream jets, decreasing in intensity while moving from upstream to downstream angles. This component is thought to be generated by the interaction of the shock-cell system in the secondary stream, with the turbulent structures convected in the outer shear-layer. The second BBSAN component has a different directivity and it is mainly radiated in the downstream direction. The interaction of the shock-cell system with the inner shear-layer generates this

contribution, characterised by higher frequency peaks [41].

For both BBSAN components, the peaks get broader in wave number by decreasing the angle from the jet axis. Tam *et al.* [41] derived analytical formulae relating the peak frequency and the directivity of the two BBSAN components, by using a stochastic instability wave model and generalised Fourier series, to model the pressure fluctuations associated respectively with turbulent structures (in both the inner and outer shear-layer) and with a shock-cell system.

The noise from dual-stream jets is also influenced by the confluence of the secondary flow with the primary flow. At the primary nozzle exit section, the secondary supersonic flow, that is following the primary convergent nozzle wall, turns to run parallel with the primary nozzle shear layer. This turning generates a shock in the secondary flow of intensity proportional to the deviation angle, which is trapped within the secondary flow and produces a second shock-cell system. The latter is typically weak for small turning angles [42], but it influences the shock-cell system geometry farther downstream.

In this research, a dual-stream jet configuration proposed by Airbus SAS is considered, as described in Appendix A, with the inner flow run subsonic and the outer flow supersonic and under-expanded, as in Figure 1.3(b). Both nozzles are convergent and run unheated air. The velocity profile is inverted (IVP) with the outer stream velocity $U_s > U_p$, where U_p is the inner stream velocity.

The selection of unheated air as the working fluid is to match experimental conditions at the Von Karman Institute for Fluid Dynamics, where the test facility could not generate heated air jets. This facility was developed by Guariglia [43], who provided reference measurements for the numerical aerodynamic and aeroacoustic predictions.

In the outflow from current turbofan engines, the velocity profile is of the normal type (NVP) with a higher inner velocity. However, the elevated temperature of the core flow increases the local speed of sound so that the primary flow Mach number M_p can be subsonic, as in the test case studied. The full-scale flow Mach numbers are therefore approximately reproduced by the model in Appendix A.

1.4 Acoustic source non-compactness in jets

Jet noise can be studied in the acoustic near-field and/or in the acoustic far-field. The acoustic far-field is typically defined as the region of \mathbb{R}^3 where the distance r between the source \mathbf{y} and the observer \mathbf{x} locations is large compared to the acoustic wavelength [44]: $r = |\mathbf{x} - \mathbf{y}| \gg \lambda$. In the far-field, a specific approximation (the Fraunhofer approximation [44]) can be applied when $r = |\mathbf{x} - \mathbf{y}| \gg \lambda$.

However, $r = |\mathbf{x} - \mathbf{y}| \gg \lambda$ is not a rigorous definition of the acoustic far-field, as there are several regions into which the acoustic domain can be split, according to the relative magnitude of the acoustic wavelength λ , the maximum extent of the source region L_{\max} (usually measured orthogonally with respect to the radiation direction \mathbf{r}) and the source to observer distance r . A comprehensive review of the relevant definitions can be found in Morfey [45], including hydrodynamic and geometric near-field, Fresnel region, Fraunhofer approximation and far-field criteria. The definitions of the Fresnel region and of the hydrodynamic/geometric near-field goes beyond the objective of this section, while the acoustic far-field criteria and the Fraunhofer approximation are discussed below and reported respectively in Equations 1.3 and 1.5. The reader is referred to the work by Morfey [45] for further details.

Following Morfey [45], the far-field can be defined as the region of \mathbb{R}^3 where the following relations are satisfied [45]

$$\begin{cases} r \gg \lambda, \\ r \gg L_{\max}^2/\lambda, \\ r \gg L_{\max}, \end{cases} \quad (1.3)$$

where the quantity L_{\max}^2/λ is referred to as the Rayleigh distance [45]. This distance represents the limit beyond which the high-frequency radiation from a coherent source region of finite extent approaches the far-field behaviour [45]. The other conditions express respectively the fact that in the acoustic far-field the distance between source and observer r needs to be much greater than both the characteristic wavelength of the sound waves λ and the maximum extension of the source region L_{\max} (compactness).

When Equation 1.3 is satisfied, the Fraunhofer approximation can be applied to estimate the pressure fluctuation to the acoustic far-field [44]. It is worth saying that,

the objective of the current research is the development of a code able to estimate near-field as well as far-field noise prediction from unsteady flows. Consequently, no far-field approximation is applied, and this holds for all the tests considered in Chapters 3 to 5.

For free-field radiation in a uniform medium at rest from an acoustic source \mathbf{y} , the disturbance emitted at a certain time will be perceived by a specific observer \mathbf{x} , after a time of flight that is required for sound to travel from \mathbf{y} to \mathbf{x} . Specifically, the travel time can be expressed as $|\mathbf{x} - \mathbf{y}|/c_0 = r/c_0$, with c_0 the speed of sound of the uniform medium. Also, the noise radiation will be attenuated by a factor which depends again on the distance $r = |\mathbf{x} - \mathbf{y}|$, but with inverse proportionality. The geometric scaling with distance from the source as well as the phase of the acoustic radiation are therefore dependent on the location \mathbf{y} considered.

The emission time is usually referred to as retarded time τ_{ret} and the time delay between the reception (observer) and the emission (source) is given by $t - \tau_{ret} = r/c_0$. Hereafter, τ_{ret} is called τ_e , where the subscript e is for emission, to make it clear that τ_e refers to the sound emission time. This enables to introduce the “advanced time” method in Section 2.2.2 with a distinct nomenclature with respect to the “retarded time” approach of Lighthill [1].

If there is more than one position $\mathbf{y}^{(i)}$, with $i = 1 \dots N_y$ and $N_y > 1$, from which sound is generated, then the sound at receiver \mathbf{x} is obtained by summing over all N_y source positions $\mathbf{y}^{(i)}$. Equivalently, by considering a continuous source distribution $\mathcal{Q}(\mathbf{x}, t)$, the pressure fluctuation at receiver \mathbf{x} at time t is given by the following integral [44]:

$$p'(\mathbf{x}, t) = \frac{1}{4\pi} \int_{\mathbb{R}^3} \frac{\mathcal{Q}\left(\mathbf{y}, t - \frac{|\mathbf{x} - \mathbf{y}|}{c_0}\right)}{|\mathbf{x} - \mathbf{y}|} d^3y. \quad (1.4)$$

The source function \mathcal{Q} inside the integral in Equation 1.4 is evaluated at emission time τ_e , given by subtracting the travel time $|\mathbf{x} - \mathbf{y}|/c_0$ to the reception instant t , and the attenuation factor is proportional to $1/|\mathbf{x} - \mathbf{y}|$. In order to correctly estimate the sound radiation to the near-field, differences in both travel time and attenuation factor within the source region need to be accounted for.

On the other hand, when Equation 1.3 is satisfied, the Fraunhofer approxima-

tion [44]

$$\begin{cases} \frac{|\mathbf{x}-\mathbf{y}|}{c_0} \approx \frac{1}{c_0} \left(|\mathbf{x}| - \frac{\mathbf{x}\cdot\mathbf{y}}{|\mathbf{x}|} \right), \\ \frac{1}{|\mathbf{x}-\mathbf{y}|} \approx \frac{1}{|\mathbf{x}|}, \end{cases} \quad (1.5)$$

allows simplification of Equation 1.4 to

$$p'(\mathbf{x}, t) \approx \frac{1}{4\pi |\mathbf{x}|} \int_{\mathbb{R}^3} \Omega \left(\mathbf{y}, t - \frac{|\mathbf{x}|}{c_0} + \frac{\mathbf{x}\cdot\mathbf{y}}{c_0 |\mathbf{x}|} \right) d^3y. \quad (1.6)$$

It can be noticed that differences in the scaling factor are neglected in the Fraunhofer approximation, while the emission time needs still to be calculated over the whole source region in order to perform the integration correctly.

An important distinction related to the extension of the source region is between compact and non-compact sources. An acoustically compact source is defined as having a small characteristic dimension L_{\max} compared to the acoustic wavelength λ it generates: $L_{\max} \ll \lambda$. For non-compact sources, an observer in the near-field will perceive sound generated from different locations \mathbf{y} within the acoustically active volume, as arriving from different emission times τ_e and attenuated with a different scaling factor. In the far-field, the Fraunhofer approximation expressed by Equation 1.5 is valid, and the differences in scaling factor can be neglected, while the travel time will approach a constant limit.

For a compact source distribution $\Omega(\mathbf{x}, t)$ over a source region \mathcal{V}_s , a further approximation (Equation 1.7) is available in the acoustic far-field. If the overall source strength obtained by integrating $\Omega(\mathbf{x}, t)$ over the whole acoustically active volume \mathcal{V}_s is significantly different from zero, the compact region is seen by an observer in the far-field as a point source (monopole) and both changes in scaling factor and travel time due to the extent of \mathcal{V}_s can be neglected [46] in Equation 1.4. By placing the origin of the reference system within \mathcal{V}_s , the distance source observer $|\mathbf{x} - \mathbf{y}|$ can be approximated by $|\mathbf{x}|$:

$$\begin{cases} \frac{|\mathbf{x}-\mathbf{y}|}{c_0} \approx \frac{|\mathbf{x}|}{c_0}, \\ \frac{1}{|\mathbf{x}-\mathbf{y}|} \approx \frac{1}{|\mathbf{x}|}. \end{cases} \quad (1.7)$$

If the overall strength of the source distribution is zero, the compact source distribution can still be approximated by a point source (dipole) if the first spatial moment of the source strength [47], integrated over the acoustically active volume

\mathcal{V}_s , gives a finite value [46]. If both the integral of the source strength and its first moment are equal to zero, the condition needs to be applied to the moment of the next order (quadrupole moment) [46].

In summary, the point source approximation for a compact source in the far-field is valid when the source strength distribution $\mathcal{Q}(\mathbf{x}, t)$ (or its moments) integrated over the whole acoustically active region \mathcal{V}_s is found to be different from zero. The strength of the point source is equivalent to the minimum order moment of the source strength $\mathcal{Q}(\mathbf{x}, t)$, which integrated over the whole source region \mathcal{V}_s , gives a value that is significantly different from zero. This approximation is not valid in a jet flow, where the volume of the acoustic sources that are active has approximately a conical trunk shape, with axial length and base diameter of the order of several jet diameters D_e . Therefore, in the jet noise tests considered in Chapters 4 and 5, the source field is extended and non-compact.

Where non-compact source regions are considered, the time of flight of each disturbance, generated from each position \mathbf{y} in the source field, to an observer \mathbf{x} needs to be correctly estimated, so as to obtain an accurate prediction of both the acoustic near and far-field. This process represents a numerical complexity [48] that can be addressed with two different approaches, referred to as the “retarded time” approach and the “advanced time” approach, respectively (Section 2.2.2).

1.5 Approach to modelling jet noise

The noise generated by unsteady flows can be predicted by different approaches [49] that can be first classified as either one-step [50] (such as direct CAA), or hybrid methods [51] (*e.g.* acoustic analogies). The main difference between these two categories is in the way the phenomena of noise generation by unsteady flows and of noise propagation in the surroundings are treated.

The approach followed in the present work is the use of a numerical implementation of the Ffowcs Williams and Hawkings (FW-H) acoustic analogy on time and space resolved jet flow predictions. The FW-H acoustic analogy [52] is a method for extrapolating unsteady flow data defined on a closed surface outwards into the acoustic field. The intended output is a FW-H noise extraction software package

that can be used as an advanced signal processing tool on numerical simulations, experiments, and reduced order models of unsteady, unbounded single and dual-stream jets. The main challenge is the prediction of noise in the acoustic near-field, where the acoustic sources are non-compact (Section 1.4) and the far-field approximation becomes invalid. This involves the correct evaluation of the acoustic source emission time (Section 2.2.2), in addition to the source amplitude and phase.

The implementation of the FW-H acoustic analogy is first carried out in the advanced time formulation [53], described by Casalino [54] (Section 2.2.3). This is followed by a second implementation (Section 2.2.4) that uses a convective FW-H formulation by Najafi-Yazdi *et al.* [55]. This is still an advanced time formulation, but it also takes into account the flight velocity, by directly including the effect of a uniform co-flow surrounding the jet in the acoustic analogy equation.

Both formulations are coded in Python and embedded in Antares 1.4.0 [12]. Antares is a software package of wide access and usability developed by Cerfacs, France, which provides post-processing tools for CFD. The availability in Antares [12] of input and output data interfaces, for popular structured and unstructured CFD geometries and solutions, provides a good starting point for developing a FW-H extractor of wide access and usability. The aim is to build a numerical tool that is accessible to the wider research community to use, develop, and improve.

1.6 Thesis outline

The thesis is structured as follows: the methodology is described in Chapter 2, while the validation and the main results are reported in Chapters 3–5. The numerical implementations of the FW-H formulations in Casalino [54] and in Najafi-Yazdi *et al.* [55] are presented in Sections 2.2.3 and 2.2.4 respectively. The acoustic analogy theory is introduced in Section 2.1.2.1, and the standard and the porous FW-H analogies are detailed respectively in Sections 2.2 and 2.2.1. CAA techniques alternative to the selected FW-H approach are briefly outlined in Section 2.1.

The validation and the main applications from the stationary advanced time formulation [54] are reported respectively in Chapters 3 and 4. Elementary sources of increasing complexity are considered in Chapter 3, by progressing from an omnidi-

rectional source in Section 3.1.1 (monopole), to a dipole source in Section 3.1.2, and to two types of quadrupole sources in Sections 3.1.3 and 3.1.4. The noise radiation from three different jet configurations is investigated in Chapter 4. Single-stream jets are considered in Section 4.1 with both subsonic (Section 4.1.1) and supersonic (Section 4.1.2) nozzle exit conditions, while a dual-stream under-expanded jet test case is discussed in Section 4.2.

The convective acoustic analogy applications are discussed in Chapter 5. Section 5.1 validates the convective acoustic analogy implementation on elementary sources. In Section 5.2, the effects of forward flight on both mixing noise and SCN radiation from a single-stream under-expanded jet are discussed. The main results of the thesis are summarised in Chapter 6, highlighting the key advances (Section 6.1) with respect to the state of the art and the significance of the achievements. Considerations for future work are finally given in Section 6.3.

Chapter 2

Methodology

This chapter presents the analytical development and the numerical implementation of the aeroacoustic models that have been used for obtaining the results presented in Chapters 3–5. Specifically, the stationary jet noise predictions in Chapter 4 are obtained by an implementation of the Casalino advanced time formulation [54], described in Section 2.2.3. The noise radiation from jets with co-flow discussed in Chapter 5 is modelled through the convective acoustic analogy formulation by Najafi-Yazdi *et al.* [55], discussed in Section 2.2.4.

An overview of the currently available aeroacoustic approaches is presented in Section 2.1 to contextualise the motivation behind the choice of two specific acoustic analogies. A concise description of the different acoustic analogies developed over the last half century based on the seminal work of Lighthill [1], Lilley [56], and Ffowcs Williams and Hawkings [52] is given in Section 2.1.2.1. Section 2.2.1 then focuses on the porous FW-H formulation. For a comprehensive review of aeroacoustic techniques, the reader is referred to Colonius & Lele [57], and Kurbatskii & Mankbadi [49]. Bennet *et al.* [58] describe the current aeroacoustic research field in Europe. Finally, the details of the numerical implementation of both the FW-H formulations used in Chapters 3–5 are presented in Section 2.3.

2.1 Aeroacoustic techniques

An overview of the different approaches available in aeroacoustics is given in this section. The direct computation of sound is discussed first, in Section 2.1.1, and

hybrid approaches are then presented in Section 2.1.2. Four hybrid method options are discussed, which are the acoustic analogy (Section 2.1.2.1), the Kirchhoff integral method (Section 2.1.2.2), the incompressible/acoustic split (Section 2.1.2.3), and the vortex sound theory (Section 2.1.2.4).

The Kirchhoff method is shown to be a particular case of the FW-H porous acoustic analogy in Section 2.2.1 and the direct computation of sound presents some limitations, specifically in its application to predicting far-field noise. This led the author together with the supervisory team to choosing the acoustic analogy approach for unsteady CFD predictions.

The AeroTraNet2 project briefly introduced in Appendix A was aimed to address all the aspects of the modelling of the noise radiation from a supersonic dual-stream jet, including numerical, experimental and theoretical research. Direct computation of sound methods were applied by Mancini [15] and Pérez [16] to estimate the noise radiation to the near-field of the supersonic dual-stream test case (Appendix A) investigated in the AeroTraNet2 project. The use of an integral method to project the noise radiation to the near-field and far-field outside the CFD domain is therefore complementary to references [15] and [16], and it allowed both interchange of data and comparison of acoustic results between numerical partners.

Vortex sound theory and incompressible/acoustic split techniques are less widely used in the literature and appear less generally applicable than the FW-H porous acoustic analogy. Consequently, the acoustic analogy approach has a wider database of validations and implementations reported in the literature than other CAA approaches.

The implementation of the formulations detailed in Section 2.2.3 and 2.2.4 is a well-established numerical procedure, once appropriate expressions for the monopole, dipole, and quadrupole contributions are obtained analytically. The challenges are the numerically-efficient estimation of the emission time, which is addressed in Section 2.2.2, and the application to a dual-stream jet noise configuration, which has not hitherto been investigated in the literature for the prediction of both near and far-field noise, including radiation from non-compact sound sources and forward flight effects.

2.1.1 Direct computation of sound

The main challenge in the direct computation of sound, which is also referred to as a one-step simulation [50], is in the necessity of designing a numerical model that properly simulates two phenomena characterised by significantly different length scales and numerical requirements. In this approach, a single simulation predicts the pressure fluctuation at any given observer position by resolving both the unsteady vortical motion of the fluid, which is governed by the compressible Navier-Stokes equations and is responsible for the noise generation, and the noise radiation outside the turbulent flow, which follows the laws of acoustics. The numerical requirements for resolving the unsteady flow field and the noise radiation are significantly different and somehow contrasting, as reported in Section 1.2.

From a numerical viewpoint, to perform a direct computation of sound, not only the computational mesh needs to include both the source and observer locations, but also there are stringent numerical requirements to be satisfied for the solution to be accurate [30], as explained in Section 1.2. The affordability of the domain extent to include the observer positions in the computation depends on many factors, such as the specific geometry of the problem, the flow conditions, the available resources, and the required spatial and temporal resolutions. Whilst this approach allows to take into account flow/sound interaction effects [50], by solving directly the unsteady flow field (noise generation) and its noise radiation, it is computationally demanding and, at present, it does not represent a generally applicable technique.

Direct noise computations are currently restricted to a small number of flows [57] that can be modelled either by a Direct Numerical Simulation (DNS), to resolve the whole range of turbulent scales in the flow, or by a Large Eddy Simulation (LES), which resolves the larger energy-containing scales by filtering out the sub-grid scales. Sample DNS applications to jet noise are given by Freund, both for subsonic [59] and supersonic [60] jets.

As far as cabin noise is concerned, the geometry of current wide-body civil aircraft could make direct noise computations feasible. An investigation of this approach using Implicit LES (ILES) was published by the author in collaboration with the supervisory team in Rona *et al.* [62]. In this work, a regional civil transport aircraft is considered, for which the distance between the jet axis and the fuselage is relatively

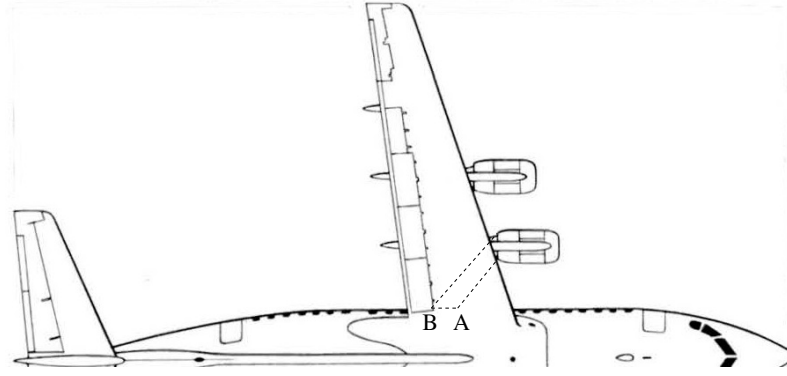


Figure 2.1: Plan view of a regional civil transport aircraft showing the cabin position relative to the inboard engine bypass nozzle. Plan view adapted from “Jane's all the world's aircraft” [61].

small, as shown in Figure 2.1. An axisymmetric domain is used to reduce the computational cost compared to a three-dimensional flow model. The results show that, within the limitations of the axisymmetric geometry, it is possible to directly estimate the noise radiation to the cabin (located in the acoustic near-field), with limited computational resources [62].

In many other cases, a direct sound computation is either not affordable with current computing facilities or requires lengthy simulations. Therefore, an approach that splits the two phenomena of sound generation and propagation is preferable. This allows to extend the solution to the acoustic near-field and to the acoustic far-field, while confining the full unsteady CFD simulation to a smaller control volume (see also Figure 2.2, Section 2.1.2.1). The computational cost is therefore decreased and the overall numerical requirements are less stringent than in a one-step simulation.

Mankbadi *et al.* [63] discuss the direct noise computation of supersonic jets, comparing it to a Lighthill analogy approach. They argue that a direct noise computation is far more computationally expensive than the Lighthill analogy approach, while the latter struggles to deal with acoustically non-compact sources. However, non-compact acoustic sources can be taken into account by the proper estimation of the emission time of each disturbance reaching the observer locations, as reported in Section 2.2.2, provided they are fully contained within the boundaries of the Lighthill analogy integration volume.

Di Francescantonio [64] and Lyrintzis [48] also argue that the direct noise computation is not a practical method for all aeroacoustic problems, because of the typically large distance between the source region and the observer location in common engineering applications.

Colonus [57] highlights the limitations of the direct computation of sound. Given its high computational cost, this method used to be confined to idealized geometries. Over the last two decades, it has started producing results of engineering relevance, by simulating realistic flows [27, 59, 60]. Colonus highlights the important role of the direct computation of sound in the development of theoretical models, by reproducing the physics of the problem in a progressively more accurate way.

Separating the aerodynamic and the aeroacoustic simulations usually offers the possibility of a better insight into the problem and the use of different physical models describing the flow, in regions where the flow follows different simplified laws. From a practical viewpoint, hybrid methods also offer the possibility to run different aeroacoustic simulations on the same CFD dataset, by storing the solution of the acoustically active region. This is especially convenient with surface integral methods, such as with the Kirchhoff method or with the FW-H porous surface approach, when the quadrupole noise contribution is negligible.

2.1.2 Hybrid methods

An alternative to a one-step aeroacoustic simulation is provided by hybrid methods, such as the acoustic analogy. Hybrid methods are typically used for estimating both the near-field and the far-field noise from unsteady flow predictions (see Section 1.4 for the acoustic near-field and far-field definition). Hybrid methods require the coupling of separate hydrodynamic and aeroacoustic simulations. The flow field is modelled first, for instance by time-dependent CFD simulations. The unsteady hydrodynamic flow field is then given as input to the aeroacoustic solver, which estimates the noise radiation to arbitrary observer positions. At each acoustic time step, this process is repeated, in order to build up a pressure time history at the observer positions, which is then stored. By splitting the generation of the flow field data from the evaluation of the acoustic pressure at the observer positions, it is possible to obtain a CAA tool of more general applicability than by a direct noise

computation. In this process, a simple data structure interface needs to be developed, so that custom CFD output can be read by the CAA solver.

Despite their computational cost advantage, hybrid approaches do not model explicitly the interactions between the flow and the noise it generates. In the acoustic analogy, for instance, it is assumed that the noise active flow region solved by the CFD simulation has a finite extent and that it can be isolated from an “acoustic source free” domain. The flow/acoustic interactions are usually included in the source term of the inhomogeneous wave equation integrated by the aeroacoustic solver. This source term is estimated from the unsteady flow field prediction.

Therefore, acoustics and aerodynamics, which are coupled in the direct approach, are separated in the acoustic analogy and in the other hybrid techniques and the two phenomena of noise generation and propagation, which are modelled by using different assumptions, are treated separately. An approach that gives a better insight of the physics is preferable, ultimately allowing the investigation of where and how to intervene to reduce noise generated aerodynamically.

In the next sections, an introduction to the acoustic analogy theory is given first (Section 2.1.2.1), followed by three examples of different hybrid methods, *i.e.* the Kirchhoff integral method (Section 2.1.2.2), the viscous/acoustic split (Section 2.1.2.3), and the theory of vortex sound (Section 2.1.2.4).

2.1.2.1 Acoustic analogy

Sir James Lighthill is credited with laying the foundations of aeroacoustics, which is a branch of aerodynamics dealing with the generation of noise by fluid motion. From his seminal work [1], many acoustic analogy formulations and alternative approaches have been developed.

Lighthill's approach is referred to as an acoustic analogy, because it establishes a parallel between sound propagation in a physical turbulent flow and in an ideal uniform medium at rest. In the latter medium, a non-linear wave equation derived exactly from the compressible conservation laws is integrated to estimate the radiated sound. Whilst this is a relatively simple theoretical framework, the propagation in a turbulent flow remains a complex phenomenon, characterised by both linear and non-linear effects, as well as by the interaction between several physical mechanisms

that are not yet fully explained by aeroacoustic researchers.

An important aspect enlightened by Lighthill [1] concerns the flow energy budget. A very small fraction of the flow kinetic energy propagates as sound after the conversion from kinetic to acoustic energy, as opposed to being dissipated by viscous stresses. This makes the acoustic pressure fluctuation amplitude far smaller than its hydrodynamic counterpart, which does not radiate as sound. Resolving the interaction between these very different energy scales is a significant modelling challenge in CAA.

The sound produced by a turbulent flow interacts with the complex flow structures across different scales and frequencies, giving rise to sound convection and propagation with a variable speed, as well as refraction, and sound scattering phenomena [1]. Taking into account all these complexities is not trivial and Lighthill developed a simple concept to tackle them. By rearranging the Navier-Stokes equations, he obtained a convenient formulation in the form of an inhomogeneous wave equation for a uniform medium at rest,

$$\square^2 [c_0^2 (\rho - \rho_0)] = \frac{\partial^2 T_{ij}}{\partial x_i \partial x_j}, \quad (2.1)$$

where $\square^2 = (1/c_0^2) \partial^2 / \partial t^2 - \partial^2 / (\partial x_j \partial x_j)$ is the d'Alembertian or linear wave operator, c_0 and ρ_0 are, respectively, the constant sound speed and the unperturbed density in the uniform medium of the analogy, and T_{ij} is the Lighthill stress tensor. The mathematical details of the Lighthill acoustic analogy are reported in Appendices B and C.

Adopting this approach, sound can be considered as if generated in a uniform medium at rest and the noise estimation is reduced to the evaluation, in the acoustically active flow region, of the quadrupole-type source term which appears on the right-hand side of Equation 2.1:

$$\begin{aligned} T_{ij} &= \rho u_i u_j + P_{ij} - c_0^2 \rho \delta_{ij}, \\ P_{ij} &= p \delta_{ij} - \tau_{ij}, \end{aligned} \quad (2.2)$$

where P_{ij} is the compressive stress tensor and δ_{ij} is the Kronecker delta. Lighthill assumed that this term, representing time-dependent stresses acting upon a linear acoustic medium, is known or can be modelled from an unsteady flow field prediction. Once the Lighthill stress tensor T_{ij} is known, the radiated sound to an arbitrary

position (\mathbf{x}, t) can be calculated, by evaluating the integral solution of Equation 2.1 in terms of the acoustic density fluctuation as:

$$4\pi c_0^2 (\rho(\mathbf{x}, t) - \rho_0) = \int_{\mathcal{V}_s} \frac{\partial^2}{\partial y_i \partial y_j} T_{ij} \left(\mathbf{y}, t - \frac{r}{c_0} \right) \frac{d^3 y}{r}. \quad (2.3)$$

In Equation 2.3, \mathbf{y} and \mathbf{x} are, respectively, the source and the observer positions, $t - r/c_0$ is the emission time τ_e , and $r = |\mathbf{x} - \mathbf{y}|$ is the source-observer distance.

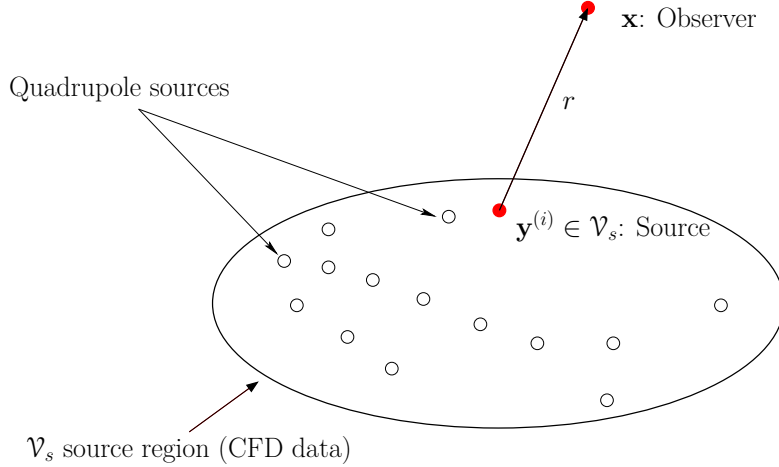


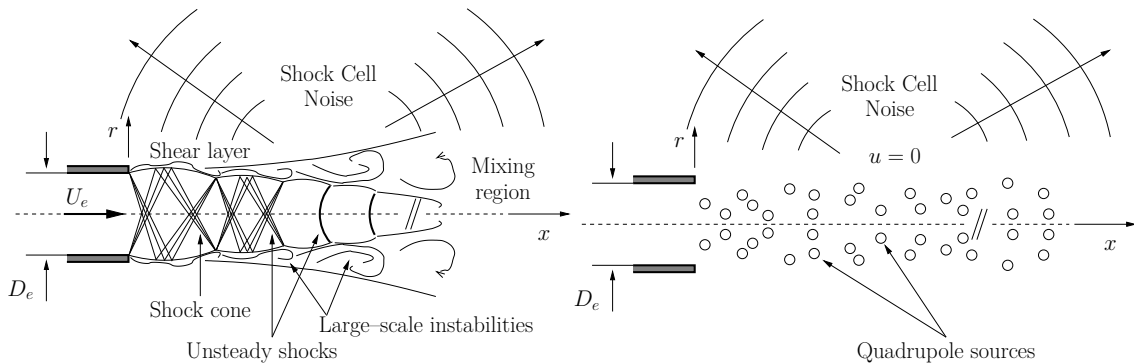
Figure 2.2: Schematic of the acoustic analogy approach.

Figure 2.2 schematically shows the general concept of the acoustic analogy. The acoustically active region is defined by the volume \mathcal{V}_s where quadrupole point sources are distributed in order to reproduce the acoustic radiation in the outer domain. An elementary source $\mathbf{y}^{(i)}$ radiating to the observer located at \mathbf{x} is also shown. The acoustically active region, which can have theoretically an infinite extent, needs to be confined to a finite domain where flow field variables are computable, for instance by CFD. This allows the estimation of the Lighthill stress tensor T_{ij} and of its derivatives in Equation 2.3. By integrating Equation 2.3 over the volume \mathcal{V}_s , the acoustic density fluctuation $\rho(\mathbf{x}, t) - \rho_0$ can be estimated for an arbitrary observer position \mathbf{x} .

In 1954, Lighthill [65] investigated turbulence as a source of sound and obtained results in good agreement with previous experiments for a subsonic cold jet. He found a first confirmation of the acoustic power law $P \propto U_e^8$ he derived analytically in 1952 [1]. Furthermore, he assessed the broadband nature of the jet noise phenomenon for a subsonic cold jet. The latter is characterized by low frequency components

emitted at small angles from the jet axis, in a region mainly confined between 5 and 20 jet diameters D_e from the nozzle exit section. Higher frequency components are also emitted, radiating at higher angles from a region closer to the nozzle lip [65]. These high frequency components are affected by the mean flow refraction effect and their radiation is characterised by the presence of a “cone of silence”, as previously discussed in Section 1.2.

In the Lighthill [65] acoustic analogy, convection effects are modelled as moving noise sources in T_{ij} . Ffowcs Williams [7] corrected Lighthill's analysis for distributed moving sources, and extended it to account for transonic and supersonic speed steady convection of sources, deriving the dependence of the acoustic power P from high-speed jets with the third power of the jet velocity: $P \propto U_e^3$.



(a) Noise radiation from a turbulent under-expanded jet. (b) Noise radiation modelled by the Lighthill acoustic analogy.

Figure 2.3: Schematic of the Lighthill acoustic analogy model for turbulent jets.

In Figure 2.3, a turbulent jet is compared with the uniform medium at rest in the acoustic analogy approach. In Figure 2.3(a), the schematic representation of the under-expanded jet shows both the aerodynamic features of the flow and the noise radiation with downstream and upstream components, which were briefly introduced in Section 1.2 for single-stream jets and in Section 1.3 for coaxial jets. In Figure 2.3(b), the same phenomenon of noise radiation is modelled with a volume distribution of quadrupole sources in the jet shear layer, which reproduces the same acoustic propagation as the real flow. In this acoustic analogy, the noise propagates in a uniform medium at rest, following the linear wave equation of acoustics. All flow turbulence effects are included in the volume distribution of T_{ij} , which also accounts for any flow non-linearity.

Lilley [56] highlighted the importance of the term $(p - c_0^2\rho) \delta_{ij}$ in the Lighthill stress tensor for hot jets, deriving a dependence of the acoustic power $P \propto U_e^4$ for very low Mach number flows [66]. Morfey [67] stressed the importance of flow inhomogeneities in the sound radiation to the far-field, obtaining a modified acoustic power law with a 6th power rather than an 8th power [1], when considering a turbulent jet with local density different from the surrounding quiescent and uniform medium.

Ffowcs Williams and Hawkings [52] tried to develop a general expression for sources in arbitrary motion convected in a turbulent flow, confirming Curle's theory in which boundaries are modelled with a surface distribution of dipole sources [68].

A considerable complexity neglected by Lighthill is the presence of solid boundaries, which occurs in jet noise problems in which the nozzle lip is modelled. Curle [68] discussed the influence of rigid bodies on the noise radiation. He observed that a solid boundary in a turbulent flow reflects and diffracts the sound waves generated by the quadrupole source of Lighthill's theory.

Mathematically, the solid boundary limits the quadrupole source distribution to the region external to the solid body. To take account of this, Curle [68] added a surface integration term to the integral solution proposed by Lighthill, modelling the solid boundary effects with a surface distribution of dipole-like sources on the boundary itself.

Many researchers developed the Lighthill acoustic analogy concept by taking into account additional complexities. Their goal has been to formulate a more practical and applicable model, which is able to generate quantitative noise predictions for a number of unsteady turbulent flows. The assumption that the Lighthill stress tensor of Equation 2.2 is known or can be modelled from an independent flow field prediction is legitimate in many simple cases and Lighthill's theory allows the estimation of the radiated sound in such cases. Nevertheless, in many applications, this estimation is very challenging.

The Lighthill stress tensor T_{ij} is often approximated by its first term $\rho u_i u_j$, representing the momentum flux per unit area in the i^{th} direction generated from fluid crossing a control volume surface in the j^{th} direction [56]. Both the viscous effects, that are small for high Reynolds number flows, and the non-isentropic contribution $(p - c_0^2\rho) \delta_{ij}$ are neglected in this approximation. Besides, the fluid

density ρ in T_{ij} is usually replaced by its mean value ρ_0 . Following the Lighthill approximation, assuming that velocity fluctuations in the unsteady flow are not dependent on density fluctuations and can be estimated from an incompressible flow problem, the left-hand side (LHS) and the right-hand side (RHS) of Equation 2.1 are independent from one another. The resulting approximation for the Lighthill stress tensor $T_{ij} \approx \rho_0 u_i u_j$, first proposed by Lighthill [1] for flows with small temperature non-uniformities, is not generally valid and its applicability is restricted to low Mach number acoustically compact flows [69].

To overcome these complexities, Lilley [56, 70, 71] proposed a different version of the acoustic analogy, by deriving an inhomogeneous moving medium wave equation for the sound radiation process, considering a steady parallel shear flow instead of a medium at rest. A third-order wave equation with a non-linear source term is obtained. A third-order wave operator appears on the LHS of the equation, applied to a modified pressure-based dependent variable. The source term on the RHS of the equation has a more complex form than in the Lighthill analogy, which does not offer an intuitive physical interpretation. Nevertheless, the main advantage of the Lilley formulation is that first order pressure disturbance components, representing refraction, diffraction, and convection by the turbulent flow, are not considered as sources, but are included in the wave operator [56]. In this way, flow/acoustic interaction effects are directly taken into account in the “propagation part” of the Lilley equation [56]. Furthermore, the latter shows the importance of mean velocity and of mean temperature distribution effects on the radiated sound, through the third-order wave operator form [56, 70, 71].

Many researchers focused on the importance of the flow/acoustic interaction effects [72] for predicting noise from unsteady turbulent flows. Lilley [70] argued that these effects, although included in the Lighthill stress tensor, are better addressed by considering a more realistic base flow than a uniform medium at rest. He showed that these effects become more important in heated jets. Goldstein tried to model the flow/acoustic interaction effects through asymptotic expansions of the disturbances [73].

A number of acoustic analogies involving a convective non-linear wave operator, eventually linearised before getting noise estimations, were proposed by many authors

[74, 75, 76, 77, 78]. The complexity of the formulation increases in these developments, but the analytical cost is compensated by not requiring the Lighthill source field term of Equation 2.2 to be estimated. A review of these acoustic analogy theories is given by Lilley [70].

Following the approach stated by Lilley and developing it, Goldstein [79] tried to find a more general formulation, recovering Lilley's equation [56] as a particular case of such a general formulation. Starting from the Navier-Stokes equations, Goldstein decomposed the flow field variables into a base flow and a residual component. The result is a general set of Linearised Inhomogeneous Euler equations (LIE) that establishes an analogy between the fluctuations in a real flow and the inviscid fluctuations about an arbitrary base flow. This generalised acoustic analogy theory takes into account the fluctuating component of the velocity field in the noise radiation process.

Goldstein's work [79] attempts to unify many different approaches using the LIE for modelling noise propagation. In the homogeneous case, a non-trivial root of the Linearised Euler Equations (LEE) is an instability wave solution of the Kelvin-Helmholtz type that is unbounded and can contaminate the acoustic field [57]. In many approaches, this homogeneous solution is suppressed with some numerical technique [80, 81]. In his generalised acoustic analogy theory [79], Goldstein proposed a tailored base flow that can be used to make the homogeneous solution bounded, allowing noise prediction through the LIE. Goldstein [82] highlighted the importance of instability waves in jet noise radiation problems and investigated their effect by proposing a non-parallel convecting mean base flow.

Despite the development of a number of acoustic analogy formulations that attempt to improve on the Lighthill acoustic analogy, the FW-H acoustic analogy, discussed in Section 2.2, has become the most widely used acoustic analogy approach. Progress in the computational power of high-performance computers suggests that a major development would be the application of the FW-H acoustic analogy with the estimation of both surface and volume integrals, which is still a challenge with the current computational resources.

2.1.2.2 The Kirchhoff formulation

The Kirchhoff formula was first published in 1883 [83]. Most recently, Lyrintzis [84] produced a review of the application of this theory in aeroacoustics, referring to the methodology as a surface integral method [48].

The basic concept of the Kirchhoff method, which is derived under the assumption of linear acoustic disturbances, is the use of a control surface on which the pressure and its surface normal and time derivatives are estimated, typically by numerical methods. The acoustic pressure in the far-field can then be obtained from an integration over this control surface of the above mentioned quantities.

The noise propagation to the surroundings is assumed to follow the linear wave equation and the control surface is required to enclose all the non-linearities of the flow and all the noise sources. Consequently, the Kirchhoff method does not allow the presence of any non-linearity on or outside the control surface. This represents a limitation with respect to the FW-H acoustic analogy method, described in Section 2.2, that allows the placement of the control surface in the non-linear region of the flow. In the Kirchhoff method, the position of the integration surface is therefore critical, typically requiring a larger computational domain compared to the FW-H acoustic analogy method.

Differently from the Kirchhoff and from the FW-H methods, the Lighthill acoustic analogy described in Section 2.1.2.1 includes only a volume integral contribution of the quadrupole type, without the use of a control surface. The same quadrupole term appears in the FW-H acoustic analogy (Section 2.2), which includes both volume and surface integration. Possible non-linearities outside the FW-H control surface are included in the quadrupole source term integrated over the volume external to the surface itself. Therefore, the full FW-H integral solution requires an expensive volume integration with a consequent increase in the computational effort with respect to Kirchhoff methods. However, also when this volume integration is neglected, the FW-H acoustic analogy appears to give more accurate results compared to the Kirchhoff method [85], for a given size of the integration surface.

The first Kirchhoff formulation [83] was limited to a stationary control surface integration. Morgans [86] extended the use of the method to moving control surfaces, introducing the use of Green's functions in this integral method. Ffowcs Williams

and Hawkings [52] derived a general formulation to deal with the effect of arbitrarily moving surfaces on the generation of sound, which represents a fundamental link between the acoustic analogy theory and the surface integral methods for aeroacoustics. Hawkings [87] applied the Kirchhoff formula to a transonic open rotor, introducing the idea of using a surface, surrounding the rotating blades, which follows the helicopter moving at the flight forward speed.

Notwithstanding the generalization obtained by Ffowcs Williams and Hawkings [52], their modification to the original theory presented a numerical complication, as the time and space derivatives are taken in the observer reference frame. Farassat and Myers [88] found a formulation that prevents the numerical issue of evaluating space and time partial derivatives in the observer reference system. They brought these derivatives in the source frame, which made their estimation more practical from a computational viewpoint. They showed that their development represented a more general formula, applicable to both deformable and rigid piecewise smooth moving surfaces. In this framework, they included the original Kirchhoff formula [83] for stationary surfaces as a special case.

Extended Kirchhoff methods have been proposed by many authors, by including additional non-linearities in the region outside the control surface, where a volume integration is therefore required [48]. These are Kirchhoff-type methods in the sense they start from the use of a surface integral approach, including then volume integral non-linear terms. An example of this “Kirchhoff/Lighthill” approach is given by Pilon & Lyrantzis in 1998 [89], who applied this methodology to supersonic jets.

Mitchell *et al.* [90] applied a Kirchhoff stationary-surface integral method to a jet noise problem. An application of the moving-surface Kirchhoff approach with a uniform surface velocity can be found in Morris *et al.* [91] and in Lyrantzis & Mankbadi [92].

2.1.2.3 Viscous/acoustic split

The viscous/acoustic split is a hybrid method in which the noise radiation is estimated in two separate steps. First, the time-dependent flow is solved with a set of incompressible viscous equations. Then, linearised inviscid compressible equations allow the estimation of sound radiation. Hardin & Pope [93] first proposed the

viscous/acoustic split theory and applied it to estimate the noise radiation from a flow over a two dimensional cavity [94]. In this first formulation, a density correction was applied to the constant incompressible density, after the unsteady flow was predicted by solving the incompressible Navier-Stokes equations. The sound radiation was finally estimated by considering acoustic fluctuations as perturbations to the incompressible flow solution.

Shen & Sørensen [95] revised the theory by Hardin & Pope, claiming that the formulation presented some inconsistency. They proposed a modified version of the aerodynamic/acoustic splitting technique, investigating sound radiation from low-speed flows over a circular cylinder [96] and over a turbulent aerofoil [97]. Ewert & Schröder [98] proposed a model in which a source term, estimated through either an incompressible or a compressible flow field prediction, provides the forcing to a set of linearised equations for the acoustic perturbation. They obtained good results for simple source tests and for a circular cylinder in a transverse flow problem. While investigating the tonal component emitted by a flow over a circular cylinder, Cheong *et al.* [99] proposed a new formulation of the incompressible/acoustic split. An incompressible Reynolds Averaged Navier-Stokes (RANS) simulation is used for the estimation of a more complex source term, of the Lighthill type, which provides the input to the acoustic model, based on the Linearised Euler Equations (LEE).

The hypothesis that all the compressibility effects are originated from the acoustic irrotational field [100] confines the application of viscous/acoustic splitting techniques to low Mach number flows, including non-compact sources [101]. A new formulation of the theory should be developed to extend its applicability to supersonic flows.

2.1.2.4 Theory of vortex sound

In 1964, Powell [102] first proposed the theory of vortex sound, which follows a different concept from the acoustic analogy and represents a different approach in aeroacoustics, to which many authors have contributed. Powell argued that both the hydrodynamics and the acoustics of a flow are governed by vorticity fluctuations in low Mach number turbulent flows [76]. Acoustic sources are associated with limited regions of flow in which the vorticity vector is non-vanishing, rather than to the whole hydrodynamic field as in Lighthill's theory [76].

Howe [76] tried to develop a revised formulation of the Lighthill acoustic analogy, able to deal with problems characterized by an extended region of non-uniform flow, in which a non-uniform base flow is more appropriate than the uniform medium at rest of Lighthill's theory. He proposed the stagnation enthalpy as acoustic variable, identifying the source terms of such acoustic variable as confined in regions of non-vanishing vorticity and entropy gradients [76], so to develop a revised version of the vortex sound theory of Powell [102].

Howe [44] gives a complete and exhaustive explanation of the vortex sound theory, focusing on trailing edge scattering problems. He defines vortex sound as the branch of fluid mechanics dealing with the conversion between rotational kinetic energy in a turbulent flow and longitudinal disturbances corresponding to sound waves. He argued that Lighthill's equation can be rearranged by showing the importance of the vorticity in the sound production [44]. To do so, the total enthalpy is chosen as the acoustic field variable, instead of the Lighthill acoustic density fluctuation. This new acoustic variable can be introduced by rearranging the momentum equation into Crocco's form [44], differently from Lighthill's derivation. The justification for the use of total enthalpy as acoustic variable comes from the consideration that, in inviscid steady irrotational flows, such a variable is constant. Consequently, at large distances from the acoustic sources, a perturbation in the total enthalpy represents an acoustic wave [44].

2.2 FW-H acoustic analogy theory

Ffowcs Williams and Hawkings [52] developed a generalization of the Lighthill acoustic analogy for flows including bodies in arbitrary motion. In their work, they used the theory of generalised functions [103], which enabled a milestone progress in theoretical aeroacoustics. The FW-H equation introduces the concept of partitioning an unbounded continuous medium, which is defined everywhere in space, into two regions by a surface. The latter is referred to as the FW-H integration surface. This surface needs not to coincide with a physical body and can be penetrable (permeable or porous) [104]. Further details about the FW-H surface requirements are given in Brentner and Farassat [85, 104].

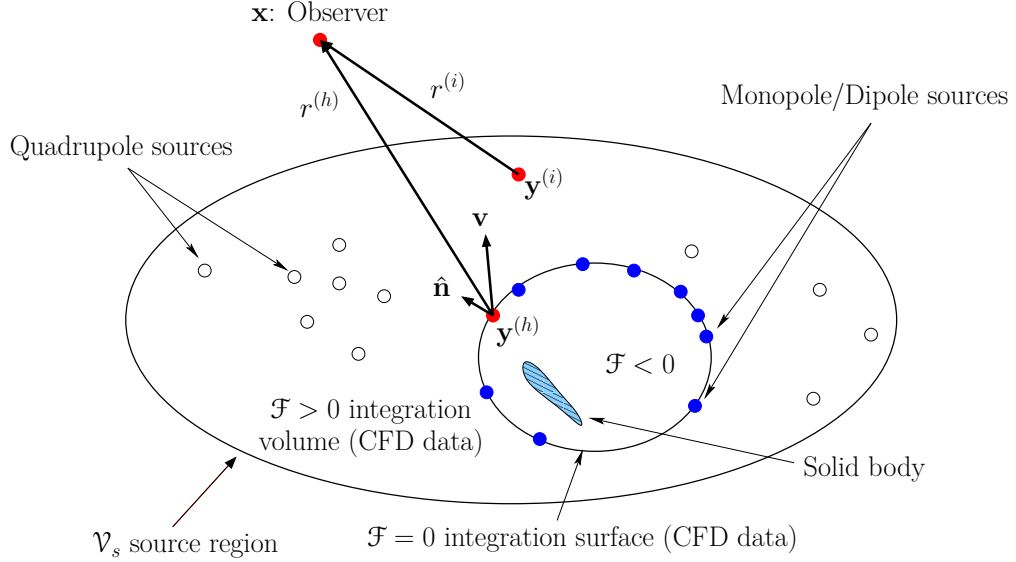


Figure 2.4: Schematic of the FW-H acoustic analogy approach including the presence of solid bodies enclosed by a control surface.

A schematic of the FW-H acoustic analogy approach is shown in Figure 2.4. The acoustically active source region is confined to a volume \mathcal{V}_s as for the Lighthill analogy (see Figure 2.2 for comparison), but a control surface within \mathcal{V}_s defines an excluded region that encloses any solid bodies. Additional surface sources of monopole and dipole type are introduced on the control surface in order to represent the excluded region. Thus, the sound field is represented by the sum of a volume integral over \mathcal{V}_s , and a surface integral (similar to Kirchhoff) over the control surface. Unsteady flow field data needs to be available both in the integration volume and on the integration surface, which can be either stationary or moving.

Referring to Figure 2.4, let $\mathcal{F}(\mathbf{x}, t) = 0$ be the equation describing the moving control surface, the points of which move at velocity $\mathbf{v}(\mathbf{x}, t)$ [54]. The component of this velocity in the direction normal to the surface v_n either coincides with the fluid velocity u_n in the same direction ($v_n = u_n$), which gives an impenetrable/solid FW-H surface, otherwise $v_n \neq u_n$, which gives a permeable/porous FW-H surface. The surface $\mathcal{F}(\mathbf{x}, t) = 0$ is defined to satisfy the property $\nabla\mathcal{F} = \hat{\mathbf{n}}$ on the surface, where $\hat{\mathbf{n}}$ is the outward-pointing unit-normal vector. Following this procedure, the flow is partitioned into three regions according to the value of \mathcal{F} , as shown in Figure 2.4. The unbounded fluid satisfies the Navier-Stokes equations on and outside the surface, where $\mathcal{F}(\mathbf{x}, t) \geq 0$. Its motion matches that of a real flow in this continuum. Inside

the surface, where $\mathcal{F}(\mathbf{x}, t) < 0$, the conservation laws are assumed not to apply and the flow state can be defined arbitrarily. The flow is usually replaced by a quiescent fluid in the complement $\mathcal{F}(\mathbf{x}, t) < 0$, so generating a discontinuity in the flow state at the surface itself.

In order to maintain this discontinuity, mass and momentum sources are distributed on the integration surface $\mathcal{F}(\mathbf{x}, t) = 0$, so that the conservation laws across it are satisfied. These surface source distributions act as sound generators ($\mathbf{y}^{(h)} \in \mathcal{F}(\mathbf{x}, t) = 0$) and their strength is given by the difference between the flux requirements of the state variables in the two regions $\mathcal{F}(\mathbf{x}, t) > 0$ and $\mathcal{F}(\mathbf{x}, t) < 0$. The contribution given by the inner region $\mathcal{F}(\mathbf{x}, t) < 0$ is included in the surface source distribution itself, while outside the integration surface a distribution of quadrupole sources of the Lighthill type is considered, at $\mathbf{y}^{(i)} \in \mathcal{F}(\mathbf{x}, t) > 0$. The estimation of the volume and of the surface source distributions is carried out from the time-resolved estimates of pressure, density, and velocity in the region $\mathcal{F}(\mathbf{x}, t) \geq 0$, which are obtained independently (for instance by a CFD simulation).

Expressions for the source terms are obtained by recasting the mass and the momentum conservation laws into an inhomogeneous wave equation. The mathematical details are given in Appendices B and C. The result is the FW-H equation [52]:

$$\square^2 [H(\mathcal{F}) c_0^2 (\rho - \rho_0)] = \frac{\partial [\delta(\mathcal{F}) \rho_0 u_n]}{\partial t} - \frac{\partial [\delta(\mathcal{F}) P_{ij} \hat{n}_j]}{\partial x_i} + \frac{\partial^2 [H(\mathcal{F}) T_{ij}]}{\partial x_i \partial x_j}, \quad (2.4)$$

where $H(\mathcal{F})$ is the Heaviside function and $\delta(\mathcal{F})$ is the Dirac delta function, which are both defined in Appendix B. The quantities $\hat{\mathbf{n}}$ and u_n are, respectively, the outward-pointing unit-normal vector and the flow velocity normal to the surface $\mathcal{F}(\mathbf{x}, t) = 0$. The tensors T_{ij} and P_{ij} are, respectively, the Lighthill stress tensor and the compressive stress tensor defined in Equation 2.2, the latter representing the force acting on a portion of fluid per unit surface area [1]. Equation 2.4 is obtained by assuming the control surface as impenetrable ($v_n = u_n$) as in the original FW-H formulation [52].

Equation 2.4 determines the acoustic density fluctuation of the radiating noise using three kinds of sound sources, in order to take into account the different aspects of a significantly heterogeneous phenomenon. These sources are respectively referred to as the monopole, the dipole, and the quadrupole source. The monopole and dipole contributions, representing the source distributions of mass and momentum, are also

called, respectively, thickness and loading noise, for analogy with helicopter rotor applications.

The quadrupole term represents a volume distribution. The dipole and monopole noise are instead surface source distributions, as indicated by the presence of the Dirac delta function in the first two terms on the right hand side of Equation 2.4, which sifts the value of the variables on the FW-H integration surface. The sifting property is a characteristic of the Dirac delta function, as detailed by Farassat [105], who discussed the analytical development of the generalised function theory focusing on aeroacoustic applications.

The volume source distribution accounts for all the non-linearities in the flow. The effects of non-linear wave propagation and steepening, local fluctuations in the speed of sound, generation of noise by shocks, vorticity, and turbulence in the flow field are all included in this source term [85]. If the integration surface is taken coincident with a solid body, a physical interpretation of the dipole and of the monopole noise contributions is available. The dipole noise takes into account the effect of the interaction of the unsteady flow with steady or moving rigid surfaces. The solid body is replaced with fluid plus a distribution of normal dipoles over the surface, whose strength equals the instantaneous force per unit area acting on the fluid. If the body dimensions are small in comparison with the acoustic wavelength, this dipole distribution may be replaced for far-field purposes by a point force acting on the fluid, whose strength equals the instantaneous total force that the body exerts on the fluid. The monopole noise is originated by the motion of the surface in the normal direction [106] with respect to the fluid and it represents a displacement effect [52]. It is fully determined by the geometry and by the kinematics of the body [85].

The FW-H integral solution [52] to Equation 2.4 is

$$\begin{aligned}
4\pi c_0^2 (\rho(\mathbf{x}, t) - \rho_0) = & \frac{\partial^2}{\partial x_i \partial x_j} \int_{\mathcal{F}>0} \left[\frac{T_{ij} J}{r|1 - M_r|} \right]_{\tau_e} d^3\eta \\
& - \frac{\partial}{\partial x_i} \int_{\mathcal{F}=0} \left[\frac{P_{ij} \hat{n}_j A}{r|1 - M_r|} \right]_{\tau_e} d^2\eta \\
& + \frac{\partial}{\partial t} \int_{\mathcal{F}=0} \left[\frac{\rho_0 u_n}{r|1 - M_r|} \right]_{\tau_e} d^2\eta,
\end{aligned} \tag{2.5}$$

with:

$$y_i = \eta_i + \int_{-\infty}^{\tau_e} c_0 M_i(\boldsymbol{\eta}, \tau') d\tau', \quad \hat{n}_j = \frac{\frac{\partial \mathcal{F}}{\partial x_j}}{|\nabla_x \mathcal{F}|}, \quad (2.6)$$

$$J = \exp\left(\int_{-\infty}^{\tau_e} \frac{\partial}{\partial y_i} (c_0 M_i(\boldsymbol{\eta}, \tau')) d\tau'\right), \quad A = J \frac{|\nabla_y \mathcal{F}|}{|\nabla_\eta \mathcal{F}|}, \quad (2.7)$$

$$u_n = u_i \hat{n}_i, \quad M_r = M_i r_i. \quad (2.8)$$

In Equations 2.5–2.8, \mathbf{x} is the observer position defined in the \mathbf{y} reference system. The \mathbf{y} reference system is fixed with the undisturbed medium and it is used to carry out the integration in $\boldsymbol{\eta}$ in the source region. The variable $\boldsymbol{\eta}$ represents a Lagrangian coordinates reference frame, moving with the sources. The Jacobian J of the transformation between the fixed reference system \mathbf{y} and the moving reference frame $\boldsymbol{\eta}$ accounts for any local dilation of the volume element in the change of coordinates (ratio between volume elements in \mathbf{y} and $\boldsymbol{\eta}$), and it is related to the divergence of the convection velocity $c_0 \mathbf{M}$. The variable A is the surface dilation factor (same as J in 2D). $c_0 M_i$ and M_r are, respectively, the source convection velocity defined in the \mathbf{y} reference frame and the source convection Mach number in the direction $\mathbf{r} = \mathbf{x} - \mathbf{y}$.

The square brackets in Equation 2.5 indicate evaluation of the terms within at the source emission time τ_e (Section 1.4), estimated through the “emission time” equation

$$\tau_e = t - \frac{|\mathbf{x} - \mathbf{y}(\tau_e)|}{c_0}. \quad (2.9)$$

Equation 2.9, traditionally referred to as the “retarded time” equation, expresses that a disturbance emitted from the source location $\mathbf{y}(\tau_e)$ at time τ_e is perceived by an observer \mathbf{x} at time t , with a time delay $t - \tau_e = |\mathbf{x} - \mathbf{y}(\tau_e)|/c_0$, due to the noise propagation at the speed of sound c_0 .

The FW-H acoustic analogy, given by Equations 2.4 and 2.5, extended the acoustic analogy approach to a broader range of applications, by allowing more freedom in the definition of the source field and of its boundaries compared to the Lighthill analogy. The theory of generalised functions has continued to be used in aeroacoustics after Ffowcs Williams and Hawkings, and it is developed with a rigorous mathematical approach by Farassat [105].

Farassat [106] applied the FW-H acoustic analogy to helicopter rotors, showing the effectiveness of this approach in predicting aerodynamic sound in the presence

of moving surfaces in an unsteady turbulent flow, with non-compact sources. The embedding procedure (Section B.1), which converts the standard fluid dynamic problem to an unbounded fluid case, through the use of the generalised function theory, is also detailed by Farassat [106].

In numerical simulations, the main disadvantage of the original FW-H acoustic analogy formulation, compared to surface integral methods such as the Kirchhoff approach (Section 2.1.2.2), is the need to perform a numerical volume integration that is far more expensive than a two dimensional one. However, the quadrupole source term is usually some order of magnitude smaller than the surface source distribution and, even if this is not the case, a wise choice of the integration surface could still lead to a negligible volume source contribution. Therefore, the quadrupole source term is often neglected [64].

Nevertheless, sample computations that include the quadrupole term are reported by Brentner [107, 108] and by Rona [53]. The current progress in computational power of computer clusters gives hope towards including the volume source contribution more often in future applications.

2.2.1 The porous FW-H formulation

As stated in Section 2.2, the control surface in the FW-H acoustic analogy can either coincide with a solid body or be permeable (porous FW-H). Di Francescantonio [64] presented analytical developments concerning the use of the permeable surface by trying to combine the advantages of the Kirchhoff method with the ones of the FW-H acoustic analogy. He derived a new formulation that he referred to as Kirchhoff FW-H (KFW-H). He pointed out that the main advantage of this approach is that the derivatives of CFD quantities in the direction normal to the integration surface, which are necessary in the standard Kirchhoff formula, are not required. In the application of the KFW-H equation, Di Francescantonio neglected the volume source distribution by considering a surface placed in a linear acoustic region. This allows for a fast computation, as with the Kirchhoff method. However, the general form of the KFW-H solution includes a volume integral, to take into account any non-negligible quadrupole source outside the permeable surface.

Di Francescantonio [64] developed the concepts of formulation 1 and 1A by

Farassat, by explicitly allowing the data surface to be porous. Formulation 1 was first published in 1975 [106] and then revised in 1981 [109]. Formulation 1A was proposed in 1980 [110]. Boundaries moving at a subsonic speed are taken into account and the equations have been successfully applied to rotor and propeller noise prediction, before their exhaustive redefinition in 2007 by Farassat [104]. The difference between the two formulations lies in the estimation of the observer time derivative. In formulation 1A, this is done analytically, resulting in a decreased execution time and a higher accuracy [104]. Di Francescantonio [64] showed how the method that does not require the numerical estimation of the time derivative is twice as fast.

Brentner and Farassat [85] compared the Kirchhoff method using the pressure as acoustic variable, and the porous FW-H integral method with the quadrupole non-linear contribution neglected. They concluded that the FW-H acoustic analogy is more accurate and allows more freedom in the surface placement [85]. The Kirchhoff method could be considered as a particular case of the porous FW-H (without the volume integral term) when the surface is placed in the linear region. In this configuration, the two integral methods are equivalent [85].

As stated in Section 2.1.2.2, in the Kirchhoff formulation all the non-linearities of the flow are assumed enclosed within an integration surface, referred to as the Kirchhoff surface. This assumption avoids having to perform a volume integration, which is usually more expensive from a computational viewpoint than a surface integration. This advantage is also available in the FW-H acoustic analogy, if the FW-H surface is thought as penetrable, or permeable [85], and it is placed in the linear acoustic region of the flow, so that the quadrupole source contribution outside the surface is negligible. On the other hand, the FW-H acoustic analogy has the advantage of better representing the physics of the problem and it is possible to give a physical interpretation to the various terms in the formulation, as explained in Section 2.2. Furthermore, it offers a more robust approach and it is easier to be interfaced to CFD codes [85].

Lyrintzis [48] also argues that the porous FW-H equation method is equivalent to the Kirchhoff's method and that it represents a preferable alternative to it, given the current state of the art of numerical techniques and of computing hardware. Even

though the porous FW-H requires a larger memory usage due to the volume integral term, it is less limiting in the control surface placement and it does not require the normal derivative of flow field variables to be estimated.

The porous FW-H formulation allows non-linearities to be present on the integration surface, which can consequently be placed closer to sources of noise generated aerodynamically, such as the ones from a jet, compared to the Kirchhoff method. Shur *et al.* [111] claimed that placing the surface in the inviscid non-linear region proximal to the jet, in the porous FW-H method, is beneficial both in terms of mesh design and of the solution accuracy at the integration surface. Specifically, a refined computational mesh can be applied over the turbulent region of the jet enclosed by the integration surface. The mesh can then be gradually coarsened in the outer domain, where the mesh function becomes mainly to prevent spurious reflections of outgoing waves [111]. The shorter path from the source region to the integration surface also typically reduces the numerical dissipation and dispersion that affect the acoustic waves travelling towards the FW-H surface.

Even if the more recent contributions to the theory of aeroacoustics [64, 85, 104] have broadened and consolidated the permeable surface theory, the porous FW-H acoustic analogy concept was already included in Ffowcs Williams & Hawkings [52], as argued by Farassat [104].

2.2.1.1 Effect of neglecting the FW-H volume integral contribution

As far as the jet noise problem is concerned, the FW-H surface placement is a crucial factor, due to the slow development of the turbulent flow in the axial direction. Hydrodynamic perturbations are convected many jet diameters D_e downstream of the nozzle exit section, extending the turbulent region beyond the boundary of the numerical domain, which is limited by the computational resources. The computational domain is truncated typically at about 20 – 30 jet diameters D_e from the nozzle exit section and jet mixing farther downstream is not resolved.

A permeable FW-H surface of finite extent cannot enclose the whole jet. The FW-H surface is typically defined so that the flow crosses the downstream end of it, which is usually referred to as the outflow disk. The FW-H acoustic analogy allows for this implementation, provided the full integral solution is estimated. The volume

integration outside the surface allows the correct estimation of the noise radiation, by modelling the turbulent perturbations in the exterior domain as quadrupole sources.

Neglecting the quadrupole noise sources in the exterior region, $\mathcal{F}(\mathbf{x}, t) > 0$ in Figure 2.4, results in spurious noise contributions being emitted by the flow crossing the outflow disk. If left untreated, this spurious noise affects both the near-field and the far-field acoustic predictions.

Several solutions have been adopted to mitigate this pseudo-noise radiation. The easiest modification is the exclusion of the outflow disk from the surface integration, by leaving the FW-H surface open at the downstream end. Good agreement has been shown in recent publications [112, 113, 114, 115] between the noise predicted with an open FW-H surface and experimental measurements. This suggests that the outflow disk contribution to noise radiation is small compared to the contribution from the whole integration surface and that the pseudo-noise cancellation obtained by neglecting this small contribution can be beneficial for the accuracy of the noise prediction.

An alternative approach consists in applying some particular treatment to the acoustic analogy formulation, in order to include the outflow disk while minimizing the volume integral contribution from the excluded downstream region of the jet. For instance, different versions of the FW-H equation have been proposed, replacing the acoustic density fluctuations with derived variables based on pressure fluctuations [5, 67, 116, 117, 118, 119]. The benefit comes from the pressure fluctuations being lower than the density fluctuations at the outflow disk, especially for hot jets [5]. This results in a weaker spurious noise emission as the flow crosses the downstream end of the surface [111, 117, 119].

Shur *et al.* [5] also proposed a disk-averaging procedure, obtained from a set of nested FW-H surfaces. The contribution from the outflow disk is averaged between different positions of the surface and the pseudo-noise was shown to reduce. This technique works on the principle that, whereas the pseudo-noise is affected by the position of the integration surface, the physical sound should be essentially unaffected by the axial position of the outflow disk, beyond a certain axial distance. Mendez [119] proposed a formula for determining the number and the spacing of the outflow disks that optimize the disk-averaging procedure.

While similar conclusions about the advantages of using the porous FW-H formulation, in place of the Kirchhoff method, are drawn by Rahier *et al.* [120], their findings about the open vs closed surface comparison are in contrast with the ones by Shur *et al.*. According to Rahier *et al.* [120], a closed FW-H surface, requiring additional storage memory and more expensive computations compared to an open surface, does not improve the noise prediction. For some cases, it is shown to overestimate the far-field sound intensity, degrading the accuracy of the noise prediction [120]. Uzun *et al.* [121] also showed no significant improvement in the results by closing the FW-H surface at the downstream end.

Whether an open FW-H surface is preferable to a closed FW-H surface, for applications in which noise sources cross it, remains unclear. A closed surface appears to give significant improvements for hot jets but only when coupled with a disk-averaging procedure and with a tailored change of the acoustic variable. On the basis of this review, it was decided to adopt an open integration surface for the jet noise applications in Chapters 4 and 5, also due to the attraction of its lower memory-storage requirements. An additional constraint was represented by the CFD input to the new FW-H tools developed by the author, which was provided by third parties (Cerfacs, Toulouse for instance). This was produced and stored before the new FW-H tools were completed. Therefore, the author did not have full freedom on the choice of the FW-H surface shape and size.

Another variant to the implementation of the FW-H acoustic analogy consists in approximating the volume integral in a convenient way, instead of completely neglecting its contribution. Additional surface integral terms, both in the frequency domain [122] and in the time domain [123], have been proposed. The computational cost is just slightly increased by this additional terms and the noise prediction has been shown to be more accurate for simple source problems. Even though this represents an interesting development of the theory that could give significant improvements in the future, there is still insufficient evidence of the effectiveness of these formulations for jet noise applications and an optimal rearrangement of the source terms needs to be found.

2.2.2 Advanced time vs retarded time approach

In jet aeroacoustics, an algorithm to correctly take into account the propagation of the disturbance from the source position \mathbf{y} to the observer position \mathbf{x} is required, due to the non-compactness of the source, as stated in Section 1.4. Two different methods can be adopted, which are referred to as the retarded time [108, 124, 125] and the advanced/forward time approach [48, 54, 55, 126, 127, 128].

In the retarded time approach, the aeroacoustic simulation runs in the observer temporal frame, meaning that the computation time axis is representative of the reception phenomenon. In this case, it can happen that different disturbances reaching the observer at the same time were not emitted simultaneously. For each disturbance, *i.e.* each source position \mathbf{y} , the emission time τ_e needs therefore to be calculated, by solving an implicit emission time equation of the type of Equation 2.9. Once τ_e is known, the unsteady flow field solution has to be interpolated at time τ_e . This involves selecting the value of the flow variables relative to the emission of each disturbance and estimating the source terms of Equation 2.4 at τ_e . Consequently, CFD flow field predictions at different times τ_e are required at each observer time step, making the retarded time algorithm computationally expensive. Furthermore, the retarded time approach is dependent on the specifications of the test case and, for supersonic speed, it presents the issue of multiple roots [54] deriving from Equation 2.9.

A different approach is described in Rona [53] and in Casalino [54], where the aeroacoustic simulation runs in the emission time frame and, for each different disturbance, an advanced time t_{adv} is calculated for a specific observer. This represents the reception time that takes into account the time of flight for the disturbance to travel from the emission to the reception locations. In this approach, the CFD and the aeroacoustic simulations advance in the same time frame and the flow field prediction does not need to be interpolated. Consequently, the aeroacoustic and the CFD simulation can be run simultaneously and the storage of the flow-field time history is not required [54]. Furthermore, the advanced time t_{adv} (corresponding to t in Equation 2.9) can be explicitly determined as

$$t_{adv} = \tau_e + \frac{|\mathbf{x} - \mathbf{y}(\tau_e)|}{c_0}, \quad (2.10)$$

without the requirement of an iterative method [54].

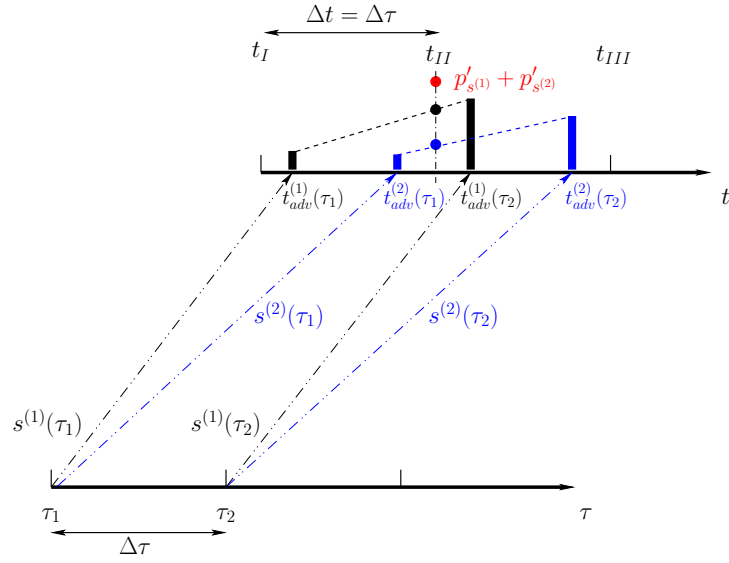


Figure 2.5: Advanced time algorithm schematic showing the observer time-domain interpolation for the simple case of two sources and one observer.

In Figure 2.5, the advanced time algorithm is schematically represented for a simplified model with two point sources $s^{(1)}$ and $s^{(2)}$. The source (τ) and the reception (t) time axes are shown, respectively, at the bottom and at the top of the figure. It is convenient to apply the same discretization to both time frames ($\Delta\tau = \Delta t$), from a numerical viewpoint.

Given this configuration, the time-of-flight to reach the observer location \mathbf{x} , for a disturbance emitted at τ_1 by the point source $s^{(1)}$ located at $\mathbf{y}^{(1)}(\tau_1)$, is proportional to the distance $|\mathbf{x} - \mathbf{y}^{(1)}(\tau_1)|$ and the advanced time $t_{adv}^{(1)}(\tau_1)$ can be determined through Equation 2.10. The latter does not necessarily coincide with a discrete observer instant $t_i = i\Delta t$, with i integer. The contribution from the point source $\mathbf{y}^{(1)}$ at time τ_1 can fall within two discrete reception times (t_I and t_{II} in Figure 2.5). The same occurs for source $s^{(2)}$, as indicated by the blue symbols in Figure 2.5.

By storing the contributions from two consecutive time steps, a time interpolation can be performed between the acoustic pressure perturbations from $s^{(1)}$ received at the observer time $t_{adv}^{(1)}(\tau_1)$ and at $t_{adv}^{(1)}(\tau_2)$, to obtain the pressure perturbation from $s^{(1)}$ at the discrete observer time t_{II} . This interpolation process is schematically represented by the black dashed line in Figure 2.5. Once the contributions from all point sources have been projected to the adjacent discrete observer time t_{II} , the

acoustic pressure fluctuation (red dot in Figure 2.5) is computed by adding over all the sources. A linear interpolation is applied in the new implementation of the advanced time algorithm in Python for both the stationary (Section 2.2.3) and the convective (Section 2.2.4) acoustic analogy, as sketched in Figure 2.5.

2.2.3 Casalino advanced time approach (AFW-H)

By the derivation in Appendix B, the FW-H equation for a stationary medium is obtained as

$$\square^2 \left(H(\mathcal{F}) c_0^2 (\rho - \rho_0) \right) = \frac{\partial [\delta(\mathcal{F}) Q_j \hat{n}_j]}{\partial t} - \frac{\partial [\delta(\mathcal{F}) L_{ij} \hat{n}_j]}{\partial x_i} + \frac{\partial^2 [H(\mathcal{F}) T_{ij}]}{\partial x_i \partial x_j}, \quad (2.11)$$

where:

$$\square^2 = \left[\frac{1}{c_0^2} \frac{\partial^2}{\partial t^2} - \frac{\partial^2}{\partial x_j \partial x_j} \right], \quad (2.12)$$

$$Q_j = \rho (u'_j - v_j) + \rho_0 v_j, \quad (2.13)$$

$$L_{ij} = \rho u'_i (u'_j - v_j) + P'_{ij}. \quad (2.14)$$

In Equations 2.11–2.14, H is the Heaviside function and δ is the Dirac delta function, both defined in Appendix B. The primed variables represent fluctuations about the state of the fluid at rest in the acoustic analogy. v_j is the FW-H surface velocity component in the j^{th} direction.

Casalino [54] applied the advanced time approach to the integral solution of Equation 2.11 proposed by Farassat [106] and Brentner [108]. The mathematical details of this Advanced-time Ffowcs Williams and Hawkings acoustic analogy formulation, here referred to as AFW-H, are given in Appendices B and C.

By using the free-space Green's function:

$$G(\mathbf{x}, t, \mathbf{y}, \tau) = \begin{cases} \frac{\delta(g)}{4\pi r}, & \text{if } t \geq \tau \\ 0, & \text{if } t < \tau, \end{cases} \quad (2.15)$$

where:

$$g = \tau - t + \frac{r}{c_0}, \quad r = |\mathbf{x} - \mathbf{y}|, \quad (2.16)$$

to convolve Equation 2.11, the acoustic pressure fluctuation $p' = p - p_0$ perceived by an observer located at the vector position \mathbf{x} at time t is expressed as follows:

$$p'(\mathbf{x}, t) = p'_T(\mathbf{x}, t) + p'_L(\mathbf{x}, t) + p'_Q(\mathbf{x}, t), \quad (2.17)$$

where subscripts T , L , and Q refer to thickness, loading, and quadrupole noise, respectively.

As discussed in the following Section 2.3, the noise radiation is estimated in this study by performing only the surface integration. The volume source distribution is assumed to be negligible compared to the thickness and to the loading noise contributions. The expressions for the T and L noise components are respectively

$$4\pi p'_T(\mathbf{x}, t) = \int_{\mathcal{F}=0} \left[\frac{\dot{Q}_j \hat{n}_j + Q_j \dot{\hat{n}}_j}{r(1-M_r)^2} \right]_{\tau_e} d^2\eta + \int_{\mathcal{F}=0} \left[\frac{Q_j \hat{n}_j \left(r \frac{\partial M_r}{\partial \tau} + c_0 (M_r - M^2) \right)}{r^2 (1-M_r)^3} \right]_{\tau_e} d^2\eta, \quad (2.18)$$

$$4\pi p'_L(\mathbf{x}, t) = \frac{1}{c_0} \int_{\mathcal{F}=0} \left[\frac{\dot{L}_{ij} \hat{n}_j \hat{r}_i}{r(1-M_r)^2} \right]_{\tau_e} d^2\eta + \int_{\mathcal{F}=0} \left[\frac{L_{ij} \hat{n}_j \hat{r}_i - L_{ij} \hat{n}_j M_i}{r^2 (1-M_r)^2} \right]_{\tau_e} d^2\eta + \frac{1}{c_0} \int_{\mathcal{F}=0} \left[\frac{L_{ij} \hat{n}_j \hat{r}_i \left(r \frac{\partial M_r}{\partial \tau} + c_0 (M_r - M^2) \right)}{r^2 (1-M_r)^3} \right]_{\tau_e} d^2\eta, \quad (2.19)$$

with:

$$M_i = \frac{v_i}{c_0}, \quad M = \frac{\sqrt{v_1^2 + v_2^2 + v_3^2}}{c_0}, \quad M_r = M_i \hat{r}_i. \quad (2.20)$$

In Equations 2.18 and 2.19, the convention $[...]_{\tau_e}$ is adopted to indicate that the quantities inside the square brackets are evaluated at the emission time τ_e .

Equations 2.18 and 2.19 can be simplified for jet noise applications. A FW-H surface enclosing the jet can be defined as fixed in the nozzle frame of reference, by which its velocity $v_i = 0$, its Mach number $M = M_r = 0$, and its outward-normal unit vector $\hat{\mathbf{n}}$ is invariant with time, hence $\dot{\hat{n}}_j = 0$.

Under these conditions, Equations 2.18 and 2.19 simplify as

$$4\pi p'_T(\mathbf{x}, t) = \int_{\mathcal{F}=0} \left[\frac{\dot{Q}_j \hat{n}_j}{r} \right]_{\tau_e} d^2\eta, \quad (2.21)$$

$$4\pi p'_L(\mathbf{x}, t) = \int_{\mathcal{F}=0} \left[\frac{1}{c_0} \frac{\dot{L}_{ij} \hat{n}_j \hat{r}_i}{r} + \frac{L_{ij} \hat{n}_j \hat{r}_i}{r^2} \right]_{\tau_e} d^2\eta. \quad (2.22)$$

Equations 2.21 and 2.22 are discretised and implemented in Antares [12], as discussed in Section 2.3. Noise estimations for elementary point sources, as well as stationary jet noise applications, are presented respectively in Chapters 3 and 4.

2.2.4 Convective acoustic analogy (CFW-H)

The FW-H acoustic analogy of Section 2.2.3 models sound waves propagating in a uniform medium at rest. A usual way to model a moving medium relative to a fixed observer is to reverse the reference frame, by considering a case in which the observer moves in a medium at rest [54, 104, 125]. In 2011 Najafi-Yazdi *et al.* [55] developed an interesting convective formulation of the FW-H acoustic analogy, by explicitly taking into account the presence of a mean flow. The application of the convective analogy in [55] was restricted to elementary noise sources (monopoles and dipoles). In the current work, the CFW-H formulation is used to investigate the flight effects on the noise radiation from jets (Section 5.2). The mathematical details to get the moving-medium formulation are omitted here for conciseness and reported in Appendix B. The result is the inhomogeneous wave equation

$$\begin{aligned} \square^{(c)2} \left(H(\mathcal{F}) c_0^2 \rho' \right) = & \left[\frac{\partial}{\partial t} + U_{0i} \frac{\partial}{\partial x_i} \right] \left[\delta(\mathcal{F}) Q_j^{(c)} \hat{n}_j \right] \\ & - \frac{\partial \left[\delta(\mathcal{F}) L_{ij}^{(c)} \hat{n}_j \right]}{\partial x_i} + \frac{\partial^2 \left[H(\mathcal{F}) T_{ij} \right]}{\partial x_i \partial x_j}, \end{aligned} \quad (2.23)$$

where:

$$\square^{(c)2} = \left[\frac{1}{c_0^2} \frac{\partial^2}{\partial t^2} - \frac{\partial^2}{\partial x_j \partial x_j} + \frac{1}{c_0^2} 2U_{0j} \frac{\partial^2}{\partial t \partial x_j} + \frac{1}{c_0^2} U_{0i} U_{0j} \frac{\partial^2}{\partial x_i \partial x_j} \right], \quad (2.24)$$

$$Q_j^{(c)} = \rho \left(u'_j + U_{0j} - v_j \right) + \rho_0 \left(v_j - U_{0j} \right), \quad (2.25)$$

$$L_{ij}^{(c)} = \rho u'_i \left(u'_j + U_{0j} - v_j \right) + P'_{ij}. \quad (2.26)$$

The superscript (c) indicates the convective frame of reference, which is moving at the subsonic uniform velocity $U_{0j} = (U_{01}, U_{02}, U_{03})$. In this analogy, sound waves propagate in an analogous medium of uniform velocity U_{0j} at the constant speed of sound c_0 . Substituting $U_{0j} = 0$ in Equations 2.23–2.26 recovers the stationary form of Equations 2.11–2.14.

An important difference with respect to the FW-H equation for a stationary medium is the presence of the convective wave operator (Equation 2.24) in place of the wave operator (Equation 2.12), by which the effect of convection by the uniform flow on the sound field is accounted for in the left hand side of Equation 2.23. A Lagrangian derivative also appears in the thickness noise and the source terms $Q_j^{(c)}$ and $L_{ij}^{(c)}$ are slightly different compared to Equations 2.13 and 2.14.

The solution of Equation 2.23 is estimated by convolution with the convective Green's function $G^{(c)}$ stated in Blokhintsev [129], which is

$$G^{(c)}(\mathbf{x}, t, \mathbf{y}, \tau) = \begin{cases} \frac{\delta(g^{(c)})}{4\pi R^*}, & \text{if } t \geq \tau \\ 0, & \text{if } t < \tau, \end{cases} \quad (2.27)$$

where:

$$g^{(c)} = \tau - t + \frac{R}{c_0}, \quad (2.28)$$

$$R = \frac{-M_0(x_1 - y_1) + R^*}{\beta^2}, \quad (2.29)$$

$$R^* = \sqrt{(x_1 - y_1)^2 + \beta^2 [(x_2 - y_2)^2 + (x_3 - y_3)^2]}, \quad (2.30)$$

$$\beta = \sqrt{1 - M_0^2}, \quad M_0 = \frac{U_0}{c_0}. \quad (2.31)$$

In Equation 2.27, δ is the Dirac delta function defined in Appendix B and a uniform flow at velocity U_0 in the x_1 direction is considered, without loss of generality. This is convenient in jet noise applications, where the co-flow around an installed jet, due to aircraft motion, can be defined in the x_1 direction.

The convolution of Equation 2.23 with Equation 2.27 is detailed in Appendix C. From this convolution, after neglecting the quadrupole noise contribution, the acoustic pressure perturbation $p'(\mathbf{x}, t)$ is obtained as the sum of two contributions, the thickness $p'_T(\mathbf{x}, t)$ and the loading $p'_L(\mathbf{x}, t)$ noise contributions, which are defined respectively as

$$\begin{aligned} 4\pi p'_T(\mathbf{x}, t) = & \int_{\mathcal{F}=0} \left[\frac{\dot{Q}_j \hat{n}_j + Q_j \dot{\hat{n}}_j}{R^* (1 - M_R)^2} \right]_{\tau_e} d^2\eta + \int_{\mathcal{F}=0} \left[\frac{-\partial R^*}{\partial \tau} \frac{Q_j \hat{n}_j}{R^{*2} (1 - M_R)^2} \right]_{\tau_e} d^2\eta \\ & + \int_{\mathcal{F}=0} \left[\frac{Q_j \hat{n}_j}{R^* (1 - M_R)^3} \frac{\partial M_R}{\partial \tau} \right]_{\tau_e} d^2\eta \\ & - M_0 \int_{\mathcal{F}=0} \left[\frac{\dot{\tilde{R}}_1 Q_j \hat{n}_j + \tilde{R}_1 \dot{Q}_j \hat{n}_j + \tilde{R}_1 Q_j \dot{\hat{n}}_j}{R^* (1 - M_R)^2} \right]_{\tau_e} d^2\eta \\ & + M_0 \int_{\mathcal{F}=0} \left[\frac{\partial R^*}{\partial \tau} \frac{\tilde{R}_1 Q_j \hat{n}_j}{R^{*2} (1 - M_R)^2} \right]_{\tau_e} d^2\eta \\ & - M_0 \int_{\mathcal{F}=0} \left[\frac{\partial M_R}{\partial \tau} \frac{\tilde{R}_1 Q_j \hat{n}_j}{R^* (1 - M_R)^3} \right]_{\tau_e} d^2\eta \\ & - U_0 \int_{\mathcal{F}=0} \left[\frac{\tilde{R}_1^* Q_j \hat{n}_j}{R^{*2} (1 - M_R)} \right]_{\tau_e} d^2\eta, \end{aligned} \quad (2.32)$$

$$\begin{aligned}
4\pi p'_L(\mathbf{x}, t) &= \frac{1}{c_0} \int_{\mathcal{F}=0} \left[\frac{\dot{L}_{ij} \hat{n}_j \tilde{R}_i + L_{ij} \dot{\hat{n}}_j \tilde{R}_i + L_{ij} \hat{n}_j \dot{\tilde{R}}_i}{R^* (1 - M_R)^2} \right]_{\tau_e} d^2\eta \\
&\quad - \frac{1}{c_0} \int_{\mathcal{F}=0} \left[\frac{\partial R^*}{\partial \tau} \frac{L_{ij} \hat{n}_j \tilde{R}_i}{R^{*2} (1 - M_R)^2} \right]_{\tau_e} d^2\eta \\
&\quad + \frac{1}{c_0} \int_{\mathcal{F}=0} \left[\frac{\partial M_R}{\partial \tau} \frac{L_{ij} \hat{n}_j \tilde{R}_i}{R^* (1 - M_R)^3} \right]_{\tau_e} d^2\eta \\
&\quad + \int_{\mathcal{F}=0} \left[\frac{L_{ij} \hat{n}_j \tilde{R}_i^*}{R^{*2} (1 - M_R)} \right]_{\tau_e} d^2\eta.
\end{aligned} \tag{2.33}$$

In Equations 2.32 and 2.33, the superscript (c) is omitted for brevity, while $M_R = (\tilde{R}_i v_i) / c_0$ is the Mach number of a point source on the surface $\mathcal{F} = 0$ (with v_i the components of the surface velocity in the convective reference frame). $\tilde{\mathbf{R}}^*$ and $\tilde{\mathbf{R}}$ are defined in Equations 2.34 and 2.35 (see Appendix C for more details).

$$\tilde{\mathbf{R}}^* = \nabla R^* = \left(\frac{x_1 - y_1}{R^*}; \frac{x_2 - y_2}{R^*} \beta^2; \frac{x_3 - y_3}{R^*} \beta^2 \right). \tag{2.34}$$

$$\tilde{\mathbf{R}} = \nabla R = \left(\frac{1}{\beta^2} \left(-M_0 + \frac{x_1 - y_1}{R^*} \right); \frac{x_2 - y_2}{R^*}; \frac{x_3 - y_3}{R^*} \right). \tag{2.35}$$

Equations 2.32 and 2.33 can be simplified for jet noise applications in which a wind tunnel [55] configuration is used. In this configuration, both the nozzle and the observers are defined in a fixed reference frame \mathbf{x} . For jet noise applications, the FW-H surface needs to enclose the jet and can be fixed to the nozzle. The $\boldsymbol{\eta}$ reference system is defined in Appendix C as fixed to the FW-H surface. Consequently, in a wind tunnel test, the \mathbf{x} and $\boldsymbol{\eta}$ reference frames coincide and the nozzle, the integration surface, and the observers do not experience any relative motion from one another.

Several terms in Equations 2.32 and 2.33 can be simplified as shown by Equation 2.36. Specifically, the surface velocity \mathbf{v} (and consequently M_R) is zero. Also, the outward-normal unit vector $\hat{\mathbf{n}}$, the radiation vectors $\tilde{\mathbf{R}}^*$ and $\tilde{\mathbf{R}}$, and the Mach number M_R do not change with time (fixed surface). This gives

$$v_i = 0, \quad M_R = 0, \quad \dot{\hat{n}}_j = 0, \quad \frac{\partial R^*}{\partial \tau} = 0, \quad \dot{\tilde{R}}_i = 0, \quad \frac{\partial M_R}{\partial \tau} = 0. \tag{2.36}$$

Replacing 2.36 in Equations 2.32 and 2.33, the thickness and the loading noise in a wind tunnel test can be expressed as follows:

$$4\pi p'_T(\mathbf{x}, t) = \int_{\mathcal{F}=0} \left[\left(1 - M_0 \tilde{R}_1 \right) \frac{\dot{Q}_j \hat{n}_j}{R^*} - U_0 \frac{\tilde{R}_1^* Q_j \hat{n}_j}{R^{*2}} \right]_{\tau_e} d^2\eta, \tag{2.37}$$

$$4\pi p'_L(\mathbf{x}, t) = \int_{\mathcal{F}=0} \left[\frac{1}{c_0} \frac{\dot{L}_{ij} \hat{n}_j \tilde{R}_i}{R^*} + \frac{L_{ij} \hat{n}_j \tilde{R}_i^*}{R^{*2}} \right]_{\tau_e} d^2\eta. \quad (2.38)$$

Equations 2.37 and 2.38 are discretised and implemented in Antares [12], as discussed in the next session. Noise estimations for simple sources, as well as a jet noise application, are obtained and presented in Chapter 5.

2.3 Implementation in Antares

A discretised form of Equations 2.21-2.22 and 2.37-2.38 is implemented in Antares, respectively in the new AFW-H and CFW-H tools. As mentioned in Section 1.5, Antares [12] is a software package embedding post-processing tools for CFD applications. In the new Antares tools, the quadrupole volume source term contribution is not modelled. Besides the motivations already discussed in Sections 2.2 and 2.2.1, neglecting the quadrupole source term contribution allows a direct comparison of the acoustic predictions from the new Python AFW-H and CFW-H tools against reference numerical solutions obtained at Cerfacs. These reference solutions were obtained respectively from the ONERA solver elsA [130], for the stationary test cases presented in Chapter 4, and from the ONERA KIM software [131, 120], for the convective case presented in Section 5.2. In both the elsA and the KIM software, a FW-H acoustic analogy formulation that neglects $p'_Q(\mathbf{x}, t)$ is used.

The significant advantage in terms of the computational cost given by restricting the numerical integration to a surface integral, typical of Kirchhoff's methods, is therefore preserved. An additional advantage arises when the Python tool is used as a post-processor and inputs a stored CFD solution. Neglecting the quadrupole noise source translates in a lower storage requirement, because the flow field variables data are stored only on the FW-H surface $\mathcal{F}(\mathbf{x}, t) = 0$, rather than on the entire source volume \mathcal{V}_s of Figure 2.4.

In the Python implementation, the CAA tool is built to be used with structured meshes only, which are used in many CFD codes. According to this CFD mesh topology, the FW-H surface $\mathcal{F}(\mathbf{x}, t) = 0$ is partitioned into different zones S_j , corresponding to different mesh blocks B_j , as represented in Figure 2.6. The intersection between $\mathcal{F}(\mathbf{x}, t) = 0$ and the CFD mesh determines the set S_j of faces lying on the

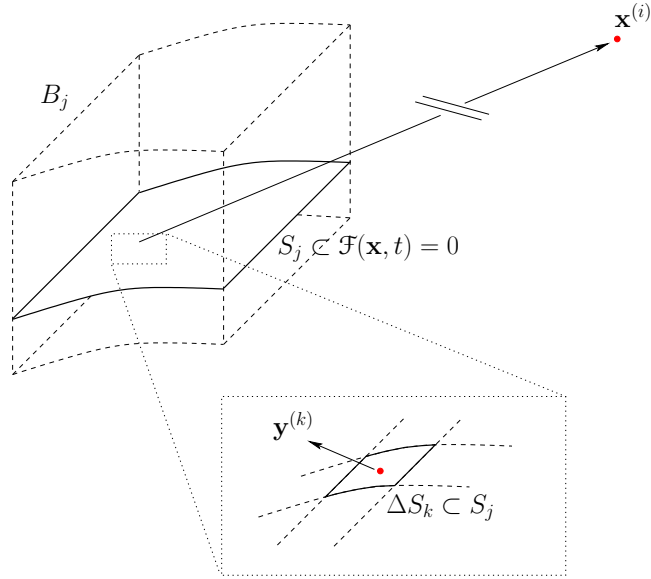


Figure 2.6: Schematic of the FW-H surface discretization, showing the surface element ΔS_k , on the face S_j , defined by intersection with the mesh block B_j .

FW-H surface. For each S_j , the FW-H tool estimates its contribution to p' at the observer position.

The FW-H algorithm is structured so that, at each discrete acoustic time τ^n , a loop over the faces S_j is performed. For each S_j , a second loop is implemented over the surface elements ΔS_k defined as in Figure 2.6, where the discretised form of the loading and of the thickness noise terms in the FW-H acoustic analogy is computed. The advanced times relative to the pairs $\Delta S_k - \mathbf{x}^{(i)}$ are estimated from the “advanced time” Equation 2.10, in order to save the p' contribution from ΔS_k at the correct observer time [54]. By summing over all the ΔS_k s, the contribution from face S_j is determined. The noise radiated by the entire FW-H surface is then estimated by summing over all faces S_j .

This process is then repeated at the next acoustic time τ^{n+1} . Advancing in time, a partial pressure fluctuation history is reconstructed that is not the final acoustic output. A specific filtering technique is required in order to remove the data relative to an initial and a final transient, in which the solution is not converged.

The computation has a limited time range in which acoustic disturbances are predicted. As the simulation starts at the initial time $\tau = \tau_0$, the disturbances emitted by each source element ΔS_k , in which the source region (FW-H surface) is

discretised, needs a finite time to travel to the observer position $\mathbf{x}^{(i)}$, this finite time depending on the distance $\Delta S_{k-\mathbf{x}^{(i)}} (r^{(k,i)} = |\mathbf{x}^{(i)} - \mathbf{y}^{(k)}|)$. The acoustic pressure time history starts when the first disturbance from the closest ΔS_k reaches $\mathbf{x}^{(i)}$, at a receiver time $t_0 = \tau_0 + r_{\min}^{(k,i)}/c_0$, and the acoustic pressure output is only a partial result.

At a later time $t > t_0$, the disturbance emitted by the second closest ΔS_k reaches the observer $\mathbf{x}^{(i)}$ and progressively all the source elements contribute to the sound perceived at $\mathbf{x}^{(i)}$ at a given receiver time $t_{0-\text{conv}} > t_0$. Only at this point the summation of the contributions to $p'(\mathbf{x}, t)$ is complete and the pressure fluctuation time-history can be defined as “converged”.

A similar issue occurs towards the end of the time range considered. Therefore a correction procedure is implemented which consists in simply cutting out (deleting) the initial and final transients from the acoustic pressure time-history.

An additional variable, $\Phi_{\text{conv}}(\mathbf{x}^{(i)}, t)$, is computed for monitoring the completion of the summation of all contributions to $p'(\mathbf{x}, t)$. This variable stores the number of disturbances that reach each observer, at each acoustic time step. The value of this variable increases during the initial transient of the simulation till the time $t_{0-\text{conv}}$, at which all the source elements ΔS_k have contributed to the sound radiation at $\mathbf{x}^{(i)}$. At this point, the monitor variable assumes its maximum value and it remains constant thereafter for most part of the simulation. When the acoustic time history enters in the final transient, the monitor variable starts to decrease.

A typical shape of the normalized monitor variable is shown in Figure 2.7, from which the deletion of the initial and of the final transients of the acoustic pressure history is performed. The “converged” acoustic output is enclosed within the time range of a maximum plateau of the monitor variable ($\Phi_{\text{conv}} = 1$ in Figure 2.7). The deletion procedure is applied at the end of the simulation, by discarding the signal before and after the time range of constant Φ_{conv} . The final output of the tool is a matrix that stores, for each observer position, the pressure fluctuation $p'(\mathbf{x}^{(i)}, t)$ as a discretised time array.

For each discrete acoustic-source time τ^n , the acoustic analogy tool reads the density, the static pressure, and the velocity field on the FW-H surface from the CFD solution and retains the flow field data relative to the previous discrete acoustic-source

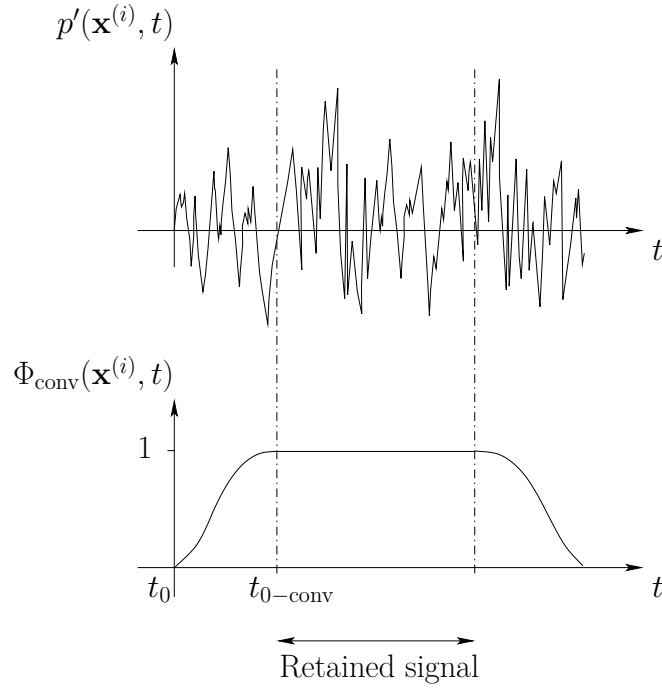


Figure 2.7: Procedure to discard time segments of the acoustic fluctuation p' at the i^{th} observer $\mathbf{x}^{(i)}$ that feature an incomplete sum of acoustic pressure fluctuation contributions.

field time τ^{n-1} . This enables the estimation of the source time derivatives using the backward finite difference approximation

$$\dot{\zeta} = \frac{\partial \zeta}{\partial \tau} \approx \frac{(\zeta^n - \zeta^{n-1})}{\Delta \tau}, \quad (2.39)$$

where ζ is a general source term variable. It also enables to perform the interpolation procedure described in Section 2.2.2.

The new CAA tools can either be run as post-processors or synchronously with the CFD simulation. In this work, the new AFW-H and CFW-H noise extractors were used to post-process previously stored CFD data, as shown by the flowchart in Figure 2.8. Both the CFD and the CAA processes run in the source time τ reference frame. In many applications, the CAA time step $\Delta \tau_{\text{CAA}}$ can be larger than the CFD time step $\Delta \tau_{\text{CFD}}$, because of differences in characteristic wavelength between the aerodynamic and the acoustic fields. This enables to define $\Delta \tau_{\text{CAA}} = k \Delta \tau_{\text{CFD}}$, where k is a positive integer. The CFD solution projected onto the predefined FW-H surface is saved at several contiguous discrete acoustic times $\tau = m \Delta \tau_{\text{CAA}}$, where $m = 1, 2, 3, \dots$ is integer, or, equivalently, when $\text{mod}(\tau, \Delta \tau_{\text{CAA}}) = 0$, as shown by

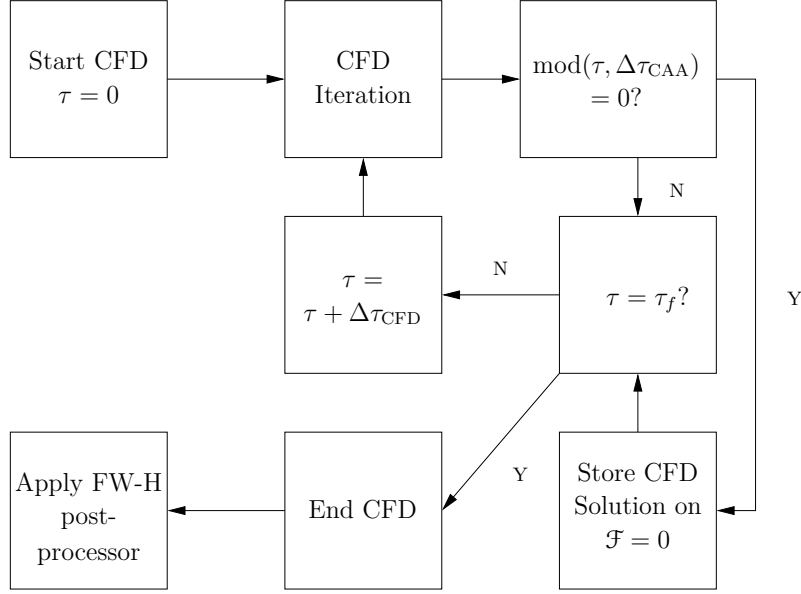


Figure 2.8: CFD/FW-H post-processor flowchart.

Figure 2.8. After the unsteady CFD simulation completes at time $\tau = \tau_f$, a time history of the flow state on the integration surface is available. The new FW-H post-processors use this dataset to predict the noise radiation both to the near-field and to the far-field.

2.3.1 Parallel MPI implementation

A parallel version of the FW-H post-processor is built for both the stationary and the convective acoustic analogy implementations, by using the Message Passing Interface (MPI) available in Python (MPI4Py). The parallelization is designed according to the discretization of the surface, by allocating the FW-H processing of different faces S_j to different computer cores. By optimizing the mesh design and by increasing the number of cores $N_c \leq N_f$, where N_f is the number of faces S_j , a significant speed up can be obtained, compared to the serial implementation of the FW-H algorithm.

In the parallel version of the code, the sequence of the loops over the time level n and the face index j is inverted, looping over the faces S_j first and then over time τ^n . This allows the estimation of the entire p' time-history resulting from a specific face S_j with a single core. The MPI schematic algorithm is shown in Figure 2.9. Specifically, the number of tasks N_{task} equals the number of faces N_f . Each $task_j$ consists in the estimation of the contribution to the noise radiation from a face S_j .

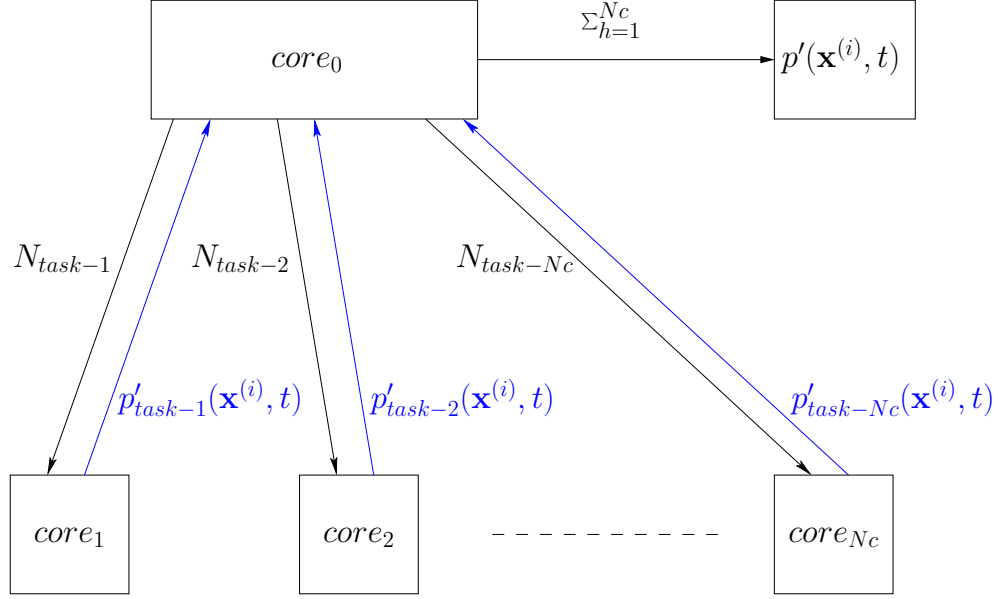


Figure 2.9: Flowchart of the FW-H MPI algorithm.

The N_f tasks are split between the N_c computer cores, by assigning a number of tasks N_{task-h} to each core, so that $\sum_{h=1}^{N_c} N_{task-h} = N_f \equiv N_{task}$.

Each face S_j is then processed separately, by post-processing the entire flow field time-history on S_j , obtained by CFD. At the end of the post-processing, the contributions to $p'(\mathbf{x}^{(i)}, t)$ from different processes $task_j$ on faces S_j are summed up by each slave $core_h$ and the result is passed to the master core 0. The latter sums the contributions to $p'(\mathbf{x}^{(i)}, t)$ from all N_c cores to obtain the $p'(\mathbf{x}^{(i)}, t)$ at the observer positions.

2.4 CFD dataset

The time-dependent flow prediction given in input to the new AFW-H and CFW-H tools for the jet noise applications presented in Chapters 4 and 5 was obtained by CFD. The density, velocity, and pressure fields on the control FW-H surfaces were provided by two numerical partners of the AeroTraNet2 project [13], *i.e.* the University of Leicester (UoL) and the Centre Européen de Recherche et de Formation Avancée en Calcul Scientifique (Cerfacs). Specifically, the Detached Eddy Simulation (DES) method implemented in the in-house code Cosmic [15, 132] was used at UoL, while the LES approach in the ONERA elsA software [130] was used at

Cerfacs [16, 133, 134, 135, 136].

The database for the single-stream jets investigated in Section 4.1 was obtained by LES [134, 135] for the subsonic case (Section 4.1.1) and by DES [15] for the supersonic case (Section 4.1.2). Both DES [15, 132] and LES [16, 133] data were available for the dual-stream under-expanded jet discussed in Section 4.2. Finally, for the in-flight single-stream jet presented in Section 5.2, LES data by Pineau [136] was used.

In Chapter 4, the results from the new Python AFW-H tool are indicated by a dual label referring to both the CFD code and the FW-H formulation adopted in the two-step hybrid approach coupling CFD and acoustic analogy. For instance, the “Cosmic/AFW-H” label indicates that DES predictions by Cosmic [15, 132] were post-processed by applying the stationary formulation of Section 2.2.3 to extract the noise radiation from the jet. Where LES predictions by elsA were given in input to the AFW-H tool, the label “elsA/AFW-H” is used. The same convention is adopted in Chapter 5 for the acoustic estimation obtained by the new convective analogy CFW-H tool.

2.4.1 DES by Cosmic

The in-house code Cosmic implements a DES method that aims to combine the advantages of both LES and Reynolds Averaged Navier-Stokes (RANS) approaches. Both LES and RANS consist in splitting the time-resolved variables in the flow governing equations (Navier-Stokes equations) between an averaged component and a fluctuation [15]. The main difference is in the averaging procedure. A spatial average is used in LES, while in RANS simulations the averaging is performed over time [15]. Averaging the Navier-Stokes equations generates additional unknown terms that need to be modelled either with a Sub Grid Scale (SGS) model or with a RANS model, respectively for LES and RANS [15].

In the DES approach in Cosmic, LES and RANS are alternatively used in different regions of the CFD domain. Specifically, a pure RANS is used at short distances from the wall, where this method is known to provide accurate mean boundary layer predictions [15]. As the distance from the wall is increased, a blending function converts the behaviour of the code first to a coupled RANS/LES approach and then

to a pure LES [15]. The blending function acts on the closure turbulence model that functions as an SGS model in regions where the mesh is fine enough to allow for LES and as a RANS model where the mesh is coarser [15].

In terms of spatial discretization, Cosmic is a finite-volume code up to third-order accurate in space, compatible with structured meshes only [15]. The time integration is performed with an explicit multi-stage Runge-Kutta time step algorithm, giving a second-order accuracy in time [15]. The use of a low-order code for DES predictions produces some computational savings with respect to a LES approach on a high-order CFD code, such as elsA [130]. The feasibility of this cheaper computation is tested in [15].

As far as the single-stream and the dual-stream under-expanded jets investigated in Sections 4.1.2 and 4.2 are concerned, the computational domain was discretised with a structured multi-block body-fitted Cartesian mesh [15]. The mesh is built with a butterfly topology in order to avoid any singularity on the jet axis as it occurs with cylindrical meshes [15]. In order to save computational cost without degrading the accuracy of the solution with spurious reflections at the boundaries of the domain, a sponge region surrounds the physical domain [15]. The function of the sponge region is to damp outgoing waves in order to reduce their amplitude to values that can be handled by the non-reflective boundary conditions [15]. The total number of cells in the finite volume discretization is around 65.8×10^6 for the single-stream under-expanded jet and 226×10^6 for the dual-stream under-expanded jet [15].

2.4.2 LES by elsA

The elsA software [130] is a high-order CFD solver developed by ONERA that was used at Cerfacs to generate LES predictions of the flow for the test cases investigated in Chapters 4 and 5. ElsA is a finite-volume multi-block structured solver with a sixth-order space accurate scheme [16]. It uses for the time integration a six-step low storage Runge-Kutta Dispersion Relation Preserving (DRP) scheme by Bogey and Bailly [137] [16]. As in the Cosmic code, the mesh used in elsA has a butterfly topology that allows for a more uniform mesh close to the jet axis [16]

In the test cases investigated in this work, the LES obtained by elsA is initialized by a RANS simulation used as boundary and initial conditions [16]. The RANS

prediction is first interpolated to a coarse LES mesh in order to accelerate the transient phase characterised by a non-physical behaviour of the jet [16]. Afterwards, the simulation is progressed in time with the finer LES mesh used for the data acquisition process [16]. As far as the time step is concerned, the simulation is initialised with a constant CFL that allows for a variable time step. The time step achieved during this phase is then used for the constant time step LES.

2.4.3 FW-H surface placement in the CFD domain

The FW-H surface could theoretically be placed everywhere in the flow, as the FW-H acoustic analogy allows for non-linearities to be present on or outside the $\mathcal{F}(\mathbf{x}, t) = 0$ surface (see Section 2.2). However, if the quadrupole noise distribution in the volume outside the surface is neglected, as in the jet noise applications presented in Chapters 4 and 5, special care needs to be taken to ensure the correct placement of the control surface, as previously discussed in Sections 2.2 and 2.2.1. In 2006, Suzuki and Colonius [138] discussed the different regions of the pressure field in a single round jet, identifying three main regimes. The mixing layer of the jet is characterised by non-linear hydrodynamic perturbations. These perturbations decay exponentially outside the mixing layer, with increasing radial distance from the jet axis [138]. This behaviour allows to identify both a “non-linear hydrodynamic” (mixing layer) and a “linear hydrodynamic” (near-field outside the mixing layer) regime [138]. In the latter, the non-linear perturbations associated with instability waves generating at the shear-layer become negligible and the pressure field is characterized by a mixture of linear hydrodynamic perturbations and of radiating pressure waves [138]. Further away from the jet axis, where the hydrodynamic perturbations are far weaker than the acoustic waves, a “linear acoustic” regime can be identified. The three regimes are shown in Figure 2.10, from [138].

In Chapters 4 and 5, the correct placement of the FW-H surface is tested by comparing the acoustic prediction between nested surfaces enclosing the jet. The surfaces have the same shape and axial size, but the radial size increases moving from the innermost to the outermost surface. If the acoustic estimation is essentially invariant between two or more surfaces, this means that the control surface is correctly placed in the linear regime of the pressure field [138]. The specific regime in which the

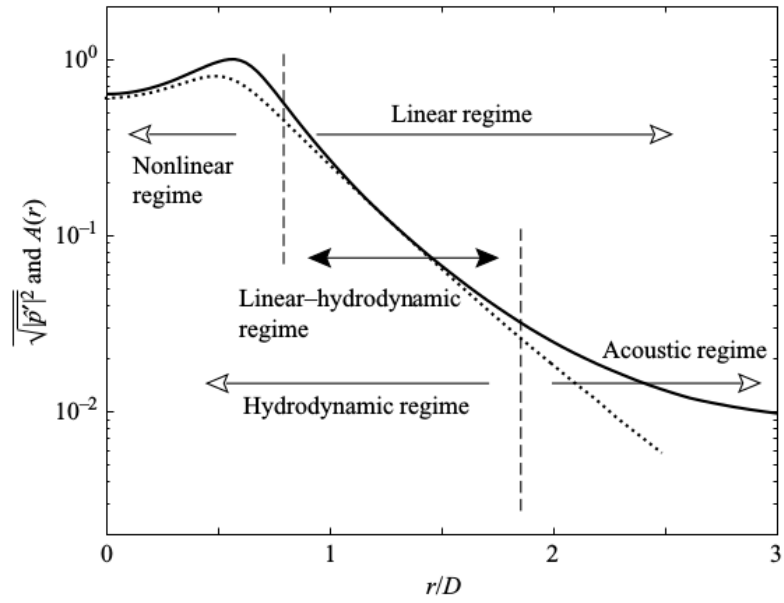


Figure 2.10: Diagram of the flow regimes of a round jet in the radial direction at $x/D = 4$ from Suzuki and Colonius [138].

surface is placed is also discussed in Chapters 4 and 5 for the test cases considered, based on Figure 2.10.

Chapter 3

Advanced-time FW-H acoustic analogy code validation

In this chapter, the new Advanced-time Ffowcs Williams-Hawkings acoustic analogy (AFW-H) tool is validated on a set of elementary noise sources of increasing complexity. Both omnidirectional and directive sources are considered, including monopole (Section 3.1.1), dipole (Section 3.1.2), and quadrupole sources (Sections 3.1.3 and 3.1.4). These elementary sources are often used for modelling the acoustic radiation from unsteady flows. Specifically, quadrupole sources are used to represent the noise generated aerodynamically from free jets [1], while a distribution of dipole-type sources is used in the presence of solid bodies [68] (see Section 2.2).

This validation process provides confidence in using the time-domain code to predict the near-field and the far-field noise from unsteady flows, leading to single and dual-stream jet noise applications, in either a stationary or a uniformly convected medium, respectively in Chapters 4 and 5.

An unexpected behaviour of the acoustic analogy numerical tool is found with a lateral quadrupole source placed close to the FW-H surface corners, in Section 3.1.4. Section 3.2 presents the results of a parametric study that further investigates this behaviour and aims to explain its occurrence.

3.1 Predicting noise radiated from elementary sources

Figure 3.1 shows the layout of the elementary source test cases that is used to validate the AFW-H tool. Specifically, a prismatic FW-H integration surface is defined relative to the observer and to the source locations. The surface size and position are defined in the Cartesian reference system shown in Figure 3.1.

All tests use FW-H integration surfaces of the same topology, which is a square prism of cross-section $a \times a$, and length 2ℓ normal to this cross-section. The prism extends symmetrically about the $x_1 = 0$ plane over the range $-\ell \leq x_1 \leq \ell$, enclosing the source locations $s^{(1)}$ and $s^{(2)}$.

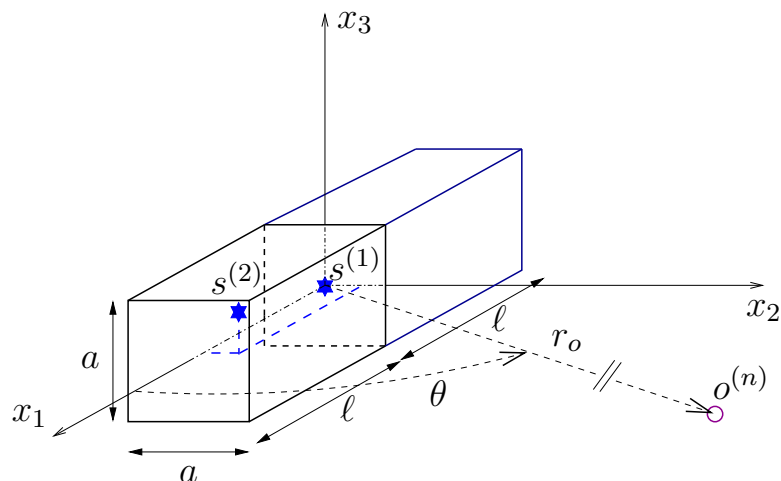


Figure 3.1: Sketch of the prismatic FW-H integration surface, showing the n^{th} observer $o^{(n)}$ of a circular array centred at the origin and the source locations $s^{(1)}$ (origin) and $s^{(2)}$ (proximal to the corner of the FW-H surface).

The location $s^{(1)}$ is chosen to reproduce the known directivity pattern of the elementary noise sources, for which analytical reference solutions are available [47, 139]. The radiation pattern of each noise source is discussed in Sections 3.1.1– 3.1.4, where it is shown that the AFW-H code correctly reproduces these patterns. Position $s^{(2)}$ is defined to test the robustness of the AFW-H code on the source being proximal to the corner of the prismatic FW-H surface.

A circular array of 40 observers in the $x_3 = 0$ plane set at a radial distance r_o from the origin of the reference system is considered. These observers are uniformly

spaced in θ , with $\Delta\theta = 9^\circ$. Their position is defined by the distance from the origin r_o and the angle θ from the x_1 -axis, as shown in Figure 3.1. The coordinates in the Cartesian reference system of the n^{th} observer are $\mathbf{x}^{(n)} = r_o (\cos \theta^{(n)}, \sin \theta^{(n)}, 0)$, with $\theta^{(n)} = (n - 1) \Delta\theta$, $n = 1, 2, \dots, 40$, and $\theta \in [0; 2\pi)$. The radius of the circular array of observers is denoted by r_o to distinguish it from the distance source-observer $r = |\mathbf{x} - \mathbf{y}|$. Whereas $r = r_o$ for a source located at $s^{(1)}$, $r \neq r_o$ for any source located off-origin, as at position $s^{(2)}$.

The noise radiation is estimated for each observer of the circular array in terms of the pressure fluctuation time-history. Collectively, the amplitudes of the acoustic disturbance at each observer determine the source directivity that is compared against the reference analytical solutions. Pressure fluctuations and radiation patterns are reported for each source, for both locations $s^{(1)}$ and $s^{(2)}$, in Sections 3.1.1– 3.1.4.

The effect of the FW-H surface position on the acoustic prediction is also investigated by varying the size of the square prism (a and ℓ) around the sources located at $s^{(2)}$. The solution is shown to be independent from the FW-H surface (Section 3.1.4), as it is expected in a well-posed porous FW-H formulation application [54, 85].

If a source is located at $s^{(2)}$ within a short distance d from the corner of the FW-H square prism compared to the acoustic wavelength λ ($d/\lambda \ll 1$), a discrepancy between the analytical solution and the numerical prediction is found. Unexpectedly, Section 3.2 shows that increasing either the time resolution or the space resolution does not improve the noise prediction for d/λ below a certain limit value, even for simple elementary sources.

Further numerical tests are performed to investigate this behaviour by varying the source location $s^{(2)}$ along the prism diagonal, from the origin of the axes to positions proximal to the $(\ell, a/2, a/2)$ corner of the FW-H integration surface. This provides two parametric studies of the mismatch between the reference analytical solution and the numerical prediction in Sections 3.2.1 and 3.2.2. This study produces a guideline for the normalised distance d/λ that gives an acceptable numerical error for practical engineering applications of the new AFW-H code.

It is inferred that the integration on the FW-H surface for $d/\lambda \ll 1$ presents some numerical issue that cannot be overcome by simply improving the discretization. The integral solution of the FW-H acoustic analogy was found by the author,

in collaboration with the supervisory team and Emeritus Professor Christopher Morfey, to be characterised by large contributions of opposite sign cancelling out by summation, when $d/\lambda \ll 1$. These are extremely challenging to evaluate numerically, even with double precision arithmetics, causing a significant numerical error when the point source is located proximal to the FW-H corner. A further investigation is required to clearly determine the cause of this unexpected behaviour.

3.1.1 Monopole

The first source considered is a monopole of sound power level $L_W = 96.83$ dB re 1pW radiating at a frequency $f = 5.67$ kHz ($\lambda = 0.06$ m). This acoustic power gives a Sound Pressure Level (SPL) of 80 dB re 20 μ Pa at 33.33λ from the source [140]. A FW-H surface is used with base side $a = \lambda/3$ and half height $\ell = \lambda/6$, resulting in a surface of a cube centred at the origin of the reference system. This integration surface is discretised with a uniform mesh of N nodes in each spatial direction that corresponds to $N_\lambda = (\lambda/a) \times N = 3N$ points per wavelength.

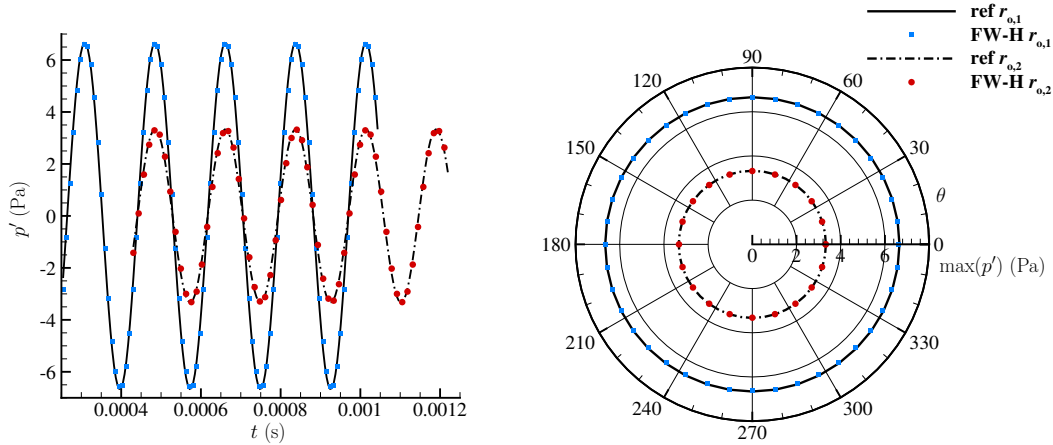
The reference analytical solution for the acoustic pressure fluctuation from the monopole source is [47]

$$p'(\mathbf{r}, t) = -\frac{Bq}{r} \sin(\omega t - kr) , \quad (3.1)$$

where $B = \rho_0 c_0 k (4\pi)^{-1}$, $\rho_0 = 1.225$ kg/m³, $c_0 = 340.25$ m/s, $k = \omega/c_0$, $q = (8\pi c_0 W \rho_0^{-1} \omega^{-2})^{1/2}$, $W = 10^{L_w}$ pW, and $\omega = 2\pi f$. $r = |\mathbf{r}| = |\mathbf{x} - \mathbf{y}|$ is the source-observer radiation distance, from the monopole position \mathbf{y} to the observer position \mathbf{x} . In Equation 3.1, $\sin(\omega t - kr)$ represents the oscillatory part (both in time and in space) and the amplitude of the pressure fluctuation is $Bq/r \propto 1/r$.

The source strength q is obtained by imposing SPL=80 dB re 20 μ Pa at $r = 33.33\lambda$ in Equation 3.1. Noise predictions are obtained at $r_{o,1} = \lambda$ and at $r_{o,2} = 2\lambda$ on the circular array of observers of Figure 3.1, from the application of the acoustic analogy of Section 2.2.3. Figure 3.2 shows the time-resolved acoustic pressure fluctuation and the directivity for a monopole source located at $s^{(1)}$. Solid and dash-dot black lines denote the reference analytical solution, respectively at $r_{o,1}$ and at $r_{o,2}$, which is labelled as “ref”. Blue and red symbols show the corresponding numerical solutions at $r_{o,1}$ and at $r_{o,2}$, respectively.

The acoustic pressure fluctuation p' in Figure 3.2(a) is from the observer $o^{(4)}$ at $\theta^{(4)} = 27^\circ$. This result shows that the AFW-H tool matches the analytical pressure fluctuation in amplitude, phase, and frequency, at both radial distances [140]. A small time shift is present in the numerical solution that is not noticeable from Figure 3.2(a), because the order of magnitude of this time shift is $\Delta\tau/2$, where $\Delta\tau = \lambda/(N_T c_0) = 4.41 \times 10^{-6}$ s is the time step of the numerical calculation, with $N_T = 40$ the number of points per period T and c_0 the speed of sound in the undisturbed medium. This discrepancy is due to the backward finite difference approximation of Equation 2.39 that is used to discretise the source time derivatives. This phase shift error can be decreased by increasing the time resolution, by reducing $\Delta\tau$.



(a) Pressure fluctuation at observer $o^{(4)}$ at $\theta^{(4)} = 27^\circ$.

(b) Directivity pattern.

Figure 3.2: Radiation in a stationary medium from an omnidirectional noise source (monopole), located at the origin $s^{(1)}$, to observers placed at radial distances $r_{o,1} = \lambda$ and $r_{o,2} = 2\lambda$ from the origin. $a = \lambda/3$, $\ell = \lambda/6$, $\lambda = 0.06$ m, $N_T = 40$, and $N_\lambda = 120$.

The ratio of the peak to peak pressure fluctuation amplitude at $r_{o,2}$ and at $r_{o,1}$ for both the numerical and the analytical p' is 2.0. This shows that the AFW-H method correctly predicts the geometric scaling of the acoustic intensity with increasing radial distance from the monopole source, that is $I \propto 1/r^2$ (acoustic intensity), by which $p' \propto 1/r$. The spherically symmetric radiation pattern of the monopole is correctly captured by the FW-H method, at both radial distances $r_{o,1}$ and $r_{o,2}$, as

shown by Figure 3.2(b).

The effect of the spatial discretization error of the FW-H surface on the numerical predictions is investigated by varying the number of ΔS_k discrete surface elements (see Section 2.3) on the FW-H surface from 6×20^2 ($N_\lambda = 60$) to 6×40^2 ($N_\lambda = 120$) and to 6×80^2 ($N_\lambda = 240$). In this analysis, the time step is kept constant to a very small value, $\Delta\tau = 1.380 \times 10^{-7}$ s, in order to reduce as much as possible the error contribution due to the temporal discretization. The error

$$e_d = \frac{\left| \max(p'_{\text{FW-H}}(t)) - \max(p'_{\text{ref}}(t)) \right|}{\max(p'_{\text{ref}})} \times 100 \quad (3.2)$$

in the fluctuating pressure amplitude between the numerical and the analytical solutions at $o^{(4)}$ at $r_{o,1}$ reduces from 0.1122% on the baseline mesh to 0.0243% and to 0.0024%, respectively on the 6×40^2 mesh and on the 6×80^2 mesh. No appreciable differences in frequency are observed.

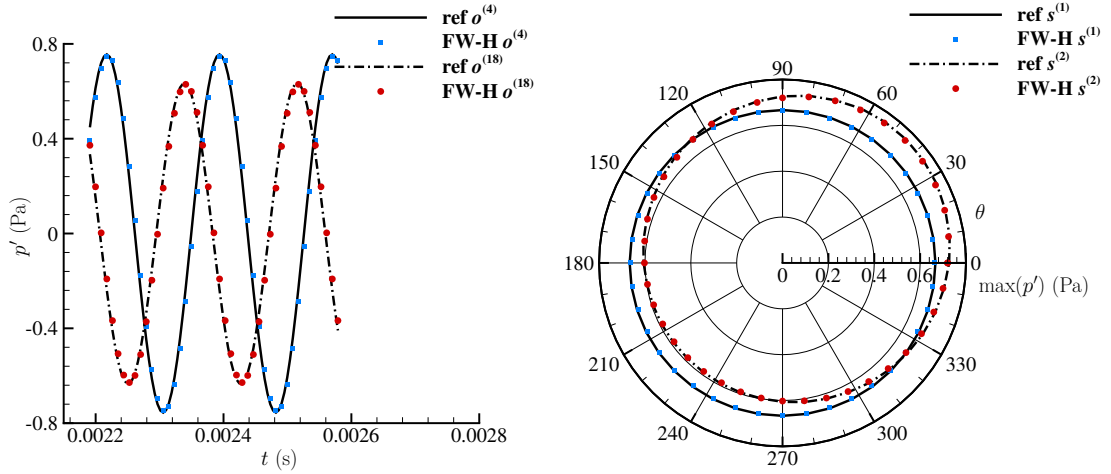
The effect of the temporal discretization is also examined by increasing the temporal resolution from $\Delta\tau = 8.820 \times 10^{-6}$ s ($N_T = 20$) to $\Delta\tau = 4.410 \times 10^{-6}$ s ($N_T = 40$) and to $\Delta\tau = 2.205 \times 10^{-6}$ s ($N_T = 80$), resulting in a decrease of the error e_d from 2.7198% to 0.7690% and to 0.2273% at the same observer location. In this case, the mesh is refined to 6×160^2 in order to reduce the error contribution due to the spatial discretization.

Thus, as both the spatial and the temporal resolutions are improved, the numerical solution converges to the analytical solution [140]. The spatial and the temporal resolutions of $N_\lambda = 60$ points per wavelength (6×20^2 ΔS_k discrete faces) and $N_T = 40$ points per period ($\Delta\tau = 4.41 \times 10^{-6}$ s) give an error lower than 1% and appear appropriate for this application.

Figure 3.3 displays the acoustic results for the off-centre source location $s^{(2)}$ versus the benchmark analytical solution, on a circular array of 40 uniformly spaced observers at the constant radial distance $r_o = 10\lambda$ from the origin. r_o does not coincide with the radiation distance $r = |\mathbf{x} - \mathbf{y}|$ in this case. For this test, the FW-H surface of a cube is used with $a = 2\lambda$ and $\ell = \lambda$.

Figure 3.3(a) shows the predicted acoustic pressure fluctuation p' at the observer positions $o^{(4)}$ ($\theta^{(4)} = (n-1)\Delta\theta|_{n=4} = 27^\circ$) and $o^{(18)}$ ($\theta^{(18)} = 180^\circ - 27^\circ$). The analytical solution is labelled “ref” and it is denoted by the solid-black line and by

the dash-dot black line, respectively for $o^{(4)}$ and $o^{(18)}$. Blue and red symbols are used respectively for the numerical predictions at $o^{(4)}$ and at $o^{(18)}$.



(a) Pressure fluctuation at observers $o^{(4)}$ at $\theta^{(4)} = 27^\circ$ and $o^{(18)}$ at $\theta^{(18)} = 180^\circ - 27^\circ$, from the source located at $s^{(2)}$ (Di Stefano *et al.* [141]). (b) Directivity pattern (Di Stefano *et al.* [141]).

Figure 3.3: Radiation in a stationary medium from an omnidirectional noise source (monopole), located at $s^{(1)}$ (origin) and at $s^{(2)}$ ($\mathbf{y}^{(2)} = (0.92, 0.92, 0.92) \lambda$), to observers placed at a constant radial distance $r_o = 10\lambda$ from the origin. $a = 2\lambda$, $\ell = \lambda$, $\lambda = 0.06$ m, $N_T = 40$, and $N_\lambda = 20$.

The source $s^{(2)}$ is placed at $\mathbf{y}^{(2)} = (0.92, 0.92, 0.92) \lambda$, while the corner of the FW-H surface is at $(1.00, 1.00, 1.00) \lambda$. In Figure 3.3(a), the prediction substantially matches the analytical solution in amplitude, phase, and frequency at both observers $o^{(4)}$ and $o^{(18)}$, despite the small distance $d/\lambda = 0.14$ between the source and the corner of the FW-H integration surface. The acoustic pressure fluctuation amplitude at the observer $o^{(4)}$ is greater than that at $o^{(18)}$, due to the shorter source-observer distance. This causes the directivity to lose its spherical symmetry as the source is placed off-origin at $s^{(2)}$, as shown by Figure 3.3(b).

Figure 3.3(b) reports the directivity on the $r_o = 10\lambda$ circular array centred at the origin for both $s^{(1)}$ and $s^{(2)}$. The black lines denote the analytical solution and the symbols denote the corresponding numerical prediction. A substantial match is found between the analytical solution and the numerical prediction of the sound pressure directivity for both source locations. A spherically-symmetric pattern is

obtained with the source placed at $s^{(1)}$. For a monopole located at $s^{(2)}$, towards the corner of the FW-H surface, an oval directivity pattern is obtained that has a 45° line axis of symmetry. The maximum p' amplitude is reached at $\theta^{(6)} = 45^\circ$, in the direction of the shortest distance from the source to the observer, while the minimum p' amplitude is predicted at $\theta^{(26)} = 180^\circ + 45^\circ = 225^\circ$.

3.1.2 Dipole

In the second test, a directional source is considered. This is a x_2 -axis dipole sound source, which radiates at the same frequency $f = 5.67$ kHz ($\lambda = 0.06$ m) as the monopole in Section 3.1.1. The same layout of Figure 3.1 is used as in Section 3.1.1. The two source locations $s^{(1)}$ and $s^{(2)}$ test respectively the dipole source radiation directivity and the influence on the acoustic analogy prediction of placing a source close to the FW-H integration surface corner.

The time-resolved acoustic pressure fluctuation for the source position $s^{(1)}$ at the origin of the reference system is reported in Figure 3.5, together with the analytical solution labelled “ref”. The reference analytical solution is [139]

$$p'(\mathbf{r}, t) = -Bk \frac{(q\epsilon)}{r} (\hat{\mathbf{r}} \cdot \hat{\boldsymbol{\epsilon}}) \left[\cos(\omega t - kr) + \frac{\sin(\omega t - kr)}{kr} \right], \quad (3.3)$$

where $\boldsymbol{\epsilon}$ is the dipole direction vector, oriented along the x_2 -axis in the current test, while $\epsilon = |\boldsymbol{\epsilon}|$ and $\hat{\boldsymbol{\epsilon}} = \boldsymbol{\epsilon}/\epsilon$ are respectively its magnitude and its unit vector.

The magnitude ϵ of the dipole direction vector $\boldsymbol{\epsilon}$ represents the dipole source size. Its meaning can be explained by considering two point monopole sources, located close to one another, to approximate the dipole radiation as in Figure 3.4. In this case, ϵ represents the distance between the two monopole sources, which is set to a small value with respect to the smallest acoustic distance source-observer $r = |\mathbf{x} - \mathbf{y}|$. For $\epsilon < 10^{-3}r$, the acoustic field generated by the two monopole sources approximates well the sound field of a dipole acoustic source. The dipole source strength is therefore represented by the quantity $(q\epsilon)$, which assumes a finite value normalised to give the SPL of 80 dB re $20\mu\text{Pa}$ on the x_2 -axis, 33.33λ away from the source, as in Section 3.1.1.

By referring to Figure 3.1, the dot product between the two unit vectors $\hat{\mathbf{r}}$ and $\hat{\boldsymbol{\epsilon}}$

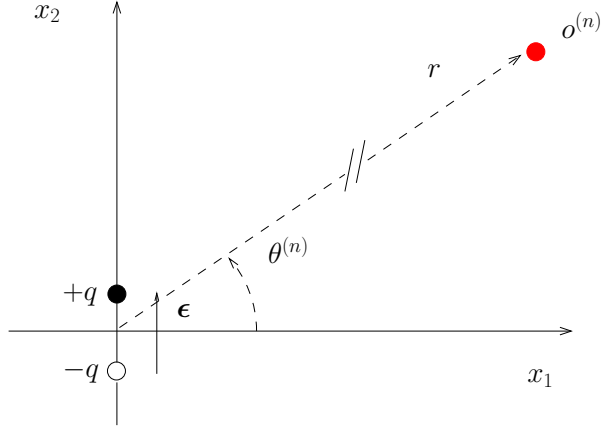


Figure 3.4: Schematic of the dipole source approximated by two monopole sources of equal and opposite strength q spaced $\epsilon \rightarrow 0$ apart. The plane $x_3 = 0$ is shown, together with a generic observer $o^{(n)}$ from the circular array defined in Section 3.1.

can be stated as

$$\hat{\mathbf{r}} \cdot \hat{\boldsymbol{\epsilon}} = \cos(90^\circ - \theta) = \sin(\theta), \quad (3.4)$$

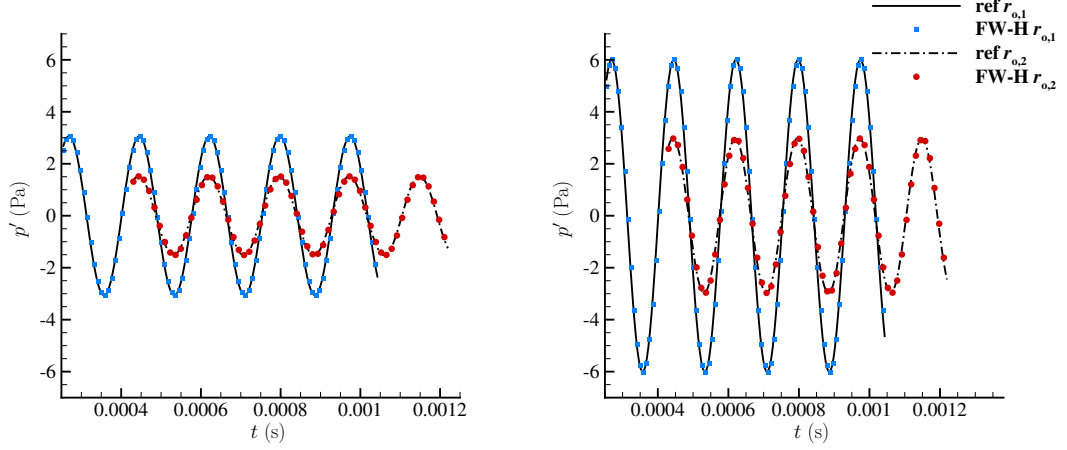
which represents the directivity pattern of the source. The maximum radiation is therefore at $\theta = 90^\circ$ and at $\theta = 270^\circ$ from the positive x_1 -axis (*i.e.* on the x_2 -axis), where $\sin(\theta) = \pm 1$. In all the other directions, the amplitude of the pressure fluctuation is lower, as $|\sin(\theta)| < 1$ for $\theta \neq 90^\circ + n180^\circ$. Along the x_1 -axis direction, the dipole does not radiate, as $\sin(\theta) = 0$ where $\theta \rightarrow 0$.

The second term in the square brackets in Equation 3.3 is a near-field term, because of its dependence on $1/(kr)$ that approaches zero where $kr \gg 1$. The scaling factor with distance r from the source, along any specific θ direction, is given by

$$\zeta_{\text{dip}}(r) = \frac{\sqrt{1 + \frac{1}{(kr)^2}}}{r}. \quad (3.5)$$

Consequently, the amplitude of the acoustic pressure fluctuation in the far-field, where $kr \gg 1$, decays as $1/r$.

Figure 3.5 uses the same notation as Figure 3.2(a), by which the black lines and the symbols indicate respectively the reference solutions and the numerical predictions. The numerical solution is obtained using the FW-H surface of a cube with $a = \lambda/3$ and $\ell = \lambda/6$. Two circular arrays with 40 observers each, equispaced in θ , are defined respectively at $r_{o,1} = \lambda$ and at $r_{o,2} = 2\lambda$.



(a) Pressure fluctuation at observer $o^{(4)}$ at $\theta^{(4)} = 27^\circ$. (b) Pressure fluctuation at observer $o^{(8)}$ at $\theta^{(8)} = 63^\circ$.

Figure 3.5: Radiation in a stationary medium from a dipole point source, located at the origin $s^{(1)}$, to observers placed at radial distances $r_{o,1} = \lambda$ and $r_{o,2} = 2\lambda$ from the origin. $a = \lambda/3$, $\ell = \lambda/6$, $\lambda = 0.06$ m, $N_T = 40$, and $N_\lambda = 120$.

Figures 3.5(a) and 3.5(b) show the acoustic pressure time-history respectively at the observer $o^{(4)}$, for which $\theta^{(4)} = 27^\circ$, and at $o^{(8)}$, for which $\theta^{(8)} = 63^\circ$. There is no noticeable difference in amplitude, phase, or frequency between the analytical and the numerical time traces, at both observers, indicating that the acoustic pressure is correctly predicted by the AFW-H method.

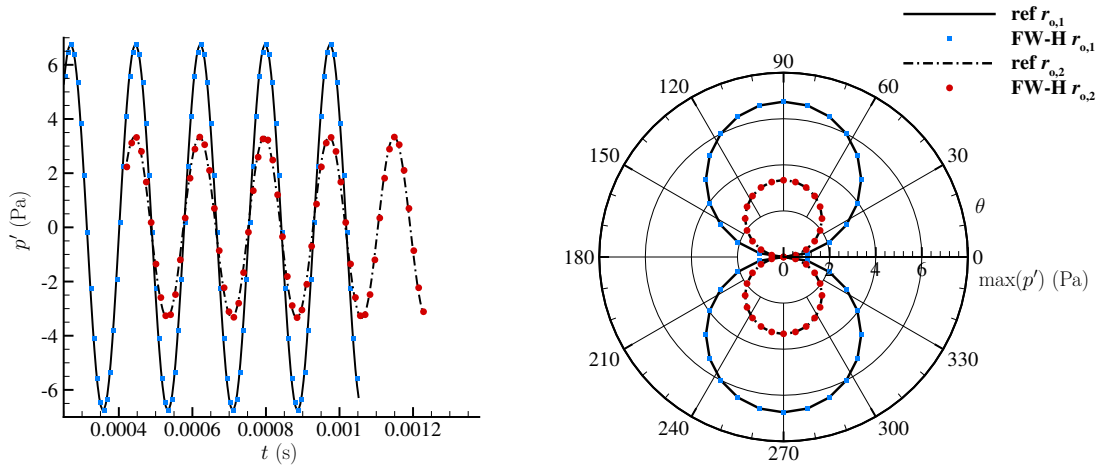
Upon close examination of the results, a small phase shift due to the backward finite difference approximation of the source time derivatives is found as in Section 3.1.1, which is not noticeable in Figures 3.5(a) and 3.5(b). Doubling the radial distance of the observers from the origin to $r_{o,2} = 2\lambda$ doubles the source-observer distance, as the dipole is located at $s^{(1)}$. The pressure perturbation amplitude is reduced by a factor of 0.495 in both the analytical and the numerical results, confirming that the analytical scaling of the sound pressure with distance from the source in Equation 3.5 is correctly captured. The good match in amplitude, phase, and frequency between the reference analytical pressure fluctuation and the AFW-H integration surface method prediction is maintained at this increased radial distance.

Figure 3.6(a) displays the acoustic pressure fluctuation at $\theta^{(11)} = 90^\circ$, on the dipole axis, where the dipole radiation reaches its maximum amplitude. The AFW-H prediction matches again the reference solution in amplitude, phase, and frequency,

for both radial distances $r_{o,1}$ and $r_{o,2}$.

Comparing Figures 3.5(a) and 3.5(b) with Figure 3.2(a) in the previous section, it can be observed that the dipole radiation at $o^{(4)}$ and at $o^{(8)}$ exhibits a lower amplitude at the same distance from the source compared to the monopole, even though the strength of the two elementary sources is defined to obtain the same 80 dB re $20\mu\text{Pa}$ on the x_2 -axis, 33.33λ away from the source. According to Equations 3.3 and 3.4, away from the x_2 -axis, the acoustic pressure fluctuation amplitude reduces by a factor of $\sin(\theta)$ for a dipole point source. Therefore, at the observers $o^{(4)}$ and $o^{(8)}$, the pressure fluctuation amplitude is expected to be respectively 0.454 and 0.891 of the maximum amplitude at $\theta^{(11)} = 90^\circ$, as confirmed by the numerical predictions in Figures 3.5(a)– 3.6(a).

The $\sin(\theta)$ directivity of the dipole point source is confirmed by Figure 3.6(b). The typical figure-of-eight shape of the dipole radiation pattern [47, 139] is clearly visible at both radial distances $r_{o,1}$ and $r_{o,2}$ and the numerical prediction correctly follows the analytical solution. This indicates that the new AFW-H tool is able to capture the radiation characteristics of directive sources to a good approximation.



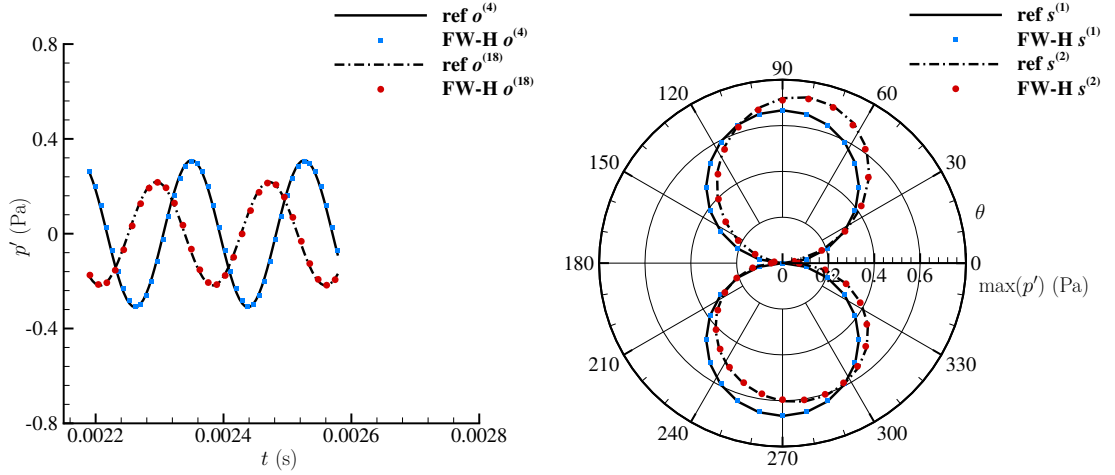
(a) Pressure fluctuation at observer $o^{(11)}$ at $\theta^{(11)} = 90^\circ$.

(b) Directivity pattern.

Figure 3.6: Radiation in a stationary medium from a dipole point source, located at the origin $s^{(1)}$, to observers placed at radial distances $r_{o,1} = \lambda$ and $r_{o,2} = 2\lambda$ from the origin. $a = \lambda/3$, $\ell = \lambda/6$, $\lambda = 0.06$ m, $N_T = 40$, and $N_\lambda = 120$.

Figure 3.7 shows the results for a dipole source of the same strength placed

off-origin at $s^{(2)}$, at location $\mathbf{y}^{(2)} = (0.92, 0.92, 0.92) \lambda$. 40 observers equispaced in θ are set at constant $r_o = 10\lambda$ from the origin. The FW-H surface has base side $a = 2\lambda$ and half height $\ell = \lambda$ in this test. The acoustic pressure fluctuations predicted at $o^{(4)}$ and at $o^{(18)}$ are reported in Figure 3.7(a). A good match is shown between the prediction and the reference solution. The noise radiation to observers $o^{(4)}$ and $o^{(18)}$, which are placed symmetrically about the x_2 -axis, differs, displaying a greater amplitude at $o^{(4)}$, which is located in the first quadrant. This is due to placement of the dipole source off-origin, at $s^{(2)}$, giving a different source-observer distance r distribution around the circular arc of observers, which is defined about the origin.



(a) Pressure fluctuation at observers $o^{(4)}$ at $\theta^{(4)} = 27^\circ$ and $o^{(18)}$ at $\theta^{(18)} = 180^\circ - 27^\circ$, from the source located at $s^{(2)}$ (Di Stefano *et al.* [141]).

Figure 3.7: Radiation in a stationary medium from a dipole point source, located at $s^{(1)}$ (origin) and at $s^{(2)}$ ($\mathbf{y}^{(2)} = (0.92, 0.92, 0.92) \lambda$), to observers placed at a constant radial distance $r_o = 10\lambda$ from the origin. $a = 2\lambda$, $\ell = \lambda$, $\lambda = 0.06$ m, $N_T = 40$, and $N_\lambda = 20$.

In Figure 3.7(b), the directivity pattern from the source at the off-origin position $s^{(2)}$ is compared to the characteristic figure-of-eight shape of the dipole radiation, obtained from a source of the same strength located at $s^{(1)}$. Placing the dipole at $s^{(2)}$ breaks the symmetry in directivity about the x_2 -axis. The radiation is amplified in the first and fourth quadrants, respectively for angles $30^\circ < \theta < 90^\circ$ and $300^\circ < \theta < 360^\circ$, while an attenuation is produced in the third quadrant ($180^\circ < \theta < 270^\circ$) and in

most of the second quadrant ($120^\circ < \theta < 180^\circ$). A good match can be appreciated between the analytical and the numerical results for the off-origin source location $s^{(2)}$, which is characterised by a short distance d between the source and the corner of the prismatic FW-H surface, $d/\lambda = 0.14$.

3.1.3 Longitudinal quadrupole

The second directional sound source considered in this study is a x_2 -axis longitudinal quadrupole that can be approximated by two dipole sources with equal strength and in-line axes [47], as shown in Figure 3.8. The analytical solution for the pressure perturbation [139] at distance \mathbf{r} from the source is

$$p'(\mathbf{r}, t) = -B_1 \frac{(q\epsilon^2)}{r} (\hat{\mathbf{r}} \cdot \hat{\boldsymbol{\epsilon}})^2 \left[\frac{3}{kr} \cos(\omega t - kr) + \left(\frac{3}{(kr)^2} - 1 \right) \sin(\omega t - kr) \right] + B_1 \frac{(q\epsilon^2)}{r} \left[\frac{1}{kr} \cos(\omega t - kr) + \frac{1}{(kr)^2} \sin(\omega t - kr) \right], \quad (3.6)$$

where $B_1 = \rho_0 c_0 k^3 (4\pi)^{-1}$, the vector $\boldsymbol{\epsilon}$ is the orientation of the longitudinal quadrupole, $\epsilon^2 = |\boldsymbol{\epsilon}|^2$, and $\hat{\boldsymbol{\epsilon}} = \boldsymbol{\epsilon}/\epsilon$. The magnitude ϵ of the longitudinal quadrupole orientation vector $\boldsymbol{\epsilon}$ assumes a similar meaning as for the dipole test case, as shown in Figure 3.8. The longitudinal quadrupole source strength is represented by the quantity $(q\epsilon^2)$ in Equation 3.6.

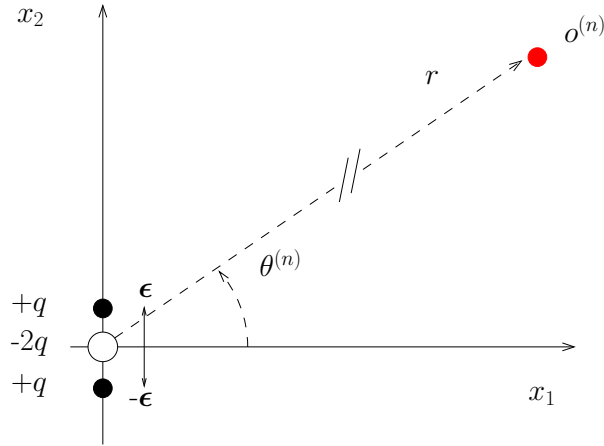


Figure 3.8: Schematic of the longitudinal quadrupole source approximated by two in-line dipole sources (four monopoles) of equal and opposite strength ($q\epsilon$). The plane $x_3 = 0$ is shown, together with a generic observer $o^{(n)}$ from the circular array defined in Section 3.1.

Equation 3.6 does not allow an immediate reading of the source directivity. However, a far-field ($kr \gg 1$) approximation to Equation 3.6 can be obtained by neglecting the terms proportional to $1/kr$ and to $1/(kr)^2$ in the square brackets in Equation 3.6, which simplifies to

$$p'(\mathbf{r}, t) = B_1 \frac{(q\epsilon^2)}{r} (\hat{\mathbf{r}} \cdot \hat{\boldsymbol{\epsilon}})^2 \sin(\omega t - kr), \text{ as } kr \rightarrow \infty. \quad (3.7)$$

From Equation 3.7, the far-field directivity of the longitudinal quadrupole radiation is

$$(\hat{\mathbf{r}} \cdot \hat{\boldsymbol{\epsilon}})^2 = \cos^2(90^\circ - \theta) = \sin^2(\theta), \quad (3.8)$$

which is the square of the dipole far-field directivity represented by Equation 3.4. Therefore, the pressure fluctuation amplitude is likewise maximum at $\theta = 90^\circ$ and at $\theta = 270^\circ$, along the longitudinal quadrupole axis. The minimum amplitude for p' is on the x_1 -axis and a similar figure-of-eight is obtained (in the far-field) as for the dipole. Narrower lobes are obtained compared to the dipole radiation, due to the square power in Equation 3.8.

In the far-field, Equation 3.7 shows that the acoustic pressure fluctuation amplitude scales with the source-observer distance as $1/r$. In the near-field, the approximation of Equation 3.7 is not valid and the pressure fluctuation is given by Equation 3.6. From Equation 3.6, it can be derived that the pressure fluctuation scales with distance from the source by the factor

$$\zeta_{\text{lo-q}}(r) = \frac{\sqrt{1 + \frac{4}{(kr)^4}}}{r}, \quad (3.9)$$

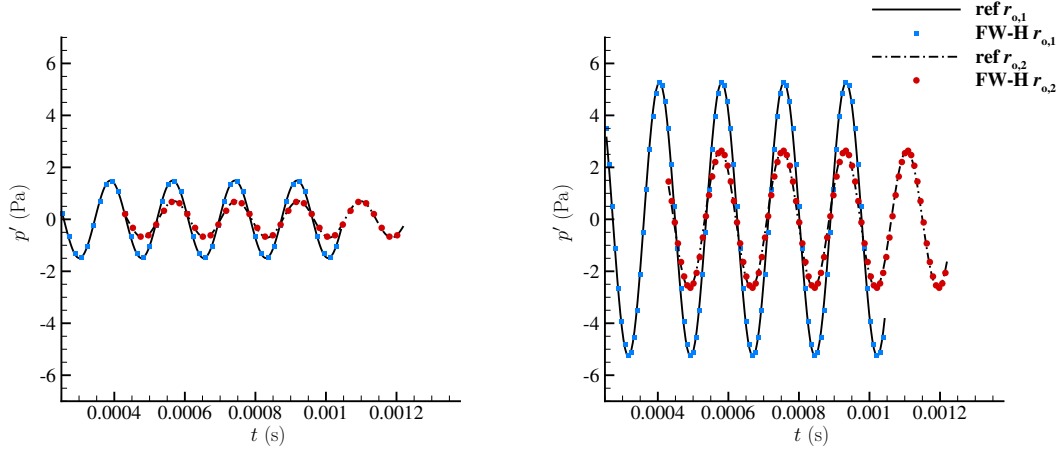
where the subscript “lo-q” stands for longitudinal-quadrupole.

In terms of the near-field directivity, it can be noticed that, in Equation 3.6, the first term has a directivity of sine squared (Equation 3.8), while the second term is a spherically symmetric source. The latter radiates equally in all directions and vanishes in the far-field, where the first term is dominant. Thus, in the near-field, the directivity pattern is obtained by summing a spherical pattern with a figure-of-eight shaped pattern. The result is a four-lobes pattern, with the x_2 -axis lobes becoming increasingly dominant as the observers are moved away from the point source.

The layout in Figure 3.1 is also used for this longitudinal quadrupole source test and the source strength $q\epsilon^2$ is determined by imposing the same SPL of 80 dB

re $20\mu\text{Pa}$ on the x_2 -axis, 33.33λ away from the source, as in Section 3.1.2. The source is placed at the origin $s^{(1)}$, at $\mathbf{y}^{(1)} = (0.0, 0.0, 0.0)\lambda$, and then at $s^{(2)}$, at $\mathbf{y}^{(2)} = (0.92, 0.92, 0.92)\lambda$, proximal to the FW-H surface corner.

The acoustic results for the longitudinal quadrupole point source are reported in Figures 3.9 and 3.10 for the $s^{(1)}$ source location and in Figure 3.11 for the off-origin source position $s^{(2)}$.



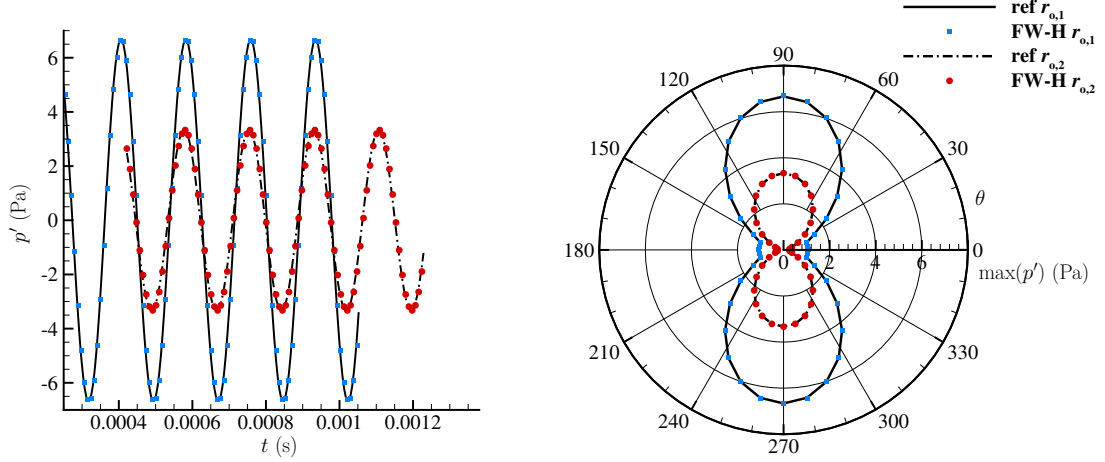
(a) Pressure fluctuation at observer $o^{(4)}$ at $\theta^{(4)} = 27^\circ$. (b) Pressure fluctuation at observer $o^{(8)}$ at $\theta^{(8)} = 63^\circ$.

Figure 3.9: Radiation in a stationary medium from a longitudinal quadrupole point source, located at the origin $s^{(1)}$, to observers placed at radial distances $r_{o,1} = \lambda$ and $r_{o,2} = 2\lambda$ from the origin. $a = \lambda/3$, $\ell = \lambda/6$, $\lambda = 0.06$ m, $N_T = 40$, and $N_\lambda = 120$.

The acoustic pressure fluctuations from the longitudinal quadrupole located at $s^{(1)}$ predicted by the AFW-H tool at observers $o^{(4)}$ ($\theta^{(4)} = 27^\circ$), $o^{(8)}$ ($\theta^{(8)} = 63^\circ$), and $o^{(11)}$ ($\theta^{(11)} = 90^\circ$) are plotted against the reference solution of Equation 3.6, respectively in Figures 3.9(a), 3.9(b), and 3.10(a). Results are reported for two radial positions of the circular array of observers, $r_{o,1} = \lambda$ and $r_{o,2} = 2\lambda$. In Figure 3.10(b), the directivity predicted by the AFW-H tool at $r_{o,1}$ and at $r_{o,2}$ is compared with the reference analytical solution.

Solid and dash-dot black lines denote the analytical solution at $r_{o,1}$ and at $r_{o,2}$, respectively, while blue and red symbols denote the numerical prediction. The latter correctly reproduces both the pressure fluctuation time-history and the directivity pattern, as shown by the good match with the reference solution labelled “ref” in Figures 3.9 and 3.10.

Figures 3.9(a)–3.10(a) show an increase in the pressure fluctuation amplitude as the angle θ increases from 27° to 90° . The peak to peak ratio between the disturbances at observers $o^{(4)}$ and $o^{(11)}$, $o^{(8)}$ and $o^{(11)}$ are respectively 0.21 and 0.79, in agreement with the analytical directivity pattern $\sin^2(\theta)$ for the longitudinal quadrupole, confirming the good prediction capability of the code in terms of angular scaling with θ .



(a) Pressure fluctuation at observer $o^{(11)}$ at $\theta^{(11)} = 90^\circ$.

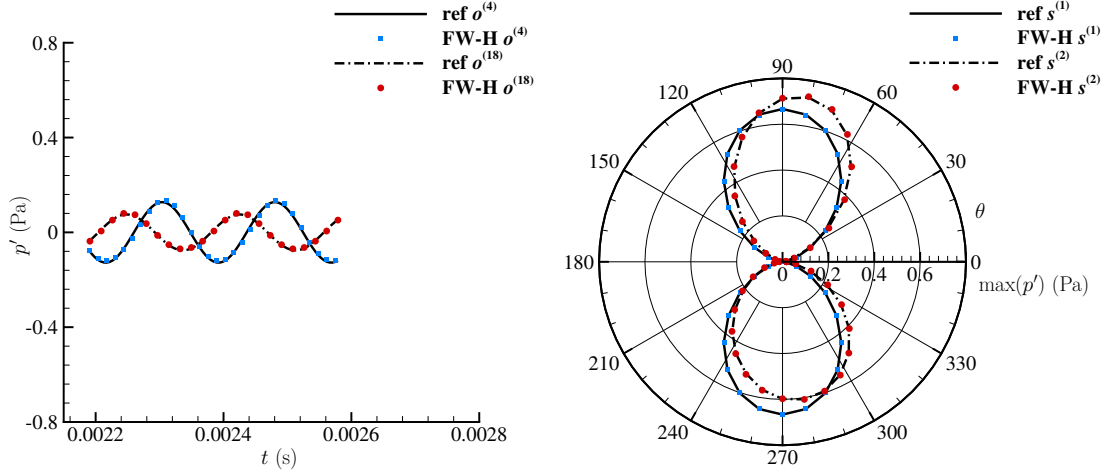
(b) Directivity pattern.

Figure 3.10: Radiation in a stationary medium from a longitudinal quadrupole point source, located at the origin $s^{(1)}$, to observers placed at radial distances $r_{o,1} = \lambda$ and $r_{o,2} = 2\lambda$ from the origin. $a = \lambda/3$, $\ell = \lambda/6$, $\lambda = 0.06$ m, $N_T = 40$, and $N_\lambda = 120$.

The scaling with r is correctly reproduced by the AFW-H tool. For instance, at observer $o^{(8)}$, the ratio of the amplitudes of the acoustic pressure fluctuation at $r_{o,2} = 2\lambda$ and at $r_{o,1} = \lambda$ is 1.995 for the numerical prediction and it is 1.994 for the analytical solution.

At the radial distance $r_{o,1} = \lambda$, the directivity pattern shown in Figure 3.10(b) is influenced by the near-field omnidirectional term in Equation 3.6 and four lobes are visible. The x_2 -axis lobes are far greater than the x_1 -axis lobes that almost vanish when the distance is doubled to $r_{o,2} = 2\lambda$. It is worth noticing that both distances $r_{o,1}$ and $r_{o,2}$ are of the same order of magnitude of the acoustic wavelength λ and, therefore, do not satisfy the far-field condition $kr \gg 1$. However, at $r_{o,2}$ the directivity pattern reported in Figure 3.10(b) is better approximating the figure-of-

eight shape, typical of the longitudinal quadrupole radiation in the far-field. This trend is confirmed by the $s^{(1)}$ directivity pattern in Figure 3.11(b), which reports equivalent predictions at the increased radial distance of $r_o = 10\lambda$. The directivity shows the same topology as for the dipole source, with the two lobes slightly narrower, as determined by Equations 3.7 and 3.8.



(a) Pressure fluctuation at observers $o^{(4)}$ ($\theta^{(4)} = 27^\circ$) and $o^{(18)}$ ($\theta^{(18)} = 180^\circ - 27^\circ$), from a longitudinal quadrupole source located at $s^{(2)}$.

(b) Directivity pattern.

Figure 3.11: Radiation in a stationary medium from a longitudinal quadrupole point source, located at $s^{(1)}$ (origin) and at $s^{(2)}$ ($\mathbf{y}^{(2)} = (0.92, 0.92, 0.92)\lambda$), to observers placed at a constant radial distance $r_o = 10\lambda$ from the origin. $a = 2\lambda$, $\ell = \lambda$, $\lambda = 0.06$ m, $N_T = 40$, and $N_\lambda = 20$.

Figure 3.11(a) shows the pressure fluctuation time history at observers $o^{(4)}$, at $\theta^{(4)} = 27^\circ$, and $o^{(18)}$, at $\theta^{(18)} = 180^\circ - 27^\circ$, from the longitudinal quadrupole placed at the off-origin location $s^{(2)}$. These are two observers from a circular array of 40 observers evenly spaced in θ and placed at a constant radial distance $r_o = 10\lambda$ on the $x_3 = 0$ plane. A FW-H surface of a cube was used with a base side $a = 2\lambda$ and a half height $\ell = \lambda$. The black lines denote the analytical solution labelled “ref” and the symbols denote the numerical prediction. A good match is shown, at both observers, in terms of amplitude, phase, and frequency of the pressure fluctuation.

Observers $o^{(4)}$ and $o^{(18)}$ are symmetrically placed about the x_2 -axis, but the predicted pressure fluctuation amplitude is weaker at $o^{(18)}$, due to this observer being farther away from the longitudinal quadrupole source sited at $s^{(2)}$, at $\mathbf{y}^{(2)} =$

$(0.92, 0.92, 0.92) \lambda$.

A comparison between the directivity patterns from the source placed at $s^{(1)}$ and at $s^{(2)}$ is shown in Figure 3.11(b). With a source placed at the origin at $s^{(1)}$, the directivity has the typical far-field shape of a figure-of-eight, while with a source placed off the origin at $s^{(2)}$, the radiation pattern becomes asymmetric, with the direction of maximum radiation in the first quadrant ($\theta < 90^\circ$). The near-field term in Equation 3.6 appears to make a negligible contribution at the radial distance $r_o = 10\lambda$, as the radiation pattern of Figure 3.11(b) displays only two lobes, as for the dipole source.

3.1.4 Lateral quadrupole

The last test case for the validation of the advanced time Ffowcs Williams and Hawkings acoustic analogy code is the numerical prediction of the radiating pressure field from a lateral quadrupole. The analytical expression of the acoustic pressure fluctuation from a lateral quadrupole at distance \mathbf{r} from the source is [47]

$$p'(\mathbf{r}, t) = -4B_1 \frac{(q\epsilon_1\epsilon_2)}{r} (\hat{\mathbf{r}} \cdot \hat{\boldsymbol{\epsilon}}_1) (\hat{\mathbf{r}} \cdot \hat{\boldsymbol{\epsilon}}_2) \left[\frac{3}{kr} \cos(\omega t - kr) + \left(\frac{3}{(kr)^2} - 1 \right) \sin(\omega t - kr) \right], \quad (3.10)$$

where $B_1 = \rho_0 c_0 k^3 (4\pi)^{-1}$ and $\boldsymbol{\epsilon}_1$ and $\boldsymbol{\epsilon}_2$ are the quadrupole axes, with $\epsilon_1 = |\boldsymbol{\epsilon}_1|$ and $\epsilon_2 = |\boldsymbol{\epsilon}_2|$. The caret variables $\hat{\boldsymbol{\epsilon}}_1$ and $\hat{\boldsymbol{\epsilon}}_2$ indicate the corresponding unit vectors. In this test, $\boldsymbol{\epsilon}_1$ and $\boldsymbol{\epsilon}_2$ are oriented respectively in the positive x_1 -axis direction and in the positive x_2 -axis direction, as shown in Figure 3.12. The quadrupole strength $q\epsilon_1\epsilon_2$ is defined to obtain a SPL of 80 dB re $20\mu\text{Pa}$ on the $x_1 = x_2$ line of the $x_3 = 0$ plane ($\theta = 45^\circ$ in Figure 3.1), 33.33λ away from the lateral quadrupole source as placed at the origin of the reference system. ϵ_1 and ϵ_2 assume infinitesimally small values compared to the minimum distance source-observer $r = |\mathbf{x} - \mathbf{y}|$ considered herein, in order to accurately approximate a point lateral quadrupole source.

The directivity pattern for this source is given in Equation 3.10 by the term

$$(\hat{\mathbf{r}} \cdot \hat{\boldsymbol{\epsilon}}_1) (\hat{\mathbf{r}} \cdot \hat{\boldsymbol{\epsilon}}_2) = \cos(\theta) \cos(90^\circ - \theta) = \cos(\theta) \sin(\theta) = \frac{1}{2} \sin(2\theta). \quad (3.11)$$

Equation 3.11 states that the lateral quadrupole directivity is characterised by four lobes. Along the x_1 -axis ($\theta = 0$ and $\theta = 180^\circ$) and along the x_2 -axis ($\theta = 90^\circ$ and

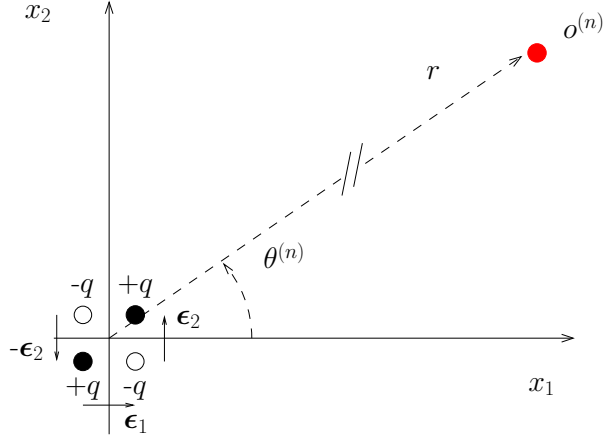


Figure 3.12: Schematic of the lateral quadrupole source approximated by two dipole sources (four monopoles) with equal and opposite strength ($q\epsilon_2$) and parallel axes spaced $\epsilon_1 \rightarrow 0$ apart. The plane $x_3 = 0$ is shown, together with a generic observer $o^{(n)}$ from the circular array defined in Section 3.1.

$\theta = 270^\circ$), the lateral quadrupole does not radiate, while four maxima in the noise radiation amplitude form at angles $\theta = 45^\circ \pm n90^\circ$, with n integer.

The terms proportional to $1/(kr)$ and to $1/(kr)^2$ in the square brackets in Equation 3.10 are near-field contributions vanishing for $kr \rightarrow \infty$. By neglecting these terms, the far-field approximation of Equation 3.10

$$p'(\mathbf{r}, t) = 4B_1 \frac{(q\epsilon_1\epsilon_2)}{r} (\hat{\mathbf{r}} \cdot \hat{\boldsymbol{\epsilon}}_1) (\hat{\mathbf{r}} \cdot \hat{\boldsymbol{\epsilon}}_2) \sin(\omega t - kr), \text{ as } kr \rightarrow \infty, \quad (3.12)$$

is obtained, in which $p'(\mathbf{r}, t)$ scales as $1/r$.

In the near-field, the approximation of Equation 3.12 is inaccurate and the scaling with distance r from the source is given by Equation 3.10 as

$$\zeta_{\text{la-q}}(r) = \frac{\sqrt{1 + \frac{3}{(kr)^2} + \frac{9}{(kr)^4}}}{r}, \quad (3.13)$$

where the subscript “la-q” refers to the lateral quadrupole source.

The results reported herein are obtained using the layout of Figure 3.1. A prismatic FW-H integration surface is defined and 40 observers are evenly spaced in θ on a circular array at a radial distance r_o from the origin of the reference system. Two locations for the lateral quadrupole position are tested. One is the origin $s^{(1)}$, at $\mathbf{y}^{(1)} = (0.0, 0.0, 0.0) \lambda$. The other location is $s^{(2)}$, used in Figures 3.16 and 3.17, placed proximal to the corner of the FW-H surface at $\mathbf{y}^{(2)} = (0.92, 0.92, 0.92) \lambda$.

Figures 3.13 and 3.14 report the time-dependent acoustic pressure fluctuation and the directivity due to the lateral quadrupole point source located at $s^{(1)}$, obtained with FW-H surface of a cube of base side $a = \lambda/3$ and half height $\ell = \lambda/6$. In this layout, the radial distance origin-observer r_o is the same as the distance source-observer r and the radiation is centrally symmetric about the origin. Predictions are obtained for two values of the radial distance to the observers, which are $r_{o,1} = \lambda$ and $r_{o,2} = 2\lambda = 2r_{o,1}$.

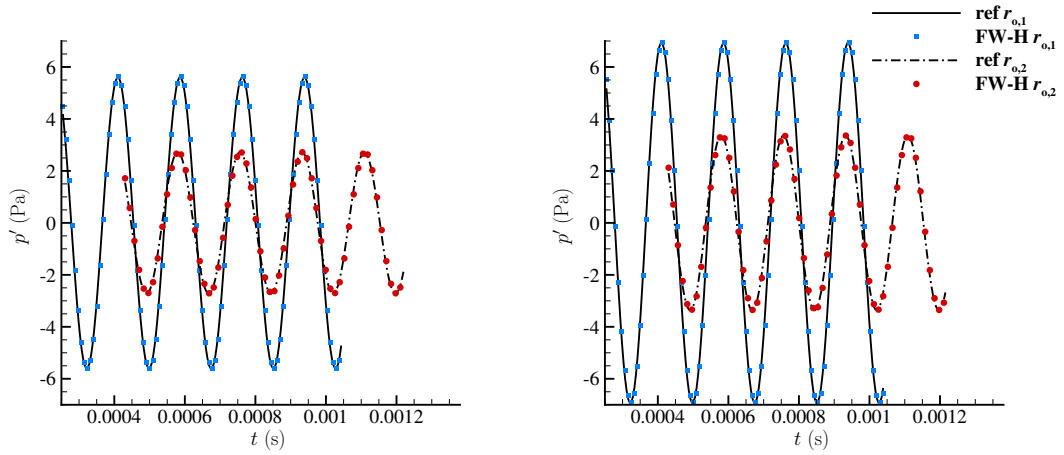
The p' time-history at three observers is given in Figures 3.13(a), 3.13(b), and 3.14(a). Solid and dash-dot black lines denote the analytical solution, labelled “ref”, respectively for $r_{o,1}$ and $r_{o,2}$. Blue and red symbols denote the FW-H tool estimations.

The three observers are $o^{(6)}$ at $\theta^{(6)} = 45^\circ$ in the direction of maximum radiation, and two other observers placed symmetrically about the $\theta = 45^\circ$ line, at $\theta^{(4)} = 27^\circ$ ($o^{(4)}$) and at $\theta^{(8)} = 63^\circ$ ($o^{(8)}$). The acoustic pressure fluctuation at $o^{(4)}$, displayed in Figure 3.13(a), has the same amplitude and phase as for observer $o^{(8)}$ in Figure 3.14(a). Figure 3.13(b) relative to $o^{(6)}$ shows an acoustic pressure fluctuation of higher amplitude than at $o^{(4)}$ and at $o^{(8)}$. These results are in agreement with the analytical directivity pattern of Equation 3.11.

The scaling of the pressure fluctuation amplitude with increasing radial distance from the source is well predicted by the AFW-H tool for the lateral quadrupole source. In Figure 3.13(b), the ratio of the pressure fluctuation amplitudes at $r_{o,2}$ and at $r_{o,1}$ is 2.067 from the tool, compared to 2.060 from Equation 3.13.

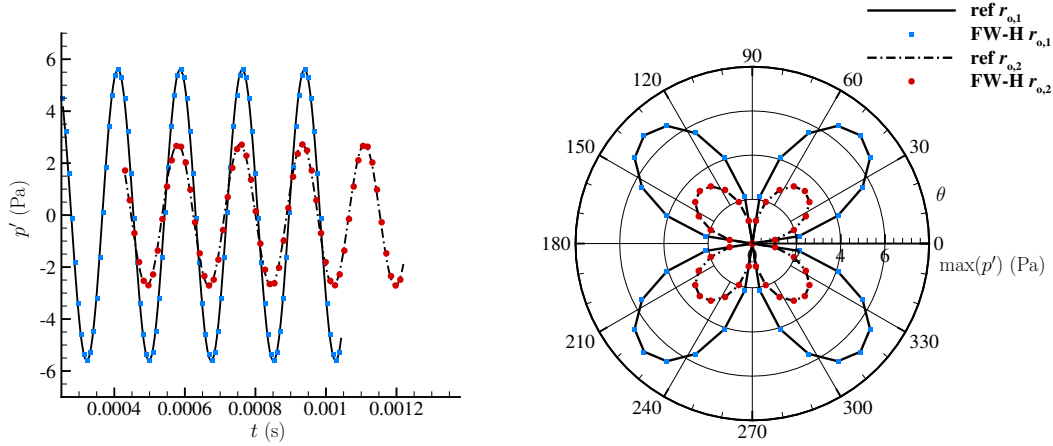
The typical four-leaved clover shape is obtained for the directivity of the lateral quadrupole source, as shown in Figure 3.14(b), where the numerical prediction is shown to reproduce very accurately the reference solution at both radial distances $r_{o,1}$ and $r_{o,2}$. A good overall match is shown between the analytical solution of Equation 3.10 and the numerical prediction obtained by implementing Equations 2.21-2.22, of Section 2.2.3.

Figures 3.16 and 3.17 document the validation of the AFW-H code with a source placed at $s^{(2)}$, proximal to the FW-H prism corner, and observers placed at $r_o = 10\lambda$. Specifically, Figures 3.16(a), 3.16(b), and 3.17(a) display the directivity patterns for a lateral quadrupole source radiating from locations $s^{(1)}$ and $s^{(2)}$, with three different FW-H surfaces, which are represented in Figure 3.15 and referred to as $\mathcal{F}_1 = 0$,



(a) Pressure fluctuation at observer $o^{(4)}$ at $\theta^{(4)} = 27^\circ$. (b) Pressure fluctuation at observer $o^{(6)}$ at $\theta^{(6)} = 45^\circ$.

Figure 3.13: Radiation in a stationary medium from a lateral quadrupole point source, located at the origin $s^{(1)}$, to observers placed at radial distances $r_{o,1} = \lambda$ and $r_{o,2} = 2\lambda$ from the origin. $a = \lambda/3$, $\ell = \lambda/6$, $\lambda = 0.06$ m, $N_T = 40$, and $N_\lambda = 120$.



(a) Pressure fluctuation at observer $o^{(8)}$ at $\theta^{(8)} = 63^\circ$. (b) Directivity pattern.

Figure 3.14: Radiation in a stationary medium from a lateral quadrupole point source, located at the origin $s^{(1)}$, to observers placed at radial distances $r_{o,1} = \lambda$ and $r_{o,2} = 2\lambda$ from the origin. $a = \lambda/3$, $\ell = \lambda/6$, $\lambda = 0.06$ m, $N_T = 40$, and $N_\lambda = 120$.

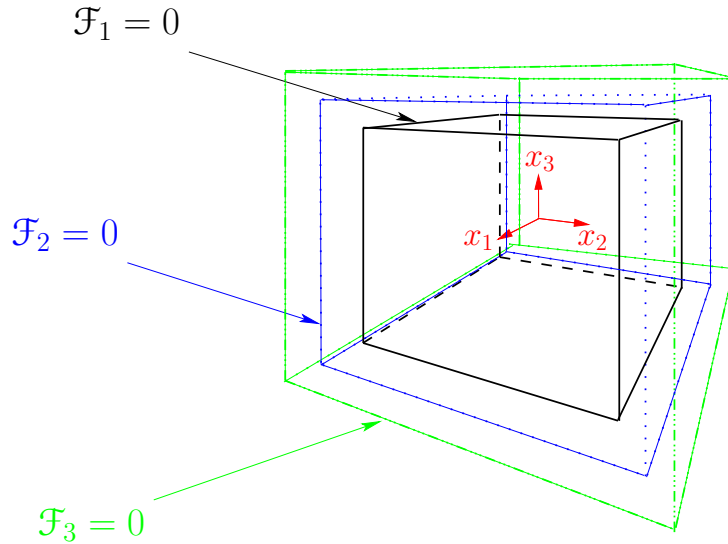


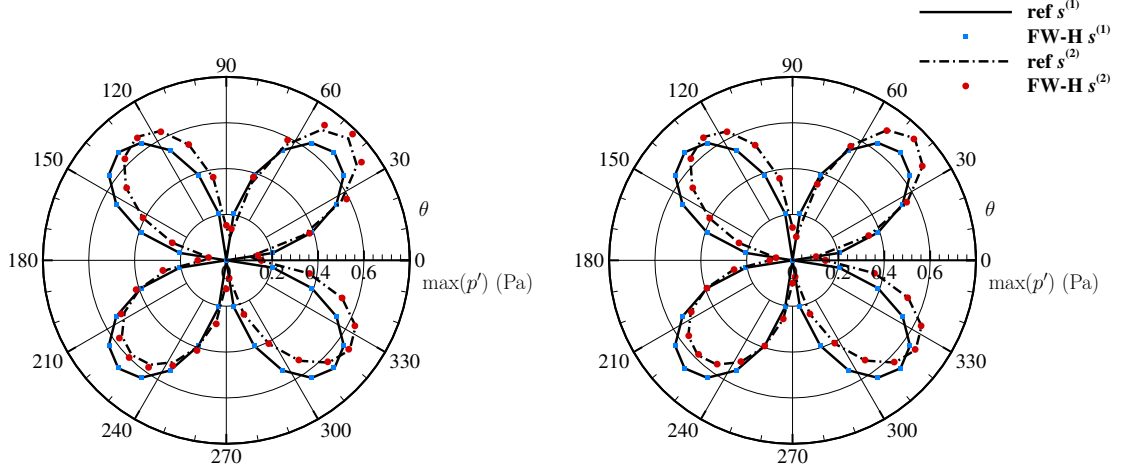
Figure 3.15: Sketch of the three integration surfaces used to test the sensitivity of the acoustic predictions on the FW-H surface position.

$\mathcal{F}_2 = 0$, and $\mathcal{F}_3 = 0$, respectively.

$\mathcal{F}_1 = 0$, shown in black in Figure 3.15, is the innermost FW-H surface of a cube, of base side $a_1 = 2\lambda$ and half height $\ell_1 = \lambda$. It is the same surface used in the previous sections for predicting the acoustic radiation from sources at $s^{(2)}$. The intermediate surface $\mathcal{F}_2 = 0$, which is shown in blue in Figure 3.15, and the largest surface $\mathcal{F}_3 = 0$, which is shown in green in Figure 3.15, have size $(a_2, \ell_2) = (2.34\lambda, 1.17\lambda)$ and $(a_3, \ell_3) = (2.66\lambda, 1.33\lambda)$, respectively.

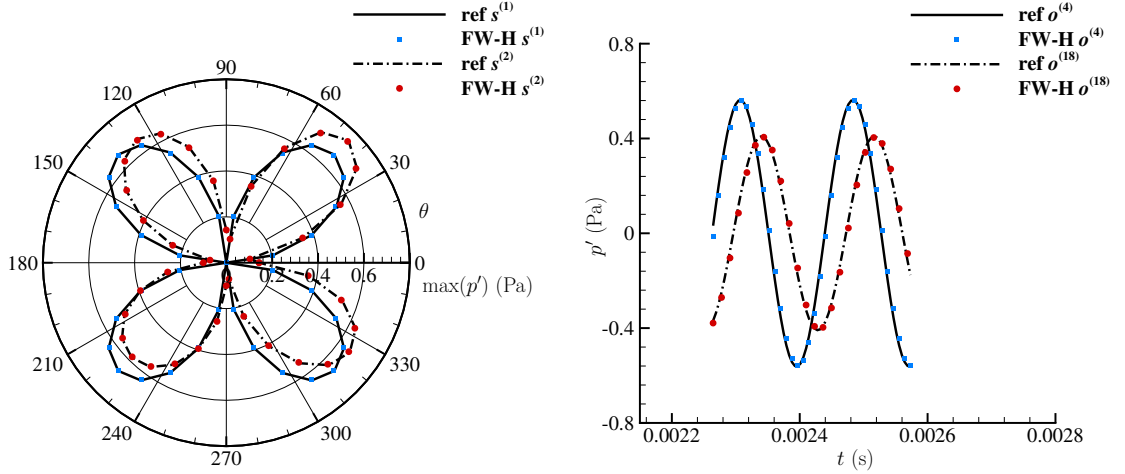
Surfaces $\mathcal{F}_1 = 0$, $\mathcal{F}_2 = 0$, and $\mathcal{F}_3 = 0$ test the sensitivity of the predictions from the AFW-H tool to the integration surface size and position. The results in Figure 3.16(a), for which the innermost control surface $\mathcal{F}_1 = 0$ is used, show that, by keeping the same FW-H prism size as for the monopole, dipole, and longitudinal quadrupole tests, the numerical prediction for the off-origin source $s^{(2)}$ does not reproduce correctly the analytical solution. This is especially noticeable in the direction of maximum radiation amplitude $\theta = 45^\circ$, where the numerical solution denoted by the red squares overestimates the analytical solution denoted by the dash-dot line by a 3% factor.

By increasing the control surface size from $(a_1, \ell_1) = (2\lambda, \lambda)$ to $(a_2, \ell_2) = (2.34\lambda, 1.17\lambda)$, a good match between the AFW-H code prediction and the reference analytical solution is recovered, as shown in Figure 3.16(b). Figure 3.17(a) shows



(a) Directivity pattern with $\mathcal{F}_1 = 0$: $(a_1, \ell_1) = (2\lambda, \lambda)$ (Di Stefano *et al.* [141]).
 (b) Directivity pattern with $\mathcal{F}_2 = 0$: $(a_2, \ell_2) = (2.34\lambda, 1.17\lambda)$ (Di Stefano *et al.* [141]).

Figure 3.16: Radiation in a stationary medium from a lateral quadrupole point source, located at $s^{(1)}$ (origin) and at $s^{(2)}$ ($\mathbf{y}^{(2)} = (0.92, 0.92, 0.92)\lambda$), to observers placed at a constant radial distance $r_o = 10\lambda$ from the origin. $\lambda = 0.06$ m, $N_T = 40$, and $N_\lambda = 20$.



(a) Directivity pattern with $\mathcal{F}_3 = 0$: $(a_3, \ell_3) = (2.66\lambda, 1.33\lambda)$ (Di Stefano *et al.* [141]).
 (b) Pressure fluctuation at observers $o^{(4)}$ ($\theta^{(4)} = 27^\circ$) and $o^{(18)}$ ($\theta^{(18)} = 180^\circ - 27^\circ$), from the source located at $s^{(2)}$, with $\mathcal{F}_2 = 0$: $(a_2, \ell_2) = (2.34\lambda, 1.17\lambda)$.

Figure 3.17: Radiation in a stationary medium from a lateral quadrupole point source, located at $s^{(1)}$ (origin) and $s^{(2)}$ ($\mathbf{y}^{(2)} = (0.92, 0.92, 0.92)\lambda$), to observers placed at a constant radial distance $r_o = 10\lambda$ from the origin. $\lambda = 0.06$ m, $N_T = 40$, and $N_\lambda = 20$.

that using the outermost FW-H surface $\mathcal{F}_3 = 0$ does not produce any appreciable further improvement in the match between the analytical and the numerical results compared to the directivities obtained with $\mathcal{F}_2 = 0$. This indicates that the numerical prediction is independent of the surface size for $(a_2, \ell_2) \geq (2.34\lambda, 1.17\lambda)$, with an error $e < 0.1\%$ between the numerical prediction and the analytical reference solution of Equation 3.10.

Having determined that surface $\mathcal{F}_2 = 0$ is appropriate for predicting the acoustic pressure fluctuations from the lateral quadrupole placed off-origin at $s^{(2)}$ by the AFW-H tool, the directivity and time-dependent pressure fluctuation history by using $\mathcal{F}_2 = 0$ are discussed in further details. Figure 3.16(b) shows that a lateral quadrupole source placed at the origin at $s^{(1)}$ generates a symmetric directivity pattern in the form of a four-leaved clover shape, which is a recognisable feature of the lateral quadrupole radiation pattern [47, 139].

By placing the sound source off-centre, as with $s^{(2)}$, the sound radiation pattern becomes asymmetric and the directivity lobe in the first quadrant increases, giving a peak radiation in the $\theta = 45^\circ$ direction. The directivity lobe in the third quadrant reduces in size and remains symmetric about the $\theta = 225^\circ$ line. The remaining two lobes become asymmetric and lean towards the first quadrant. The reduced source-observer distance in the first quadrant is responsible for the radiation peak in the $\theta = 45^\circ$ direction. By positioning the sound source on the $\theta = 45^\circ$ line, the quadrupole retains a symmetric radiation about this line.

In spite of the greater complexity of the lateral quadrupole radiation pattern, Figure 3.16(b) shows that the AFW-H tool has correctly captured this pattern, as the numerical prediction shown by the symbols overlaps the analytical solution shown by the lines.

The good noise prediction capability of the AFW-H tool is confirmed by Figure 3.17(b), in which the pressure fluctuation p' from the noise source $s^{(2)}$ is plotted against time t , for two observers $o^{(4)}$ at $\theta^{(4)} = 27^\circ$ and $o^{(18)}$ at $\theta^{(18)} = 180^\circ - 27^\circ$. The FW-H surface $\mathcal{F}_2 = 0$ of $a_2 = 2.34\lambda$ and $\ell_2 = 1.17\lambda$ is used. The numerical predictions indicated by the symbols match the analytical time traces plotted with black lines.

3.2 Numerical error sources in the AFW-H tool

Section 3.1.4 showed how increasing the extent of the FW-H surface from $(a_1, \ell_1) = (2\lambda, \lambda)$ to $(a_2, \ell_2) = (2.34\lambda, 1.17\lambda)$, respectively for surfaces $\mathcal{F}_1 = 0$ and $\mathcal{F}_2 = 0$ in Figure 3.15, improved the numerical prediction of the lateral quadrupole radiation from source $s^{(2)}$ that is proximal to the surface corner. This improvement is shown by the comparison between Figure 3.16(a) and Figure 3.16(b).

The discrepancy between the reference analytical solution and the numerical prediction from the AFW-H code in Figure 3.16(a) was thought at first to be due to the spatial discretization of the FW-H surface. However, by increasing the spatial discretization of $\mathcal{F}_1 = 0$, the numerical prediction did not improve. For this reason, a detailed investigation of the source of this numerical error was undertaken.

With the source located at $s^{(2)}$, the characteristic length scales governing the accuracy of the numerical quadrature of the FW-H surface integral are the mesh size h , the wavelength λ of the radiated sound, and the distance d between the source and the closest corner of the FW-H surface. The non-dimensional ratio d/λ expresses how close the source is to the corner of the FW-H integration surface in terms of the acoustic wavelength λ .

In Figure 3.16(a) the results from the FW-H surface $\mathcal{F}_1 = 0$ are obtained with $d/\lambda = 0.144$, which is lower than $d/\lambda = 0.433$ for $\mathcal{F}_2 = 0$ in Figure 3.16(b). Using $d/\lambda = 0.144$ with $\mathcal{F}_1 = 0$ does not allow the correct estimation of the noise radiation using the current AFW-H code, showing that the placement of the integration surface in the application of the acoustic analogy to elementary sources is an important aspect.

Two series of tests are described below to quantify the error sources. In Section 3.2.1, the integration surface $\mathcal{F}_2 = 0$ of Figure 3.15 is used and a point lateral quadrupole of the type described in Section 3.1.4 is brought progressively closer to one corner. $\mathcal{F}_2 = 0$ is kept of constant size $(a_2, \ell_2) = (2.34\lambda, 1.17\lambda)$, while the mesh size h and the distance d from the source to the corner of the FW-H surface are systematically varied.

In Section 3.2.2, a point dipole of the type described in Section 3.1.2 is used. The surface $\mathcal{F}_2 = 0$ is kept of constant size, while the distance d from the source to the corner of $\mathcal{F}_2 = 0$ and the wavelength λ of the acoustic waves vary over specified

ranges. The FW-H surface size is therefore given in meters, rather than in number of wavelengths, with $(a_2, \ell_2) = (0.14, 0.07)$ m.

3.2.1 Lateral quadrupole proximity to the FW-H surface corner

For the elementary source tests, the FW-H surface is discretised uniformly by the spacing h , which gives $N_\lambda = \lambda/h$ points per wavelength. A numerical experiment was conducted by which the position of the lateral quadrupole source $s^{(2)}$ from Section 3.1.4 was systematically varied along the first quadrant diagonal of the FW-H surface $\mathcal{F}_2 = 0$, as sketched in Figure 3.18. 40 source positions were considered over the range $0.845 < \lambda/d < 17.321$. For each source location, the FW-H surface integration was performed using 50 different spatial discretization levels of $\mathcal{F}_2 = 0$, over the range $0.0147 < h/\lambda = 1/N_\lambda < 0.1944$.

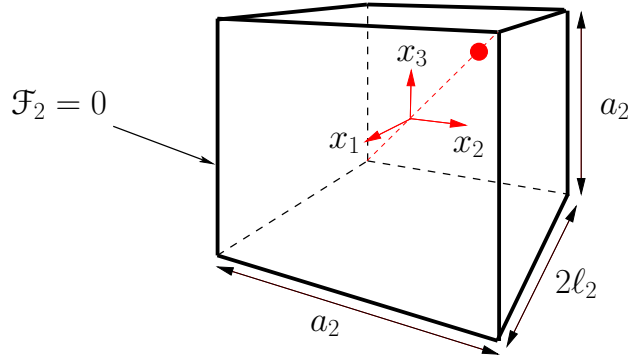


Figure 3.18: Range of source locations $s^{(2)}$ along the diagonal of the FW-H surface. $a_2 = 2.34\lambda$, $\ell_2 = 1.17\lambda$.

At each location, the normalized difference between the reference analytical solution \check{p}'_{ref} and the numerical prediction \check{p}'_{FW-H} of the sound pressure amplitude was computed as

$$e = \frac{\max_{1 \leq i \leq N_\theta} \left| \check{p}'_{ref}(\mathbf{x}^{(i)}) - \check{p}'_{FW-H}(\mathbf{x}^{(i)}) \right|}{\check{p}'_{ref}[\mathbf{x}(r, \theta_{\max})]}, \quad (3.14)$$

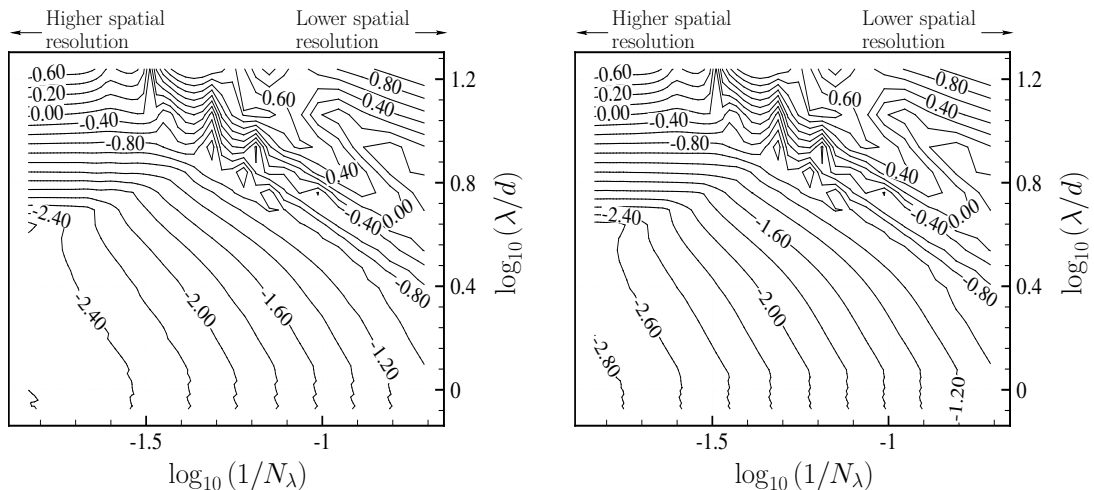
where

$$\check{p}' = \max_{0 \leq t \leq T} [p'(\mathbf{x}, t)]. \quad (3.15)$$

In Equation 3.14, N_θ is the number of the observers $o^{(n)}$ located on an arc centred at the origin of the Cartesian reference system, as shown in Figure 3.1. θ is the

polar angle as defined in Figure 3.1. The observers are located at the constant radial distance from the origin $r_o = 10\lambda$. $\check{p}'_{ref}[\mathbf{x}(r, \theta_{\max})]$ normalizes the error by the sound pressure fluctuation amplitude from the lateral quadrupole directivity peak.

In Figures 3.19(a) and 3.19(b), the numerical error e evaluated by Equation 3.14 is plotted on a base 10 logarithmic scale against $\log_{10}(1/N_\lambda)$ and $\log_{10}(\lambda/d)$. The results are obtained for two time resolution levels that give $N_T = 40$ and $N_T = 60$ points per period T , respectively. Figure 3.19(a) shows that with a spatially well-resolved acoustic sound field, meaning $1/N_\lambda \rightarrow 0$, the $\log_{10}(e)$ iso-contours appear to be regularly spaced in $\log_{10}(\lambda/d)$ from one another, indicating an exponential error decay of order $m = 5.64$. As the source $s^{(2)}$ is moved relatively far from the corner, meaning $\lambda/d \rightarrow 0$, then the $\log_{10}(e)$ iso-contours appear also regularly spaced in $\log_{10}(1/N_\lambda)$, indicating an exponential error decay of order $n = 1.81$ [141].



(a) $N_T = 40$ points per period (Di Stefano *et al.* [141]).

(b) $N_T = 60$ points per period.

Figure 3.19: Normalised error contours of acoustic pressure fluctuation amplitude from Equation 3.14, in logarithmic scale, obtained by a lateral quadrupole radiating from different locations along the diagonal of the FW-H surface. $0.845 < \lambda/d < 17.321$, $0.0147 < 1/N_\lambda < 0.1944$. $\ell = 1.17\lambda$, $a = 2.34\lambda$, $r_o = 10\lambda$, and $\lambda = 0.06$ m.

The $\log_{10}(e)$ iso-contour level -2 indicates a 1% error in the prediction of the acoustic pressure amplitude. This contour line and the lines to the left of it appear to run diagonally parallel to one another. This suggests that a given level of error can be maintained by keeping constant the product $(1/N_\lambda)^n (\lambda/d)^m$ so that, for a source

located 50% closer to the FW-H surface corner, a spatial refinement of the acoustic domain in the ratio $2^{m/n}$ is required. At higher values of $1/N_\lambda$ and of proximity to the FW-H surface corner λ/d , e increases more rapidly and the curvature of the contours in the $[\log_{10}(1/N_\lambda), \log_{10}(\lambda/d)]$ plane indicates a possible non-linear interaction between these two sources of error [141].

Figure 3.19(b) shows the effect of increasing the temporal resolution. Specifically, the top part of the plot, where large values of λ/d appear as being a dominant source of numerical error, is not affected by the increased time resolution of Figure 3.19(b). As the source is placed farther away from the FW-H surface corner, the time resolution starts influencing the numerical error. Increasing the number of points per period N_T from 40 in Figure 3.19(a) to 60 in Figure 3.19(b) reduces the error e between the numerical prediction and the reference solution only at error levels lower than 1% (-2 iso-contour). This can be noticed by the shift to the right of the $\log_{10}(e)$ iso-contours in the bottom left part of Figure 3.19(b), compared to Figure 3.19(a).

Figure 3.19 can be used to perform a first estimate of the magnitude of the numerical error that can be expected by a quadrupole source approaching the FW-H integration surface corner, for a given level of spatial discretization of the acoustic pressure field. The sensitivity of this error to changes in the source position and in the spatial discretization is also computable.

3.2.2 Dipole proximity to the FW-H surface corner

It is of interest to define a d/λ range that allows a numerical error contribution due to the short distance source-corner lower than that from the discretization in the FW-H code. A second parametric analysis has been undertaken to show a way of selecting this “safe” range, by considering the dipole source of Section 3.1.2 placed along the diagonal of the FW-H surface $\mathcal{F}_2 = 0$.

The dipole source is located at 50 different positions along the diagonal of the FW-H surface as shown in Figure 3.18, covering the source-corner distance range: $d \in [8.66 \times 10^{-4}; 3.98 \times 10^{-2}]$ m. For each position, 50 simulations are performed, with acoustic wavelengths within the range: $\lambda \in [0.02; 1]$ m. The mesh size h is kept constant so that higher wavelengths result in an increased N_λ .

In the previous tests, all the characteristic lengths were normalised by λ , which

was fixed to the value 0.06 m. In this last test, the wavelength is varied between different simulations in the parametric study. Therefore, the size of the FW-H surface $\mathcal{F}_2 = 0$, as well as the radial distance of the circular array from the origin, are expressed in meters. Specifically $(a_2, \ell_2) = (0.14, 0.07)$ m and $r_o = 0.6$ m. These correspond to the normalised values $(a_2, \ell_2) = (2.34\lambda, 1.17\lambda)$ and $r_o = 10\lambda$, with $\lambda = 0.06$ m.

The results are reported in Figure 3.20, where the logarithm of the error e estimated by Equation 3.14 is plotted against $\log_{10}(\lambda)$ and $\log_{10}(d)$, for two values of the temporal resolution, $N_T = 40$ in Figure 3.20(a), and $N_T = 60$ in Figure 3.20(b). For this application, in Equation 3.14, p'_{ref} is the analytical pressure fluctuation from the dipole source and p'_{FW-H} is the corresponding numerical prediction. The top part of Figures 3.20(a) and 3.20(b) refer to configurations with larger source-surface distances, while in the lower part of these figures the dipole is more proximal to the corner of the FW-H prism. The numerical resolution increases moving from left to right in each of the two figures.

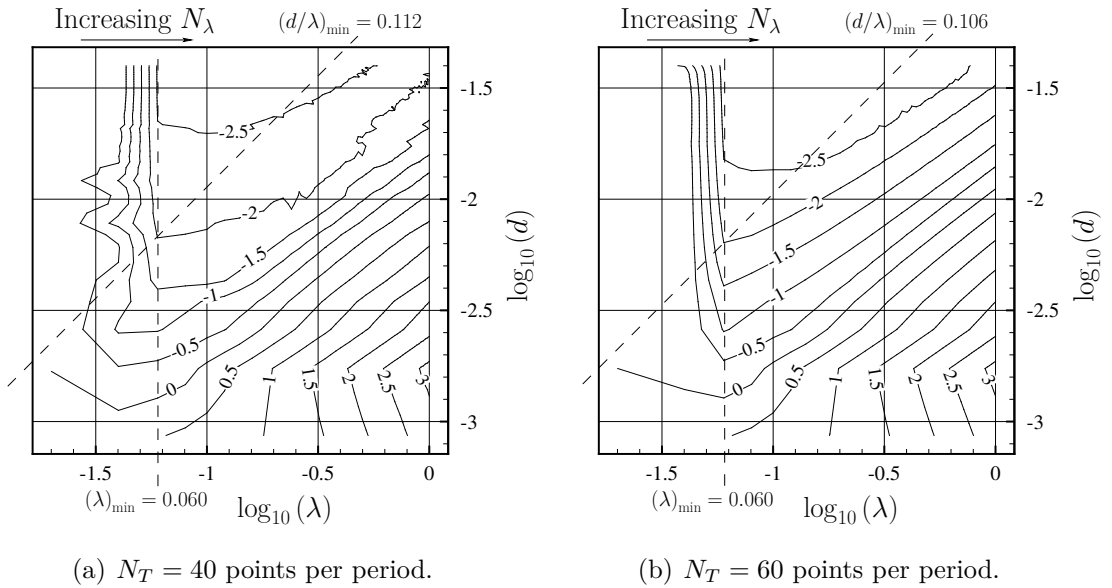


Figure 3.20: Normalised error contours of acoustic pressure fluctuation amplitude from Equation 3.14, in logarithmic scale, obtained by a dipole radiating from different locations along the diagonal of the FW-H surface. $d \in [8.66 \times 10^{-4}; 3.98 \times 10^{-2}]$ m, $\lambda \in [0.02; 1]$ m. $\ell = 0.07$ m, $a = 0.14$ m, $r_o = 0.6$ m, and $h = 1.167 \times 10^{-3}$ m.

Figure 3.20 shows that the AFW-H prediction of the dipole source radiation is also affected by a loss of accuracy if the ratio d/λ is small. The omnidirectional

radiation from the monopole source of Section 3.1.1 is the only test in which this behaviour was not observed.

In many practical engineering applications, it is often required to provide an estimate of the acoustic pressure amplitude within a set level of error. Figure 3.20 can be used to determine which (d, λ) combinations generate predictions with a numerical error that is within this set level. Assume, for instance, an acceptable level of error of 1%. The area above the -2 iso-contour in Figure 3.20 represents the (d, λ) region where $e \leq 1\%$.

The minimum value $(d/\lambda)_{\min}$ that gives an error of $e \leq 1\%$ over a useful λ range is determined by the $\log_{10}(d) = \log_{10}(\lambda) + \log_{10}[(d/\lambda)_{\min}]$ line at 45° in the $(\log_{10}(\lambda), \log_{10}(d))$ plane that crosses the -2 iso-contour at the change-of-slope point, as shown in Figure 3.20. Another condition is given by the minimum spatial resolution $(\lambda/h)_{\min}$ assuring $e \leq 1\%$ over a useful d range. Given the constant mesh size h , this requirement translates in a minimum wavelength λ_{\min} , represented, in Figure 3.20, by the vertical line crossing the -2 iso-contour at the change-of-slope point. Furthermore, in the case $d/\lambda < (d/\lambda)_{\min}$ (bottom right part of the plot), Figure 3.20 shows that the error e between the numerical prediction and the reference solution does not reduce with increasing spatial resolution.

Figure 3.20(b) shows that increasing the temporal resolution has no tangible effect on e for small values of d/λ (bottom right part of the plot). A reduction in the numerical error can be observed in Figure 3.20(b), compared to Figure 3.20(a), at larger values of d/λ (top left part of the plot) and the threshold $(d/\lambda)_{\min}$ is less stringent, decreasing from 0.112 for $N_T = 40$, to 0.106 for $N_T = 60$.

3.3 Chapter 3 summary

The AFW-H tool has been tested on monopole, dipole, and quadrupole elementary sources in Sections 3.1.1– 3.1.4. A good match with the corresponding analytical time-domain reference solution was shown in terms of pressure fluctuation amplitude, phase, and frequency. Both the geometrical scaling of the acoustic radiation with distance from the source and the source directivity were correctly captured in all the tests.

The acoustic prediction was shown to be independent of the FW-H surface placement, except for the case of a point source proximal to the surface corner. The numerical error generated by this configuration was investigated in two parametric analyses in Sections 3.2.1 and 3.2.2. In Section 3.2.2, guidelines for the appropriate design of the FW-H surface are suggested, aimed at circumventing this exception. The numerical error did not arise for the point monopole and it was found to be more significant for lateral quadrupole sources, compared to both dipoles and longitudinal quadrupoles. This appears to suggest an increase in the numerical error with increasing order of the elementary source.

For jet noise problems, this numerical error issue does not generally occur because the limit condition investigated in Section 3.2 is not reached. The FW-H surface is usually axisymmetric, *i.e.* with no corners or edges, and it is designed to enclose the jet at a distance which prevents a close proximity between the surface itself and the jet acoustic sources. The origin of the numerical error arising in this limit condition from the application of the AFW-H analogy to predicting noise from directive sources remains unclear. Section 3.1 advanced an hypothesis concerning large and opposite contributions to the FW-H integral failing to cancel each other out in the numerical integration procedure. However, this hypothesis remains to be verified.

Chapter 4

Application to stationary jets

The AFW-H method of Section 2.2.3 is applied in this chapter to both single-stream and dual-stream stationary jets, in order to get noise estimations through the new Python AFW-H tool, both in the acoustic near-field and in the acoustic far-field.

Two single-stream jet test cases are considered in Section 4.1. The first one is a subsonic isothermal jet (Section 4.1.1) with a nozzle exit Mach number of 0.9 [142]. A supersonic cold jet is then investigated in Section 4.1.2, generated by a contoured convergent nozzle that is operated under-expanded to give a 1D nozzle exit Mach number of 1.0, and a fully expanded jet Mach number $M_j = 1.15$ [143].

CFD predictions of the unsteady jets are available for both test cases from Large Eddy Simulations performed at Cerfacs (Toulouse), respectively by Biolchini [135] for the subsonic jet and by Pérez [16] for the supersonic jet, who used the elsA code [130] by ONERA. Details of the CFD technique applied in [135] are given by Biolchini in [134]. A time history of the thermodynamic variables was produced, and it was stored on a set of FW-H integration surfaces [16, 135]. As far as the single-stream supersonic jet test case is concerned, Detached Eddy Simulations (DES) were also performed at the University of Leicester [15] with the low order code Cosmic, and a CFD database was built to be used as input to the new AFW-H tool. This constitutes an independent check on the supersonic single-stream jet results by Pérez [16].

The single-stream jet tests validate the AFW-H tool beyond the elementary noise source field tests in Chapter 3. They contribute to building confidence in the acoustic analogy tool, towards its application to the more complex geometry of an under-expanded dual-stream cold jet in Section 4.2. The dual-stream nozzle geometry

and operating conditions are detailed in Appendix A. These were proposed by Airbus SAS, partner of the AeroTraNet2 project. The dual-stream jet represents a new application with flow conditions that differ from the ones explored in the previous aeroacoustic literature. DES and LES simulations of the coaxial jet were performed within AeroTraNet2 by Mancini [15] and by Pérez [16], by using respectively a low-order code at the University of Leicester (Cosmic) and a high-order code at Cerfacs (elsA [130]).

The main features of the CFD simulations providing the input to the AFW-H code are briefly summarised in Sections 4.1 and 4.2. Further details can be found in Biolchini [135, 134], in Mancini [15], and in Pérez [16, 133].

Before presenting the results obtained through the new Python AFW-H tool applied to stationary jets, it is worth recalling that, in this specific implementation of the FW-H acoustic analogy, the sound pressure p'_Q due to the volume source distribution in Equation 2.17 is neglected. The quadrupole source contribution from the volume external to the FW-H surface is assumed to be small compared to the monopole and to the dipole contributions of Equations 2.21 and 2.22, which are discretised and estimated on the integration surface.

With this assumption, the FW-H surface needs to be placed far enough from the jet in the “linear acoustic” region [138], allowing the error due to the absence of the volume integration to be negligible. Furthermore, if part of the surface is placed in a region of vorticity, as the downstream closing face of a FW-H integration surface enclosing a jet, a special treatment is required locally. This treatment is necessary to prevent the generation of spurious dipole noise sources as vortical structures cross the integration surface [116, 121], which would affect the noise prediction.

Among the possible solutions described in Section 2.2.1.1, the “open” surface strategy is adopted throughout the current chapter. Specifically, the closing disk, located at the downstream end of the FW-H surfaces enclosing the jet, is omitted from the surface integration in Equations 2.21 and 2.22, both for the supersonic single-stream jet investigated in Section 4.1.2 and for the dual-stream jet presented in Section 4.2. As far as the subsonic single-stream jet is concerned, the FW-H surface is prismatic with both the upstream and the downstream faces crossed by the jet. Both faces are omitted and the surface integration in Section 4.1.1 is limited

to the lateral surface of the square prism.

This choice is dictated by the CFD data collection being omitted on these closing disks (or squares) by Mancini [15], Pérez [16], and Biolchini [135]. The dataset used by the new Python AFW-H tool is a previously stored CFD prediction of the unsteady flow field on the “open” FW-H surfaces, obtained by LES at Cerfacs, Toulouse [16, 135], and by DES at the University of Leicester [15]. The main advantage resides in the reduced computational effort and memory requirements of this strategy, compared to other techniques described in Section 2.2.1.1, such as the evaluation of surface integrals on multiple end-domain disks.

The “open” surface FW-H integration was also carried out at Cerfacs (Toulouse) using the elsA software, from ONERA, on the same CFD data set for the jet test cases investigated in this chapter. This allows a direct comparison of the numerical noise predicted by the new Python AFW-H tool to that from the reference implementation by ONERA.

Moreover, as reported in Section 2.2.1.1, there are many examples in the literature of acoustic analogy applications to jet noise that used an “open” surface strategy for the surface integration, producing satisfactory results, also because a reliable treatment of the face crossed by the jet is still not generally agreed within the aeroacoustic community. However, the Python AFW-H tool allows the use of different configurations for the FW-H surface, such as that of a closed surface with outflow disk averaging [5], provided CFD data is available over these surfaces.

4.1 Single jet noise predictions

4.1.1 Subsonic fully expanded isothermal jet

In this section, the AFW-H method of Section 2.2.3 is used to estimate the noise radiation from a single-stream subsonic jet [142]. A three-dimensional jet issues from a circular nozzle with an exit Mach number of 0.9. The jet is isothermal and it is modelled at a Reynolds number based on the nozzle exit diameter of $Re = (\rho_j U_j D_e) / \mu = 4 \times 10^5$, where μ is the dynamic viscosity. The CFD domain geometry, the FW-H surface, and the location of the far-field acoustic observer $o^{(1)}$ for this test case are shown in Figure 4.1. The geometry is symmetric with respect

to the $y = 0$ plane, therefore only the top half of the CFD domain is shown in Figure 4.1.

The CFD domain extends from the nozzle exit plane, located at $x = 0.0D_e$, to $x = 25.0D_e$ in the positive axial direction, which coincides with the nozzle outflow direction. The domain extends up to $\pm 8.0D_e$ both in y and z , in Cartesian coordinates, and the portion $0.0D_e \leq y \leq 8.0D_e$ is shown in Figure 4.1. The nozzle is located upstream of the CFD domain, as described in Figure 4.1, and the nozzle lip thickness σ_e is not modelled. The prismatic FW-H surface $\mathcal{F}_0(\mathbf{x}, t) = 0$ has extent $0.0D_e \leq x \leq 12.5D_e$, $-3.0D_e \leq y \leq 3.0D_e$, and $-3.0D_e \leq z \leq 3.0D_e$, and the contributions from the square faces with side $6D_e$ at $x = 0.0D_e$ and at $x = 12.5D_e$ have been excluded from the integration procedure in the application of the AFW-H method.

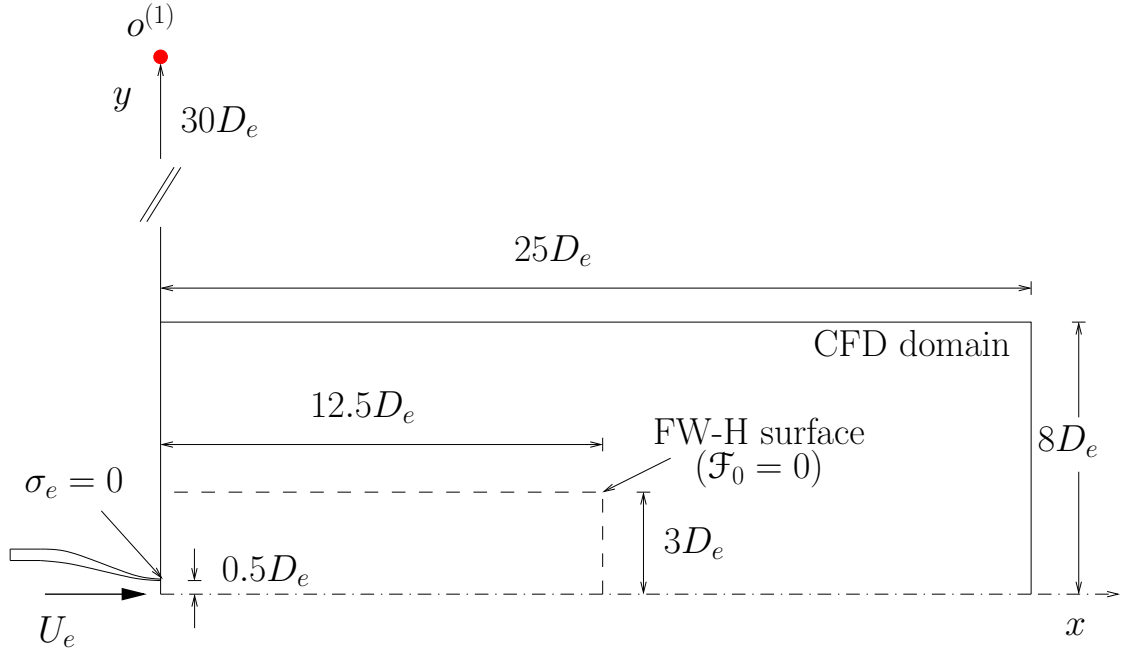


Figure 4.1: Domain schematic for the subsonic single-stream jet (Di Stefano *et al.* [144]) showing the CFD domain, a sample observer position, and the location of the FW-H integration surface. Lengths are scaled by the nozzle exit diameter D_e .

Noise predictions are obtained on a spherical array of 110 numerical observers at a polar distance of $30.0D_e$ from the origin of the Cartesian reference system, distributed between 11 different axial locations over the range $-15.0D_e \leq x \leq 28.2D_e$. At each axial location, 10 numerical observers are equally spaced in azimuth. The observers

span the range $20^\circ \leq \theta \leq 120^\circ$, where θ is the polar angle measured with respect to the jet axis. The observer $o^{(1)}$ from the spherical array, located on the nozzle exit plane at $\mathbf{x}^{(1)} = (0, 30.0, 0) D_e$, is shown in Figure 4.1 and it corresponds to $\theta = 90^\circ$.

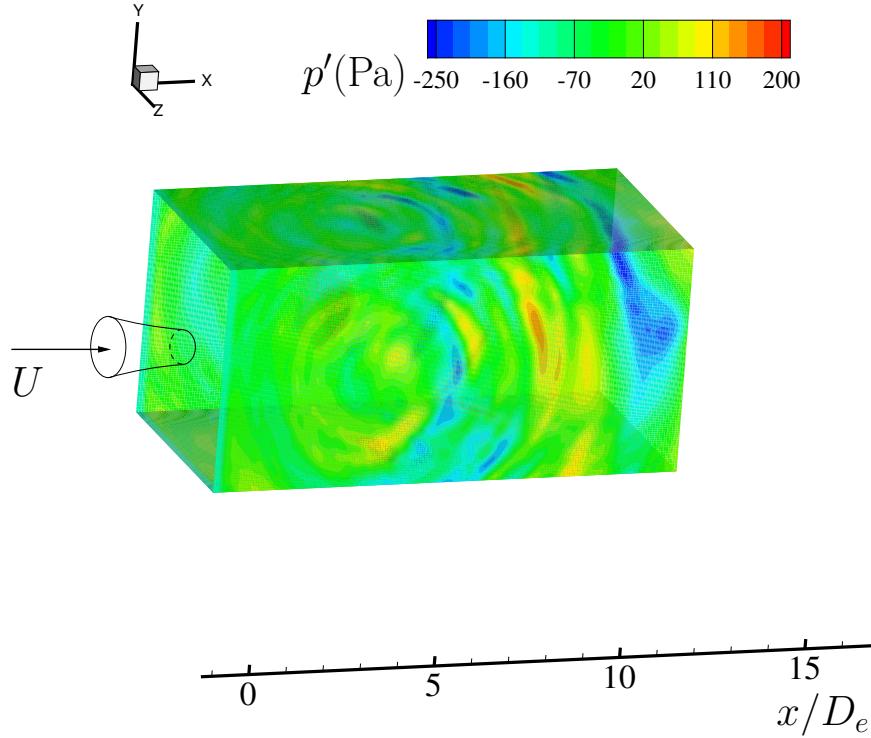


Figure 4.2: Large Eddy Simulation of a single-stream Mach 0.9 jet modelled at $Re = 4 \times 10^5$ [142], obtained at Cerfacs (Toulouse) by the elsA software [130]. Instantaneous pressure fluctuation iso-levels on the FW-H surface $\mathcal{F}_0 = 0$ from [135].

The time-history of the flow prediction is available on the FW-H surface $\mathcal{F}_0(\mathbf{x}, t) = 0$, obtained by LES. The unsteady numerical simulation was performed at Cerfacs by Biolchini [135] by using the ONERA elsA code [130]. The flow in the database is sampled on $\mathcal{F}_0(\mathbf{x}, t) = 0$ with a CAA sampling time $\Delta\tau_{CAA} = 6 \times 10^{-6}$ s, that is ten times the CFD time step ($\Delta\tau_{CFD} = 6 \times 10^{-7}$ s). The time length of the LES dataset is 0.0528 s, with 8800 acoustic time steps overall. Figure 4.2 shows the colour iso-levels of the instantaneous pressure fluctuation p' from this CFD dataset [135]. Specifically, the radiating near-field pressure fluctuation on the FW-H surface, which is essentially of acoustic nature, is displayed. This pressure fluctuation radiates beyond the CFD domain and this propagation is modelled by the acoustic analogy

implementation described in Section 2.2.3.

The correct placement of the integration surface is usually checked by verifying that the acoustic prediction is independent of the surface position itself. In Section 4.1.2, where a supersonic single-stream jet is investigated, this test is performed by using the CFD prediction stored on three nested surfaces $\mathcal{F}_1 = 0$, $\mathcal{F}_2 = 0$, and $\mathcal{F}_3 = 0$ and Figure 4.7 shows that the BBSAN and the mixing noise contributions are independent of the choice of the FW-H surface. However, for the subsonic jet investigated here, only the CFD prediction on the prismatic surface of Figure 4.1 is available.

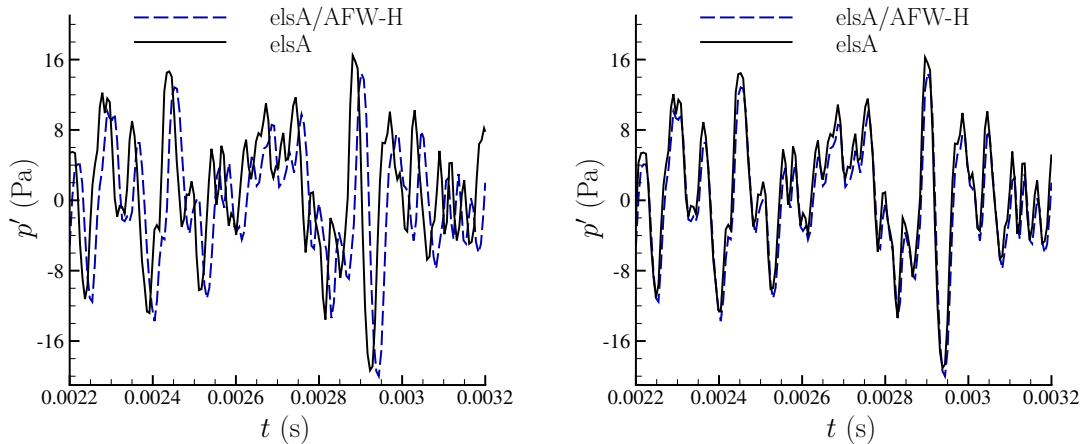
FW-H Surface	$x_{\min} = 0.0D_e$	$x = 9.7D_e$	$x_{\max} = 12.5D_e$
$\mathcal{F}_0(\mathbf{x}, t) = 0$	$-3.0D_e \leq y, z \leq 3.0D_e$	$-3.0D_e \leq y, z \leq 3.0D_e$	$-3.0D_e \leq y, z \leq 3.0D_e$
$\mathcal{F}_1(\mathbf{x}, t) = 0$	$-2.0D_e \leq y, z \leq 2.0D_e$	$-3.0D_e \leq y, z \leq 3.0D_e$	$-3.5D_e \leq y, z \leq 3.5D_e$

Table 4.1: Dimensions of the FW-H surface $\mathcal{F}_0 = 0$ used for the $M_j = 0.9$ subsonic test case compared to the surface $\mathcal{F}_1 = 0$ of Table 4.2, relative to the supersonic single-stream jet of Section 4.1.2. Dimensions scaled by the corresponding jet diameter D_e .

Table 4.1 compares the size of the integration surface in Figure 4.1 with the dimensions of the smallest integration surface adopted for the supersonic single-stream jet, that is $\mathcal{F}_1 = 0$ in Table 4.2. It can be noticed that, in the range $0.0D_e \leq x \leq 9.7D_e$, the prismatic surface $\mathcal{F}_0 = 0$ is external to the hourglass-shaped surface $\mathcal{F}_1 = 0$. At $x = 9.7D_e$, the square section of the prismatic surface $\mathcal{F}_0 = 0$ is tangent to the round section of the axisymmetric surface $\mathcal{F}_1 = 0$. Further downstream, over the range $9.7D_e \leq x \leq 12.5D_e$, the prismatic surface $\mathcal{F}_0 = 0$ is contained within $\mathcal{F}_1 = 0$.

As far as the axial extent is concerned, $\mathcal{F}_0 = 0$ reaches $x = 12.5D_e$ at the downstream edge, whereas $\mathcal{F}_1 = 0$ extends to $x = 19.0D_e$. Still, the potential core of the subsonic jet extends up to $x \approx 5.0D_e$ [142] and the FW-H prismatic surface $\mathcal{F}_0 = 0$ encloses both the potential core and the turbulent mixing region downstream, which contribute most to the noise generation from the $M = 0.9$ single-stream jet [142]. In the supersonic jet, the potential core stretches up to $x = 9.0D_e$ [16]. This justifies the use of a FW-H surface $\mathcal{F}_1 = 0$ of greater axial extent, which is able

to enclose the acoustically active region of the supersonic jet in Section 4.1.2.



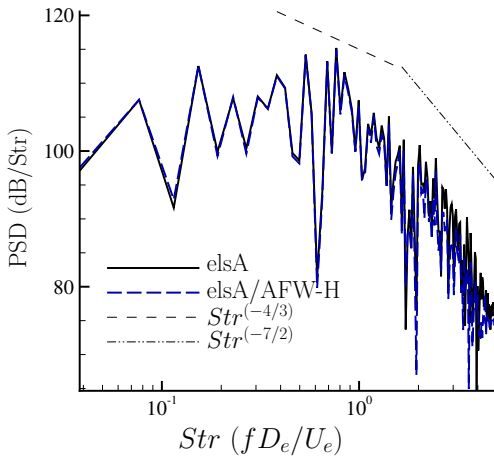
(a) Reference solution incorrectly normalized (Di Stefano *et al.* [140]). (b) Reference solution correctly normalized (Di Stefano *et al.* [144]).

Figure 4.3: Predicted sound radiation at observer $o^{(1)}$ from a single-stream, isothermal, and circular jet (Bogey and Bailly [142]) modelled by LES [135]. Mach 0.9, $Re = 4 \times 10^5$. $r_o = 30.0D_e$ from the nozzle exit section centre.

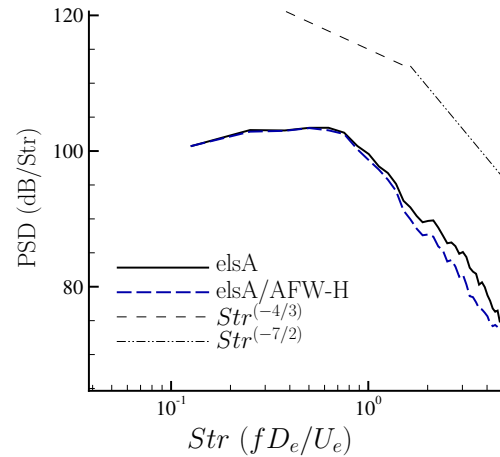
Figure 4.3 shows the acoustic pressure fluctuation estimated using the current AFW-H implementation versus the reference prediction from elsA at $o^{(1)}$ (see Figure 4.1). The solid-black lines labelled by “elsA” represent the reference solution provided by Cerfacs, Toulouse, while the dashed-blue lines labelled by “AFW-H” show the current prediction. The acoustic pressure fluctuation at the observer $o^{(1)}$ is broadband and non-periodic, as shown by the combination of large and small amplitude pressure oscillations in Figure 4.3. This results in a complex pressure perturbation time-history. The current implementation of the AFW-H method appears to follow this time-history well in Figure 4.3(b) [144]. In Figure 4.3(a) from [140], the AFW-H code result shows a small phase lead and a small negative mean pressure offset with respect to the reference solution, due to an initial incorrect normalization of the reference solution itself.

Figure 4.4(a) reports the Power Spectral Density (PSD) of the single-observer pressure fluctuation time-history of Figure 4.3(b). The Python AFW-H tool prediction is compared against the reference solution and the same notation is used as in Figure 4.3. The values are in dB/Str (dB per unit Strouhal), meaning that

$\int \text{PSD}(Str)dStr$ provides the overall sound energy. The overall sound power can be obtained dividing the overall sound energy by the acquisition time. The Strouhal number is defined using the diameter D_e and the jet velocity U_e at the nozzle exit plane. Two lines with slope of $-4/3$ and $-7/2$ are reported in Figure 4.4 to appreciate how the PSD at $o^{(1)}$ follows the trends for noise generated by unheated convected turbulence, obtained by dimensional analysis by Lilley [71] and by Zhou [145]. At Strouhal numbers less than 2.0, a good match of the prediction with the reference solution is shown. At Strouhal numbers above 2.0, the short period of flow time modelled by LES, compared to a typical acoustic recording by microphones, generates an irregular PSD trace in Figure 4.4(a), which is commonly referred to as a “noisy” spectrum in experiment. Some form of signal averaging is required to reduce these spectral fluctuations and to evaluate the PSD decay rate with Str .



(a) PSD (Di Stefano *et al.* [144]).



(b) PSD obtained by the Welch method [146], averaged over the azimuthal array of observers on the plane $x = 0$.

Figure 4.4: Far-field PSD vs Strouhal number at observer $o^{(1)}$ from a single-stream, isothermal, and circular jet (Bogey and Bailly [142]) modelled by LES [135]. Reference discontinuous-grey lines with slope $-4/3$ and $-7/2$ display the PSD decay for noise generated by unheated convected turbulence, predicted by dimensional analysis by Lilley [71]. Mach 0.9, $Re = 4 \times 10^5$. $r_o = 30.0D_e$ from the nozzle exit section centre.

Figure 4.4(b) shows the outcome from a first attempt at reducing the PSD fluctuations at $Str > 2.0$. The Welch method [146] is used to compute the Power

Spectral Density from each of the 10 observers on the plane $x = 0$ and the result is then averaged in azimuth. Figure 4.4(b) shows significantly smoother trends. All the PSDs presented in Chapters 4 and 5 are smoothed with the same technique explained here for Figure 4.4(b).

Figure 4.4(b) confirms that the new Python AFW-H tool follows very closely the reference prediction at $Str < 1.0$. As the Strouhal number increases, the dashed-blue line and the solid-black line start to diverge. This is due to a difference in sampling frequency of the CFD solution between the two FW-H tools. In the elsA FW-H combined solver, the acoustic analogy is performed every CFD time step, with $\Delta\tau_{CAA,elsA} = \Delta\tau_{CFD}$. On the other hand, the Python AFW-H tool is used as a post-processor and it is applied to a previously stored CFD database that was recorded at $\Delta\tau_{CAA,AFW-H} = 10\Delta\tau_{CFD}$. This longer acoustic time step lowers the sampling frequency, which degrades the accuracy of the solution at the high Strouhal number end of the spectrum in Figure 4.4.

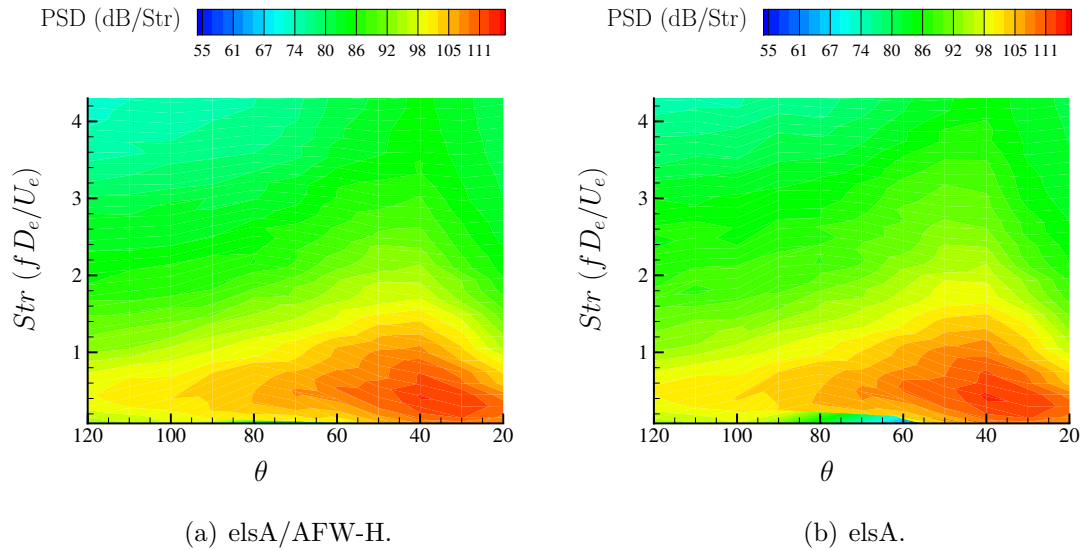


Figure 4.5: Far-field PSD vs Strouhal number and radiation angle θ from a single-stream, isothermal, and circular jet (Bogey and Bailly [142]) modelled by LES [135]. Mach 0.9, $Re = 4 \times 10^5$. $r_o = 30.0D_e$ from the nozzle exit section centre. PSD smoothed as in Figure 4.4(b).

In Figure 4.5, the PSD in the acoustic far-field is plotted against both the Strouhal number and the radiation angle θ and a good match is obtained between the AFW-H tool prediction, shown in Figure 4.5(a), and the reference numerical prediction by the

elsA code [130], shown in Figure 4.5(b). From Figure 4.5, an *a posteriori* qualitative assessment of the correct placement of the FW-H surface $\mathcal{F}_0 = 0$, used for the integration procedure, can be provided. The mixing noise component that dominates the noise radiation from the $M = 0.9$ jet reaches its peak at $\theta \approx 30^\circ$, as shown by the red 111 dB iso-level in Figure 4.5, in agreement with the results by Bogey and Bailly in [142]. The line at $\theta = 30^\circ$ reaches a distance of $3D_e$ from the jet axis at $(x = 5.2D_e; y = 3.0D_e)$, intersecting $\mathcal{F}_0 = 0$ well before its downstream boundary located at $x = 12.5D_e$. The prismatic integration surface $\mathcal{F}_0 = 0$ of Figure 4.1 appears therefore to be placed correctly, allowing to capture the peak of the noise radiation as shown by the PSD reported in Figure 4.5.

Overall, the AFW-H tool prediction follows satisfactorily the reference numerical solution for the observer $o^{(1)}$ in Figure 4.4, as well as for the other observers in the far-field array, as it is shown in Figure 4.5. This indicates that the new Python AFW-H tool produces frequency content and directivity characteristics consistent with the reference acoustic prediction from elsA. The satisfactory outcome from this first application of the AFW-H tool to jet noise warrants the investigation of more complex cases in Sections 4.1.2 and 4.2, where under-expanded jets are considered.

4.1.2 Supersonic under-expanded cold jet

The second jet noise application of the new AFW-H tool is to a supersonic $M_j = 1.15$ jet, from an axisymmetric convergent nozzle. The nozzle geometry does not allow the flow to be accelerated to the fully-expanded supersonic velocity U_j and the pressure p_e at the nozzle exit is higher than the ambient pressure p_0 , with $M_e < M_j$. The jet is therefore under-expanded and an expansion wave generates at the nozzle lip, accelerating the flow to supersonic velocities that cannot be reached before or at the convergent nozzle throat. The expansion wave is reflected at the shear layer as a compression wave and a system of consecutive expansions and compressions is established (shock-cells). Shock-Cell Noise (SCN) is then generated and the flow configuration is similar to the one described in Section 1.2 and sketched in Figure 1.2(b).

The flow is modelled at a Nozzle Pressure Ratio (NPR) of 2.27 and at a Reynolds number based on the nozzle exit diameter $Re = \rho_j U_j D_e / \mu = 1.25 \times 10^6$. A DES

of the jet was performed at the University of Leicester by Alessandro Mancini and details of both the numerical parameters and the flow prediction can be found in [15]. Comparative LES results are also obtained by Pérez at Cerfacs [16]. Experimental measurements are available, obtained both at the Von Karman Institute for fluid dynamics (VKI), Brussels, by Guariglia [43] and at the Laboratoire de Mécanique des Fluides et d'Acoustique (LMFA) of the École Centrale de Lyon, by André [143].

Mancini [15] and Pérez [16] compared their respective numerical predictions of the flow against the aerodynamic measurements by André [143] and by Guariglia [43]. The numerical simulations predict higher expansion rates, resulting in a shorter spacing after the first three shock-cells that affects the peak frequencies of the BBSAN contribution to the far-field noise. However, the length of the potential core is in agreement between both numerical predictions and the experimental measurements and a good match is achieved overall. The appearance of screech in the experiment could explain the difference in the shock-cell structure after the first three shock-cells [16].

FW-H Surface	$x_{\min} = -3.0D_e$	$x = 0.0D_e$	$x_{\max} = 19.0D_e$
$\mathcal{F}_1(\mathbf{x}, t) = 0$	$-2.8D_e \leq y, z \leq 2.8D_e$	$-2.0D_e \leq y, z \leq 2.0D_e$	$-4.7D_e \leq y, z \leq 4.7D_e$
$\mathcal{F}_2(\mathbf{x}, t) = 0$	$-3.3D_e \leq y, z \leq 3.3D_e$	$-2.5D_e \leq y, z \leq 2.5D_e$	$-5.0D_e \leq y, z \leq 5.0D_e$
$\mathcal{F}_3(\mathbf{x}, t) = 0$	$-3.8D_e \leq y, z \leq 3.8D_e$	$-3.0D_e \leq y, z \leq 3.0D_e$	$-5.4D_e \leq y, z \leq 5.4D_e$

Table 4.2: Dimensions of the FW-H surfaces used for the $M_j = 1.15$ test case, scaled by the jet diameter D_e .

The AFW-H formulation of Section 2.2.3 is applied to the flow time-history obtained by DES by Mancini [15]. The flow prediction is stored on three nested surfaces with increasing size that surround the jet. Table 4.2 summarises the dimensions of the three surfaces in terms of the radial extent at three axial locations, *i.e.* the upstream and the downstream ends of the surfaces and the nozzle exit plane.

The FW-H surfaces follow the CFD mesh axial profile, resulting in a shape that is similar to that of an hourglass, with a convergent section for $x < 0$, followed by a divergent section downstream of the jet outflow. All three surfaces are of the “open” type (see Section 2.2.1) at the aft edge $x_{\max} = 19.0D_e$. The monopole and the dipole contributions expressed by Equations 2.21 and 2.22 are discretised and estimated on

$\mathcal{F}_1 = 0$, $\mathcal{F}_2 = 0$, and $\mathcal{F}_3 = 0$ of Table 4.2.

The DES flow prediction by the Cosmic software (Mancini [15]) was stored on these open surfaces with an acoustic time step $\Delta\tau_{CAA} = 5 \times 10^{-6}$ s, that is 500 times larger than the CFD counterpart ($\Delta\tau_{CFD} = 1 \times 10^{-8}$ s). 1800 snapshots of the CFD prediction on the FW-H surfaces are available, for an overall time length of 0.009 s. The instantaneous pressure fluctuation p' on the FW-H surface $\mathcal{F}_2 = 0$ from one of these snapshots is shown in Figure 4.6. The hourglass shape of the surface can be appreciated, as well as the open end at the downstream edge. The pressure fluctuation is of the acoustic type, being the surface placed in the “linear acoustic” region of the pressure field [138], almost free from non-linear hydrodynamic contributions (see Section 2.4.3). The trace of acoustic waves travelling downstream is also noticeable in Figure 4.6, as axially alternating ring bands of high (red) and low (green) pressure perturbations.

A comparison of the results from the three surfaces $\mathcal{F}_1 = 0$, $\mathcal{F}_2 = 0$, and $\mathcal{F}_3 = 0$ was performed and the result is reported in Figure 4.7 for two radiation angles in the upstream arc, where the BBSAN contribution is clearly present, *i.e.* $\theta = 100^\circ$ in Figure 4.7(a) and $\theta = 120^\circ$ in Figure 4.7(b). In Figure 4.7, the result obtained with the innermost surface $\mathcal{F}_1 = 0$ is shown by the solid-red lines, while short-dash green lines and long-dash blue lines display the spectra predicted by using respectively the intermediate surface $\mathcal{F}_2 = 0$ and the outermost surface $\mathcal{F}_3 = 0$. The three curves mutually overlap showing that the increase of the FW-H surface size from $\mathcal{F}_1 = 0$ to $\mathcal{F}_2 = 0$ and then from $\mathcal{F}_2 = 0$ to $\mathcal{F}_3 = 0$ does not significantly affect the noise prediction. The three surfaces are therefore correctly placed in the “linear acoustic” region of the pressure field (see Section 2.4.3), by satisfying the requirements discussed in Section 2.2.1. The choice between the three surfaces is therefore arbitrary. The results from the intermediate surface $\mathcal{F}_2 = 0$ are reported in this section.

Figure 4.8 reports the far-field Power Spectral Density versus Strouhal number $Str = fD_e/U_j$ for 8 radiation angles θ from the jet axis, between 40° and 140° . The AFW-H prediction in blue is compared against experimental measurements obtained by André at LMFA and by Guariglia at VKI, referred to as “exp LMFA” and “exp VKI”, respectively. Solid-red lines show the acoustic measurements by André [143], while dashed-green lines show the VKI noise measurements by Guariglia [43]. The

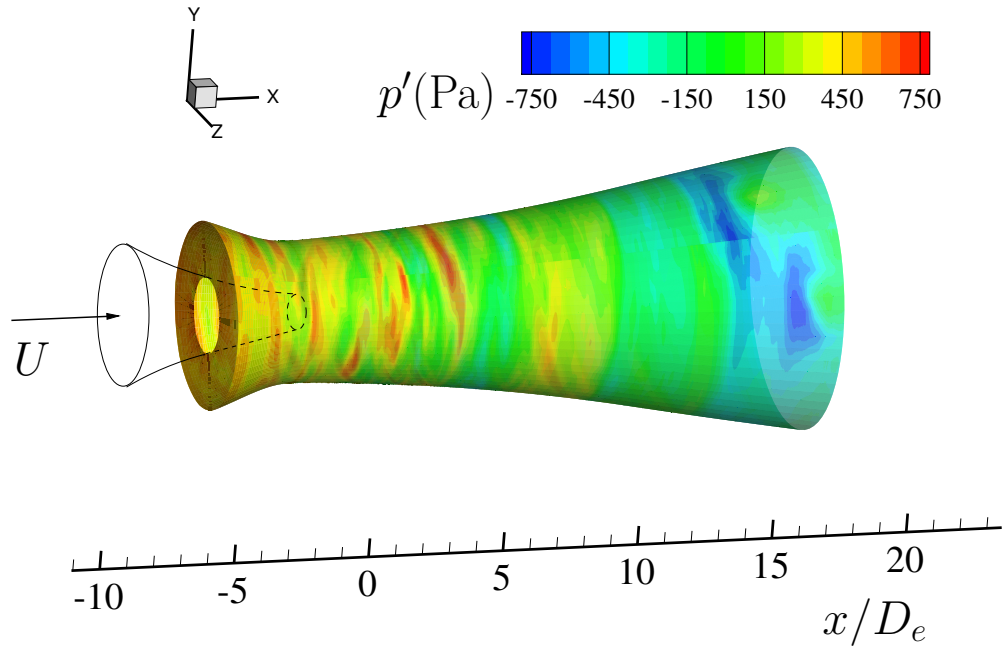


Figure 4.6: Detached Eddy Simulation of a single-stream Mach 1.15 jet [143] modelled at $Re = 1.25 \times 10^6$. Instantaneous pressure fluctuation iso-levels on the FW-H surface $\mathcal{F}_2 = 0$ from [15].

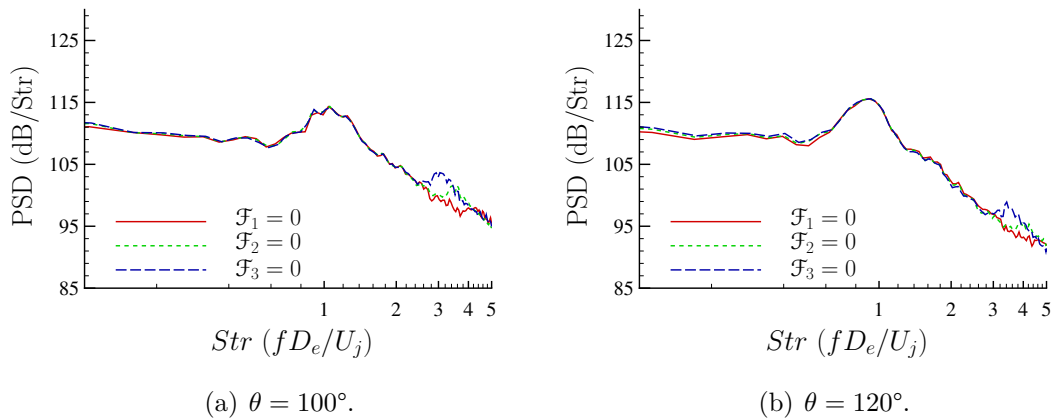


Figure 4.7: Far-field PSD from a single-stream under-expanded jet modelled by DES [15]. Comparison between the predictions obtained through the surfaces $\mathcal{F}_1 = 0$, $\mathcal{F}_2 = 0$, and $\mathcal{F}_3 = 0$. $M_j = 1.15$, $Re = 1.25 \times 10^6$, $r_o = 52.0D_e$ from the nozzle exit. PSD smoothed as in Figure 4.4(b).

experimental measurements are not corrected to lossless conditions and the atmospheric effects are ignored. This is in agreement with André [143], who showed that spectra measured at LMFA are attenuated by less than 1 dB up to $f = 30$ kHz, which corresponds to about $Str = 3$ in Figure 4.8.

Only slight discrepancies between the two experimental measurements can be noticed in Figure 4.8, except for the $\theta = 40^\circ$ direction, where the PSD by Guariglia [43] is up to 8 dB less than the corresponding measurement at LMFA [143]. Over the low Strouhal number range ($Str < 0.8$) in the upstream arc ($90^\circ < \theta < 140^\circ$), the measurements by Guariglia show lower noise levels by up to 2 – 3 dB with respect to the corresponding PSDs measured at LMFA. The measured PSD at VKI is louder with respect to the LMFA PSD over the high Strouhal number range ($Str > 2$) at $\theta = 90^\circ$. As far as the BBSAN peaks are concerned, the measurements agree very well in terms of peak frequency. The noise peak level is slightly lower in the VKI experiment [43] in the upstream arc.

These discrepancies could be explained by differences in the actual jet flows in the two cases. It is worth mentioning that the experimental set-up at VKI [43] is characterised by a smaller nozzle, with $D_e = 0.024$ m, against the value used in the CFD simulation and in the experiment by André [143] that is $D_e = 0.038$ m. The distance of the far-field array is also shorter, corresponding to $r_o = 40.0D_e$, against $r_o = 52.0D_e$ in the CFD simulation. Therefore, the “exp VKI” PSDs in Figure 4.8 are scaled geometrically to $r_o = 52.0D_e$, in order to allow a direct comparison among the results.

Figure 4.8 shows a good agreement between numerical prediction and experiment in terms of the BBSAN peak frequency and amplitude at radiation angles $\theta \geq 80^\circ$, above which the BBSAN emerges from the mixing noise background, showing that the AFW-H tool applied to the DES flow prediction correctly captures this noise component. However, over the Strouhal number range below the BBSAN peak, the numerical prediction shows louder noise levels compared to the experimental measurements, by about 5 to 10 dB, especially in the upstream quadrant ($\theta > 90^\circ$). The reason for this elevated contribution at low Strouhal numbers can be attributed to a coarse flow domain discretization in the azimuthal coordinate [15, 16]. Due to this coarse discretization, larger scale structures develop in the CFD simulation

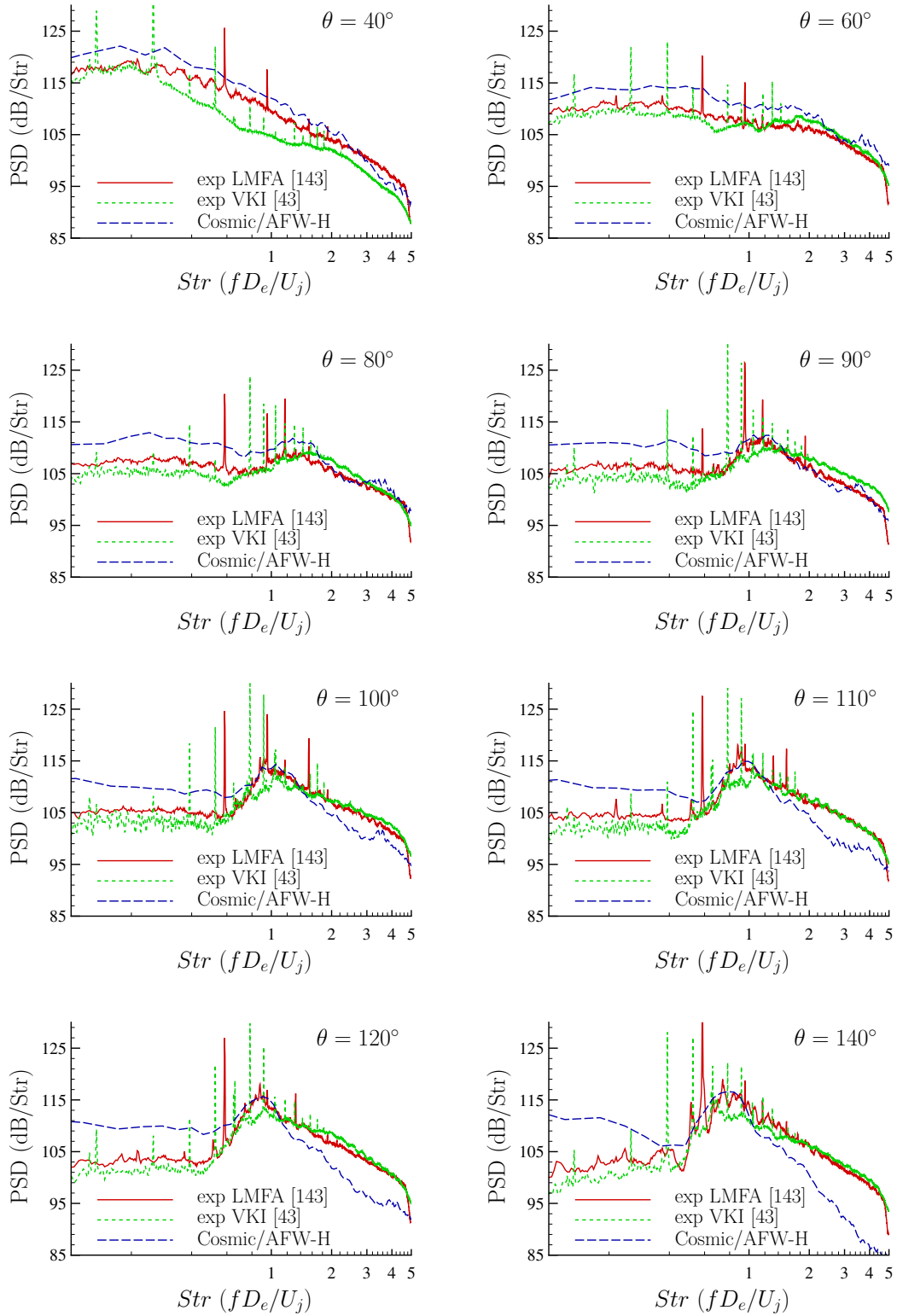


Figure 4.8: Far-field PSD from a single-stream under-expanded jet modelled by DES [15]. Comparison with experimental measurements by André [143] (“exp LMFA”) and by Guariglia [43] (“exp VKI”). FW-H surface $\mathcal{F}_2 = 0$. $M_j = 1.15$, $Re = 1.25 \times 10^6$, $r_o = 52.0D_e$ from the nozzle exit. PSD smoothed as in Figure 4.4(b).

compared to the experiment, as documented by larger velocity autocorrelation lengths reported in [15]. As the low frequency contribution to turbulent mixing noise is mainly generated by the large scales, these bigger structures in the CFD flow prediction are likely to be responsible for the mismatch in the low Strouhal number contributions between the AFW-H post-processed CFD and the acoustic measurements.

At the opposite end of the Strouhal number range, the predicted PSD is lower in the upstream direction (angles $\theta = 100^\circ, 110^\circ, 120^\circ, 140^\circ$ in Figure 4.8). The fine-scale structures are mainly responsible for the turbulent mixing noise radiation at these high frequencies. The CFD mesh spatial resolution was probably insufficient to accurately resolve the spatial and the temporal evolution of these short scale structures in the flow. Specifically, the prediction for high-frequency small-scale flow structures is limited by the mesh cut-off Strouhal number and by the sampling frequency. In this case, the more stringent limitation is represented by the mesh that gives a cut-off Strouhal number of around 2.5 [15].

The discrepancies at high Strouhal numbers below the mesh cut-off ($1.5 \leq Str \leq 2.5$), especially at $\theta = 120^\circ$ and at $\theta = 140^\circ$, are likely to be related to the azimuthal discretization of the mesh [15]. As already mentioned, the DES prediction shows larger turbulent structures compared to the experiment that are convected many jet diameters downstream the nozzle exit section. The coarse azimuthal discretization does not allow to accurately reproduce the breakdown of these large structures into fine-scale turbulence [15]. The inadequacy of this breakdown makes the contribution from the fine-scales weaker than in experiment, especially at the high-frequency range in the upstream direction, where this contribution is dominant [15].

Figure 4.8 shows that screech noise is measured in both the experimental facilities, while the CFD simulation does not predict any significant tonal component of the resolved pressure fluctuation. This difference can be ascribed to several factors, such as a too coarse mesh close to the nozzle lip in the numerical simulation and the fact that the interior of the nozzle is not modelled [15, 16]. Moreover, the feedback loop at the nozzle lip that generates the screech noise contribution needs time to develop and establish. The flow time length in the numerical simulation was shorter than in the experiment and, in this case, it could have been insufficient to allow this feedback

loop to establish.

Notwithstanding these discrepancies, the acoustic prediction in Figure 4.8 gives a satisfactory match with both the experimental measurements by Guariglia [43] and by André [143], by correctly capturing the θ dependency of the BBSAN spectral contribution to far-field noise from the $M_j = 1.15$ under-expanded jet.

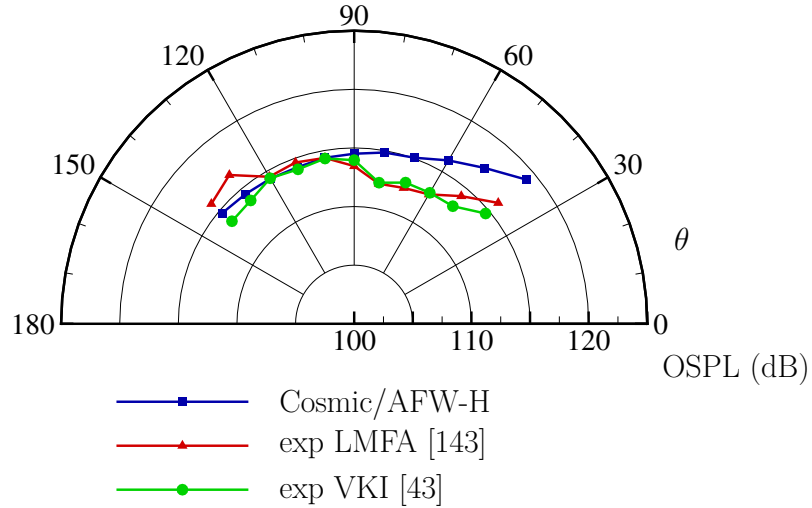


Figure 4.9: Far-field Overall Sound Pressure Level (OSPL) from a single-stream under-expanded jet modelled by DES [15]. FW-H surface $\mathcal{F}_2 = 0$. $M_j = 1.15$, $Re = 1.25 \times 10^6$, $r_o = 52.0D_e$ from the nozzle exit.

This is confirmed by Figure 4.9 that compares the Overall Sound Pressure Level (OSPL) directivity from the single-stream supersonic jet, as predicted from the AFW-H tool to measurements by André [143] and by Guariglia [43]. A good match is shown in the upstream direction, where the BBSAN contribution is dominant. The overestimation of the noise levels in the downstream arc are likely to be due to larger scale structures in the CFD prediction compared to the experiment, as mentioned above.

Therefore, the new Python AFW-H tool appears to produce satisfactory results when applied to the single-stream under-expanded jet investigated herein, also in view of the differences between the measured and the predicted flow field, which provides the input to the AFW-H tool.

4.2 Dual-stream jet noise

The last application of the Antares AFW-H tool is to a dual-stream jet configuration that is defined in Appendix A. This configuration is an idealized geometry of a civil transport turbofan exhaust developed by the Airbus SAS propulsion team as an academic test case for the AeroTraNet2 project. This dual-stream jet is generated by an axisymmetric convergent nozzle surrounded by a staggered coaxial annular convergent nozzle, as sketched in Figure A.1.

In the primary stream, the nozzle exit Mach number M_p is equal to the fully-expanded primary jet Mach number M_{jp} ($M_p = M_{jp} = 0.89$) and the Reynolds number based on the primary nozzle exit diameter $D_p = 0.024$ m is $Re_p = 0.57 \times 10^6$. In the bypass or secondary stream, the geometry of the convergent duct constrains the nozzle exit Mach number M_s to be sonic and does not allow the flow to accelerate to its fully expanded Mach number $M_{js} = 1.20$ inside the nozzle. Therefore, the secondary stream is under-expanded, resulting in the generation of SCN as described in Sections 1.2 and 1.3, due to the shock-cell system that establishes between the primary and the secondary shear layers. The Reynolds number based on the annular nozzle outer diameter $D_s = 0.055$ m is $Re_s = 1.66 \times 10^6$. The flow conditions for the dual-stream jet are summarised in Table 4.3.

Flow	$D(\text{m})$	M	M_j	Re	NPR	$T_t(\text{K})$	p_t (Pa)
Primary	0.024	0.89	0.89	0.57×10^6	1.675	283	1.6972×10^5
Secondary	0.055	1.00	1.20	1.66×10^6	2.450	283	2.4825×10^5

Table 4.3: Dual-stream jet flow conditions.

In this test, the AFW-H tool is used for post-processing an archived LES simulation performed at Cerfacs, France, from the ONERA CFD software package elsA [130]. Details of the LES are given by Pérez [16]. The flow field prediction was stored on a set of three nested integration surfaces of the “open” type (see Section 2.2.1), referred to as $\mathcal{F}_1 = 0$, $\mathcal{F}_2 = 0$, and $\mathcal{F}_3 = 0$ (Table 4.4). The CFD dataset consists of 1764 snapshots of the flow prediction on each integration surface, covering an overall time length of 0.01322 s. The CFD solution is stored every 400 CFD time steps $\Delta\tau_{\text{CFD}} = 1.9 \times 10^{-8}$ s, giving an acoustic time step $\Delta\tau_{\text{CAA}} = 7.5 \times 10^{-6}$ s.

FW-H Surface	$x_{\min} = -0.9D_s$	$x = 0.0D_s$	$x_{\max} = 10.6D_s$
$\mathcal{F}_1(\mathbf{x}, t) = 0$	$-1.5D_s \leq y, z \leq 1.5D_s$	$-1.2D_s \leq y, z \leq 1.2D_s$	$-3.1D_s \leq y, z \leq 3.1D_s$
$\mathcal{F}_2(\mathbf{x}, t) = 0$	$-2.0D_s \leq y, z \leq 2.0D_s$	$-1.7D_s \leq y, z \leq 1.7D_s$	$-3.6D_s \leq y, z \leq 3.6D_s$
$\mathcal{F}_3(\mathbf{x}, t) = 0$	$-2.3D_s \leq y, z \leq 2.3D_s$	$-2.1D_s \leq y, z \leq 2.1D_s$	$-4.1D_s \leq y, z \leq 4.1D_s$

Table 4.4: Dimensions of the FW-H surfaces scaled by the secondary jet diameter D_s .

The maximum frequency resolved by the CFD simulation is imposed by the cut-off Strouhal number $Str_{max} \approx 6.8$ [16] dictated by the spatial discretization of the LES mesh. This is lower than the Nyquist frequency limit from the data storage time sampling rate, which is $Str_{max} \approx 10.6$ [16]. The cut-off Strouhal number value is estimated via a point-per-wavelength criterion. The high-order compact scheme implemented in the elsA [130] software allows for the discretization of a wave with a negligible dispersion and dissipation using a minimum of six points per wavelength [16]. The relation between the mesh size and the resolved frequency is $f_{max} = c_0/(6\Delta s)$.

Figure 4.10 shows the CFD domain, which is axisymmetric with respect to the common axis of the two nozzles. A Cartesian reference system with the origin located on the jet axis at the primary nozzle exit plane is used to define the geometry. For the sake of simplicity, just the top half of the $x - y$ plane is shown and the sponge region used to prevent acoustic wave reflections at the computational domain outer boundaries [16, 133] is omitted.

The CFD physical domain [16] extends $15.0D_s$ in the axial direction from $x = -2.4D_s$ to $x = 12.6D_s$. It reaches $\pm 5.0D_s$ in both the y and z directions at the downstream edge, enclosing the FW-H surfaces $\mathcal{F}_1 = 0$, $\mathcal{F}_2 = 0$, and $\mathcal{F}_3 = 0$. The two nozzles are staggered and the secondary stream exits into the surrounding upstream of the primary stream, specifically at $x = -0.4D_s$. The nozzle lip thickness is $\sigma_s = \sigma_p = 0.3 \times 10^{-3}$ m for both nozzles, to match the nozzle geometry defined in Appendix A.

The axisymmetric integration surface $\mathcal{F}_1 = 0$, shown in Figure 4.10, follows the mesh axial profile and it is approximately in the shape of an hourglass, with a convergent section followed by a divergent section. Specifically, it reaches $x = 10.6D_s$

in the axial downstream direction and it extends upstream of the secondary nozzle exit plane up to $x = -0.9D_s$. At the downstream end, the surface extends to $\pm 3.1D_s$ in both y and z directions.

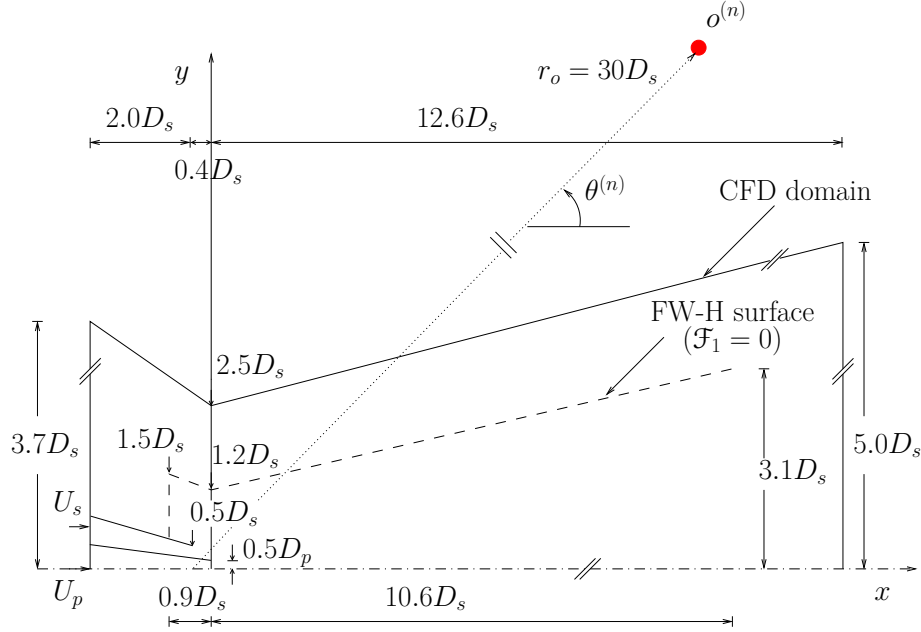


Figure 4.10: Domain schematic for the dual-stream jet (see Appendix A), showing the CFD domain, the FW-H surface $\mathcal{F}_1(\mathbf{x}, t) = 0$ and a generic observer $o^{(n)}$. Lengths are scaled by the secondary nozzle exit diameter D_s .

Surface $\mathcal{F}_1(\mathbf{x}, t) = 0$ is the smallest of three nested surfaces used in the LES simulation, on which the flow field time-history is available. The other surfaces have the same axial size as $\mathcal{F}_1(\mathbf{x}, t) = 0$, but they extend radially up to $\pm 3.6D_s$ and $\pm 4.1D_s$ at the downstream end, respectively for $\mathcal{F}_2(\mathbf{x}, t) = 0$ and $\mathcal{F}_3(\mathbf{x}, t) = 0$. Table 4.4 reports the radial extent of the three FW-H surfaces normalized by D_s , at the upstream end, the downstream end, and the origin of the reference system.

The monopole and the dipole noise contributions from Equations 2.21 and 2.22 are integrated on the FW-H surfaces of Table 4.4, with omission of the downstream disk, located at $x = 10.6D_s$. A time snapshot of the pressure fluctuation p' predicted on the “open” FW-H surface $\mathcal{F}_2(\mathbf{x}, t) = 0$ by LES [16] is shown in Figure 4.11 by iso-colour levels. The fluctuation amplitude is higher compared to that from the subsonic single-stream jet reported in Figure 4.2, while it is comparable with that from the supersonic single-stream jet, reported in Figure 4.6, and the highest values are reached close to the nozzle exit within the potential core of the jet.

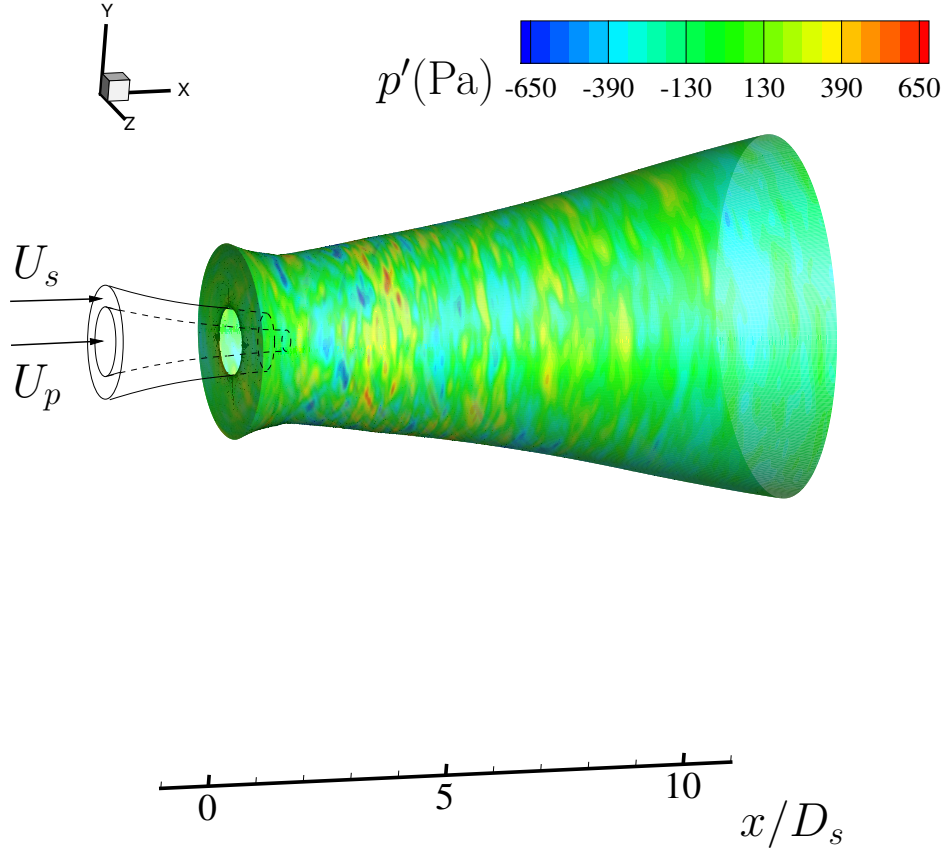


Figure 4.11: Large Eddy Simulation of a coaxial dual-stream jet by Pérez [16]. $M_{jp} = 0.89$, $M_{js} = 1.20$, $Re_p = 0.57 \times 10^6$, $Re_s = 1.66 \times 10^6$. Instantaneous pressure fluctuation iso-levels on the FW-H surface $\mathcal{F}_2 = 0$ of Table 4.4.

In this flow, two concentric jet cores develop [133]. The primary potential core is surrounded by an annular potential core, where the shock-cell structure is established. The shear layers bounding these two cores come together between $6.0D_s$ and $8.0D_s$ downstream of the primary nozzle exit and the two streams fully merge farther downstream. Three main noise sources [34] can be identified, which are the two shear layers and the fully merged jet downstream of $x = 8.0D_s$. The primary shear layer is generated by the velocity difference between the primary and the secondary flows, while the outer (or secondary) shear layer is due to the secondary flow exiting in the quiescent ambient air ($U_0 = 0$).

The inner and the outer shear layers generate two BBSAN components by interacting with the shock-cell system “trapped” between them, as explained in

Section 1.3. The fully merged jet generates turbulent mixing noise in a similar manner as a single-stream jet, by which the noise intensity is proportional up to the eight power of the mixed jet velocity.

To predict the noise radiation from the dual-stream jet configuration of Table 4.3, two different shapes are considered for the array of observers used to get far-field and near-field noise estimations, presented respectively in Section 4.2.1 and 4.2.2. This layout of observers is shared by the experimental and by the numerical partners in the AeroTraNet2 project (see Appendix A), as to enable a direct comparison among the results.

Specifically, a spherical array at $r = 30.0D_s$ from the secondary nozzle exit disk centre is used for the far-field analysis. The near-field analysis uses instead two nested conical arrays, the surfaces of which follow the jet spreading along the x -axis with a 8.0° slope. The conical surface of the innermost array is generated by a line between $(x = -0.4D_s; r = 1.5D_s)$ and $(x = 7.6D_s; r = 2.6D_s)$. The outermost array goes from $(x = -0.4D_s; r = 1.7D_s)$ to $(x = 7.6D_s; r = 2.8D_s)$.

16 observers are placed azimuthally in all the tests, in order to average the results in the azimuthal coordinate direction ϕ . This aims to get smoother frequency spectra of the signal, which are otherwise noisy due to the acquisition time of the relatively short CFD simulations [16].

4.2.1 Far-field radiation

For the far-field noise estimation, a polar arc with 15 observers is placed on the $x - y$ plane at a constant polar distance of $30.0D_s$ from $(-0.4, 0, 0)D_s$ (see Figure 4.10), which is the secondary nozzle exit disk centre. A sample observer $o^{(n)}$ is represented in Figure 4.10, located at the polar angle $\theta^{(n)}$ from the jet axis. The arc extends from $\theta = 20^\circ$ up to $\theta = 160^\circ$ anti-clockwise from the jet axis, spanning the range $-28.6D_s < x < 27.8D_s$. For each of the 15 axial positions (or radiation angles), 16 observers are placed azimuthally at a constant angular distance $\Delta\phi = \pi/8$, so that a spherical array of observers is formed with $15 \times 16 = 240$ observers overall.

Figures 4.12– 4.15 report the spectral analysis in the far-field, obtained by using as input of the AFW-H tool the CFD solution on the three nested surfaces of Table 4.4. Figure 4.12 shows iso-levels of PSD in dB/Str plotted against Strouhal

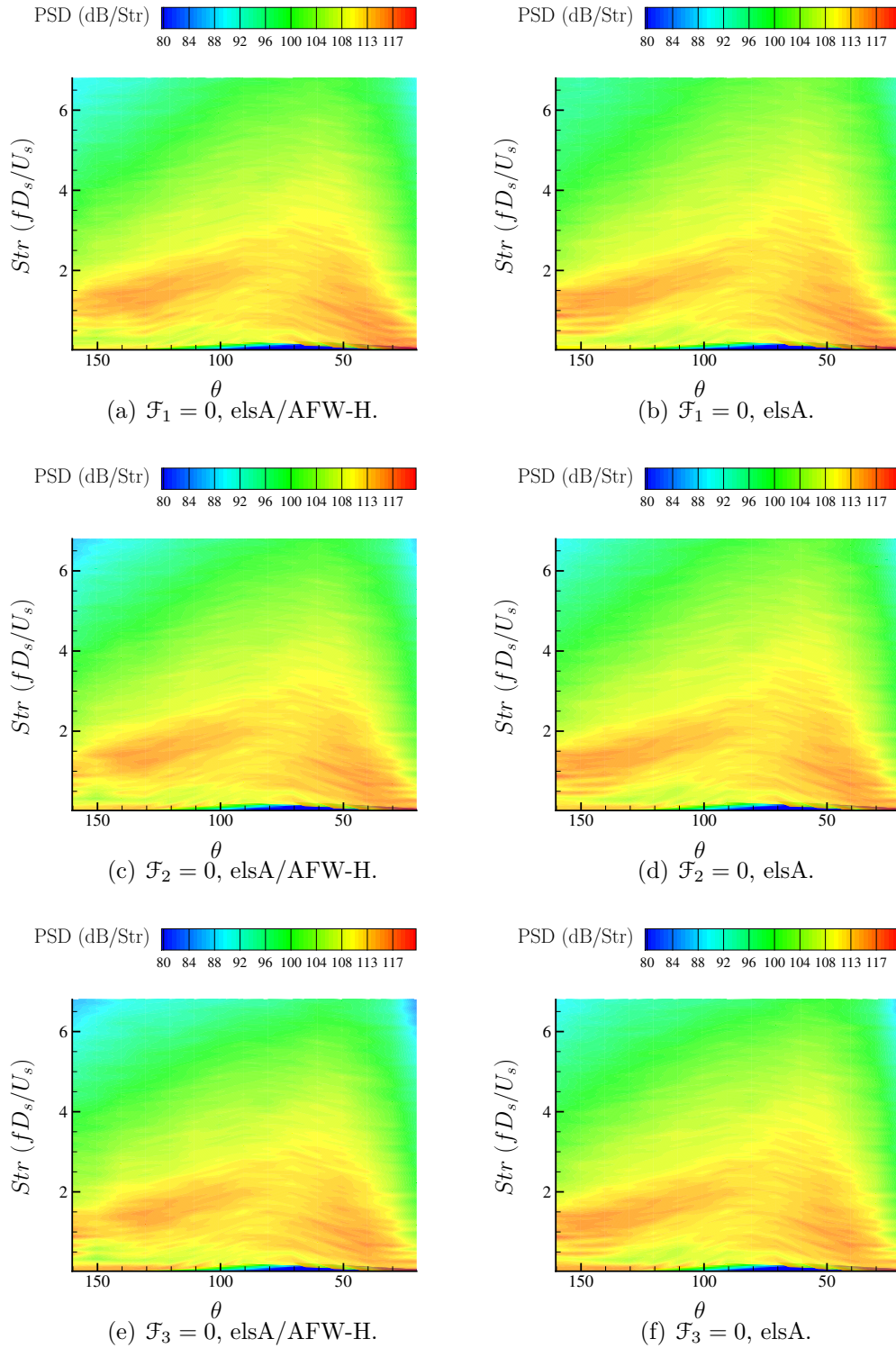


Figure 4.12: Far-field PSD vs Strouhal number and angle θ from the jet axis, from a dual-stream cold jet with the secondary flow under-expanded ($M_s = 1.0$), modelled by LES [16]. $M_{jp} = 0.89$, $M_{js} = 1.20$, $Re_p = 0.57 \times 10^6$, $Re_s = 1.66 \times 10^6$, $r_o = 30.0D_s$ from the centre of the coaxial nozzle-exit disk. PSD smoothed as in Figure 4.4(b).

number $Str = fD_s/U_s$ and polar angle θ . The AFW-H tool prediction on the left is compared against the reference numerical solution on the right, obtained at Cerfacs by Pérez [16] through the elsA code [130]. Figures 4.12(a) and 4.12(b) at the top are obtained using the smallest integration surface $\mathcal{F}_1 = 0$, Figures 4.12(c) and 4.12(d) are obtained using the intermediate surface $\mathcal{F}_2 = 0$, and Figures 4.12(e) and 4.12(f) are obtained using the largest surface $\mathcal{F}_3 = 0$. The θ axis is reversed so that the right part of the plots represent downstream directions, while upstream angles are shown on the left.

The results are in good agreement with the reference numerical prediction and show the spectral bandwidth peaking at about $\theta = 60^\circ$ from the jet axis. By increasing the polar angle, the bandwidth of significant frequencies is reduced. In the upstream direction, the predicted far-field noise is dominated by contributions over the Strouhal number range $1.0 \leq Str \leq 1.5$.

The spectral bandwidth peak at $\theta \approx 60^\circ$ appears to be less intense for the $\mathcal{F}_2 = 0$ results in Figures 4.12(c) and 4.12(d), compared to the prediction from the surface $\mathcal{F}_1 = 0$, as indicated by the yellow 108 dB/Str iso-level extending to higher Strouhal numbers in Figures 4.12(a) and 4.12(b). Increasing further the surface size from the intermediate FW-H surface $\mathcal{F}_2 = 0$ to the largest FW-H surface $\mathcal{F}_3 = 0$ does not appear to further change the acoustic prediction significantly. This shows that the results from $\mathcal{F}_2 = 0$ and $\mathcal{F}_3 = 0$ are essentially independent from the placement of the integration surface, and suggests that $\mathcal{F}_2 = 0$ and $\mathcal{F}_3 = 0$ lie within the “linear hydrodynamic” region of the jet [138], free from non-linear perturbations to a good approximation. In this region, the hydrodynamic perturbations associated with instability waves in the jet experience an exponential decay with increasing radial distance from the jet axis and the pressure field exhibits linear characteristics [138].

The specific PSD at selected radiation angles is shown in Figures 4.13– 4.15, where 8 values of θ between 30° and 130° are displayed. Figure 4.13 reports predictions from using the smallest integration surface $\mathcal{F}_1 = 0$, while Figures 4.14 and 4.15 report the results obtained with $\mathcal{F}_2 = 0$ and $\mathcal{F}_3 = 0$, respectively. In each figure, the AFW-H tool prediction, shown by the dashed-blue lines, is compared against the reference numerical solution referred to as “elsA”, which is shown by the solid-black lines.

Overall, a good agreement can be appreciated, especially on the amplitude and

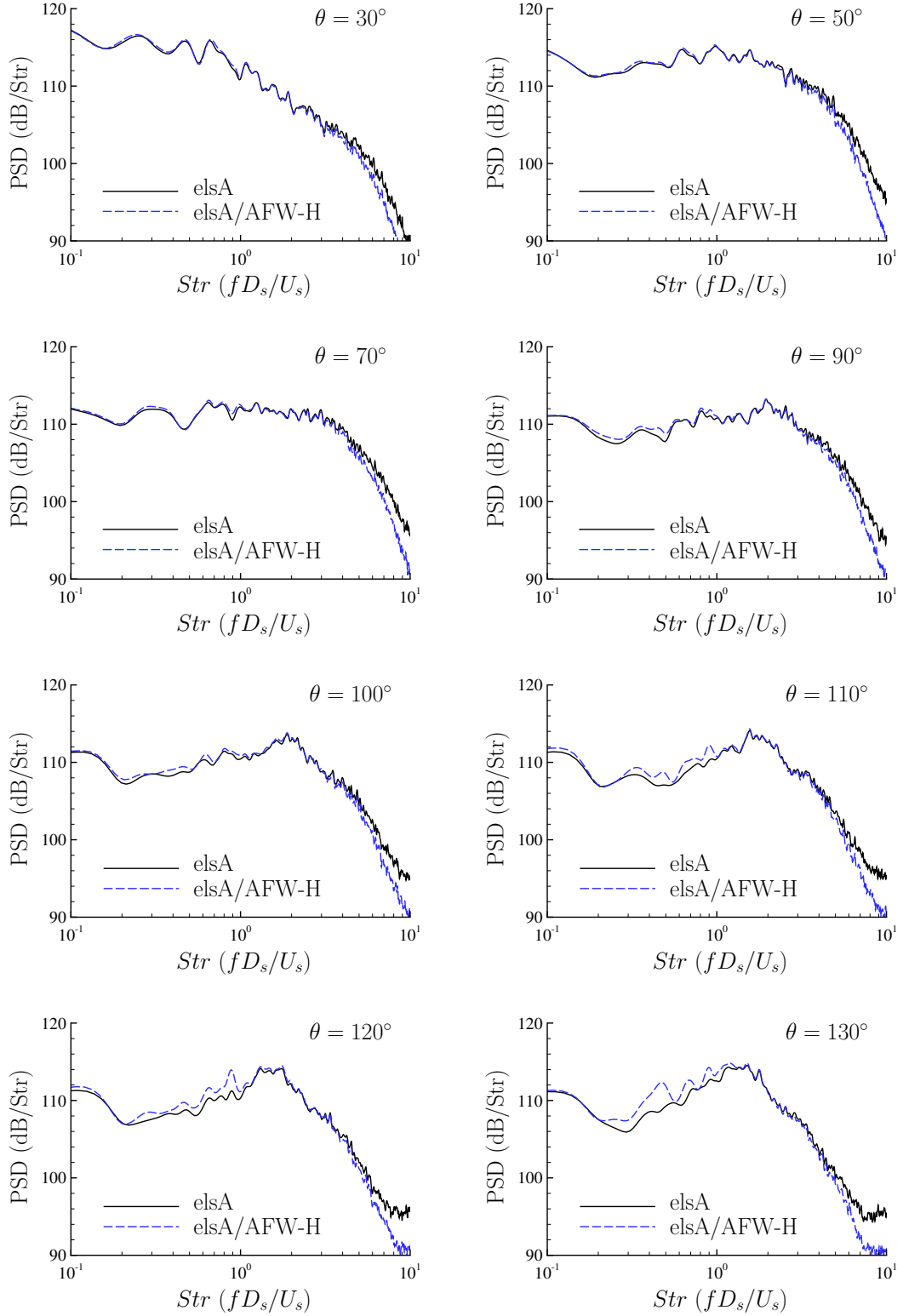


Figure 4.13: Far-field PSD from a dual-stream cold jet with the secondary flow under-expanded ($M_s = 1.0$), modelled by LES [16]. FW-H surface $\mathcal{F}_1 = 0$. $M_{jp} = 0.89$, $M_{js} = 1.20$, $Re_p = 0.57 \times 10^6$, $Re_s = 1.66 \times 10^6$, $r_o = 30.0D_s$ from the coaxial nozzle exit. PSD smoothed as in Figure 4.4(b).

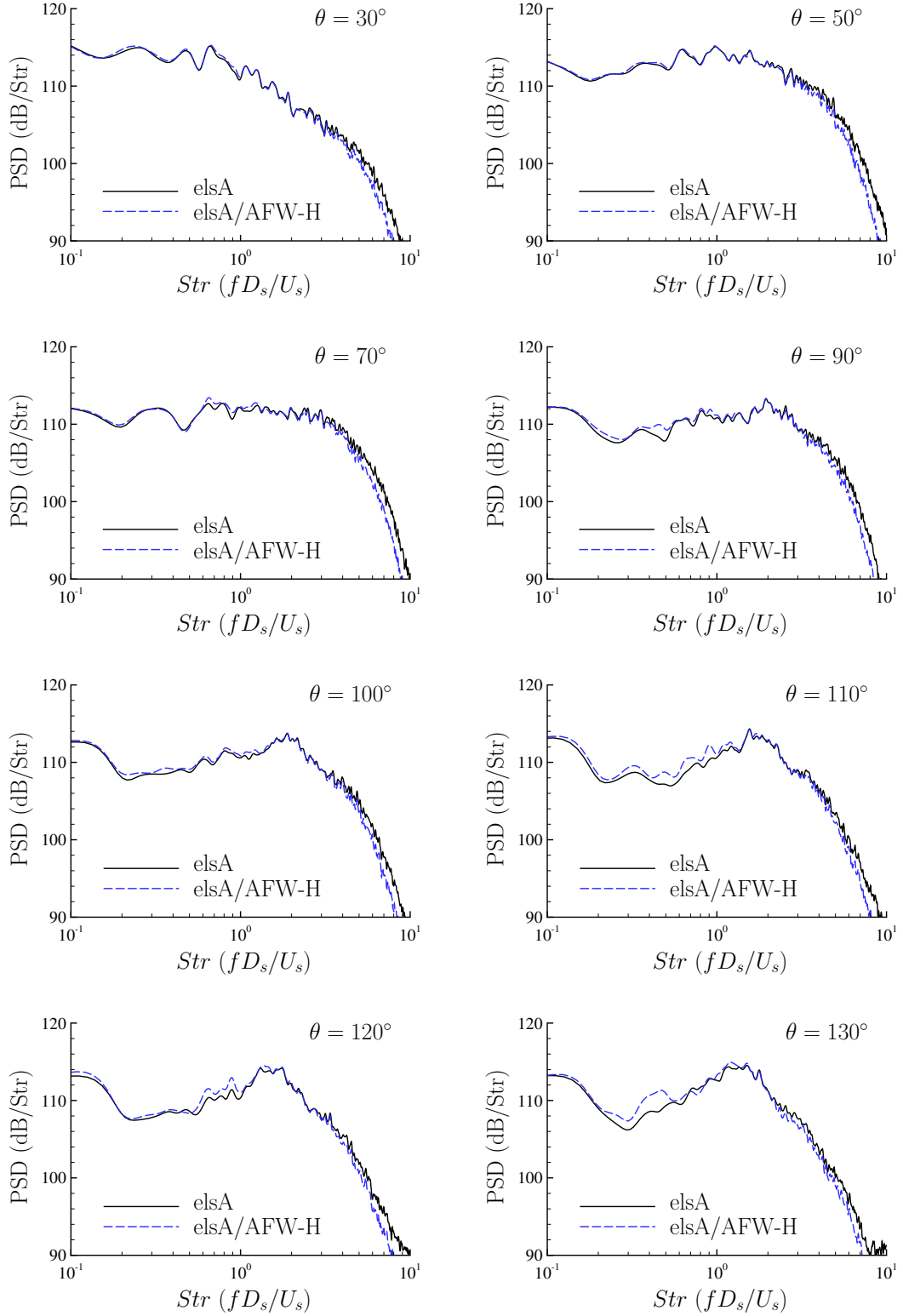


Figure 4.14: Far-field PSD from a dual-stream cold jet with the secondary flow under-expanded ($M_s = 1.0$), modelled by LES [16]. FW-H surface $\mathcal{F}_2 = 0$. $M_{jp} = 0.89$, $M_{js} = 1.20$, $Re_p = 0.57 \times 10^6$, $Re_s = 1.66 \times 10^6$, $r_o = 30.0D_s$ from the coaxial nozzle exit. PSD smoothed as in Figure 4.4(b).

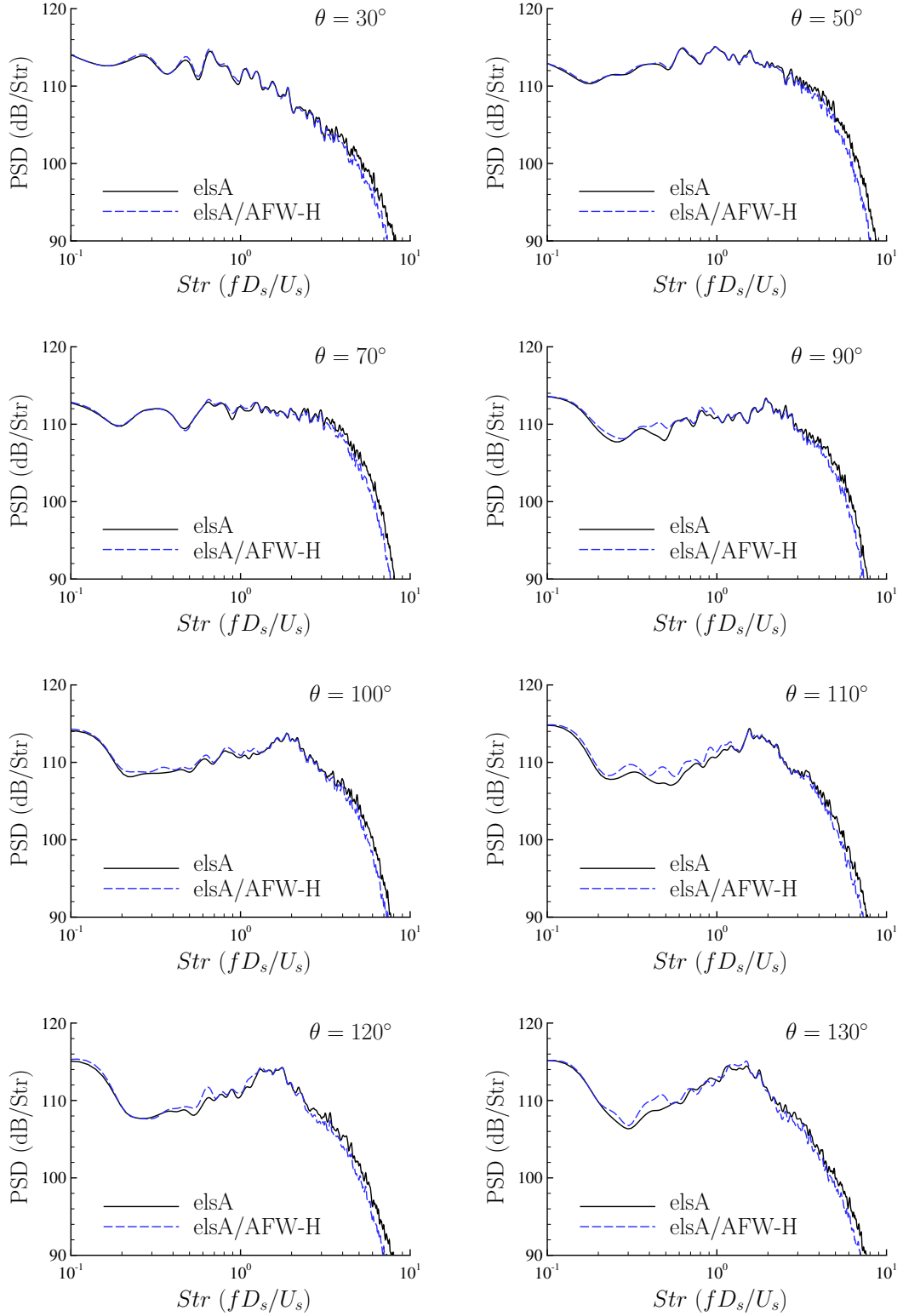


Figure 4.15: Far-field PSD from a dual-stream cold jet with the secondary flow under-expanded ($M_s = 1.0$), modelled by LES [16]. FW-H surface $\mathcal{F}_3 = 0$. $M_{jp} = 0.89$, $M_{js} = 1.20$, $Re_p = 0.57 \times 10^6$, $Re_s = 1.66 \times 10^6$, $r_o = 30.0D_s$ from the coaxial nozzle exit. PSD smoothed as in Figure 4.4(b).

on the Strouhal number range of the BBSAN peaks. The BBSAN noise is most evident between 90° and 130° [16] and the AFW-H tool correctly reproduces the broad peak amplitude and frequency estimated by the reference solution.

As for the single-stream jet in Section 4.1, the agreement between the PSD prediction and the reference solution worsens at higher Strouhal numbers. For the dual-stream jet, this is noticeable above $Str = 5$. The reason for this worsening of the acoustic prediction at $Str \geq 5$ is due to the difference in sampling frequency between the two acoustic simulations. The elsA reference solution is obtained by applying the acoustic analogy at each CFD time step, that is $\Delta\tau_{CAA,elsA} = \Delta\tau_{CFD}$. The AFW-H tool is applied to a database in which the flow field properties are stored every $400\Delta\tau_{CFD}$, that is $\Delta\tau_{CAA,AFW-H} = 400\Delta\tau_{CFD}$. This gives different Nyquist Strouhal numbers and hence different spectral roll-off characteristics at high Strouhal numbers.

The effect of the FW-H surface placement can also be inspected by looking at Figures 4.13– 4.15. As mentioned before, the intermediate surface $\mathcal{F}_2 = 0$ seems to represent a good compromise between placing the surface far enough from the jet to prevent spurious hydrodynamic noise from contaminating the acoustic predictions, and placing it close enough in order to avoid any significant dispersion and dissipation of the acoustic waves travelling towards the surface itself.

Indeed, it can be noticed that Figure 4.14 relating to $\mathcal{F}_2 = 0$ shows a better match between the reference numerical solution elsA and the AFW-H tool prediction, compared to Figure 4.13 relating to $\mathcal{F}_1 = 0$, while minor differences can be appreciated comparing the results from $\mathcal{F}_2 = 0$ and $\mathcal{F}_3 = 0$ (respectively Figures 4.14 and 4.15). Overall, the match is slightly worse at the upstream angles ($110^\circ < \theta < 130^\circ$), over the low frequency range (mostly turbulent mixing noise contribution), while the BBSAN peaks at the same angles are well captured.

Having cross-validated the AFW-H tool prediction against the elsA numerical solution in Figures 4.12– 4.15, a comparison with experimental measurements in the far-field is reported in Figure 4.16. The measurements were taken at the Von Karman Institute for fluid dynamics (VKI), where an ad-hoc facility named FAST (Free jet AeroacouSTic facility) was designed, built and commissioned by Daniel Guariglia. Details about both the facility and the measurements on the dual-stream

jet are given by Guariglia [43].

Whereas the experiment and the numerical simulations targeted the same geometry and running conditions (see Appendix A), small differences in the nozzle geometry due to the elasticity of the rig under pressure were identified in the post-processing of the experimental readings. Choking in the air lines in experiment also prevented testing at exactly the conditions modelled by CFD [43]. Due to the high cost of the LES simulations, further runs better matching the experiment in [43] could not be run within the AeroTraNet2 project [16]. Therefore, the comparison against experiment is herein presented on the basis of this being a comparison of the best matching dataset available to the author.

In Figure 4.16, short-dashed green lines denote the experimental measurements from [43], referred to as “exp VKI”. The AFW-H prediction that is estimated starting from the LES solution on the FW-H surface $\mathcal{F}_2 = 0$ of Table 4.4, obtained at Cerfacs, is shown by the long-dashed blue lines and is referred to as “elsA/AFW-H”. It is the same solution reported in Figures 4.12– 4.15.

The solid-red lines denote a second numerical solution, estimated by the application of the AFW-H solver to the DES database generated at the University of Leicester by Mancini [15], through the Cosmic CFD code. Therefore, this solution is referred to as “Cosmic/AFW-H”. It is worth recalling that acoustic pressure predictions are obtained by a two-stage approach, as explained in Sections 1.5 and 2.1.2. The unsteady flow field prediction on the FW-H integration surface is calculated first by CFD. The acoustic pressure is then computed in the acoustic near-field and far-field by the advanced-time formulation of the FW-H acoustic analogy reported in Section 2.2.3, as implemented in the new AFW-H solver.

Figure 4.16 shows results for 8 values of the radiation angle θ and the BBSAN contribution appears over the range $90^\circ < \theta < 130^\circ$ as a broadband peak centred at $Str \approx 2.0$, raising above the turbulence associated noise, which stretches across the full Strouhal number range. The Strouhal number range of the BBSAN is well captured by the numerical prediction, but the numerical PSD is up to 10 dB louder than the experimental result across a large portion of the BBSAN Strouhal bandwidth.

The author has not arrived to a definite justification for this mismatch, but

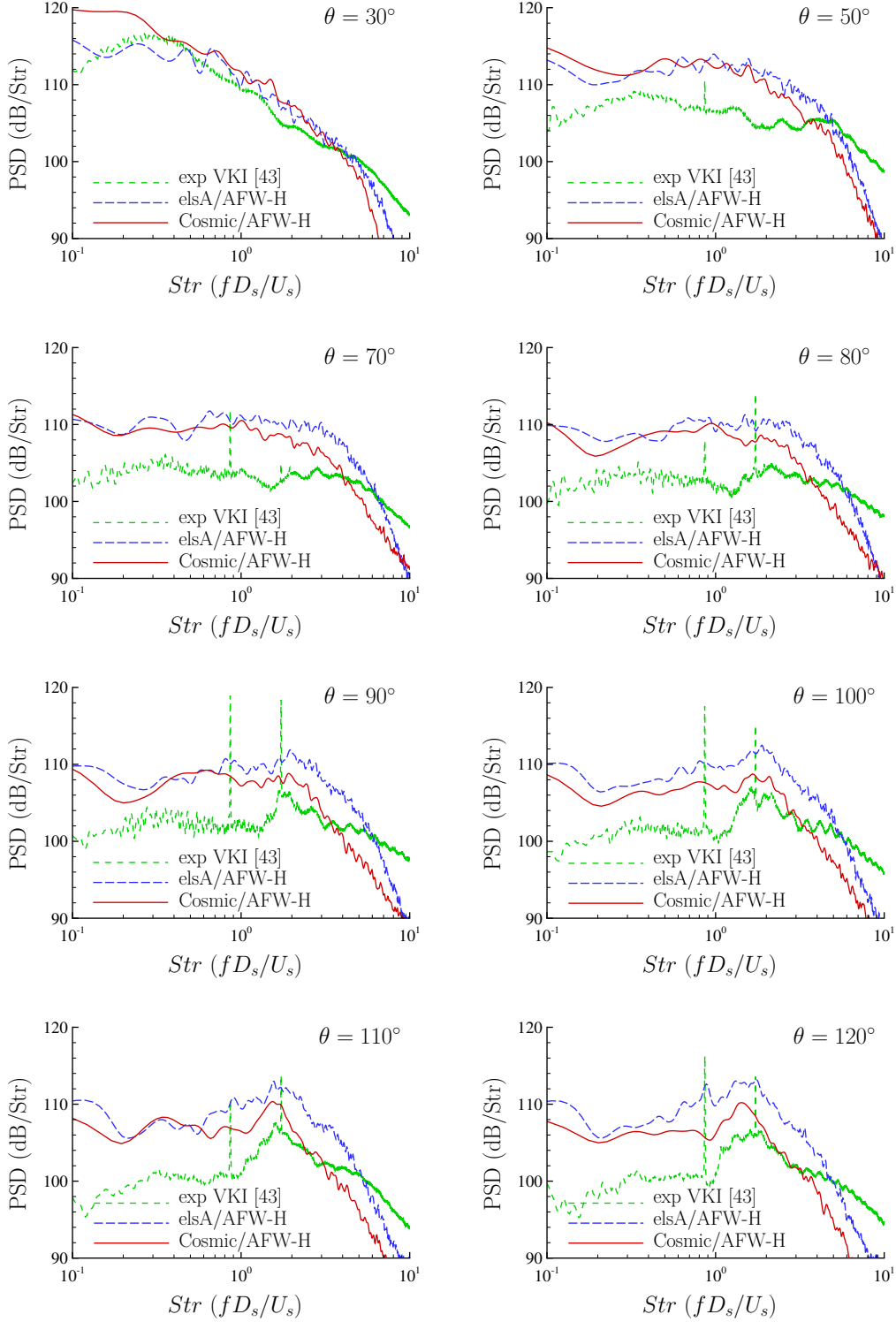


Figure 4.16: Far-field PSD from a dual-stream cold jet with the secondary flow under-expanded ($M_s = 1.0$), compared with far-field experimental measurements by Guariglia [43] at $r_o = 30.0D_s$. FW-H surface $\mathcal{F}_2 = 0$. $M_{jp} = 0.89$, $M_{js} = 1.20$, $Re_p = 0.57 \times 10^6$, $Re_s = 1.66 \times 10^6$. PSD geometrically scaled to $r_{ref} = 40.0D_{eq}$ from the secondary nozzle exit disk centre and smoothed as in Figure 4.4(b).

several hypotheses have been proposed [15, 16, 43]. It is worth highlighting that the new Python AFW-H acoustic analogy code produces results that are consistent with the elsA numerical reference solution in Figures 4.12– 4.15 and that the reason for the 10 dB gap in Figure 4.16 may to be sought in the difference between the CFD and the experimental set-ups that seem to use two slightly different test cases.

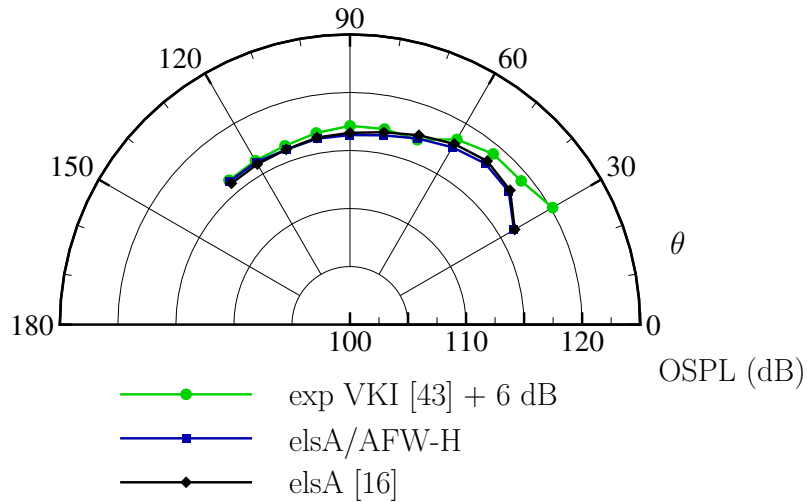


Figure 4.17: Far-field Overall Sound Pressure Level (OSPL) from a dual-stream cold jet with the secondary flow under-expanded ($M_s = 1.0$), modelled by LES [16]. $M_{jp} = 0.89$, $M_{js} = 1.20$, $Re_p = 0.57 \times 10^6$, $Re_s = 1.66 \times 10^6$. OSPL geometrically scaled to $r_{ref} = 40.0D_{eq}$ from the secondary nozzle exit disk centre.

Figure 4.17 represents an attempt to recover the match in noise levels between the numerical prediction and the experiment. Overall Sound Pressure Levels in the far-field are reported, with three curves showing the results from two numerical noise predictions and from the experimental measurements by Guariglia [43], which is denoted by the green circles. The blue squares denote the noise prediction obtained by the elsA/AFW-H method, while the black diamonds show the acoustic prediction obtained through the application of the acoustic analogy implementation in elsA [130], by Pérez [16].

In Figure 4.17, the experimental curve is modified by adding +6 dB at all radiation angles and the match in noise levels between experiment and numerical

simulation is thereby recovered. This +6 dB correction is adopted following Pérez in [16], who used a similar correction to match his numerical PSD prediction to the same measurements by Guariglia [43]. Figure 4.17 suggests that a constant gap between the acoustic numerical prediction and the noise measurements occurs over the range $60^\circ \leq \theta \leq 130^\circ$. In the downstream direction over the range $30^\circ \leq \theta \leq 50^\circ$, Figure 4.17 still shows a mismatch in the noise levels up to 4 dB, despite the +6 dB correction to the experimental result.

In the comparison between acoustic numerical predictions and measurements in Figures 4.16 and 4.17, an important aspect to be considered is that the nozzle manufactured for the FAST facility is smaller by 20% compared to the geometry used for the CFD simulations, which is shown in Figure A.1 in Appendix A. This is due to choking of the air supply lines requiring the use of a smaller nozzle diameter. As the CFD simulation had been run before the completion of the FAST facility, the numerical and the experimental investigations ended up being about different nozzle diameters.

Figures 4.16 and 4.17 attempt to account for this difference by scaling geometrically the sound pressure amplitude to the same distance $r_o = 40.0D_{eq}$ in terms of the respective equivalent jet diameter

$$D_{eq} = \sqrt{\frac{4}{\pi} (A_s + A_p)}, \quad (4.1)$$

where A_s and A_p are the nominal secondary and primary nozzle areas. Using the A_s and A_p values from CFD and from experiment determines respectively $D_{eq,CFD}$ and $D_{eq,exp}$. However, the different geometry could cause differences in the flow field features.

Moreover, with the FAST facility turned on, the elasticity of the pressure vessel led to an axial shift of the secondary nozzle lip in the downstream direction [43], resulting in an increment of the nozzle exit area A_s that needs to be taken into account in the equivalent jet diameter calculation (Equation 4.1). Consequently, the secondary mass flow rate increases and the shock-cell system in the experiment is affected by this modification. The comparison between the CFD and the experiment showed larger shock-cell lengths in the measurements, while the numerical simulation is characterised by a wider shear-layer [16].

Another aspect to be considered is that screech noise is generated in the experiment, as it can be seen from the spectra in Figure 4.16 that display tones at $Str \approx 0.9$ and at $Str \approx 1.8$ that are substantially independent from θ in the upstream arc. The numerical simulation does not predict any tonal noise component at any of the radiation angles considered. All these factors may contribute to the differences in noise levels between predictions and measurements.

It is important to recall that the results obtained independently via the new AFW-H tool developed by the author and via the FW-H analogy implemented in elsA applied to CFD data were similar to the noise levels measured in the FAST facility, for the supersonic under-expanded single-stream jet configuration by André [143].

Besides, the two acoustic numerical predictions for the dual-stream jet, obtained by the new AFW-H tool developed by the author at the University of Leicester and, independently, by the elsA software used at Cerfacs, France, give comparable noise levels in Figure 4.12– 4.15. The dual-stream jet noise levels measured at the VKI are instead lower by up to 10 dB. The reason for this quieter experimental jet could be hidden within the aerodynamics of the measured flow, but for a systematic error in the simulations or in the experiment.

4.2.2 Near-field radiation

In this section, results in the acoustic near-field of the jet are presented in Figure 4.18, in terms of Power Spectral Density (PSD), at observers located on right frusta of cones. The observers are placed at 41 axial locations between the secondary nozzle exit section ($x = -0.4D_s$) and $x = 7.6D_s$. For each axial location, the acoustic PSD is averaged across 16 observers equispaced in the azimuthal direction ϕ , in order to obtain smoother spectra of the acoustic pressure fluctuation (see Section 4.2.1). The number of observers for a single array is therefore $41 \times 16 = 656$.

Figures 4.18(a) and 4.18(b) show the predictions from the observers located along $\alpha = 8^\circ$ radially divergent lines that start respectively from $(x = -0.4D_s; r = 1.5D_s)$ and $(x = -0.4D_s; r = 1.7D_s)$. The PSD is plotted against the normalised axial position x/D_s and the Strouhal number in Figure 4.18. The iso-levels of PSD show the “banana-like” shape typical of SCN in the near-field [16, 147] and they are in good agreement with the prediction by Pérez [16], obtained by a direct computation

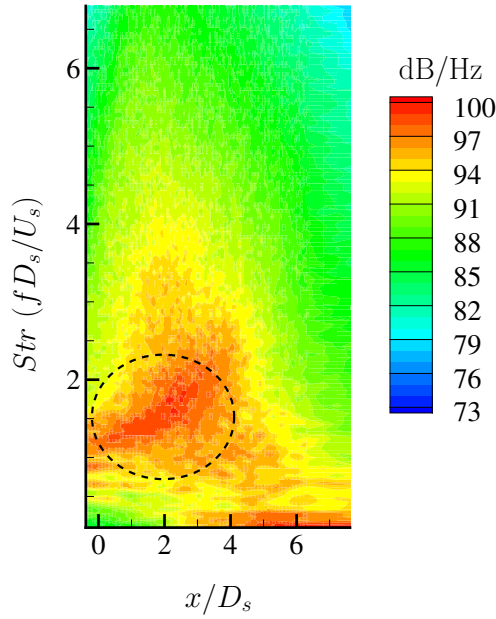
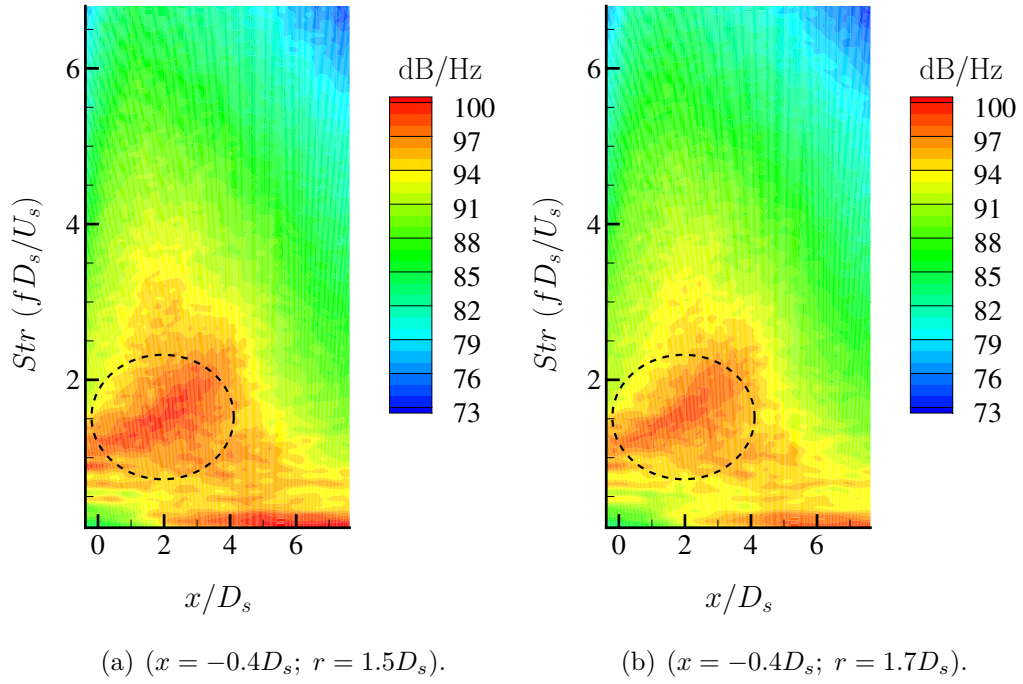


Figure 4.18: Near-field PSD vs Strouhal number (Str) at different x/D_s from a dual-stream jet with the secondary flow under-expanded (Appendix A). FW-H surface $\mathcal{F}_1 = 0$. Linear array of observers diverging by $\alpha = 8.0^\circ$ with respect to the jet axis. The dashed-line circles indicate the “banana-like” shape typical of SCN in the near-field [16, 147]. PSD smoothed as in Figure 4.4(b).

approach (Section 2.1.1), shown in Figure 4.18(c). In Figure 4.18(b) the PSD is predicted to be lower than in Figure 4.18(a), which reports the acoustic prediction from observers located closer to the jet axis.

In summary, with a porous FW-H acoustic analogy approach (see Section 2.2.1), if the volume quadrupole source distribution outside the FW-H surface is assumed to be negligible compared to the monopole and to the dipole source contributions, a good noise prediction is feasible both in the acoustic near-field and in the acoustic far-field, when the integration surface is correctly placed. This means that the surface needs to be positioned in the linear region of the flow, where non-linear hydrodynamic perturbations are negligible [138]. At the same time, the FW-H surface is required to wrap the jet closely enough for any numerical dissipation and dispersion of the acoustic waves travelling to the surface itself to be negligible.

Figure 4.18 shows that, by correctly placing the integration surface in such way, the approximation that originates from neglecting the volume integral contribution outside the surface in the FW-H acoustic analogy theory appears to be reasonable and both near-field and far-field noise can be estimated through this approach.

4.2.3 Jet acoustic source compactness

In this section, the empirical method described by Viswanathan [148, 149] is applied to the dual-stream jet test case of Table 4.3, in order to get the minimum distance in the acoustic far-field that enables the jet to be considered as an acoustically compact source for jet noise measurement purposes. The meaning of this characteristic distance, here referred to as R_f (far-field), is briefly explained in this section, before discussing the results reported in Figures 4.20– 4.24. R_f is an empirical result based on noise estimations by the AFW-H tool and it is not tested against the conditions expressed in Equation 1.3, Section 1.4.

In jets, the centre of the nozzle exit (primary exit for dual-stream jets) is commonly chosen as the origin of the Cartesian reference system, as it is in this chapter. However, the jet is intrinsically a non-compact acoustic source and the noise sources spread across several jet diameters in the downstream direction. For turbulent mixing noise, Lilley [56, 150] shows that the location of the acoustic sources in a jet relates to the axial position of maximum amplitude of the shear layer instabilities, which increases

with the instability wavelength. Therefore, the axial location of the noise source in a given bandwidth is frequency-dependent. It is sometimes possible to use the spectral peak frequency to define the “peak source” axial position when SCN is generated. For instance, for dual-stream jets, the peak source is located at $x \approx 5.0D_{eq}$ [149] in terms of equivalent jet diameters (Equation 4.1).

Therefore, assuming an equivalent point source located at the origin of the reference system for an acoustically non-compact source is inaccurate. The r^{-2} geometric scaling of the acoustic intensity in the far-field is only obtained approximately, within a given tolerance (here taken as 1 dB), beyond a polar distance R_f from the nozzle exit centre. R_f is determined later on in this section. Observers located at $r \geq R_f$ cannot distinguish among the different axial and radial positions of the acoustic sources in the acoustically active portion of the flow and the jet becomes acoustically compact at these distances. An equivalent noise source can thus be assumed to be placed at the centre of the nozzle exit plane, and both acoustic distances and radiation angles can be directly measured from this point.

Viswanathan determined the R_f that gives acoustic source compactness [148] both in single-stream jets [151, 152] and in dual-stream jets [149]. Considering just unheated jets, distances of about $35.0D_e$ and $45.0D_e$ have been found respectively for subsonic and supersonic single-stream jets. In the dual-stream jet configuration, the equivalent diameter (Equation 4.1) is used as a reference length and a shorter distance of about $30.0D_{eq}$ is determined for R_f [149].

The reason for this shorter R_f in dual-stream jets is attributed to the slowly varying Overall Sound Pressure Level (OSPL) with radiation angle θ compared to single-stream jets, where the variation with θ presents stronger gradients in the downstream quadrant [149].

The method applied here for determining R_f empirically consists in comparing the spectral results of two arrays of observers, one axial array at distance d_{sl} from the jet axis, referred to as the sideline array (SL), and an arc of observers at constant distance r_{pol} from the origin of the Cartesian reference system, referred to as the polar array (POL). Both arrays are shown schematically in Figure 4.19.

The two arrays cover 11 radiation angles between 40° and 140° , generating couples of paired observers, one for each radiation angle. Two paired observers have the same

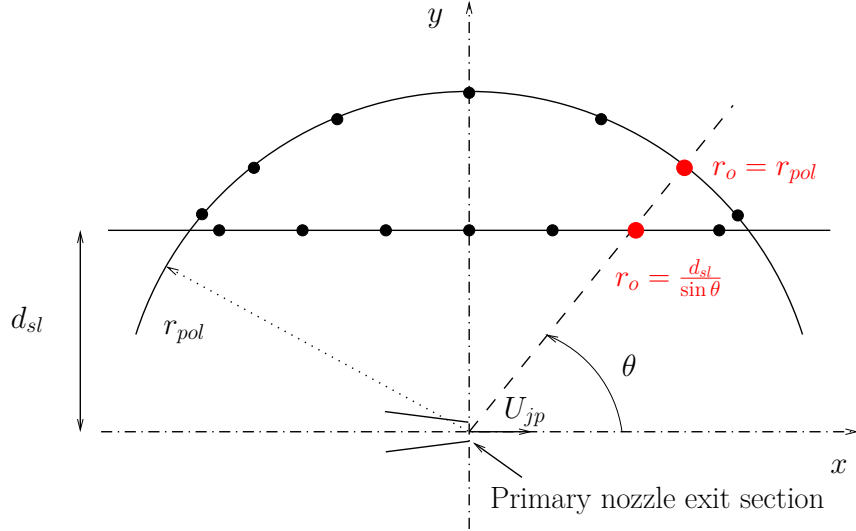


Figure 4.19: Schematic representation of the sideline array, with distance d_{sl} from the jet axis, and of the polar array, with radius r_{pol} .

polar coordinate θ but different distance r_o from the origin, as shown in Figure 4.19. As far as the polar array is concerned, the distance is independent from θ and equal to the radius of the arc ($r_o = r_{pol}$). The radial distance of an observer on the sideline array varies with θ and it reaches a minimum at $\theta = 90^\circ$. Moving along the sideline array away from the nozzle exit section, both in the upstream and in the downstream direction, the distance r_o of the observer from the origin increases, following the relation

$$r_o = \frac{d_{sl}}{\sin \theta} . \quad (4.2)$$

R_f is then found by the following procedure. Once the noise radiation to both arrays is estimated, the resulting PSDs from two corresponding observers are geometrically scaled to the same reference distance r_{ref} in order to allow for a direct comparison between them. If the two scaled PSDs for a specific radiation angle θ match, it can be concluded that the jet is acoustically compact in the θ direction considered. Thus, $R_f = d_{sl} / \sin \theta$. The criterion adopted here is that the two scaled PSDs need to match within a ± 1 dB tolerance over the whole frequency range. If the difference between the two scaled PSDs at the same θ is greater than 1 dB, the sideline array can be moved farther away from the jet axis, till the scaled PSD of the observer on this array in the θ direction matches the scaled PSD of its corresponding counterpart on the polar array, according to the above stated tolerance.

Acoustic results have been produced with the new Python AFW-H tool, on a polar array at $r_{pol} = 45.9D_{eq}$ from the origin of the reference system, and on three sideline arrays. The PSDs, geometrically scaled to $r_{ref} = 40.0D_{eq}$, are reported in Figures 4.20– 4.22.

Figure 4.20 shows the comparison with a sideline array at $d_{sl} = 24.3D_{eq}$, from which it can be inferred that there are no appreciable differences in the scaled PSDs in the directions $\theta \leq 50^\circ$ and $\theta \geq 130^\circ$. At intermediate angles, acoustic source non-compactness effects are clearly visible at the low and at the mid frequency ranges, where the PSDs from the sideline array and from the polar array differ by more than 1 dB. This first test would suggest $R_f \geq 31.7D_{eq}$ both in the upstream and in the downstream directions.

In Figure 4.21, the distance of the sideline array is increased to $d_{sl} = 27.7D_{eq}$ and this improves the agreement among the scaled PSDs from paired observers compared to Figure 4.20. However, the range in which acoustic source non-compactness effects are appreciable is still $60^\circ \leq \theta \leq 120^\circ$, where the PSDs from the sideline array and from the polar array differ by more than 1 dB. This second test suggests $R_f > 32.0D_{eq}$.

The distance of the sideline array is increased again in Figure 4.22 to $d_{sl} = 31.6D_{eq}$. In the upstream direction, the match is really good and the PSDs from the polar array and from the sideline array differ by less than 1 dB. In the downstream quadrant, the match is slightly worse and the PSDs over the range $70^\circ \leq \theta \leq 90^\circ$ do not satisfy the tolerance defined above. This suggests $r_o \approx 33.0D_{eq}$ as the researched value, for which the differences between the PSDs from the sideline array and from the polar array are lower than 1 dB over the whole frequency range. Therefore, $R_f \approx 33.0D_{eq}$ can be considered a reasonable value for the minimum distance that enables the jet to be considered as an acoustically compact source for jet noise measurements purposes.

This result is in agreement with Viswanathan [149], who investigated two jet outflow geometries, obtaining $R_f = 36.0D_{eq}$ and $R_f = 28.0D_{eq}$, respectively for the smaller and the larger nozzle. Furthermore, from Table 4.5, the distance r_o chosen for the far-field array in Section 4.2.1 is $r_o = 30.0D_s = 34.4D_{eq} > R_f$. This confirms that the analysis in Section 4.2.1 is of far-field noise.

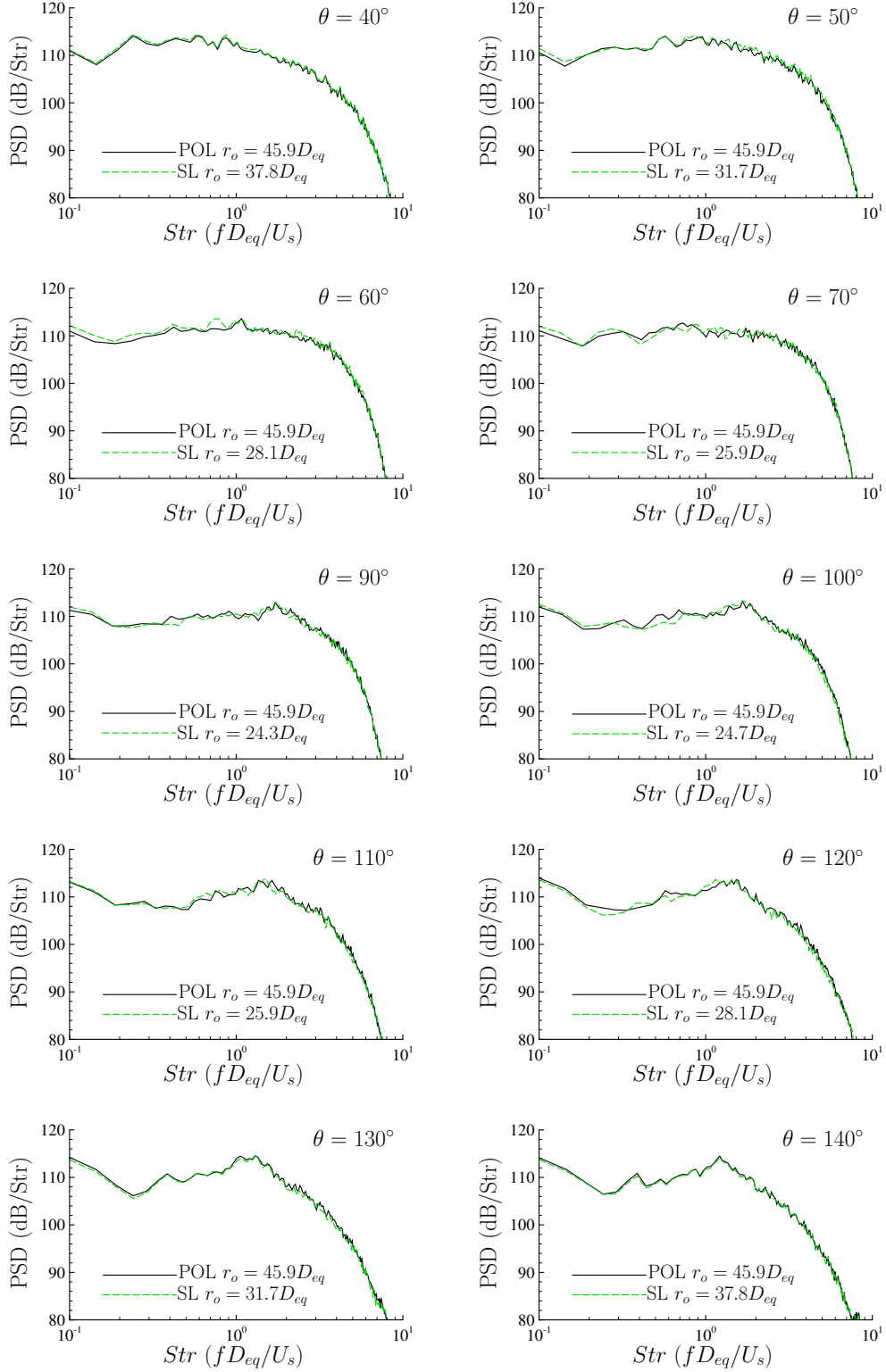


Figure 4.20: PSD comparison between the Polar (POL) and the Sideline (SL) arrays of observers for a dual-stream under-expanded jet (Appendix A). $r_{pol} = 45.9D_{eq}$ (from the origin), $d_{sl} = 24.3D_{eq}$. FW-H surface $\mathcal{F}_3 = 0$. PSD scaled to $r_{ref} = 40.0D_{eq}$ and smoothed as in Figure 4.4(b).

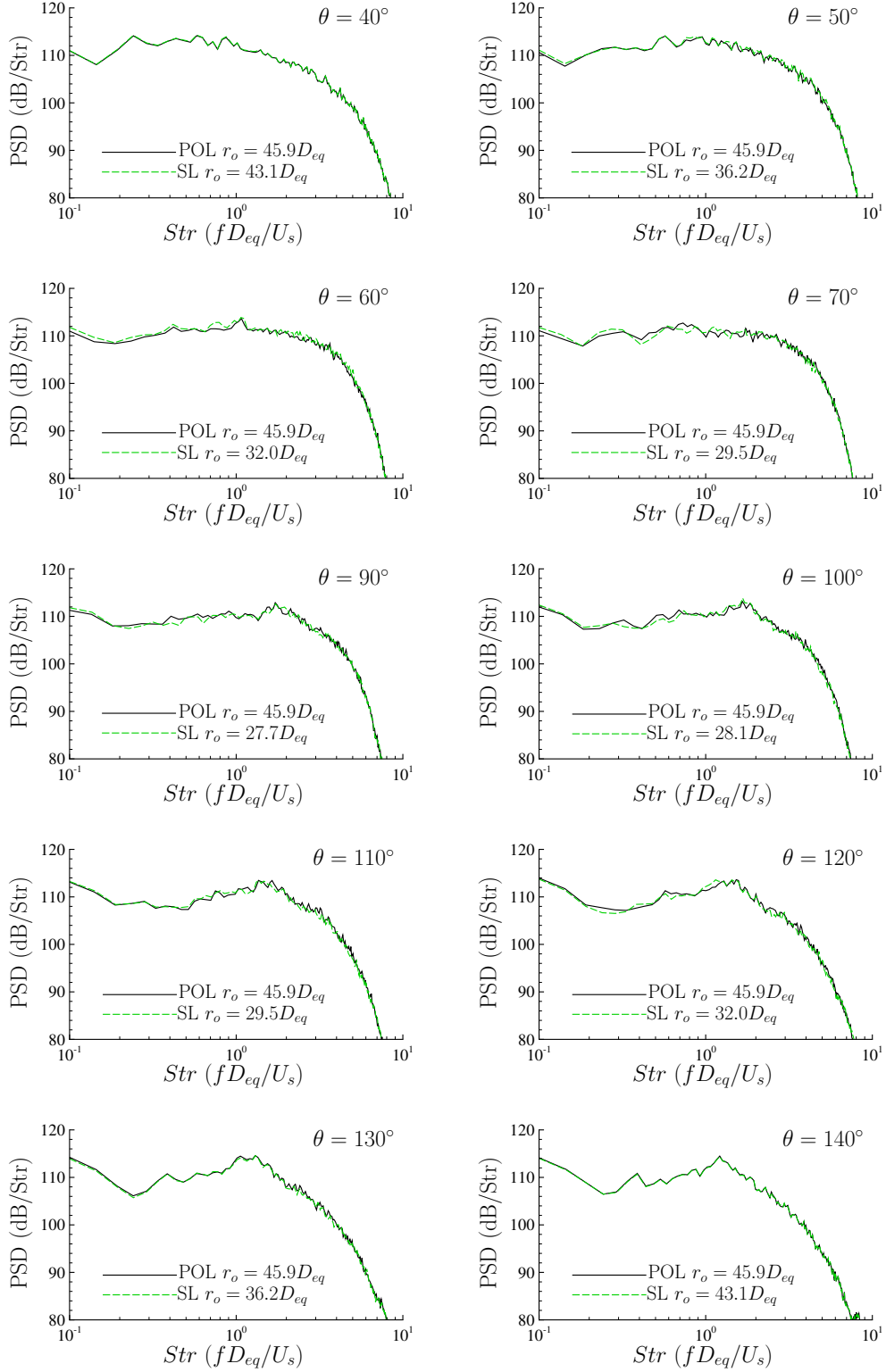


Figure 4.21: PSD comparison between the Polar (POL) and the Sideline (SL) arrays of observers for a dual-stream under-expanded jet (Appendix A). $r_{pol} = 45.9D_{eq}$ (from the origin), $d_{sl} = 27.7D_{eq}$. FW-H surface $\mathcal{F}_3 = 0$. PSD scaled to $r_{ref} = 40.0D_{eq}$ and smoothed as in Figure 4.4(b).

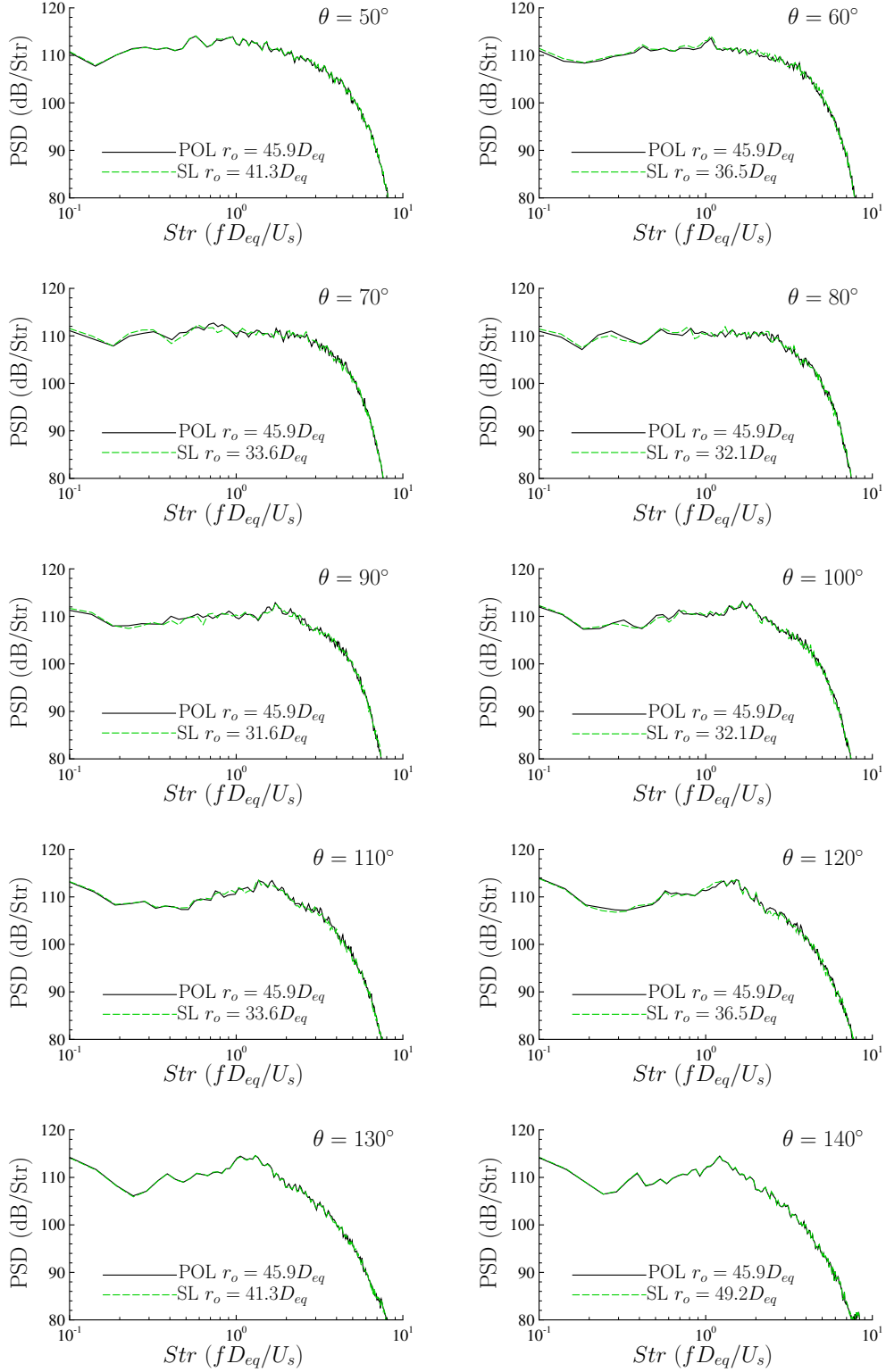


Figure 4.22: PSD comparison between the Polar (POL) and the Sideline (SL) arrays of observers for a dual-stream under-expanded jet (Appendix A). $r_{pol} = 45.9D_{eq}$ (from the origin), $d_{sl} = 31.6D_{eq}$. FW-H surface $\mathcal{F}_3 = 0$. PSD scaled to $r_{ref} = 40.0D_{eq}$ and smoothed as in Figure 4.4(b).

Flow	$D(\text{m})$	$A (\text{m}^2)$	$\sigma(\text{m})$	$D_{eq}(\text{m})$
Primary	0.024	0.43×10^{-3}	0.3×10^{-3}	0.048
Secondary	0.055	1.39×10^{-3}	0.3×10^{-3}	

Table 4.5: Jet outflow geometry and equivalent jet diameter D_{eq} .

Another test has been carried out to identify the axial location of the dominant contributions to jet noise in dual-stream jets, which is reported as $x \approx 5.0D_{eq}$ in the literature [149]. Figures 4.23 and 4.24 are obtained by moving the centre of both the polar and the sideline array to this point $(5.0D_{eq}, 0, 0)$. The radius of the polar array is kept to $45.9D_{eq}$ and two sideline arrays are considered, with distance $d_{sl} = 20.0D_{eq}$ in Figure 4.23, and $d_{sl} = 24.3D_{eq}$ in Figure 4.24.

The results for the shorter distance $d_{sl} = 20.0D_{eq}$ in Figure 4.23 show a good match for angles $\theta \leq 60^\circ$ and $\theta \geq 110^\circ$ in the scaled PSDs from paired observers at the same polar angle, while minor acoustic source non-compactness effects are visible over the range $70^\circ \leq \theta \leq 100^\circ$, where the difference between the PSDs from the polar array and from the sideline array is greater than 1 dB. Moving to the farther sideline array at $d_{sl} = 24.3D_{eq}$ in Figure 4.24, the match is satisfactory for all the radiation angles considered ($40^\circ \leq \theta \leq 140^\circ$), with noise levels differing by less than 1 dB across the whole frequency range.

Figure 4.24 shows a better match in the scaled PSDs from paired observers at the same polar angle compared with Figure 4.20, where the array is centred at the nozzle exit section, for the same distance $d_{sl} = 24.3D_{eq}$ of the sideline array from the jet axis. The farthest arrays at $d_{sl} = 27.7D_{eq}$ and $d_{sl} = 31.6D_{eq}$ for the case with the radiation angle measured from $(5.0D_{eq}, 0, 0)$ are not reported, because the geometrically scaled PSDs from the sideline and from the polar arrays essentially overlap at these distances.

These results confirm that the peak noise source is not located at the nozzle exit section, but farther downstream at $x \approx 5.0D_{eq}$ for dual-stream supersonic cold jets. A far-field minimum distance of $R_f \approx 24.0D_{eq}$ is determined when the centre of the noise radiation is assumed at $x = 5.0D_{eq}$, which is lower than $R_f \approx 33.0D_{eq}$ obtained by setting the acoustic origin at the centre of the nozzle exit area.

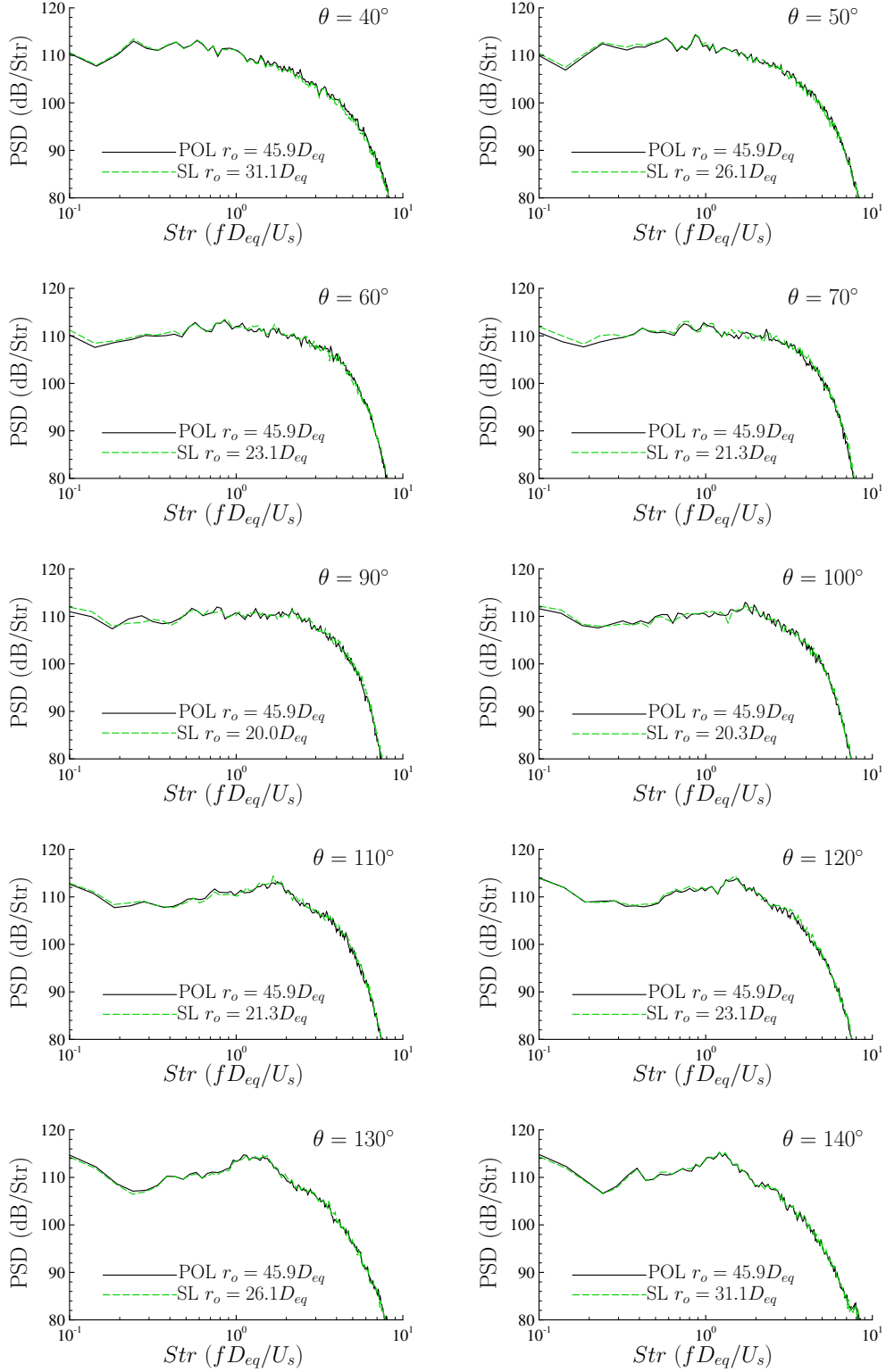


Figure 4.23: PSD comparison between the Polar (POL) and the Sideline (SL) arrays of observers for a dual-stream under-expanded jet. $r_{pol} = 45.9D_{eq}$ from $(5.0D_{eq}, 0, 0)$, $d_{sl} = 20.0D_{eq}$. FW-H surface $\mathcal{F}_3 = 0$. PSD scaled to $r_{ref} = 40.0D_{eq}$ and smoothed as in Figure 4.4(b).

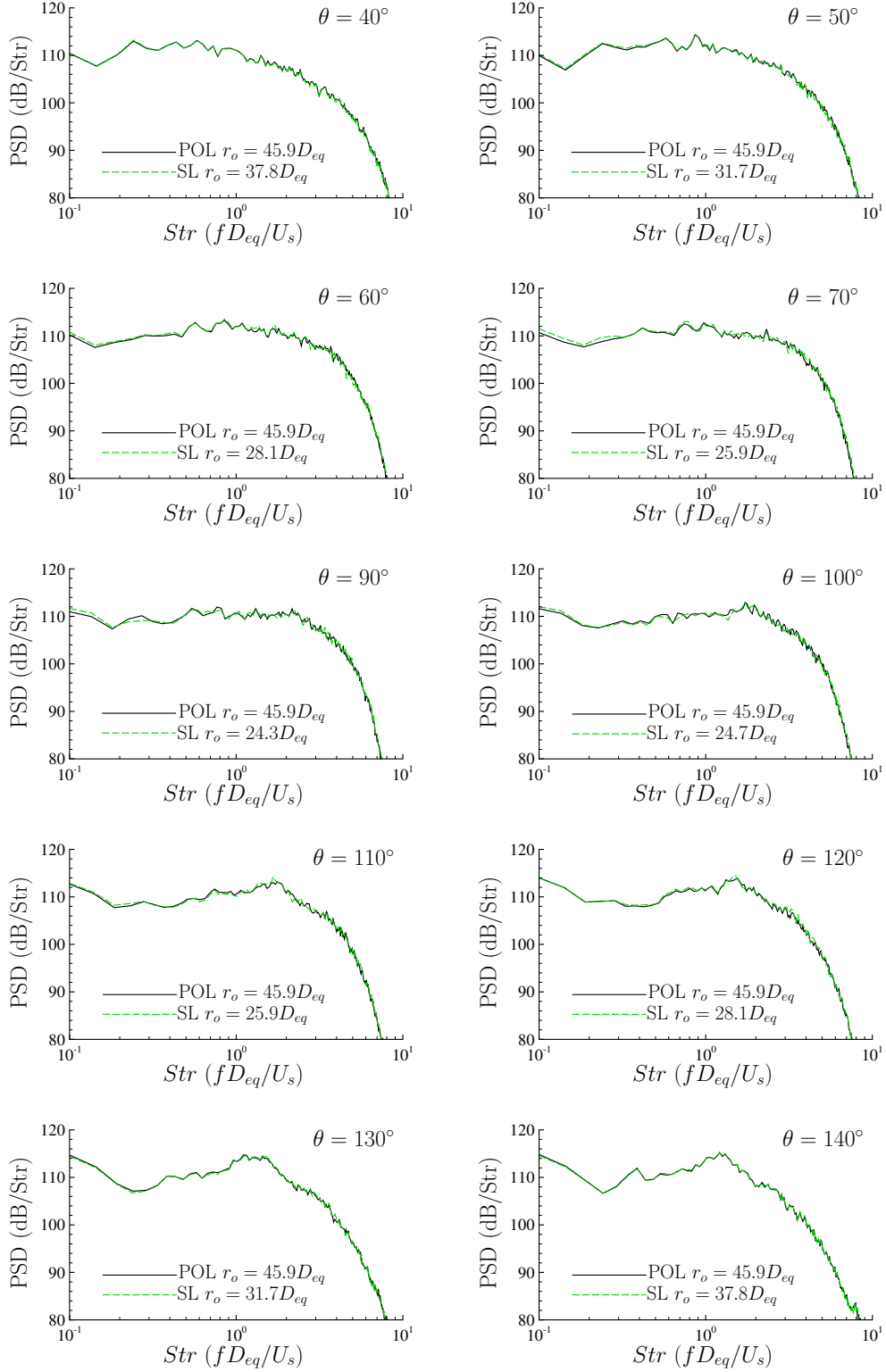


Figure 4.24: PSD comparison between the Polar (POL) and the Sideline (SL) arrays of observers for a dual-stream under-expanded jet. $r_{pol} = 45.9D_{eq}$ from $(5.0D_{eq}, 0, 0)$, $d_{sl} = 24.3D_{eq}$. FW-H surface $\mathcal{F}_3 = 0$. PSD scaled to $r_{ref} = 40.0D_{eq}$ and smoothed as in Figure 4.4(b).

As a practical conclusion, the distance $R_f \approx 33.0D_{eq}$ can be taken as the lower limit of the acoustic far-field in order to approximate the jet noise sources with an equivalent point source placed at the origin of the reference system, coinciding with the centre of the primary nozzle exit area for dual-stream cold jets, to within 1 dB of the true far-field value.

4.3 Chapter 4 summary

The AFW-H tool has been applied, as a post-processor, to previously stored time-resolved CFD predictions of single-stream jets, both subsonic (Section 4.1.1) and supersonic (Section 4.1.2), and of a dual-stream under-expanded jet (Section 4.2). LES and DES results, obtained respectively at Cerfacs, by the high-order CFD code elsA [130] and at the University of Leicester, by the second-order CFD code Cosmic, have been used. The numerical prediction by the AFW-H tool has been compared against both numerical reference solutions in Section 4.1.1 and against experimental measurements by André [143] and by Guariglia [43] in Sections 4.1.2 and 4.2.

The acoustic analogy AFW-H tool was able to correctly capture the main noise features of both single and dual-stream jets, in terms of acoustic pressure fluctuation amplitude and directivity. The comparison with both the numerical reference predictions and the experimental measurements showed a good overall match. The differences with the experimental measurements in Sections 4.1.2 and 4.2 can be attributed to differences between the CFD and the experimental set-ups. These results build confidence in the application of the AFW-H tool to extracting the aerodynamic noise generated by unsteady turbulent jets, also in the presence of shocks.

The AFW-H tool was also extremely efficient from a computational point of view. For instance, by considering the Cosmic/AFW-H method of Section 4.2.1, the AFW-H tool was used to post-process the CFD database, consisting of 1600 time steps of the flow field time-history on the integration surface. The FW-H surface was discretised by 271872 cells across 364 zones and the acoustic simulation whole time was about half an hour on 128 cores. By comparison, the 2nd order CFD code Cosmic was run on 1824 processors with a computational domain of 226

million cells. The CFD simulation was run for 800 thousands iterations, excluding the initialization phase, with an averaged time per iteration of 0.6321 s [15]. The resulting computational cost of the acoustic simulation was only 0.02% of the DES simulation.

Chapter 5

Noise radiation in a uniformly moving medium

In this chapter, the CFW-H formulation described in Section 2.2.4 is used to determine the acoustic pressure radiated from elementary sources in Section 5.1 and from an under-expanded single-stream jet in Section 5.2. The point source tests aim to validate the CFW-H code on noise radiation from elementary sources in a uniform flow. The noise sources considered herein are a monopole (Section 5.1.1) and a dipole (Section 5.1.2) of the same type studied respectively in Sections 3.1.1 and 3.1.2. The difference is in the state of the medium in which the generated noise propagates. Whereas in Chapter 3 all the elementary sources were radiating in a medium at rest, in Section 5.1 a uniform flow parallel to one of the coordinate axes is considered and the effects of the uniformly moving medium on the noise radiation are evaluated.

Section 5.2 reports an application to an under-expanded jet issuing from the same nozzle geometry at the same nozzle exit conditions as the test case analysed in Section 4.1.2, with the addition of an external flow moving at constant velocity U_0 in the jet direction. Due to the convergent shape of the axisymmetric nozzle, the flow at the nozzle exit is under-expanded and the jet is characterised by the presence of a shock-cell system. The latter generates a BBSAN contribution to the jet noise.

The U_0 external flow aims to model a jet in flight, even if the low Mach number $M_0 = 0.39$ of the external flow and the cold jet outflow make this configuration different than the jet conditions for cruise of contemporary subsonic wide-body civil aircraft. Still, the $M_0 = 0.39$ external flow enables to investigate the forward

flight effects both on the mixing noise and on the BBSAN contributions from the application of the convective acoustic analogy, by comparing the predictions with the corresponding ones for the static jet reported in Section 4.1.2.

The CFW-H formulation is also tested for the stationary case ($M_0 = 0$) and the results are reported in Appendix D. Beyond representing a preliminary validation, Appendix D shows that, since the AFW-H formulation (Equations 2.21 and 2.22) is a special case of the CFW-H formulation (Equations 2.37 and 2.38), by replacing $M_0 = 0$ in the convective acoustic analogy, the results from the AFW-H and from the CFW-H codes for $M_0 = 0$ coincide. Specifically, Appendix D shows this for the numerical noise prediction in a medium at rest, both for elementary noise sources and for noise generated aerodynamically by jets.

5.1 Noise radiation from elementary sources in a uniform flow

The first application to noise propagation in a moving medium is presented in this section. Both an omnidirectional source (monopole) and a directive source (dipole) are investigated, respectively in Sections 5.1.1 and 5.1.2. The sources are located at the origin of the reference system and the integration surface and the observers are laid out as sketched in Figure 3.1. A uniform flow with constant velocity U_0 in the positive x_1 -axis direction is imposed. Different simulations with different values of U_0 cover the Mach number range from low subsonic ($M_0 = 0.2$) to high subsonic ($M_0 = 0.85$). The choice of the flow direction is convenient in terms of the calculations, but it is not prescriptive.

5.1.1 Monopole acoustic source in a uniform flow

The analytical solution for a monopole acoustic source radiating in a uniform flow in the x_1 -axis direction is given by Lockard [153], in the form of a convective derivative of a harmonic velocity potential (see also Dowling & Ffowcs Williams [154]). From this, the acoustic pressure fluctuation is obtained analytically as

$$p'(\mathbf{x}, t) = \frac{B^{(c)}}{(kR^*)} \left\{ \frac{[SB_{\cos}]}{(kR^*)} \cos(\omega t - kR) + [SB_{\sin}] \sin(\omega t - kR) \right\}, \quad (5.1)$$

where

$$B^{(c)} = \frac{\rho_0 c_0 A k^2}{4\pi}, \quad (5.2)$$

$$SB_{\cos} = M_0 \frac{x_1 - y_1}{R^*}, \quad (5.3)$$

$$SB_{\sin} = 1 - M_0 \left(\frac{-M_0 + \frac{x_1 - y_1}{R^*}}{\beta^2} \right). \quad (5.4)$$

The monopole of Equation 5.1 is a volume velocity source [155], obtained by using the harmonic velocity potential as acoustic variable.

It is worth recalling the meaning of some of the terms in Equations 5.1– 5.4. Vectors \mathbf{x} and \mathbf{y} respectively refer to the observer position and to the source position. k is the wave number and ω the angular frequency of the acoustic waves generated by the omnidirectional source. M_0 , ρ_0 , and c_0 are the Mach number, the density and the sound speed of the moving medium.

The distances R and R^* are defined in Section 2.2.4 and in Appendix C, respectively by Equations 2.29 and 2.30, and they represent the convective counterparts of the source-observer scaling distance $r = |\mathbf{x} - \mathbf{y}|$. R is the source-observer distance at the sound emission time as sketched in Figure C.1, while R^* determines the decay of the acoustic pressure fluctuation p' amplitude with propagation distance from the source (as defined in Appendix C). Finally, β is related to M_0 through Equation 2.31 (Section 2.2.4), and A is a parameter used to define the noise source strength, in m^3s^{-1} .

Figure 5.1 compares the monopole source directivity obtained by the application of the CFW-H acoustic analogy, shown by the blue squares, against the reference analytical solution of Equation 5.1, shown by the solid-black lines, for different values of the convection Mach number M_0 of the moving medium. The solid-red lines show the directivity of a monopole source with the same acoustic power radiating in a medium at rest ($M_0 = 0$).

In all the tests reported in Figure 5.1, the FW-H surface is a cube with side $a = 2\ell = 1$ m. The shape of the integration surface was found not to affect the accuracy of the solution in tests not reported here, for brevity. The frequency of the acoustic waves is fixed to $f = 5$ Hz ($\lambda/a = 68$) and the monopole acoustic source strength to $A = 1$ m^3s^{-1} .

Two acoustic distances source-observer are considered, which are $r = r_o = 5$ m

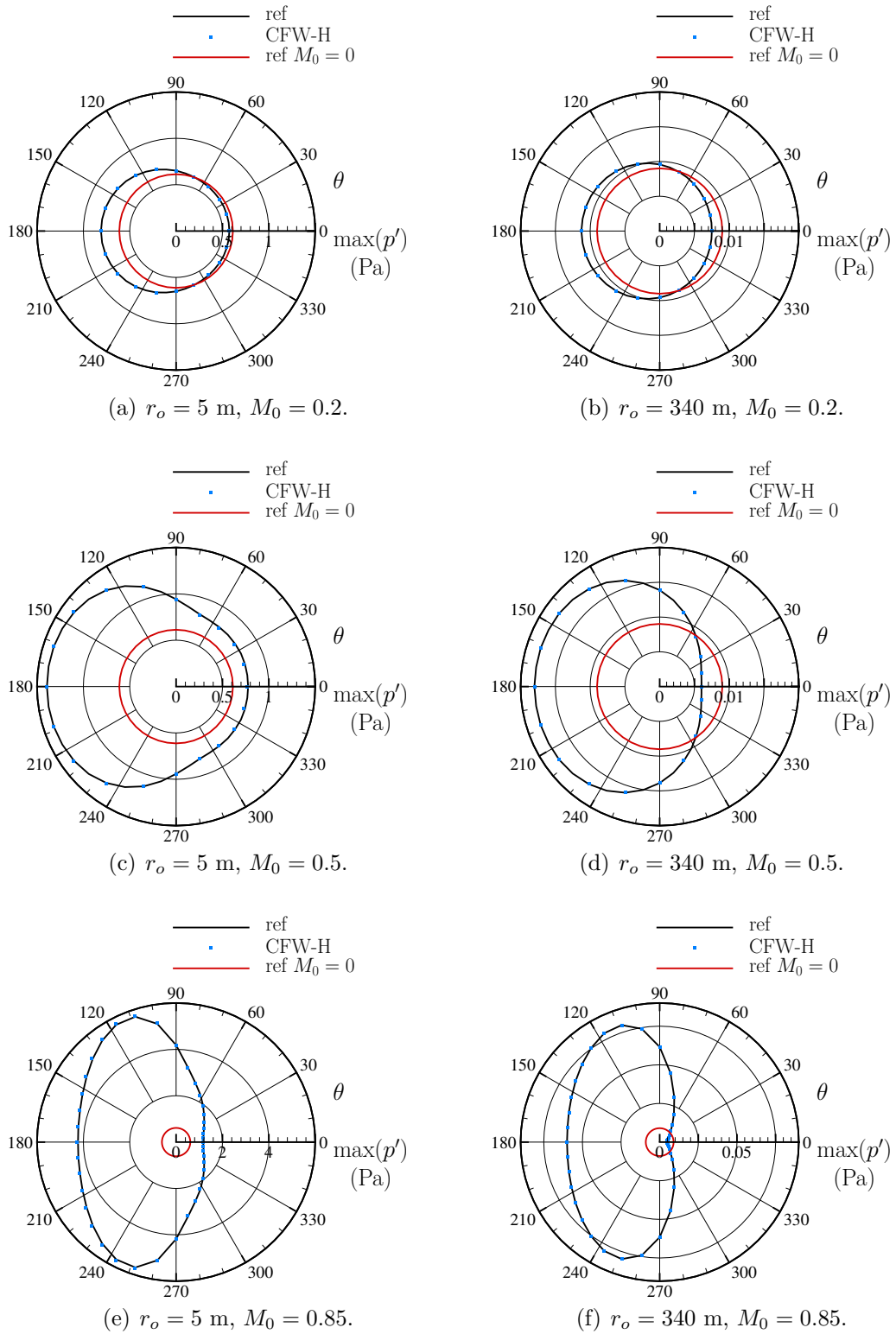


Figure 5.1: Radiation in a medium uniformly moving in the x_1 -axis direction, from an acoustic monopole source located at the origin. Prismatic FW-H surface with $a = 2\ell = 1$ m (see Figure 3.1). Source frequency $f = 5$ Hz, and source strength $A = 1 \text{ m}^3\text{s}^{-1}$.

and $r = r_o = 340$ m. Predictions are obtained for three different values of Mach number M_0 of the uniform medium in which the monopole radiates. Figures 5.1(a) and 5.1(b) show a low subsonic convection simulation at $M_0 = 0.2$. In Figures 5.1(c) and 5.1(d), the Mach number of the uniform medium is increased to $M_0 = 0.5$. In Figures 5.1(e) and 5.1(f), the Mach number of the uniform medium is further increased to $M_0 = 0.85$.

Figures 5.1(a)– 5.1(f) show the $x_3 = 0$ plane and the uniform medium moves horizontally from left to right along the x_1 -axis. The effect of the mean flow on the monopole source radiation is mainly to increase to a value higher than unity the ratio between the upstream and the downstream noise radiation amplitude. This causes the directivity pattern to lose its symmetry with respect to the x_2 -axis, which is orthogonal to the mean flow direction, compared to the red line M_0 analytical solution. This effect strengthens with increasing uniform flow Mach number M_0 , both at $r = r_o = 5$ m (Figure 5.1 on the left), and at $r = r_o = 340$ m (Figure 5.1 on the right). The symmetry of the monopole noise directivity about the x_1 -axis is unaffected by the U_0 uniform flow.

Figure 5.1 also shows that the presence of the uniform flow affects the direction of maximum noise radiation. Table 5.1 reports the angular positions and the intensities of the noise peak for the three cases considered in Figure 5.1, and for two additional values of the uniform flow Mach number M_0 , that are $M_0 = 0.55$ and $M_0 = 0.6$. From Table 5.1, it can be inferred that the noise peak is at $\theta = 180^\circ$, for $M_0 \leq 0.55$. For $M_0 = 0.6$, two peak noise radiation directions occur, at $\theta \approx 145^\circ$ and at $\theta \approx 215^\circ$, placed symmetrically about the x_1 -axis. Increasing further M_0 , the noise peaks bend towards the x_2 -axis, reaching $\theta \approx 110^\circ$ and $\theta \approx 250^\circ$ for the high subsonic Mach number $M_0 = 0.85$, as shown by Figures 5.1(e) and 5.1(f).

The shape of the monopole acoustic source directivity is significantly modified by the mean flow of $M_0 = 0.85$, generating a cardioid pattern aligned in the x_1 -axis direction but compressed in x_1 . The cardioid minimum is at $\theta = 0^\circ$, where the pressure fluctuation amplitude assumes its lowest value.

It is worth noting that the polar axes in Figures 5.1(e) and 5.1(f), pertaining to the $M_0 = 0.85$ results, have a different scale compared to Figures 5.1(a)– 5.1(d). This is because the convective amplification due to the moving medium is large and the

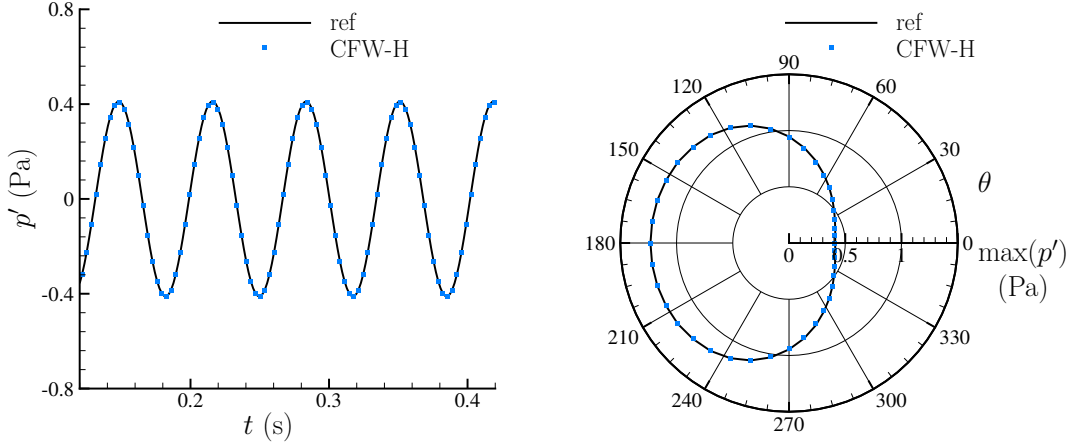
$r_o(\text{m})$	M_0	θ_{peak}	\bar{p}'_{peak}
5	0.2	180°	1.32
	0.5	180°	2.29
	0.55	180°	2.54
	0.6	180° ± 35°	2.86
	0.85	180° ± 70°	9.28
340	0.2	180°	1.25
	0.5	180°	2.00
	0.55	180°	2.23
	0.6	180° ± 35°	2.54
	0.85	180° ± 70°	8.84

Table 5.1: Amplitude of the noise radiation directivity peaks from a monopole source, normalised by the peak amplitude of the noise radiated from the same monopole in a medium at rest, at $M_0 = 0$.

noise peak intensity increases significantly compared not only to the stationary case $M_0 = 0$, but also to the low and to the intermediate Mach number cases ($M_0 = 0.2$ and $M_0 = 0.5$). This aspect is confirmed in Table 5.1 that reports the values of the pressure fluctuation amplitude in the direction of the maximum noise radiation, normalised by the corresponding value in the absence of a mean flow ($M_0 = 0$). At $M_0 = 0.85$, the peak pressure fluctuation amplitudes are reported to be almost one order of magnitude above the omnidirectional pressure fluctuation amplitude at $M_0 = 0$.

All these features are correctly reproduced in the acoustic fields obtained from the CFW-H acoustic analogy implemented in Python, which match the reference analytical solution very closely, for the directivity at all the six different conditions of Figures 5.1(a)– 5.1(f). The match is slightly worse for the ($r_o = 5$ m; $M_0 = 0.85$) case, where the distance of the observers from the FW-H surface is relatively small and the convective effects are strong. Najafi-Yazdi *et al.* [55] suggested that the match can be improved by increasing the spatial resolution of the FW-H surface.

Another test is presented in Figure 5.2, which reports the acoustic directivity pattern and the acoustic pressure fluctuation at $\theta = 0^\circ$ radiated by the monopole



(a) Pressure fluctuation at $(50, 0, 0)$ m, $\theta = 0^\circ$.

(b) Directivity pattern.

Figure 5.2: Radiation in a medium uniformly moving with $M_0 = 0.5$ in the x_1 -axis direction, from an acoustic monopole source located at the origin. Prismatic FW-H surface with $a = 2\ell = 10$ m (see Figure 3.1). Source frequency $f = 14.8$ Hz, and source strength $A = 3.4 \text{ m}^3\text{s}^{-1}$. Distance source-observers $r_o = 50$ m.

source in a uniformly moving medium, obtained with different parameters with respect to Figure 5.1. The parameters are equivalent to a test run by Lockard [153] and they are summarised in the figure caption. The match between the analytical and the numerical solution is again good, and the CFW-H prediction correctly captures the changes in the acoustic pressure with respect to time t and radiation angle θ .

The CFW-H results for the monopole radiation in a uniform flow presented in Figures 5.1 and 5.2 are very satisfactory and they agree with the previous results by Lockard [153] and by Najafi-Yazdi *et al.* [55].

5.1.2 Dipole acoustic source in a uniform flow

In this section, a directional source of dipole type radiating in a uniform flow is considered. The noise radiation, given in terms of the acoustic pressure fluctuation, is

$$p'(\mathbf{x}, t) = \frac{B^{(c)}k}{(kR^*)} \frac{x_2 - y_2}{R^*} \left\{ [SB_{\cos}] \cos(\omega t - kR) + \frac{[SB_{\sin}]}{(kR^*)} \sin(\omega t - kR) \right\}, \quad (5.5)$$

where

$$SB_{\cos} = -1 + \frac{M_0}{\beta^2} \left(\frac{x_1 - y_1}{R^*} - M_0 \right) - 3M_0\beta^2 \frac{x_1 - y_1}{R^*} \frac{1}{(kR^*)^2}, \quad (5.6)$$

$$SB_{\sin} = -\beta^2 + M_0 \left(3 \frac{x_1 - y_1}{R^*} - M_0 \right). \quad (5.7)$$

Equation 5.5 is obtained similarly to Equation 5.1 from the convective derivative of the corresponding velocity potential, which is given in [55]. This velocity potential is the same as the one used to get Equation 5.1 for the monopole point source radiating in a uniform flow, but for a spatial derivative taken in the direction of the dipole orientation. The latter is chosen to coincide with the x_2 -axis. Therefore, Equation 5.5 represents a volume-velocity dipole [155]. All the variables in Equation 5.5 are defined in Section 2.2.4 and in Appendix C.

The dipole source is located at the centre of the Cartesian reference system of Figure 3.1 and it radiates in a medium that is moving at constant velocity in the positive x_1 -axis direction. The FW-H integration surface and the layout of the observers are defined in Figure 3.1. Acoustic directivity patterns are reported in Figure 5.3, for the same mean flow Mach numbers ($M_0 = 0.2$, $M_0 = 0.5$, and $M_0 = 0.85$), and for the same distances ($r_o = 5$ m and $r_o = 340$ m) considered in Section 5.1.1. Solid-black lines denote the analytical solution from Equation 5.5 and blue squares denote the CFW-H acoustic analogy prediction. Besides, the analytical solution for the configuration with the medium at rest is shown by the solid-red lines. Figure 5.3 shows the acoustic pressure fluctuation directivity on the $x_3 = 0$ plane, on which the uniform flow moves from left to right.

As for the monopole source of Section 5.1.1, the mean flow convection has the effect of strengthening the noise intensity in the upstream direction. However, this effect is mainly noticeable in the noise radiation at $r = r_o = 340$ m, in Figures 5.3(b), 5.3(d), and 5.3(f). At this distance, the direction of the maximum noise radiation bends towards forward angles in the presence of a mean flow. This effect is amplified as the mean flow Mach number is stepped up from $M_0 = 0.2$ in Figure 5.3(b), to $M_0 = 0.5$ in Figure 5.3(d). Figure 5.3(f) shows that, at $M_0 = 0.85$, the noise peak bends back towards aft angles, so inverting the trend compared to the results at $M_0 = 0.5$.

The predicted noise directivity at $r = r_o = 340$ m from the source in Figures 5.3(b), 5.3(d), and 5.3(f), shows that the two lobes of the dipole directivity progressively narrow as the uniform convection Mach number of the moving medium increases. The radiation maximum in each lobe also increases. The noise directivity peaks, normalized by the corresponding value for the $M_0 = 0$ case, are listed in

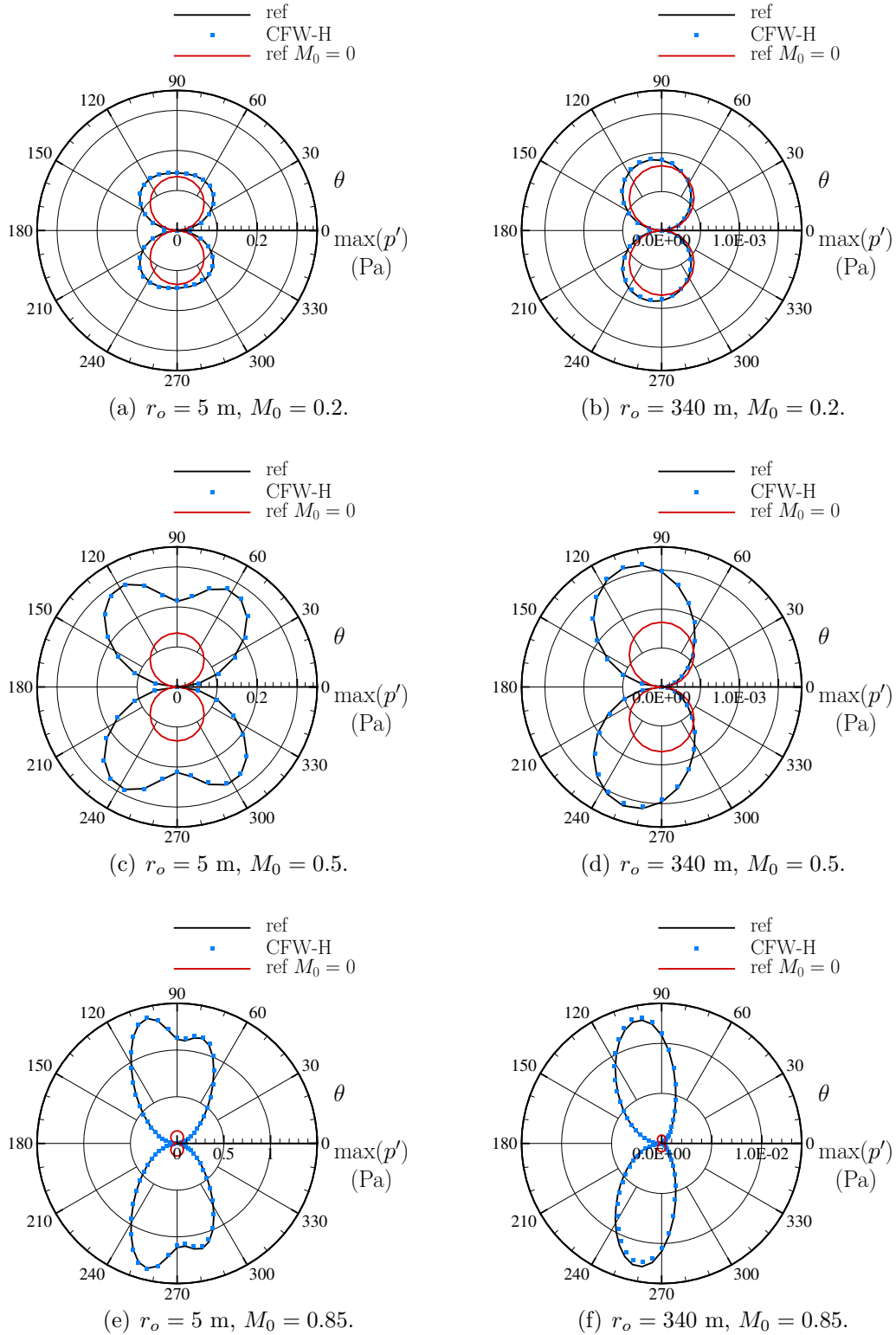


Figure 5.3: Radiation in a medium uniformly moving in the x_1 -axis direction, from an acoustic dipole source located at the origin. Prismatic FW-H surface with $a = 2\ell = 1$ m (see Figure 3.1). Source frequency $f = 5$ Hz, and source strength $A = 1 \text{ m}^4\text{s}^{-1}$. $N_T = 40$ points per period.

Table 5.2. Table 5.2 shows a monotonic increase in the acoustic pressure fluctuation amplitude with M_0 . As in Section 5.1.1, at $M_0 = 0.85$ this amplification reaches about one order of magnitude above the baseline $M_0 = 0$.

$r_o(\text{m})$	M_0	θ_{peak}	\bar{p}'_{peak}
5	0.2	$180^\circ \pm 70^\circ$	1.09
	0.5	$180^\circ \pm 60^\circ$	2.13
	0.85	$180^\circ \pm 76^\circ$	9.91
340	0.2	$180^\circ \pm 80^\circ$	1.11
	0.5	$180^\circ \pm 72^\circ$	1.93
	0.85	$180^\circ \pm 78^\circ$	14.97

Table 5.2: Amplitude of the noise radiation directivity peaks from a dipole source, normalised by the peak amplitude of the noise radiated from the same dipole in a medium at rest, at $M_0 = 0$.

At the shorter distance $r = r_o = 5$ m, the results reported in Figures 5.3(a), 5.3(c), and 5.3(e) show a reduced asymmetry in directivity about the x_2 -axis compared to Figures 5.3(b), 5.3(d), and 5.3(f). At $M_0 = 0.2$, the leaning of the dipole directivity lobes in the upstream direction is rather difficult to detect. At $M_0 = 0.5$ and $M_0 = 0.85$, the directivity pattern exhibits four lobes. This feature makes clear the presence of a directivity bias in the upstream direction in Figures 5.3(c) and 5.3(e).

At both distances $r = r_o = 5$ m and $r = r_o = 340$ m, the noise peak intensity is progressively amplified as the uniform Mach number of the moving medium increases. Due to the significant increment in the amplitude of the acoustic pressure fluctuation, the results for the high subsonic Mach number $M_0 = 0.85$ in Figures 5.3(e) and 5.3(f) are reported with a larger radial scale on the polar axis, for visualization purposes, compared to the lower Mach number configurations in Figures 5.3(a)– 5.3(d).

The numerical prediction obtained with the new Python CFW-H tool appears to be correctly capturing the noise directivity from the dipole source in a uniformly moving medium, as it displays a good match with the analytical solution of Equation 5.5, both at $r = r_o = 5$ m and at $r = r_o = 340$ m. A slight mismatch around the noise peak is only appreciable in Figure 5.3(f), concerning the highest subsonic Mach number $M_0 = 0.85$ and the largest distance $r = r_o = 340$ m. By refining the

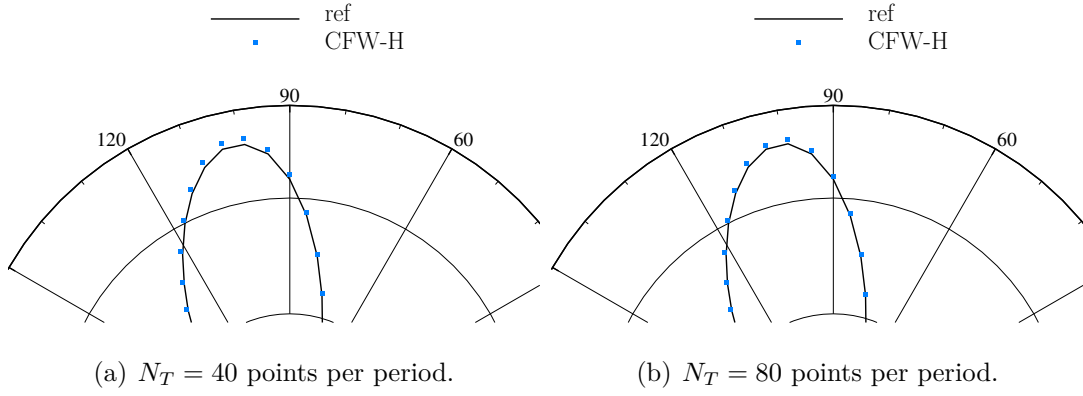


Figure 5.4: Radiation in a medium uniformly moving at $M_0 = 0.85$ in the x_1 -axis direction, from an acoustic dipole source located at the origin. Prismatic FW-H surface with $a = 2\ell = 1$ m (see Figure 3.1). Source frequency $f = 5$ Hz, and source strength $A = 1 \text{ m}^4\text{s}^{-1}$. Distance source-observers $r_o = 340$ m.

spatial and/or the temporal discretization, it is possible to improve the accuracy of the solution, as shown by the test reported in Figure 5.4. Figure 5.4(b), pertaining to the results obtained with $N_T = 80$ number of points per period, shows a better match between the CFW-H prediction and the analytical solution of Equation 5.5 compared to Figure 5.4(a), where $N_T = 40$ as for Figures 5.3(a)– 5.3(f).

It is worth pointing out that the acoustic predictions at the farthest distance $r = 340$ m in Figures 5.3(b), 5.3(d), and 5.3(f) have not been referred to as acoustic far-field predictions, either in this section, or in Section 5.1.1. The acoustic far-field has been defined in Section 1.4, by using Equation 1.3 to express the conditions that the observer location needs to satisfy for it to be a far-field one. The characteristic lengths of interest are the acoustic wavelength λ , the distance between source and observer r , and the maximum extent of the source region L_{\max} . Following Equation 1.3, the ratios r/λ , r/L_{\max} , and r/L_{Rayleigh} need to be much greater than unity for r to be considered within the acoustic far-field. By considering the test in Figure 5.3, for the distance $r = 340$ m, these ratios are

$$\begin{cases} r/\lambda = 5, \\ r/L_{\text{Rayleigh}} = r/(L_{\max}^2/\lambda) = 23120, \\ r/L_{\max} = 340. \end{cases} \quad (5.8)$$

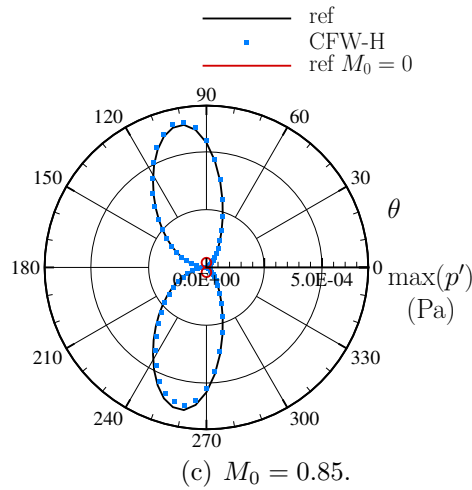
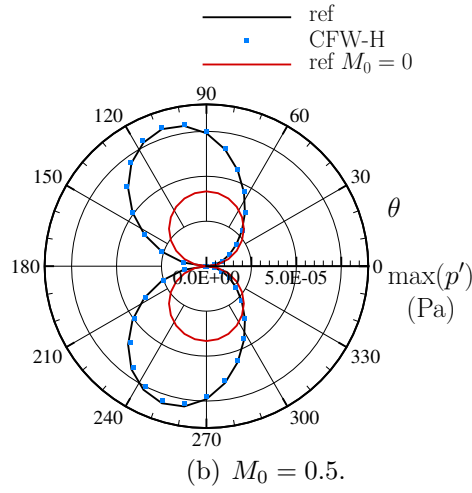
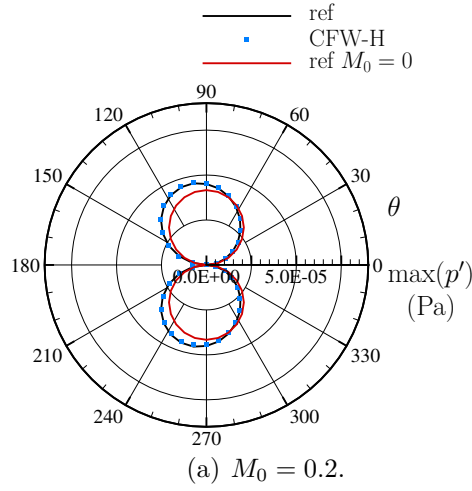


Figure 5.5: Far-field radiation in a medium uniformly moving in the x_1 -axis direction, from an acoustic dipole source located at the origin. Prismatic FW-H surface with $a = 2\ell = 1$ m (see Figure 3.1). Source frequency $f = 5$ Hz, and source strength $A = 1 \text{ m}^4\text{s}^{-1}$. Source-observers distance $r_o = 6800 \text{ m} = 100\lambda$.

Therefore, while the conditions on the maximum extent of the source region and on the Rayleigh distance are satisfied to a good extent, the requirement on the ratio $r/\lambda \gg 1$ is weakly met, being the distance source-observer only five times the acoustic wavelength.

A test with an increased distance $r = r_o = 6800$ m is reported in Figure 5.5. This distance gives a ratio $r/\lambda = 100$ that is 20 times larger than the same ratio for the test in Figure 5.3. $r = r_o = 6800$ m satisfies all the conditions in Equation 1.3 to a good extent and it can be effectively considered as acoustic far-field distance for this problem.

However, comparing Figures 5.3 and 5.5, it is clear that the directivity patterns do not undergo any significant qualitative change as the distance source-observer is increased by 20 times from $r = r_o = 340$ m to $r = r_o = 6800$ m. The only effect is the scaling of the amplitude of the acoustic pressure fluctuation by the same factor of 20. This proves not only that the scaling with distance r from the source is correctly captured by the CFW-H tool prediction, but also that the distance $r = r_o = 340$ m is sufficient for the observers to record far-field dipole radiation characteristics.

Overall, Figures 5.3 and 5.5 show that the CFW-H acoustic analogy as implemented in Python correctly predicts the noise radiation from a directional source, in terms of both directivity and intensity, for the conditions herein considered. For $N_T = 40$, the error at the peak radiation angle with respect to the analytical reference solution of Equation 5.5 is typically less than 2%, reaching values below 1% for $N_T = 80$. Besides, the spatial discretization of 80 points per each side $a = 1$ m of the FW-H cubical surface gives enough points to correctly represent the acoustic wavelength $\lambda = 68$ m.

5.2 Forward flight effects on BroadBand Shock Associated Noise

The effect of forward flight on under-expanded jets is investigated in this section, by the “wind tunnel configuration” [55] of a jet discharging in a uniform flow. A brief literature review on the forward flight effect for jets is provided, before applying the CFW-H formulation to a supersonic under-expanded jet in flight, in Section 5.2.1.

Tam [156] pointed out the dual nature of the flight effect, explaining that the presence of a uniform flow external to the jet shear layer modifies both the generation (aerodynamic effects on the noise source) and the propagation (mean flow convection effects) of noise.

Norum and Shearin [157] showed experimentally that the flight effect on the BBSAN noise radiation reduces the BBSAN peak frequency and narrows the BBSAN peak bandwidth as the Mach number M_0 of the coaxial flow increases [156, 158]. Higher frequency peaks are also detected with increasing M_0 [156], which are probably due to BBSAN higher harmonics.

The reason for these modifications have to be sought in the modification of the jet, by the external co-flow. Firstly, a reduction of the shear gradients across the jet occurs [156] that causes the rate of growth of the mixing layer to be reduced [156, 159]. The turbulent mixing with the ambient medium is weakened by the external co-flow [159] and the jet becomes stretched in the flow direction.

As a consequence of the jet stretching, an increase in the length of the potential core and in the shock-cell spacing [156, 159, 160] is produced, as M_0 is increased. The growth/decay rate of the instability waves in the jet shear layer is also attenuated [156, 159].

As well as the length, the co-flow also influences the strength of the shock-cells, by weakening the first shocks [159] closer to the nozzle exit, which are mainly responsible for the screech noise radiation. On the contrary, the shock-cells further downstream, that are responsible for the BBSAN contribution, are strengthened by the surrounding uniform flow [159].

By analysing the case of a moving noise source and a fixed ground observer, Tam [160] also pointed out that the large convective amplification that occurs for simple point sources radiating in a uniform flow (see Section 5.1) does not take place for the BroadBand Shock Associated Noise contribution of a jet.

5.2.1 Far-field noise radiation from an under-expanded jet in flight

The CFW-H formulation is applied here to a supersonic single-stream jet generated by the same nozzle operated at the same nozzle exit conditions as in Section 4.1.2.

While Section 4.1.2 reports the results obtained for the stationary case ($M_0 = 0$), a coaxial flow in the jet direction is considered here, in order to reproduce the effects of forward flight.

This uniform subsonic flow in the x -axis direction has a Mach number $M_0 = 0.39$. This allows a direct comparison with published far-field acoustic results obtained both experimentally and by computation. Specifically, acoustic measurements were obtained by André [143] at the Acoustics Center of the École Centrale de Lyon, while numerical noise estimations were obtained by Pineau [136] at Cerfacs. Pineau used a convective formulation [131] of the FW-H acoustic analogy [52] implemented in the ONERA KIM software [120, 131] to project the noise radiation to the far-field.

The supersonic jet of fully expanded Mach number $M_j = 1.15$ and Reynolds number $Re = 1.25 \times 10^6$ issues from a convergent nozzle of exit diameter $D_e = 0.038$ m. These values are the same as the ones used in experiment by André [143] and in Section 4.1.2. The convergent nozzle prevents the flow from expanding to the ambient pressure and this causes the jet to be under-expanded. The jet therefore develops shock-cells in the jet plume and generates BBSAN.

CFD data for the single-stream under-expanded jet in flight with $M_0 = 0.39$ are obtained by Pineau [136], at Cerfacs, by elsA [130]. This dataset is used as input to the CFW-H tool. Specifically, LES flow field predictions are available on the conical FW-H integration surface shown in Figure 5.6. The surface is closed upstream by the nozzle external wall and it is left open (see Section 2.2.1.1) at the downstream end.

Figure 5.6 shows the CFD domain, the integration surface $\mathcal{F}(\mathbf{x}, t) = 0$, the Cartesian reference system centred at the nozzle exit section on the jet axis, and a sample observer $o^{(n)}$ in the direction $\theta^{(n)}$. The polar angle θ is measured from the jet axis and angles over the range $0^\circ \leq \theta \leq 90^\circ$ represent downstream directions, while the upstream arc is characterised by $90^\circ \leq \theta \leq 180^\circ$. The CFD domain has a shape similar to that of an hourglass and it extends over the range $-7.0D_e \leq x \leq 25.0D_e$ in the axial direction. The radial extent of the CFD domain varies from $r = 5.0D_e$ at the nozzle exit, to $r = 6.9D_e$ at $x = -7.0D_e$, and to $r = 10.0D_e$ at $x = 25.0D_e$.

The radial and the axial size of the conical integration surface are reported in Table 5.3, together with the corresponding dimensions of the CFD domain at the same abscissas, in order to show how the FW-H surface is well within the computational

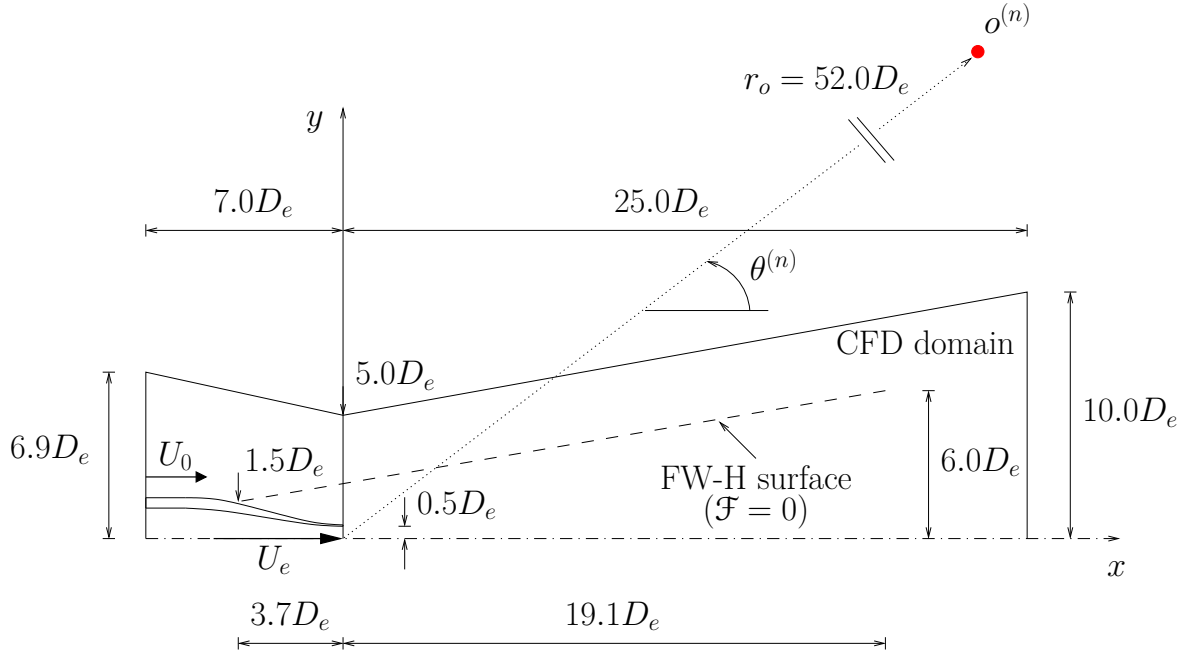


Figure 5.6: Domain schematic for the supersonic single-stream jet in flight, showing the CFD domain, a sample observer position, and the location of the FW-H integration surface. Lengths are scaled by the nozzle exit diameter D_e .

domain boundaries. Specifically, the FW-H surface reaches $x = -3.7D_e$ upstream of the nozzle exit and $x = 19.1D_e$ at its downstream boundary, with a constant slope of 11.2° from the jet axis.

	$x_{\min} = -3.7D_e$	$x_{\max} = 19.1D_e$
$\mathcal{F}(\mathbf{x}, t) = 0$	$-1.5D_e \leq y, z \leq 1.5D_e$	$-6.0D_e \leq y, z \leq 6.0D_e$
CFD domain	$-6.0D_e \leq y, z \leq 6.0D_e$	$-9.0D_e \leq y, z \leq 9.0D_e$

Table 5.3: Dimensions of the FW-H surface and of the computational domain for the $M_j = 1.15$ under-expanded jet in flight ($M_0 = 0.39$). Dimensions scaled by the nozzle exit diameter D_e .

Far-field acoustic estimations at $r_o = 52.0D_e$ are performed on a spherical array of 208 observers, covering 13 axial positions within the range $-45.0D_e \leq x \leq 45.0D_e$, covering the polar angle $30^\circ \leq \theta \leq 150^\circ$. At each radiation angle, 16 observers equispaced in the azimuthal coordinate ϕ are used to average the noise spectra, in order to get smoother PSD trends.

Figure 5.7 shows the LES prediction by Pineau [136] on the integration surface $\mathcal{F}(\mathbf{x}, t) = 0$ of Figure 5.6, in terms of iso-levels of the instantaneous pressure fluctuation p' . Downstream travelling acoustic waves are shown in Figure 5.7, as axially alternating ring bands of high (red) and low (yellow) pressure perturbations. A reduction in the pressure wave amplitude with increasing axial distance from the nozzle exit is clearly noticeable in Figure 5.7, as it was in Figure 4.6 in the previous chapter, which described the same single-stream jet but stationary. On the other hand, the effect of the increase in the radiation wavelength with axial distance from the nozzle exit section is less marked here. Besides, the amplitude of the pressure fluctuation is about three times higher compared to the stationary case in Figure 4.6.

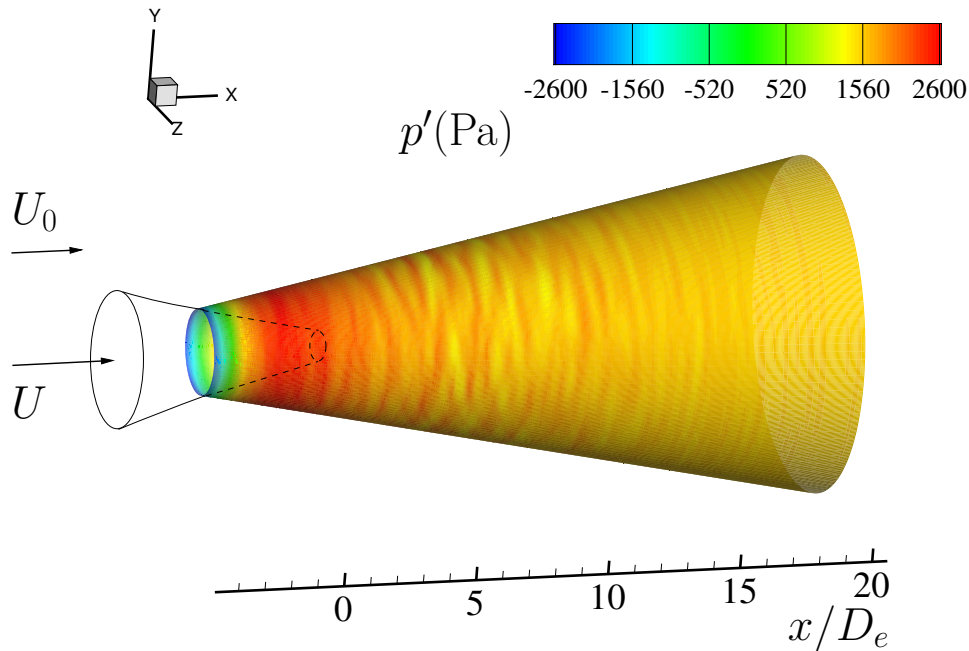


Figure 5.7: Large Eddy Simulation of a single-stream Mach 1.15 jet [143] in flight ($M_0 = 0.39$), modelled at $Re = 1.25 \times 10^6$. Instantaneous pressure fluctuation iso-levels on the FW-H surface $\mathcal{F} = 0$ from [136].

The LES simulation was performed by Pineau [136] during an internship at Cerfacs, in collaboration with the École Centrale de Lyon. The limited amount of time of the internship led to the choice of a relatively coarse mesh, with 21.06×10^6 cells, against 65.80×10^6 cells used by Mancini [15] and 75.00×10^6 cells used by Pérez [16], for modelling the same jet in the stationary case (Section 4.1.2).

This coarser spatial discretization affects the accuracy of the numerical prediction

due to the local mesh cut-off Strouhal number being lower than in [15] and in [16]. The axial discretization by Pineau [136] gives a mesh cut-off Strouhal number $Str \approx 2$ for most part of the CFD domain, including where the FW-H surface lies [136]. The azimuthal discretization imposes a more stringent limitation, giving a cut-off Strouhal number around $Str = 1$ that is not sufficient to resolve the BBSAN contribution, characterised by a peak Strouhal number of about 1 [143].

This produces unwanted numerical dissipation of the acoustic waves travelling to the integration surface in the BBSAN Strouhal number range. Therefore, it is preferable to use CFD predictions with a higher cut-off Strouhal number. Unfortunately, a LES simulation with a finer discretization is not available for this test case. Therefore, the author decided to test the CFW-H tool on the relatively coarse mesh CFD results by Pineau [136] that, despite the lack of accuracy, capture the qualitative effects of the forward flight in terms of both the aerodynamics and the acoustics of the jet [136]. The numerical results by Pineau [136] qualitatively agree with previous measurements by André [143].

This qualitative agreement is shown by the far-field noise spectra that are compared in Figures 5.8 and 5.9. Power Spectral Densities in decibel are plotted against the Strouhal number $Str = fD_e/U_j$, based on the nozzle exit diameter D_e .

In Figure 5.8, six radiation angles between 90° and 140° are considered, focusing on the upstream arc where the BBSAN is more prominent in the stationary case [16, 143, 136], as shown in Section 4.1.2. Three curves are shown, with the solid-black lines and the long-dashed blue lines denoting the noise predictions from the jet in a $M_0 = 0.39$ simulated flight, obtained respectively by Pineau [136], with the KIM software [120, 131], and by the author, with the new CFW-H tool. The experimental results from the stationary jet ($M_0 = 0$) measured by André [143] are indicated by the dashed-green lines.

It can be observed that the two numerical predictions agree for all the polar angles considered in terms of the BBSAN noise peak frequency and intensity. The KIM prediction slightly underestimates the noise levels at the high frequency range. Both predictions show a decrease in the BBSAN peak frequency and a narrowing of the BBSAN peak compared to the stationary jet prediction by André [143], which are known flight effects reported in the BBSAN literature [156, 158].

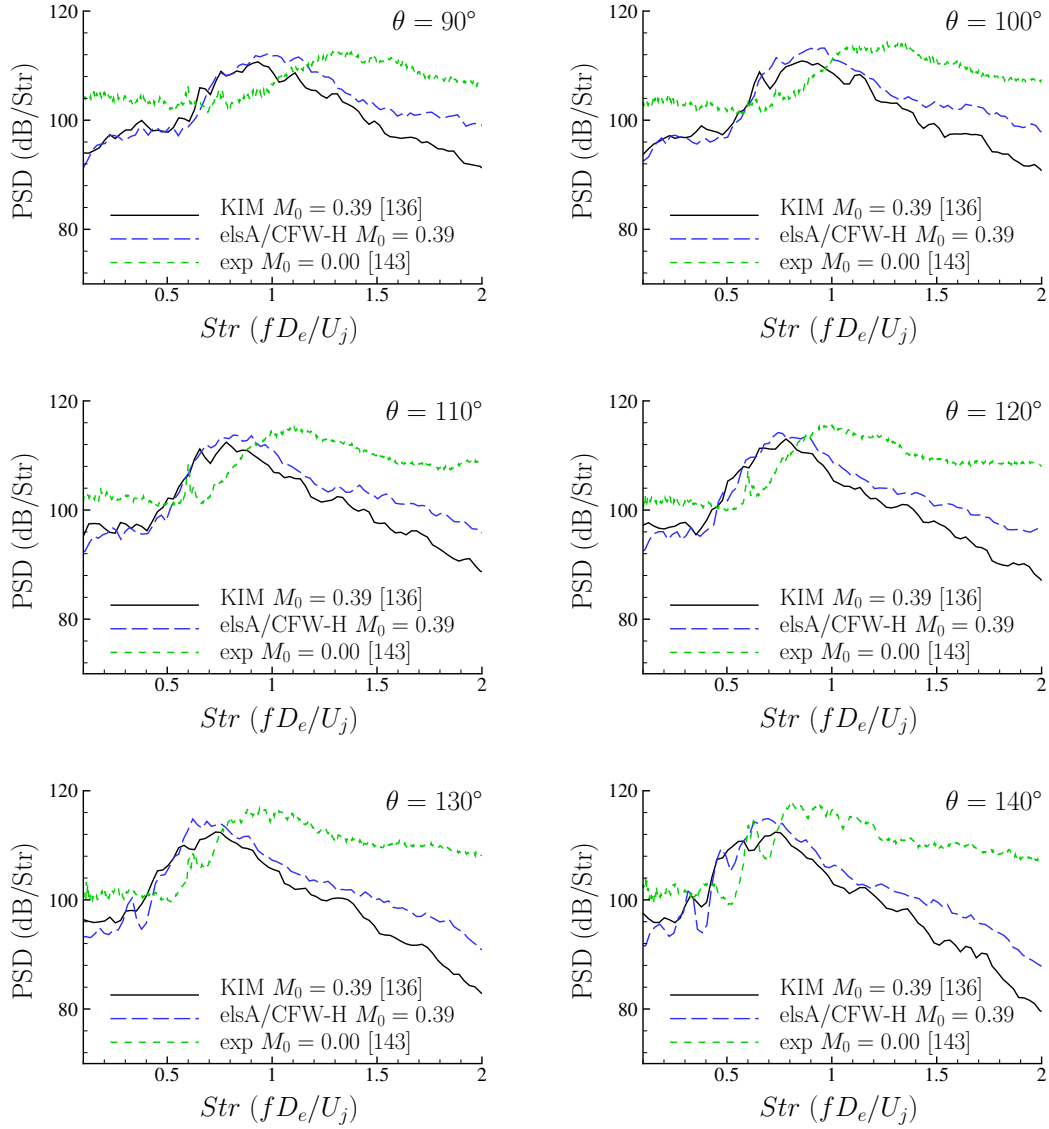


Figure 5.8: Far-field PSD from a single-stream under-expanded jet in subsonic flight, modelled by LES [136] at Cerfacs. Comparison with the reference numerical solution by Pineau [136], obtained through the software KIM [120] by ONERA. Experimental measurements by André [143] are shown, for the same jet tested under static conditions. $M_j = 1.15$, $M_0 = 0.39$, $Re = 1.25 \times 10^6$, $r_o = 52.0D_e$ from the nozzle exit. PSD smoothed as in Figure 4.4(b).

As a further consequence of the presence of a modelled flight stream, higher order BBSAN peaks should appear, but they are not noticeable in Figure 5.8, for two reasons. Firstly, these new peaks should occur at higher frequencies compared to the BBSAN main peak, *i.e.* at frequencies that are not adequately resolved by the available CFD mesh. Secondly, these higher order peaks are characterized by lower noise levels than the main peak, making them even more challenging to be captured.

The last result of this section is reported in Figure 5.9 that compares the numerical far-field spectrum at $\theta = 100^\circ$ with the same result obtained experimentally by André [143]. This is the only angle for which measurements are available for exactly the same conditions as the LES simulation, in terms of jet Mach number $M_j = 1.15$, and uniform flow Mach number $M_0 = 0.39$.

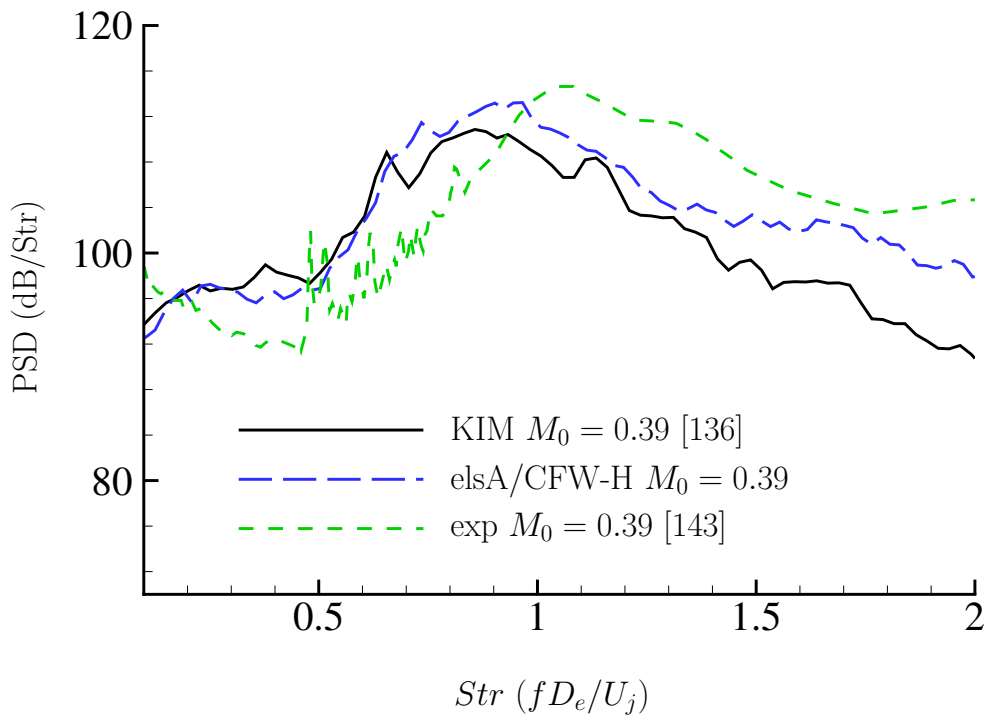


Figure 5.9: Far-field PSD from a single-stream under-expanded jet in subsonic flight, modelled by LES [136] at Cerfacs. Comparison with both the reference numerical solution by Pineau [136], obtained through the software KIM [120] by ONERA, and the experimental measurement by André [143]. $M_j = 1.15$, $M_0 = 0.39$, $Re = 1.25 \times 10^6$, $r_o = 52.0D_e$ from the nozzle exit, $\theta = 100^\circ$ from the jet axis. PSD smoothed as in Figure 4.4(b).

In Figure 5.9, the same legend is used as for Figure 5.8, with solid-black and long-dashed blue lines indicating respectively the KIM [136] and the CFW-H tool predictions. The experimental measurements, reported with a dashed-green line, are relative to the in-flight condition with $M_0 = 0.39$ in Figure 5.9. It can be appreciated that the numerical prediction is not far from the experimental result, despite the limitations given by the CFD mesh. Besides, the CFW-H solution is closer to the measurement by André [143], compared to the prediction by Pineau [136], in terms of noise level at the BBSAN peak. The underestimation of the BBSAN peak frequency is probably due to the coarse azimuthal discretization in the CFD mesh, giving a cut-off Strouhal number of about 1.

The results presented in Figure 5.8 and 5.9 are encouraging, giving confidence in the reliability of the new Python CFW-H noise extractor. However, further applications to jets in flight are necessary, possibly with a more accurate CFD simulation, in order to be able to better predict the peak frequency and the amplitude of the BBSAN contribution to jet noise radiation during cruise conditions.

Chapter 6

Conclusions

6.1 Key contributions

This work has substantially achieved its main aim of providing a Python-based aerodynamic noise extractor from time-resolved data of aerodynamic fields for noise radiating in an acoustic outer medium, both stationary and uniformly moving. In the process of achieving this aim, the following contributions to the state of the art have been made:

1. Stationary (Section 2.2.3) and convective (Section 2.2.4) formulations of the advanced-time Ffowcs Williams and Hawkings acoustic analogy are provided on a unified community shared software platform (Antares [12]), parallelised for compatibility with high performance computing.
2. The equivalence between the stationary and convective formulations is verified by numerical tests (Appendix D) against benchmark implementations of the stationary formulation that is integrated in the numerical solver elsA [130] by ONERA.
3. Salient acoustic aspects of the noise radiation from an under-expanded dual-stream jet are exposed (Section 4.2) for a dual-stream jet configuration (Appendix A) that was previously unreported in the literature and that is relevant to ultra-high bypass aircraft turbofans.
4. The convective formulation is used to demonstrate, numerically, the forward flight effects on a single-stream under-expanded jet (Section 5.2.1), providing

supporting evidence to previously inferred flight effect mechanisms affecting the noise directivity in the far-field.

5. The application of the stationary formulation to analytical jet flow descriptions obtained by the Parabolised Stability Equation (PSE), in collaboration with the Institut de Mécanique des Fluides de Toulouse (IMFT), has allowed the testing of the code on a reduced-order jet flow model [161].
6. The computational savings from using the acoustic analogy approach compared to a direct approach to modelling near-field noise by LES are quantified, enabling an informed choice to be made by prospective users of the noise extractor tool.

Important numerical aspects were also exposed by this work, specifically concerning discretization:

- (a) The effect of time sampling in the aerodynamic data on the extracted aerodynamic sound was exposed, so that lower and upper frequency limits on the acoustic predictions are identified *a priori*.
- (b) A more complex spatial discretization effect was identified for the Ffowcs Williams and Hawkings surfaces in Section 3.2. This led to the formulation of a set of heuristic “good practice” rules for obtaining engineering accurate results. It also exposed important opportunities for further work in numerical analysis, to try to fully resolve the identified problems.

Part of the results presented in Chapters 3 and 4 have been published in three conference papers by Di Stefano *et al.* [140, 141, 144], including a peer-reviewed paper [144]. A preliminary direct noise computation 2.1.1 test was presented in the 20th AIAA/CEAS Aeroacoustics conference in 2014 in Rona *et al.* [62].

6.2 Implications of the main results

As mentioned in Chapter 1, the main objective of this research was to develop a noise extractor that can be applied to unsteady predictions of turbulent flows to project the noise emission both to the acoustic near-field and to the acoustic far-field.

This objective has been realized by implementing two integral formulations of the Ffowcs Williams and Hawkings (FW-H) acoustic analogy [52] in Antares [12], a software package of wide access and usability for the aeroacoustic community. Both a stationary [54] (AFW-H) and a convective [55] (CFW-H) formulation, described respectively in Sections 2.2.3 and 2.2.4, have been coded in Python and embedded in Antares.

Given a time-dependent description of the flow on a control surface in terms of the pressure, density, and velocity fields, the AFW-H and the CFW-H tools extract the noise radiation everywhere outside the FW-H control surface.

These new AFW-H and CFW-H aeroacoustic tools have been applied to both elementary noise sources and jet test cases, in Chapters 3, 4, and 5. The elementary source tests reported in Chapter 3, for the AFW-H method, and in Section 5.1, for the CFW-H method, provided a validation of the two implementations on simple noise radiation problems.

In Sections 4.1.2, 4.2, and 5.2.1, the AFW-H and CFW-H tools have been applied to under-expanded jets, for which a CFD database on an open axisymmetric integration surface was available. In these tests, the open surface strategy was shown to produce good jet noise predictions, even in the presence of shocks, by the use of the aeroacoustic AFW-H and CFW-H tools.

The main application has been presented in Section 4.2, where the AFW-H method is applied to the dual-stream jet configuration of Appendix A, proposed by Airbus SAS, partner of the AeroTraNet2 project. For this configuration, neither numerical nor experimental results can be found in the previous aeroacoustic literature. This test case is representative of a turbofan engine configuration on contemporary wide-body civil aircraft. In Section 4.2, the AFW-H noise extractor applied to LES and DES predictions of the flow was shown to be a good tool for estimating both the acoustic near-field and the acoustic far-field from the new dual-stream under-expanded jet configuration.

An effort towards improving the numerical model for stationary jet engine noise is presented in Section 5.2.1, where the convective CFW-H formulation, described in Section 2.2.4, was applied to a single-stream under-expanded jet in flight. By adding a uniform coaxial flow external to the jet, the main flight effects on the BBSAN

noise contribution were identified. The results showed a good match with previous acoustic estimations in the jet noise literature in terms of the BBSAN contribution. This was achieved despite the low resolution mesh used to get the CFD prediction on the FW-H surface, input to the CFW-H tool.

Another application of the AFW-H code of Section 2.2.3 has been realized in collaboration with the Institut de Mécanique des Fluides de Toulouse (IMFT) and it was published by Ansaldi in [161]. The AFW-H code was applied to very-low-cost analytical jet flow descriptions, obtained by solving the Parabolised Stability Equations (PSE) [162], in order to extract the noise radiation to the acoustic far-field. The coupled PSE/AFW-H method, consisting in a two-step hybrid approach, was developed by following the work by Léon and Brazier [163]. This technique was applied to a semi-empirical supersonic single-stream jet and to the dual-stream under-expanded jet of Section 4.2. The acoustic predictions were compared with both experimental and numerical reference solutions and the results, showing a good match, were published by Ansaldi [161].

The FW-H tools are extremely efficient from a computational point of view. The computational cost of the acoustic simulation represents a very small fraction of the CFD counterpart. For instance, in the dual-stream jet test case of Section 4.2, the overall computational cost of the AFW-H simulation was 0.02% of the DES simulation for the Cosmic/AFW-H method.

Typically, the differences in characteristic wavelengths between the acoustic field and the aerodynamic field allow for a CAA time step larger than the CFD time step. Therefore, the different sampling frequency of the CAA simulation compared to the CFD simulation ($\Delta\tau_{\text{CAA}} = 500\Delta\tau_{\text{CFD}}$) in the Cosmic/AFW-H method applied in Section 4.2 contributed to the comparatively low cost of the acoustic computation. However, the value of 0.02% can be improved when the computational cost of the AFW-H simulation is compared against predictions from high order LES, where a larger range of scales is resolved in the computational domain volume.

This short time length of the acoustic simulation compared to the CFD counterpart makes the use of a CAA post-processor very advantageous. Once the simulation on the FW-H integration surface is stored, the tool can be applied to perform a number of acoustic simulations, aimed to cover all the observer regions that are worth of

investigation, at a very low computational cost. On the other hand, when the code is embedded into the CFD software, the increase in the computational cost is expected to be lower than 1%.

Beyond the practical implications stated above, it is worth concluding by recalling that the AFW-H and CFW-H tools have been developed by the author following a non-commercial approach. Current advances in computational physics are facilitated by the sharing of benchmark computations and experimental data across the community on a royalty-free non-commercial base. Open-source software contribute to these initiatives by supporting the shared use of advanced numerical methods across the research community. The development of the AFW-H and CFW-H tools in this work was devoted to academic and research purposes and it is not constrained by Intellectual Property Rights. The Antares software [12], managed and developed by Cerfacs, France is not open-source, but its distribution and use is ruled by a copyright agreement that does not require the payment of an upfront license fee. Given this non-commercial approach, the new Antares AFW-H and CFW-H packages are expected to bring advantages to the whole aeroacoustic community.

6.3 Future perspectives

The tests presented in the current research are only an example of the possible applications of the acoustic analogy tools developed by the author that can be used to extract the noise radiation from any unsteady flow predictions, provided that time-dependent data are generated on an integration surface placed in the “quasi-linear” region of the flow (see Section 4.3). Other examples are represented by rotor noise or propeller noise applications, where the FW-H acoustic analogy integral method is typically applied [106, 108, 110, 125].

Many points of interest related to the use of integral methods in aeroacoustics and the jet noise topic have already been covered by the author in this thesis. To deal with additional aspects of these topics that were partially discussed in the main body of the thesis, a number of further applications can be stated in terms of future perspectives:

1. Application of the new AFW-H and CFW-H tools to jet noise problems with a

closed control surface (provided that such a CFD database becomes available to the author), by using a tailored technique to filter out the spurious contribution to jet noise radiation, arising from the jet inevitably crossing the FW-H surface at the downstream boundary (Section 2.2.1.1). Two possible solutions are the disk averaging technique [5, 119], or the inclusion of new surface integral contributions approximating the volume source contribution, as suggested by Rahier *et al.* [164].

2. Application of the CFW-H tool of Section 2.2.4 to a dual-stream under-expanded jet in flight (subject to the availability of a tailored CFD database). This would represent a significant test to progress towards modelling the noise radiation from a turbofan engine in cruise conditions.
3. Use of the AFW-H and CFW-H tools not as post-processors but embedded to a CFD code, by developing an interface that extracts the CFD prediction on a FW-H surface defined *a priori*. The use of an object-oriented language, Python, facilitates the development of this interface. In this way, the acoustic simulation runs simultaneously with the CFD simulation and computational effort can be saved by activating the interface only at integer multiples of the acoustic time step, typically larger than the CFD counterpart.
4. Investigation on the numerical error in the AFW-H and CFW-H tools, when the acoustic source is proximal to the integration surface corners or edges (Section 3.2). In Section 3.3, an hypothesis was advanced by the author, in collaboration with the Leicester team and Emeritus Professor Christopher Morfey, but further investigations are necessary to validate this hypothesis.

The applications listed above would help to strengthen the confidence in the reliability of the new noise prediction tools, but also to contribute further to the understanding of jet noise. In the previous literature, most applications to noise radiating from under-expanded jets were limited to stationary jets. Modelling the in-flight conditions with an efficient and widely accessible tool would further contribute towards more accurate predictions of jet noise.

Appendices

Appendix A

AeroTraNet2

This research is undertaken within the AeroTraNet2 (AEROnautical TRaining NETwork in Aerodynamic Noise from Wide-body Civil Aircraft) project. “AeroTraNet2 is a Marie Curie Action of the European Commission's 7th Framework Programme (FP7). It trains Early Stage Researchers (ESRs) and Experienced Researchers (ERs) in front-line, integrated, industry relevant research in unsteady aerodynamics and noise for the next generation of environmentally friendly wide-body civil aircraft” [13].

“Six academic partners address the common objective of modelling shock-cell noise in a wide-body aircraft engine configuration from private sector partner Airbus SAS France, by shock-tolerant numerical modelling for under-expanded jets (University of Leicester), Large Eddy Simulations (LES) for turbulent jets with weak shocks (Cerfacs, Toulouse), advanced flow-noise correlations (Università degli Studi Roma Tre), jet and near-field noise experiments (Von Karman Institute for Fluid Dynamics), reduced-order modelling and flow control (Institut de Mécanique des Fluides de Toulouse, IMFT-INP), and advanced laser-based measurement techniques (the Italian Ship Model Basin, CNR-INSEAN).

Knowledge output is synthesized through a dedicated knowledge capturing programme by the University of Greenwich, which is used by private sector partner GE Power. In AeroTraNet2, the research output becomes itself object of knowledge management research, which is a novel supra-disciplinary element” [13].

Three different approaches are adopted, which are mathematical, numerical, and experimental modelling, used in synergy to push forward the state of the art of shock-cell noise prediction methods applied to aircraft design. The current research

is part of the numerical modelling effort of AeroTraNet2. An acoustic analogy tool is applied to unsteady flow field predictions obtained both at the University of Leicester and at Cerfacs in Chapters 3– 5. The results are compared against predictions from both the numerical and the experimental partners of AeroTraNet2.

A.1 Wide-body civil transport configuration

The test case proposed relates to jet noise reduction from civil aircraft, which is an active area of aeroacoustic research. In Figure A.1 and A.2, the geometry of the nozzle and the flow conditions are specified, respectively. Table A.1 reports the numerical values of the Fan-Nozzle Pressure Ratio (FNPR) and of the Core-Nozzle Pressure Ratio (CNPR) for the test points represented in Figure A.2.

The geometry is the one of a dual-stream jet issuing from coaxial nozzles for the primary and for the secondary stream. Both the primary and the secondary streams issue from axisymmetric conical convergent nozzles. The external and the internal nozzle cowls converge respectively at 12° and at 14° towards the jet axis. The exit planes of the nozzles are axially staggered. The bypass flow exits the nozzle 0.021 m upstream of the primary nozzle exit section and the secondary jet diameter is more than double the internal one. The design does not include the use of any primary nozzle central plug and the coaxial nozzle geometry is fixed.

The numerical predictions for this dual-stream jet test case obtained by the AeroTraNet2 partners were compared with measurements taken at the FAST (Free jet AeroacouSTic) facility, at the Von Karman Institute for fluid dynamics (VKI), Brussels. This facility was built within the AeroTraNet2 framework between 2013 and 2016 by the Early Stage Researcher Daniel Guariglia [43]. The total mass flow rate was constrained by the VKI compressed air supply line. This determined a target test point of 1.09 kg/s. The fully expanded Mach numbers of the primary jet and of the secondary jet at this test point are 0.89 and 1.21, respectively.

The secondary jet is sonic at the nozzle exit section of the convergent duct and it experiences a considerable degree of under-expansion. This causes the development of a shock-cell system in the secondary flow, with a configuration similar to the one of Figure 1.3. The main features of under-expanded jets are described in Section 1.2,

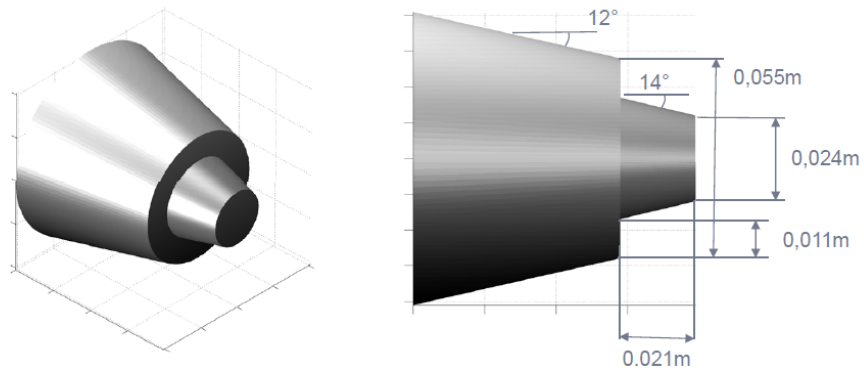


Figure A.1: Dual-stream under-expanded jet: nozzle geometry.

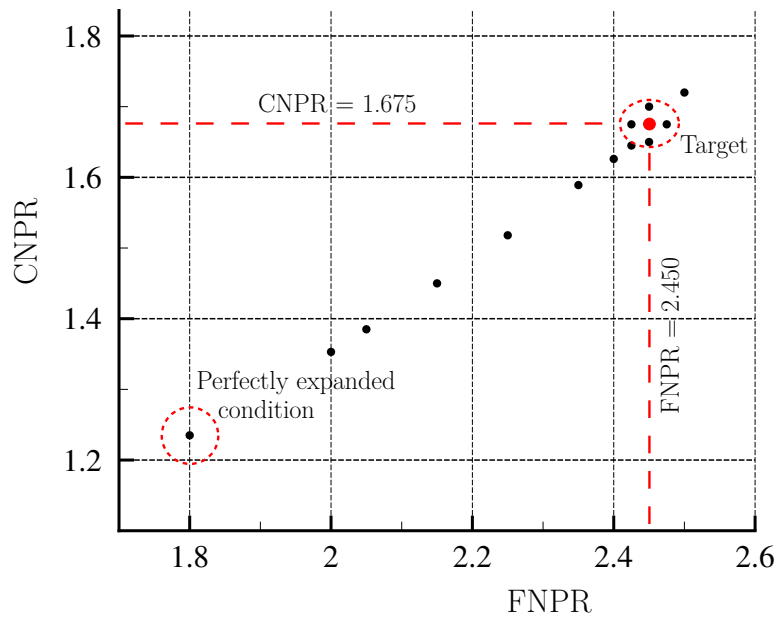


Figure A.2: Dual-stream under-expanded jet: FNPR-CNPR plane showing the Test Conditions (TC).

for single-stream jets, and in Section 1.3, for dual-stream jets. The shock-cell system in the secondary flow also affects the primary flow, by preventing the fully expanded condition to be reached in the experiment [43]. CFD [15, 16] and experimental [43] data on the test case of Figures A.1 and A.2 were produced within the AeroTraNet2 project in order to further investigate the flow features.

As far as noise estimations from dual-stream jets are concerned, there are not many publications on this topic (see Section 1.3) and the test case here reported presents peculiar features that makes it an interesting contribution to the aerodynamic and to the aeroacoustic literature.

TC	FNPR	CNPR
01	2.450	1.675
02	2.500	1.720
03	2.425	1.645
04	2.400	1.626
05	2.350	1.589
06	2.250	1.518
07	2.150	1.450
08	2.050	1.385
09	2.000	1.353
10	1.800	1.235
11	2.475	1.675
12	2.425	1.675
13	2.450	1.650
14	2.450	1.700

Table A.1: Dual-stream under-expanded jet: matrix of the Test Conditions (TC).

The current work produced both near-field and far-field noise predictions for the test case of Figures A.1 and A.2 at target conditions, by the application of the new AFW-H tool of Section 2.2.3 to post-process CFD data obtained both at the University of Leicester [15] and at Cerfacs [16].

Appendix B

Convective FW-H derivation

The derivation of the convective FW-H equation with permeable surface follows two fundamental steps that are described in this appendix:

1. embedding procedure to get the generalised form of the governing equations [106, 165];
2. rearrangement of the generalised governing equations in the form of an inhomogeneous wave equation [1, 52].

The embedding procedure [106] introduces the concept of the unbounded fluid [52], through the use of the generalised function theory [165]. The extension of the validity of the conservation equations everywhere in space enables to include the presence of solid bodies. The latter need to be enclosed by the integration surface $\mathcal{F}(\mathbf{x}, t) = 0$, represented in Figure 2.4, Section 2.2.

Before presenting the analytical development of items 1 and 2 in the next two sections, it is worth recalling that the FW-H surface $\mathcal{F}(\mathbf{x}, t) = 0$ can always be defined so that $\nabla\mathcal{F} = \hat{\mathbf{n}}$ is satisfied [165], where $\hat{\mathbf{n}}$ is the outward-normal unit vector to the surface itself. Herein, the integration surface is thought as permeable (Section 2.2.1), and it divides the unbounded fluid into three regions, according to the value of $\mathcal{F}(\mathbf{x}, t)$ (see Figure 2.4).

Considering the noise propagation in a uniform medium, characterised by constant density ρ_0 and pressure p_0 , moving at constant subsonic velocity \mathbf{U}_0 , the fluid properties can be written as follows:

$$u_i = U_{0i} + u'_i, \quad \rho = \rho_0 + \rho', \quad p = p_0 + p', \quad (\text{B.1})$$

where “0” refers to the ambient (undisturbed medium), and the local perturbations are represented by the primed variables [55]. The latter are obtained by subtracting the respective uniform value assumed at infinity to the local fluid density, pressure, and velocity, so that the (acoustic) disturbances vanish far away from the source region [106]. The index $i = 1, 2, 3$ refers to the i^{th} velocity component in a fixed Cartesian reference system, where points in the source region and observers are defined, respectively by the vectors \mathbf{y} and \mathbf{x} .

The local surface velocity is indicated by \mathbf{v} , to distinguish it from the fluid velocity \mathbf{u} . The case of an impermeable surface can be recovered by replacing everywhere in the equations $v_i = u_i$, for $i = 1, 2, 3$. The stationary case is obtained again as a particular case of the convective FW-H equation, when $\mathbf{U}_0 = 0$ is replaced in the equations.

B.1 Extension to the unbounded space

The governing laws, describing the unsteady motion of the fluid, are the compressible-viscous continuity and the momentum conservation equations. Expressing the latter in the Lagrangian formulation, using the index notation:

$$\frac{\partial \rho}{\partial t} + \frac{\partial (\rho u_j)}{\partial x_j} = 0, \quad (\text{B.2})$$

$$\frac{\partial (\rho u_i)}{\partial t} + \frac{\partial (\rho u_i u_j)}{\partial x_j} = -\frac{\partial P_{ij}}{\partial x_j}, \quad (\text{B.3})$$

where $P_{ij} = p\delta_{ij} - \tau_{ij}$.

Substituting B.1 in B.2:

$$\frac{\partial \rho_0}{\partial t} + \frac{\partial \rho'}{\partial t} + \frac{\partial (\rho U_{0j})}{\partial x_j} + \frac{\partial (\rho u'_j)}{\partial x_j} = 0. \quad (\text{B.4})$$

As ρ_0 and U_{0j} are constants, their derivatives are identically zero and B.4 can be simplified in:

$$\frac{\partial \rho'}{\partial t} + U_{0j} \frac{\partial \rho'}{\partial x_j} + \frac{\partial (\rho u'_j)}{\partial x_j} = 0. \quad (\text{B.5})$$

Substituting now B.1 in the momentum Equation B.3:

$$\begin{aligned} \frac{\partial (\rho U_{0i})}{\partial t} + \frac{\partial (\rho u'_i)}{\partial t} + \frac{\partial (\rho U_{0i} U_{0j})}{\partial x_j} + \frac{\partial (\rho U_{0i} u'_j)}{\partial x_j} + \\ \frac{\partial (\rho u'_i U_{0j})}{\partial x_j} + \frac{\partial (\rho u'_i u'_j)}{\partial x_j} = -\frac{\partial P_{ij}}{\partial x_j}. \end{aligned} \quad (\text{B.6})$$

Simplifying the derivatives of constant terms, B.6 can be rearranged as follows:

$$U_{0i} \left\{ \frac{\partial \rho}{\partial t} + \frac{\partial [\rho (U_{0j} + u'_j)]}{\partial x_j} \right\} + \frac{\partial (\rho u'_i)}{\partial t} + U_{0j} \frac{(\rho u'_i)}{\partial x_j} + \frac{\partial (\rho u'_i u'_j)}{\partial x_j} + \frac{\partial P'_{ij}}{\partial x_j} = 0. \quad (\text{B.7})$$

Noticing that the curly bracket term on the LHS is identically zero for the continuity Equation B.2, the final result for the momentum equation is:

$$\frac{\partial (\rho u'_i)}{\partial t} + U_{0j} \frac{(\rho u'_i)}{\partial x_j} + \frac{\partial (\rho u'_i u'_j + P'_{ij})}{\partial x_j} = 0. \quad (\text{B.8})$$

To extend Equations B.5 and B.8 to the unbounded space, the generalised function theory [105, 165] is applied. Specifically, two generalised functions need to be introduced, *i.e.* the Heaviside $H(\mathcal{F})$ and the Dirac $\delta(\mathcal{F})$ functions.

The Dirac delta function is defined as zero-valued everywhere but for the support (the FW-H surface $\mathcal{F}(\mathbf{x}, t) = 0$ in this case), on which it diverges to infinite:

$$\delta(\mathcal{F}) = \begin{cases} +\infty, & \text{if } \mathcal{F} = 0 \\ 0, & \text{if } \mathcal{F} \neq 0. \end{cases} \quad (\text{B.9})$$

The Heaviside function is defined as:

$$H(\mathcal{F}) = \begin{cases} 1, & \text{if } \mathcal{F} > 0 \\ 0, & \text{if } \mathcal{F} < 0. \end{cases} \quad (\text{B.10})$$

It is constant everywhere, meaning nought-valued derivative, except for the support $\mathcal{F}(\mathbf{x}, t) = 0$ where it presents a jump, responsible for the divergence of the first derivative to infinite. This naturally leads to introducing the following property satisfied by the Heaviside function:

$$\frac{\partial H(\mathcal{F})}{\partial \mathcal{F}} = \delta(\mathcal{F}), \quad (\text{B.11})$$

that expresses the equivalence between the Dirac delta function, and the first derivative of the Heaviside function [105].

The first step towards the derivation of the generalised conservation equations consists in multiplying B.5 and B.8 by the Heaviside function H :

$$H \frac{\partial \rho'}{\partial t} + H U_{0j} \frac{\partial \rho'}{\partial x_j} + H \frac{\partial (\rho u'_j)}{\partial x_j} = 0, \quad (\text{B.12})$$

$$H \frac{\partial (\rho u'_i)}{\partial t} + H U_{0j} \frac{\partial (\rho u'_i)}{\partial x_j} + H \frac{\partial (\rho u'_i u'_j + P'_{ij})}{\partial x_j} = 0. \quad (\text{B.13})$$

It can be noticed that in B.12 and in B.13 the Heaviside function appears multiplied by a partial derivative. The following relation, based on the chain rule, can therefore be used to get the generalised conservation equations:

$$H \frac{\partial \zeta}{\partial \chi} = \frac{\partial (H \zeta)}{\partial \chi} - \zeta \frac{H}{\partial \chi}, \quad (\text{B.14})$$

where ζ and χ are generic dependent and independent variables, respectively. The result is expressed by the following equations:

$$\begin{aligned} \frac{\partial (H \rho')}{\partial t} + U_{0j} \frac{\partial (H \rho')}{\partial x_j} + \frac{\partial (H \rho u'_j)}{\partial x_j} = \\ \rho' \frac{\partial H}{\partial t} + U_{0j} \rho' \frac{\partial H}{\partial x_j} + \rho u'_j \frac{\partial H}{\partial x_j}, \end{aligned} \quad (\text{B.15})$$

$$\begin{aligned} \frac{\partial (H \rho u'_i)}{\partial t} + U_{0j} \frac{\partial (H \rho u'_i)}{\partial x_j} + \frac{\partial [H (\rho u'_i u'_j + P'_{ij})]}{\partial x_j} = \\ \rho u'_i \frac{\partial H}{\partial t} + U_{0j} \rho u'_i \frac{\partial H}{\partial x_j} + (\rho u'_i u'_j + P'_{ij}) \frac{\partial H}{\partial x_j}. \end{aligned} \quad (\text{B.16})$$

By the use of Equation B.11, the Heaviside function time and space derivatives, appearing in B.15 and in B.16, can be expressed as:

$$\frac{\partial H(\mathcal{F})}{\partial t} = \delta(\mathcal{F}) \frac{\partial \mathcal{F}}{\partial t}, \quad (\text{B.17})$$

$$\frac{\partial H(\mathcal{F})}{\partial x_j} = \delta(\mathcal{F}) \frac{\partial \mathcal{F}}{\partial x_j}. \quad (\text{B.18})$$

The space and the time derivative of function $\mathcal{F}(\mathbf{x}, t)$ in B.17 and in B.18 can be simplified by considering that they are multiplied by the delta function $\delta(\mathcal{F})$, which sifts the values of the derivatives on the integration surface $\mathcal{F}(\mathbf{x}, t) = 0$ itself.

The function $\mathcal{F}(\mathbf{x}, t)$ satisfies the following properties:

$$\frac{\partial \mathcal{F}(\mathbf{x}, t)}{\partial x_j} = \hat{n}_j, \quad (\text{B.19})$$

$$\frac{D \mathcal{F}(\mathbf{x}, t)}{Dt} = 0, \quad (\text{B.20})$$

expressing the value of the gradient and of the total time derivative of the function \mathcal{F} . The surface $\mathcal{F}(\mathbf{x}, t) = 0$ is assumed by definition to satisfy the property $\nabla \mathcal{F} = \hat{\mathbf{n}}$, as recalled in the previous section. The total time derivative of the function \mathcal{F} is identically zero when estimated on the integration surface itself, where \mathcal{F} is constant

by definition. The partial time derivative of \mathcal{F} can then be expressed, using B.20, as follows:

$$\frac{\partial \mathcal{F}}{\partial t} = -\frac{\partial \mathcal{F}}{\partial x_j} \frac{\partial x_j}{\partial t} = -v_j \hat{n}_j. \quad (\text{B.21})$$

Replacing B.19 in B.18 and B.21 in B.17, the time and space derivatives of the Heaviside function become:

$$\frac{\partial H(\mathcal{F})}{\partial t} = -\delta(\mathcal{F}) v_j \hat{n}_j, \quad (\text{B.22})$$

$$\frac{\partial H(\mathcal{F})}{\partial x_j} = \delta(\mathcal{F}) \hat{n}_j. \quad (\text{B.23})$$

The generalised conservation equations B.15 and B.16 can then be rearranged as:

$$\frac{\partial (H\rho')}{\partial t} + U_{0j} \frac{\partial (H\rho')}{\partial x_j} + \frac{\partial (H\rho u'_j)}{\partial x_j} = \delta(\mathcal{F}) Q_j^{(c)} \hat{n}_j, \quad (\text{B.24})$$

$$\frac{\partial (H\rho u'_i)}{\partial t} + U_{0j} \frac{\partial (H\rho u'_i)}{\partial x_j} + \frac{\partial [H(\rho u'_i u'_j + P'_{ij})]}{\partial x_j} = \delta(\mathcal{F}) L_{ij}^{(c)} \hat{n}_j, \quad (\text{B.25})$$

where (c) stands for “convective”, and the convective mass and momentum source terms are given by:

$$Q_j^{(c)} = \rho (u'_j + U_{0j} - v_j) + \rho_0 (v_j - U_{0j}), \quad (2.25 \text{ restated})$$

$$L_{ij}^{(c)} = \rho u'_i (u'_j + U_{0j} - v_j) + P'_{ij}. \quad (2.26 \text{ restated})$$

B.2 Lighthill rearrangement

The rearrangement of the generalised conservation equations to get the convective FW-H equation consists in two steps that are described in this section:

1. the following term is added to both sides of the generalised momentum equation:

$$c_0^2 \frac{\partial (H\rho')}{\partial x_i} = c_0^2 \frac{\partial (H\rho' \delta_{ij})}{\partial x_j}; \quad (\text{B.26})$$

2. the divergence of the generalised momentum equation is subtracted to the time derivative of the generalised continuity equation:

$$\partial/\partial t [\text{continuity}] - \partial/\partial x_i [\text{momentum}]_i. \quad (\text{B.27})$$

Item 1 and 2 are actually applied in the reverse order in the original Lighthill formulation, with a double space derivative term added in item 1. However, the result is equivalent.

Adding B.26 to both sides of B.25:

$$\frac{\partial (H\rho u'_i)}{\partial t} + c_0^2 \frac{\partial (H\rho')}{\partial x_i} + U_{0j} \frac{\partial (H\rho u'_i)}{\partial x_j} = -\frac{\partial [H(\mathcal{F})T_{ij}]}{\partial x_j} + \delta(\mathcal{F})L_{ij}^{(c)}\hat{n}_j, \quad (\text{B.28})$$

where $T_{ij} = \rho u'_i u'_j + P'_{ij} - c_0^2 \rho' \delta_{ij} = \rho u'_i u'_j + (p' - c_0^2 \rho') \delta_{ij} - \tau_{ij}$ is the Lighthill stress tensor.

Applying item 2 to Equations B.24 and B.28, and moving all the source terms to the RHS:

$$\left[\frac{\partial^2}{\partial t^2} - c_0^2 \frac{\partial^2}{\partial x_i \partial x_i} + U_{0j} \frac{\partial^2}{\partial t \partial x_j} \right] (H\rho') - U_{0j} \frac{\partial^2 (H\rho u'_i)}{\partial x_i \partial x_j} = \frac{\partial [\delta(\mathcal{F})Q_j^{(c)}\hat{n}_j]}{\partial t} - \frac{\partial [\delta(\mathcal{F})L_{ij}^{(c)}\hat{n}_j]}{\partial x_i} + \frac{\partial^2 [H(\mathcal{F})T_{ij}]}{\partial x_i \partial x_j}. \quad (\text{B.29})$$

By taking the space derivative $\partial/\partial x_i$ of the generalised continuity Equation B.24, the last term on the LHS of B.29 can be expressed as follows:

$$-U_{0j} \frac{\partial^2 (H\rho u'_i)}{\partial x_i \partial x_j} = U_{0j} \frac{\partial^2 (H\rho')}{\partial x_j \partial t} + U_{0i} U_{0j} \frac{\partial^2 (H\rho')}{\partial x_i \partial x_j} - U_{0i} \frac{\partial [\delta Q_j^{(c)} \hat{n}_j]}{\partial x_i}. \quad (\text{B.30})$$

Replacing B.30 in B.29:

$$\square^{(c)2} (Hc_0^2 \rho') = \left[\frac{\partial}{\partial t} + U_{0i} \frac{\partial}{\partial x_i} \right] [\delta(\mathcal{F})Q_j^{(c)}\hat{n}_j] - \frac{\partial [\delta(\mathcal{F})L_{ij}^{(c)}\hat{n}_j]}{\partial x_i} + \frac{\partial^2 [H(\mathcal{F})T_{ij}]}{\partial x_i \partial x_j}, \quad (\text{2.23 restated})$$

where $\square^{(c)2}$ is the convective wave operator:

$$\square^{(c)2} = \left[\frac{1}{c_0^2} \frac{\partial^2}{\partial t^2} - \frac{\partial^2}{\partial x_j \partial x_j} + \frac{1}{c_0^2} 2U_{0j} \frac{\partial^2}{\partial t \partial x_j} + \frac{1}{c_0^2} U_{0i} U_{0j} \frac{\partial^2}{\partial x_i \partial x_j} \right]. \quad (\text{2.24 restated})$$

It is worth noticing that every index can assume the values 1, 2, 3 and when repeated indices appear, the summation convention is applied. For instance:

$$\frac{\partial}{\partial \chi_j} \zeta_j = \frac{\partial}{\partial \chi_i} \zeta_i = \frac{\partial}{\partial \chi_1} \zeta_1 + \frac{\partial}{\partial \chi_2} \zeta_2 + \frac{\partial}{\partial \chi_3} \zeta_3, \quad (\text{B.31})$$

where ζ and χ are generic dependent and independent (space) variables.

Equation 2.23 corresponds to the Najafi-Yazdi *et al.* [55] convective FW-H formulation, reducing to the Casalino [54] stationary FW-H formulation when $U_{0j} = 0$,

for $j = 1, 2, 3$ is replaced everywhere in the equation. The result (corresponding to Equation 2.11 in Section 2.2) is reported here for comparison:

$$\square^2 (Hc_0^2\rho') = \frac{\partial [\delta(\mathcal{F}) Q_j \hat{n}_j]}{\partial t} - \frac{\partial [\delta(\mathcal{F}) L_{ij} \hat{n}_j]}{\partial x_i} + \frac{\partial^2 [H(\mathcal{F}) T_{ij}]}{\partial x_i \partial x_j}, \quad (2.11 \text{ restated})$$

where:

$$Q_j = \rho (u'_j - v_j) + \rho_0 v_j, \quad (2.13 \text{ restated})$$

$$L_{ij} = \rho u'_i (u'_j - v_j) + P'_{ij}. \quad (2.14 \text{ restated})$$

The wave operator \square^2 (d'Alembertian) has the conventional expression for wave propagating in a medium at rest:

$$\square^2 = \left[\frac{1}{c_0^2} \frac{\partial^2}{\partial t^2} - \frac{\partial^2}{\partial x_j \partial x_j} \right]. \quad (2.12 \text{ restated})$$

The Lighthill Equation 2.1 can be obtained with the same procedure applied in this section, but considering the standard mass B.2 and momentum B.3 equations, instead of the generalised versions B.24 and B.25.

Appendix C

FW-H integral solution

The wave equation is a second-order linear Partial Differential Equation (PDE), describing the propagation of physical waves in a medium. Here the analysis is limited to sound waves propagation in the unbounded space, when no solid bodies interfere with the travelling waves. In this case, the solution to the inhomogeneous wave equation can be easily found in integral form, through the use of specific Green's functions (analytical, or numerical). For a quiescent medium, the 3D free-space Green's function [105] is used, which is expressed as follows:

$$G(\mathbf{x}, t, \mathbf{y}, \tau) = \begin{cases} \frac{\delta(g)}{4\pi r}, & \text{if } t \geq \tau \\ 0, & \text{if } t < \tau, \end{cases} \quad (2.15 \text{ restated})$$

where:

$$g = \tau - t + \frac{r}{c_0}, \quad r = |\mathbf{x} - \mathbf{y}|. \quad (2.16 \text{ restated})$$

In Equation 2.16, r is the distance covered by the wave travelling at the undisturbed-medium speed of sound c_0 , from the source to the observer locations, respectively indicated by \mathbf{y} and \mathbf{x} . τ and t refer to the emission and to the reception instant.

In the Lighthill and in the FW-H acoustic analogy application, the acoustic waves are supposed to propagate in a uniform medium at rest, and G can be used [54, 165] in order to find the acoustic pressure fluctuation at the observer location $p'(\mathbf{x}, t)$. Even though the FW-H acoustic analogy allows the presence of solid bodies, the latter are all enclosed by the integration surface, and confined to the region $\mathcal{F} < 0$ (see Figure 2.4 of Section 2.2). The propagation is investigated in the exterior domain $\mathcal{F} > 0$, that is free from solid boundaries.

The Green's function G represents the solution to the inhomogeneous wave equation, with source term given by an impulse at time $t = \tau$, at the position $\mathbf{x} = \mathbf{y}$ [44]. This means that G satisfies the following equation:

$$\square^2 G = \delta(\mathbf{x} - \mathbf{y}) \delta(t - \tau), \quad (\text{C.1})$$

where \square^2 is the linear wave operator and δ the Dirac delta function, both defined in the previous section.

As we can see from Equation 2.15, the free-space Green's function is defined as zero-valued when $t < \tau$, that represents the causality condition. Before the impulse $\delta(\mathbf{x} - \mathbf{y})$ is emitted at time $t = \tau$, there is no wave propagating in the free-space, because no source term acts on the fluid.

When the source term is different from the impulse $\delta(\mathbf{x} - \mathbf{y}) \delta(t - \tau)$, the integral solution is found by convolution of the source function with the Green's function G .

Let's consider the wave equation:

$$\square^2 p' = \mathcal{Q}(\mathbf{x}, t), \quad (\text{C.2})$$

with generic source function \mathcal{Q} . The solution to C.2 can be found by considering the source distribution \mathcal{Q} as a superposition of impulse point sources of the type $\delta(\mathbf{x} - \mathbf{y}) \delta(t - \tau)$. It is worth recalling that the wave equation is a linear PDE, meaning that the sum of two different solutions satisfies again the wave equation. The result is:

$$p'(\mathbf{x}, t) = \int_{-\infty}^t \int_{\mathbb{R}^3} \mathcal{Q}(\mathbf{y}, \tau) G(\mathbf{x}, t, \mathbf{y}, \tau) d^3 y d\tau. \quad (\text{C.3})$$

Substituting 2.15 in C.3 and applying the sifting property of the Dirac delta function [105]:

$$p'(\mathbf{x}, t) = \frac{1}{4\pi} \int_{-\infty}^t \int_{\mathbb{R}^3} \mathcal{Q}(\mathbf{y}, \tau) \frac{\delta(g)}{r} d^3 y d\tau = \frac{1}{4\pi} \int_{\mathbb{R}^3} \frac{\mathcal{Q}(\mathbf{y}, t - \frac{r}{c_0})}{r} d^3 y, \quad (\text{C.4})$$

where the source function \mathcal{Q} is estimated at $g = 0$.

Let's now consider the more interesting case of a source function of the dipole-type [44], characterized by the divergence of a generic vector function \mathcal{L} :

$$\square^2 p' = \frac{\partial}{\partial x_j} \mathcal{L}_j(\mathbf{x}, t). \quad (\text{C.5})$$

Applying the free-space Green's function:

$$p'(\mathbf{x}, t) = \frac{1}{4\pi} \int_{-\infty}^t \int_{\mathbb{R}^3} \frac{\partial}{\partial y_j} (\mathcal{L}_j(\mathbf{y}, \tau)) \frac{\delta(g)}{r} d^3 y d\tau. \quad (\text{C.6})$$

Before using the sifting property of the Dirac delta function, it is convenient to move the space derivative outside the integral. Integrating C.6 by parts:

$$p'(\mathbf{x}, t) = \frac{1}{4\pi} \int_{-\infty}^t \int_{\mathbb{R}^3} \mathcal{L}_j(\mathbf{y}, \tau) \left[-\frac{\partial}{\partial y_j} \left(\frac{\delta(g)}{r} \right) \right] d^3y d\tau. \quad (\text{C.7})$$

Noticing that:

$$-\frac{\partial}{\partial y_j} \left(\frac{\delta(g)}{r} \right) = \frac{\partial}{\partial x_j} \left(\frac{\delta(g)}{r} \right), \quad (\text{C.8})$$

Equation C.7 becomes:

$$p'(\mathbf{x}, t) = \frac{1}{4\pi} \int_{-\infty}^t \int_{\mathbb{R}^3} \mathcal{L}_j(\mathbf{y}, \tau) \frac{\partial}{\partial x_j} \left(\frac{\delta(g)}{r} \right) d^3y d\tau. \quad (\text{C.9})$$

The space derivative can now be taken outside the integral, being $\delta(g)$ and r the only variables depending on \mathbf{x} . By using the sifting property of the Dirac delta function, the solution of C.5 is finally expressed as follows:

$$p'(\mathbf{x}, t) = \frac{1}{4\pi} \frac{\partial}{\partial x_j} \int_{\mathbb{R}^3} \frac{1}{r} \left[\mathcal{L}_j \left(\mathbf{y}, t - \frac{r}{c_0} \right) \right] d^3y. \quad (\text{C.10})$$

Other useful source terms for the wave equation are the monopole and the quadrupole sources, expressed respectively by Equations C.11 and C.12, where \mathcal{Q} represents a generic source function, and \mathcal{T}_{ij} a generic tensor source function.

$$\square^2 p' = \frac{\partial}{\partial t} \mathcal{Q}(\mathbf{x}, t). \quad (\text{C.11})$$

$$\square^2 p' = \frac{\partial^2}{\partial x_i \partial x_j} \mathcal{T}_{ij}(\mathbf{x}, t). \quad (\text{C.12})$$

The same procedure, previously described for the dipole-type source term, leads to solutions C.13 and C.14, respectively for the monopole and for the quadrupole source.

$$p'(\mathbf{x}, t) = \frac{1}{4\pi} \frac{\partial}{\partial t} \int_{\mathbb{R}^3} \frac{1}{r} \left[\mathcal{Q} \left(\mathbf{y}, t - \frac{r}{c_0} \right) \right] d^3y. \quad (\text{C.13})$$

$$p'(\mathbf{x}, t) = \frac{1}{4\pi} \frac{\partial^2}{\partial x_i \partial x_j} \int_{\mathbb{R}^3} \frac{1}{r} \left[\mathcal{T}_{ij} \left(\mathbf{y}, t - \frac{r}{c_0} \right) \right] d^3y. \quad (\text{C.14})$$

The solution of the FW-H equation for a stationary medium (Equation 2.11) can be estimated by convolution with the Green's function 2.15. Equations C.13, C.10, and C.14 can be applied by replacing \mathcal{Q} , \mathcal{L}_j , and \mathcal{T}_{ij} with the specific source functions in Equation 2.11, respectively for the monopole, the dipole, and the quadrupole

source. This yields:

$$\begin{aligned}
4\pi p'(\mathbf{x}, t) &= \frac{\partial}{\partial t} \int_{-\infty}^t \int_{\mathbb{R}^3} Q_j \hat{n}_j \delta(\mathcal{F}) \frac{\delta(g)}{r} d^3y d\tau \\
&\quad - \frac{\partial}{\partial x_i} \int_{-\infty}^t \int_{\mathbb{R}^3} L_{ij} \hat{n}_j \delta(\mathcal{F}) \frac{\delta(g)}{r} d^3y d\tau \\
&\quad + \frac{\partial^2}{\partial x_i \partial x_j} \int_{-\infty}^t \int_{\mathbb{R}^3} H(\mathcal{F}) T_{ij} \frac{\delta(g)}{r} d^3y d\tau .
\end{aligned} \tag{C.15}$$

For the convective FW-H acoustic analogy formulation, the same procedure can be applied to determine the solution of Equation 2.23, but replacing the free-space Green's function (Equation 2.15) with the convective form [129]. Considering a medium moving in the x_1 direction (*e.g.* coinciding with the jet axis) at the uniform velocity $\mathbf{U}_0 = (U_0; 0; 0)$, the convective Green's function can be expressed as follows [55]:

$$G^{(c)}(\mathbf{x}, t, \mathbf{y}, \tau) = \begin{cases} \frac{\delta(g^{(c)})}{4\pi R^*}, & \text{if } t \geq \tau \\ 0, & \text{if } t < \tau \end{cases}, \tag{2.27 restated}$$

where:

$$g^{(c)} = \tau - t + \frac{R}{c_0}, \tag{2.28 restated}$$

$$R = \frac{-M_0(x_1 - y_1) + R^*}{\beta^2}, \tag{2.29 restated}$$

$$R^* = \sqrt{(x_1 - y_1)^2 + \beta^2 [(x_2 - y_2)^2 + (x_3 - y_3)^2]}, \tag{2.30 restated}$$

$$\beta = \sqrt{1 - M_0^2}, \quad M_0 = \frac{U_0}{c_0}. \tag{2.31 restated}$$

The convective Green's function shows a dependence on two distances R and R^* in place of the geometric distance $r = |\mathbf{x} - \mathbf{y}|$. Specifically, R indicates the distance travelled by the disturbance during $t - \tau$ (time interval between the emission and the reception), while R^* is the scaling factor with distance from the source in the convective formulation.

Figure C.1 shows schematically the radiation in a uniform flow, when the medium moves at velocity U_0 in the x_1 direction. The disturbance emitted at position \mathbf{y} at time τ propagates at the speed of sound of the undisturbed medium c_0 . Without co-flow ($U_0 = 0$), the disturbance would reach the position $\bar{\mathbf{x}}$ at a distance R from the source point after $t - \tau$. $\bar{\mathbf{x}}$ is the observer position as seen from (\mathbf{y}, τ) at the emission time τ . Because of the convection velocity, the disturbance reaches instead

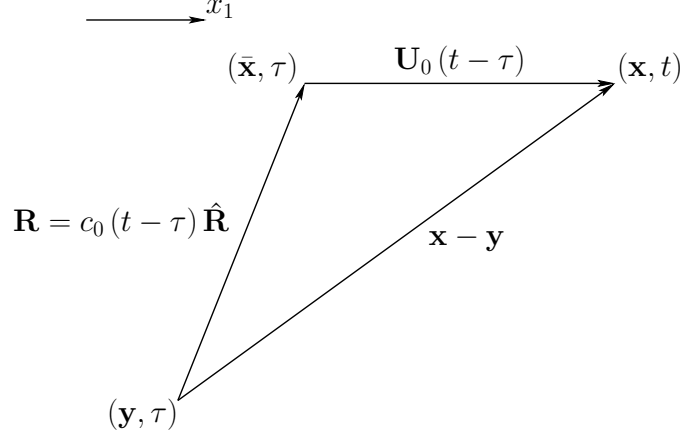


Figure C.1: Schematic of the radiation in a uniform flow with constant velocity U_0 in the x_1 direction.

position \mathbf{x} at t and the triangle shown in Figure C.1 can be drawn. R is the acoustic distance source-observer that coincides with the geometric distance r in a stationary medium problem.

Referring to Figure C.1, the following vectorial equation is satisfied:

$$\mathbf{r} - \mathbf{U}_0(t - \tau) = c_0(t - \tau) \hat{\mathbf{R}}. \quad (\text{C.16})$$

It is possible to estimate the magnitude of the vector on the LHS (Equation C.18), whose components are expressed explicitly in Equation C.17, where $r_i = x_i - y_i$.

$$\mathbf{r} - \mathbf{U}_0(t - \tau) = (r_1 - U_0(t - \tau); r_2; r_3). \quad (\text{C.17})$$

$$|\mathbf{r} - \mathbf{U}_0(t - \tau)|^2 = U_0^2(t - \tau)^2 - 2U_0r_1(t - \tau) + r_1^2 + r_2^2 + r_3^2. \quad (\text{C.18})$$

Therefore, Equation C.16 can be rearranged as:

$$(t - \tau)^2 (U_0^2 - c_0^2) - (t - \tau) 2r_1U_0 + r_1^2 + r_2^2 + r_3^2 = 0, \quad (\text{C.19})$$

that is a second order equation in the variable $(t - \tau)$. Estimating the latter:

$$(t - \tau) = \frac{r_1U_0 \pm \sqrt{r_1^2c_0^2 + (r_2^2 + r_3^2)(c_0^2 - U_0^2)}}{U_0^2 - c_0^2}, \quad (\text{C.20})$$

where the only physical solution is the one with a minus sign in front of the square root. The variable $(t - \tau)$ is positive for the causality condition, which establishes that disturbances cannot travel in the past. The denominator of Equation C.20 is

negative because a uniform subsonic co-flow is considered. Consequently, the solution with positive numerator is discarded.

Multiplying by c_0 both sides of Equation C.20 and rearranging:

$$c_0(t - \tau) = \frac{-r_1 M_0 + \sqrt{r_1^2 + (r_2^2 + r_3^2)(1 - M_0^2)}}{1 - M_0^2}. \quad (\text{C.21})$$

Using 2.30 and 2.31, the distance R is finally obtained:

$$R = c_0(t - \tau) = \frac{-r_1 M_0 + R^*}{\beta^2}. \quad (\text{C.22})$$

The acoustic distance R is used to define the support g of the Dirac delta function in $G^{(c)}$. $G^{(c)}$ allows the noise radiation at an arbitrary observer \mathbf{x} at time t to be estimated:

$$\begin{aligned} 4\pi p'(\mathbf{x}, t) = & \left[\frac{\partial}{\partial t} + U_0 \frac{\partial}{\partial x_1} \right] \int_{-\infty}^t \int_{\mathbb{R}^3} Q_j^{(c)} \hat{n}_j \delta(\mathcal{F}) \frac{\delta(g^{(c)})}{R^*} d^3 y d\tau \\ & - \frac{\partial}{\partial x_i} \int_{-\infty}^t \int_{\mathbb{R}^3} L_{ij}^{(c)} \hat{n}_j \delta(\mathcal{F}) \frac{\delta(g^{(c)})}{R^*} d^3 y d\tau \\ & + \frac{\partial^2}{\partial x_i \partial x_j} \int_{-\infty}^t \int_{\mathbb{R}^3} H(\mathcal{F}) T_{ij} \frac{\delta(g^{(c)})}{R^*} d^3 y d\tau. \end{aligned} \quad (\text{C.23})$$

C.1 Solution in a uniformly moving medium

As discussed in Section 2.3, the acoustic radiation from unsteady turbulent flows is here approximated by considering exclusively the surface integral contributions. Therefore, Equation C.23 simplifies to:

$$4\pi p'(\mathbf{x}, t) \approx 4\pi p'_T(\mathbf{x}, t) + 4\pi p'_L(\mathbf{x}, t), \quad (\text{C.24})$$

with:

$$4\pi p'_T(\mathbf{x}, t) = \left[\frac{\partial}{\partial t} + U_0 \frac{\partial}{\partial x_1} \right] \int_{-\infty}^t \int_{\mathbb{R}^3} Q_j^{(c)} \hat{n}_j \delta(\mathcal{F}) \frac{\delta(g^{(c)})}{R^*} d^3 y d\tau, \quad (\text{C.25})$$

$$4\pi p'_L(\mathbf{x}, t) = - \frac{\partial}{\partial x_i} \int_{-\infty}^t \int_{\mathbb{R}^3} L_{ij}^{(c)} \hat{n}_j \delta(\mathcal{F}) \frac{\delta(g^{(c)})}{R^*} d^3 y d\tau. \quad (\text{C.26})$$

T and L stand for thickness and loading noise, respectively. This terminology stems from rotor noise applications [106].

Equations C.25 and C.26 are now rearranged to get the Najafi-Yazdi *et al.* [55] formulation (Equations 2.32 and 2.33), that is more convenient to be applied from a

numerical viewpoint. From now on the superscript (c) is omitted, bearing in mind that the convective case is developed. In the stationary formulation, the same steps can be applied.

Before giving the mathematical details, let's define the following variables, for convenience [55]:

$$\tilde{\mathbf{R}}^* = \nabla R^* = \left(\frac{x_1 - y_1}{R^*}; \frac{x_2 - y_2}{R^*} \beta^2; \frac{x_3 - y_3}{R^*} \beta^2 \right), \quad (2.34 \text{ restated})$$

$$\tilde{\mathbf{R}} = \nabla R = \left(\frac{1}{\beta^2} \left(-M_0 + \frac{x_1 - y_1}{R^*} \right); \frac{x_2 - y_2}{R^*}; \frac{x_3 - y_3}{R^*} \right). \quad (2.35 \text{ restated})$$

Besides, it can be noticed that all the variables in the thickness and in the loading noise integrals depend on \mathbf{y} and τ only, except for the ratio $\delta(g)/R^*$, coming from the Green's function, which depends on $(\mathbf{x}, t, \mathbf{y}, \tau)$. Therefore, the space derivative can be moved inside the integrals, yielding:

$$\begin{aligned} 4\pi p'_T(\mathbf{x}, t) &= \frac{\partial}{\partial t} \int_{-\infty}^t \int_{\mathbb{R}^3} Q_j \hat{n}_j \delta(\mathcal{F}) \frac{\delta(g)}{R^*} d^3y d\tau \\ &+ U_0 \int_{-\infty}^t \int_{\mathbb{R}^3} Q_j \hat{n}_j \delta(\mathcal{F}) \frac{\partial}{\partial x_1} \left[\frac{\delta(g)}{R^*} \right] d^3y d\tau, \end{aligned} \quad (C.27)$$

$$4\pi p'_L(\mathbf{x}, t) = - \int_{-\infty}^t \int_{\mathbb{R}^3} L_{ij} \hat{n}_j \delta(\mathcal{F}) \frac{\partial}{\partial x_i} \left[\frac{\delta(g)}{R^*} \right] d^3y d\tau. \quad (C.28)$$

C.1.1 Change of variable $\mathbf{y} \longrightarrow \boldsymbol{\eta}$

Let's now consider a moving reference frame $\boldsymbol{\eta}$, fixed to the FW-H surface $\mathcal{F} = 0$. Assuming that the surface translates and rotates only, without contracting or dilating [55], the Jacobian J of the transformation $\mathbf{y} \longrightarrow \boldsymbol{\eta}$ is equal to unity. Consequently, the change of variable is straightforward:

$$d^3y = d^3\eta. \quad (C.29)$$

Applying C.29 to the thickness and to the loading noise contributions yields:

$$\begin{aligned} 4\pi p'_T(\mathbf{x}, t) &= \frac{\partial}{\partial t} \int_{-\infty}^t \int_{\mathbb{R}^3} Q_j \hat{n}_j \delta(\mathcal{F}) \frac{\delta(g)}{R^*} d^3\eta d\tau \\ &+ U_0 \int_{-\infty}^t \int_{\mathbb{R}^3} Q_j \hat{n}_j \delta(\mathcal{F}) \frac{\partial}{\partial x_1} \left[\frac{\delta(g)}{R^*} \right] d^3\eta d\tau, \end{aligned} \quad (C.30)$$

$$4\pi p'_L(\mathbf{x}, t) = - \int_{-\infty}^t \int_{\mathbb{R}^3} L_{ij} \hat{n}_j \delta(\mathcal{F}) \frac{\partial}{\partial x_i} \left[\frac{\delta(g)}{R^*} \right] d^3\eta d\tau. \quad (C.31)$$

C.1.2 Change of derivative $\frac{\partial}{\partial x_i} \longrightarrow \frac{\partial}{\partial t}$

In order to convert the space derivative to a time derivative (more convenient to be calculated numerically), it is necessary to estimate the term $\partial/\partial x_i (\delta(g)/R^*)$ in Equations C.30 and C.31. Applying the chain rule:

$$\frac{\partial}{\partial x_i} \left(\frac{\delta(g)}{R^*} \right) = \frac{\partial \delta(g)}{\partial g} \frac{\tilde{R}_i}{c_0 R^*} - \frac{\delta(g) \tilde{R}_i^*}{R^{*2}}. \quad (\text{C.32})$$

The first term on the RHS can be expressed as follows:

$$-\frac{1}{c_0} \frac{\partial}{\partial t} \left(\frac{\tilde{R}_i \delta(g)}{R^*} \right) = -\frac{\tilde{R}_i}{c_0 R^*} \frac{\partial \delta(g)}{\partial g} \frac{\partial g}{\partial t} = \frac{\partial \delta(g)}{\partial g} \frac{\tilde{R}_i}{c_0 R^*}. \quad (\text{C.33})$$

Replacing C.33 in C.32:

$$\frac{\partial}{\partial x_i} \left(\frac{\delta(g)}{R^*} \right) = -\frac{1}{c_0} \frac{\partial}{\partial t} \left(\frac{\tilde{R}_i \delta(g)}{R^*} \right) - \frac{\delta(g) \tilde{R}_i^*}{R^{*2}}. \quad (\text{C.34})$$

Using Equation C.34, the thickness and the loading noise (Equations C.30 and C.31) are rearranged as follows:

$$4\pi p'_T(\mathbf{x}, t) = \frac{\partial}{\partial t} \int_{-\infty}^t \int_{\mathbb{R}^3} Q_j \hat{n}_j \delta(\mathcal{F}) \frac{\delta(g)}{R^*} (1 - M_0 \tilde{R}_1) d^3 \eta d\tau - U_0 \int_{-\infty}^t \int_{\mathbb{R}^3} Q_j \hat{n}_j \delta(\mathcal{F}) \frac{\tilde{R}_1^* \delta(g)}{R^{*2}} d^3 \eta d\tau, \quad (\text{C.35})$$

$$4\pi p'_L(\mathbf{x}, t) = \frac{\partial}{\partial t} \int_{-\infty}^t \int_{\mathbb{R}^3} L_{ij} \hat{n}_j \delta(\mathcal{F}) \frac{\tilde{R}_i \delta(g)}{c_0 R^*} d^3 \eta d\tau + \int_{-\infty}^t \int_{\mathbb{R}^3} L_{ij} \hat{n}_j \delta(\mathcal{F}) \frac{\tilde{R}_i^* \delta(g)}{R^{*2}} d^3 \eta d\tau. \quad (\text{C.36})$$

C.1.3 Change of variable $\tau \longrightarrow g$

A second variable substitution is applied, for the time τ . The time derivative of function g needs to be estimated. The latter is expressed as:

$$\frac{\partial g}{\partial \tau} = 1 + \frac{1}{c_0} \frac{\partial R}{\partial y_i} \frac{\partial y_i}{\partial \tau} = 1 - \frac{1}{c_0} \frac{\partial R}{\partial x_i} \frac{\partial y_i}{\partial \tau} = 1 - M_R, \quad (\text{C.37})$$

with:

$$M_R = \frac{\tilde{R}_i v_i}{c_0}. \quad (\text{C.38})$$

In Equation C.38, v_i is the surface velocity component in the i^{th} direction, while \tilde{R} is the radiation vector that does not coincide with $\mathbf{r} = \mathbf{x} - \mathbf{y}$, due to the convection with the uniform flow at velocity U_0 . Consequently, M_R represents the radiation

Mach number of a source point on the surface $\mathcal{F} = 0$ towards the observer position \mathbf{x} , including the convection effects. Using C.37, the relation between the differentials dg and $d\tau$ can be estimated:

$$dg = \frac{\partial g}{\partial \tau} d\tau = (1 - M_R) d\tau \longrightarrow d\tau = \frac{dg}{1 - M_R}. \quad (\text{C.39})$$

Applying C.39 to Equations C.35 and C.36:

$$\begin{aligned} 4\pi p'_T(\mathbf{x}, t) &= \frac{\partial}{\partial t} \int_{-\infty}^t \int_{\mathbb{R}^3} Q_j \hat{n}_j \delta(\mathcal{F}) \frac{\delta(g)}{(1 - M_R) R^*} (1 - M_0 \tilde{R}_1) d^3\eta dg \\ &\quad - U_0 \int_{-\infty}^t \int_{\mathbb{R}^3} Q_j \hat{n}_j \delta(\mathcal{F}) \frac{\tilde{R}_1^* \delta(g)}{(1 - M_R) R^{*2}} d^3\eta dg, \end{aligned} \quad (\text{C.40})$$

$$\begin{aligned} 4\pi p'_L(\mathbf{x}, t) &= \frac{\partial}{\partial t} \int_{-\infty}^t \int_{\mathbb{R}^3} L_{ij} \hat{n}_j \delta(\mathcal{F}) \frac{\tilde{R}_i \delta(g)}{(1 - M_R) c_0 R^*} d^3\eta dg \\ &\quad + \int_{-\infty}^t \int_{\mathbb{R}^3} L_{ij} \hat{n}_j \delta(\mathcal{F}) \frac{\tilde{R}_i^* \delta(g)}{(1 - M_R) R^{*2}} d^3\eta dg. \end{aligned} \quad (\text{C.41})$$

C.1.4 Sifting property of the Dirac delta functions $\delta(\mathcal{F})$, $\delta(g)$

In the thickness and in the loading noise contributions, the Dirac delta functions $\delta(\mathcal{F})$ and $\delta(g)$ sift the integrals on their respective support. Specifically, $\delta(\mathcal{F})$ restrict the volume integral to a surface one on $\mathcal{F} = 0$, while $\delta(g)$ allows the estimation of the time integral, by selecting the value of the variables on $g = 0 \longrightarrow \tau_e = t - \frac{R}{c_0}$. The result is here reported in Equations C.42 and C.43, where all the variables inside the integrals are estimated on the FW-H surface $\mathcal{F} = 0$, at the emission instant τ_e .

$$\begin{aligned} 4\pi p'_T(\mathbf{x}, t) &= \frac{\partial}{\partial t} \int_{\mathcal{F}=0} \left[\frac{Q_j \hat{n}_j}{(1 - M_R) R^*} (1 - M_0 \tilde{R}_1) \right]_{\tau_e} d\eta^2 \\ &\quad - U_0 \int_{\mathcal{F}=0} \left[\frac{Q_j \hat{n}_j \tilde{R}_1^*}{(1 - M_R) R^{*2}} \right]_{\tau_e} d\eta^2. \end{aligned} \quad (\text{C.42})$$

$$\begin{aligned} 4\pi p'_L(\mathbf{x}, t) &= \frac{1}{c_0} \frac{\partial}{\partial t} \int_{\mathcal{F}=0} \left[\frac{L_{ij} \hat{n}_j \tilde{R}_i}{(1 - M_R) R^*} \right]_{\tau_e} d\eta^2 \\ &\quad + \int_{\mathcal{F}=0} \left[\frac{L_{ij} \hat{n}_j \tilde{R}_i^*}{(1 - M_R) R^{*2}} \right]_{\tau_e} d\eta^2. \end{aligned} \quad (\text{C.43})$$

C.1.5 Change of derivative $\frac{\partial}{\partial t} \longrightarrow \frac{\partial}{\partial \tau}$

It is possible to demonstrate that the time derivative in the thickness and in the loading noise (Equations C.42 and C.43) can be moved inside the integral. This is

possible through application of the Leibniz Rule:

$$\begin{aligned} \frac{d}{dt} \int_{A(t)}^{B(t)} \mathcal{Q}(\tau; t) d\tau &= \int_{A(t)}^{B(t)} \frac{\partial}{\partial t} \mathcal{Q}(\tau; t) d\tau + \dot{B}(t) \mathcal{Q}[B(t); t] \\ &\quad - \dot{A}(t) \mathcal{Q}[A(t); t] . \end{aligned} \quad (\text{C.44})$$

The additional terms generated from the application of Equation C.44 to Equations C.42 and C.43 are identically zero [55], yielding:

$$\begin{aligned} 4\pi p'_T(\mathbf{x}, t) &= \int_{\mathcal{F}=0} \frac{\partial}{\partial t} \left[\frac{Q_j \hat{n}_j}{(1 - M_R) R^*} (1 - M_0 \tilde{R}_1) \right]_{\tau_e} d\eta^2 \\ &\quad - U_0 \int_{\mathcal{F}=0} \left[\frac{Q_j \hat{n}_j \tilde{R}_1^*}{(1 - M_R) R^{*2}} \right]_{\tau_e} d\eta^2 , \end{aligned} \quad (\text{C.45})$$

$$\begin{aligned} 4\pi p'_L(\mathbf{x}, t) &= \frac{1}{c_0} \int_{\mathcal{F}=0} \frac{\partial}{\partial t} \left[\frac{L_{ij} \hat{n}_j \tilde{R}_i}{(1 - M_R) R^*} \right]_{\tau_e} d\eta^2 \\ &\quad + \int_{\mathcal{F}=0} \left[\frac{L_{ij} \hat{n}_j \tilde{R}_i^*}{(1 - M_R) R^{*2}} \right]_{\tau_e} d\eta^2 . \end{aligned} \quad (\text{C.46})$$

To convert the t derivative to a source time τ derivative, the following formula can be applied:

$$\frac{\partial}{\partial t} = \left[\frac{\partial}{\partial \tau} \frac{\partial \tau}{\partial t} \right]_{\tau_e} , \quad (\text{C.47})$$

where the derivative $\partial \tau / \partial t$ needs to be estimated at emission time τ_e . It can be noticed that the time derivative of function g at τ_e is identically zero, yielding:

$$\left. \frac{\partial g}{\partial t} \right|_{\tau_e} = \frac{\partial \tau}{\partial t} - 1 + \frac{1}{c_0} \frac{\partial R}{\partial t} = 0. \quad (\text{C.48})$$

The last term on the RHS of Equation C.48 can be expressed as follows:

$$\left. \frac{1}{c_0} \frac{\partial R}{\partial t} \right|_{\tau_e} = \frac{1}{c_0} \frac{\partial R}{\partial y_i} \frac{\partial y_i}{\partial \tau} \frac{\partial \tau}{\partial t} = -\frac{1}{c_0} \tilde{R}_i v_i \frac{\partial \tau}{\partial t} = -M_R \frac{\partial \tau}{\partial t}. \quad (\text{C.49})$$

Replacing C.49 in C.48 and rearranging:

$$\left. \frac{\partial \tau}{\partial t} \right|_{\tau_e} = \frac{1}{1 - M_R}. \quad (\text{C.50})$$

Finally, Equation C.47 can be reformulated as follows:

$$\frac{\partial}{\partial t} = \left[\frac{1}{1 - M_R} \frac{\partial}{\partial \tau} \right]_{\tau_e} , \quad (\text{C.51})$$

and the thickness and the loading noise become:

$$\begin{aligned} 4\pi p'_T(\mathbf{x}, t) &= \int_{\mathcal{F}=0} \left[\frac{1}{1 - M_R} \frac{\partial}{\partial \tau} \left(\frac{Q_j \hat{n}_j}{(1 - M_R) R^*} (1 - M_0 \tilde{R}_1) \right) \right]_{\tau_e} d\eta^2 \\ &\quad - U_0 \int_{\mathcal{F}=0} \left[\frac{Q_j \hat{n}_j \tilde{R}_1^*}{(1 - M_R) R^{*2}} \right]_{\tau_e} d\eta^2 , \end{aligned} \quad (\text{C.52})$$

$$\begin{aligned}
4\pi p'_L(\mathbf{x}, t) &= \frac{1}{c_0} \int_{\mathcal{F}=0} \left[\frac{1}{1 - M_R} \frac{\partial}{\partial \tau} \left(\frac{L_{ij} \hat{n}_j \tilde{R}_i}{(1 - M_R) R^*} \right) \right]_{\tau_e} d\eta^2 \\
&+ \int_{\mathcal{F}=0} \left[\frac{L_{ij} \hat{n}_j \tilde{R}_i^*}{(1 - M_R) R^{*2}} \right]_{\tau_e} d\eta^2 .
\end{aligned} \tag{C.53}$$

C.1.6 Estimation of $\frac{\partial}{\partial \tau}$ by the chain rule

The last step to get the final solution consists in applying the chain rule to the time derivative in Equations C.52 and C.53. In the thickness noise, the time derivative can be decomposed into two terms:

$$\begin{aligned}
\frac{\partial}{\partial \tau} \left(\frac{Q_j \hat{n}_j}{(1 - M_R) R^*} (1 - M_0 \tilde{R}_1) \right) &= \frac{\partial}{\partial \tau} \left(\frac{Q_j \hat{n}_j}{(1 - M_R) R^*} \right) \\
&- M_0 \frac{\partial}{\partial \tau} \left(\frac{Q_j \hat{n}_j \tilde{R}_1}{(1 - M_R) R^*} \right) .
\end{aligned} \tag{C.54}$$

Applying the chain rule to both terms on the RHS of C.54:

$$\begin{aligned}
\frac{\partial}{\partial \tau} \left(\frac{Q_j \hat{n}_j}{(1 - M_R) R^*} \right) &= \frac{\dot{Q}_j \hat{n}_j + Q_j \dot{\hat{n}}_j}{(1 - M_R) R^*} \\
&- \frac{\partial R^*}{\partial \tau} \frac{Q_j \hat{n}_j}{(1 - M_R) R^{*2}} \\
&+ \frac{\partial M_R}{\partial \tau} \frac{Q_j \hat{n}_j}{(1 - M_R)^2 R^*} ,
\end{aligned} \tag{C.55}$$

$$\begin{aligned}
\frac{\partial}{\partial \tau} \left(\frac{Q_j \hat{n}_j \tilde{R}_1}{(1 - M_R) R^*} \right) &= \frac{\dot{Q}_j \hat{n}_j \tilde{R}_1 + Q_j \dot{\hat{n}}_j \tilde{R}_1 + Q_j \hat{n}_j \dot{\tilde{R}}_1}{(1 - M_R) R^*} \\
&- \frac{\partial R^*}{\partial \tau} \frac{Q_j \hat{n}_j \tilde{R}_1}{(1 - M_R) R^{*2}} \\
&+ \frac{\partial M_R}{\partial \tau} \frac{Q_j \hat{n}_j \tilde{R}_1}{(1 - M_R)^2 R^*} .
\end{aligned} \tag{C.56}$$

For the loading noise, the chain rule is applied again, yielding:

$$\begin{aligned}
\frac{\partial}{\partial \tau} \left(\frac{L_{ij} \hat{n}_j \tilde{R}_i}{(1 - M_R) R^*} \right) &= \frac{\dot{L}_{ij} \hat{n}_j \tilde{R}_i + L_{ij} \dot{\hat{n}}_j \tilde{R}_i + L_{ij} \hat{n}_j \dot{\tilde{R}}_i}{(1 - M_R) R^*} \\
&- \frac{\partial R^*}{\partial \tau} \frac{L_{ij} \hat{n}_j \tilde{R}_i}{(1 - M_R) R^{*2}} \\
&+ \frac{\partial M_R}{\partial \tau} \frac{L_{ij} \hat{n}_j \tilde{R}_i}{(1 - M_R)^2 R^*} .
\end{aligned} \tag{C.57}$$

Finally, replacing C.55, C.56, and C.57 in Equations C.52 and C.53, the convective acoustic analogy solution is obtained, in the form of Equations 2.32 and 2.33 of Section 2.2.4.

Appendix D

New CFW-H tool validation for stationary test cases

In this section, the CFW-H acoustic analogy of Section 2.2.4 is applied to predict noise radiation in a medium at rest. The first test considers four elementary noise sources, which are a monopole, a dipole, a longitudinal quadrupole, and a lateral quadrupole, radiating in a uniform medium at rest ($M_0 = 0$). The configuration is the same as the one reported in Section 3.1, and Figure 3.1 displays the FW-H surface shape and the observer positions. Specifically, the integration surface has a prismatic shape with cross-section $a \times a$ and length 2ℓ and the observers are distributed on a circular array on the plane $x_3 = 0$. The array of radius r_o is centred at the origin and the observers are equally spaced at constant angular increments of 9° .

The sources are placed at the origin of the Cartesian reference system, at the location of $s^{(1)}$ in Figure 3.1. Their strength is normalised to get a Sound Pressure Level of 80 dB re 20 μPa at 33.33λ from the source in the direction of the maximum noise radiation, as in Section 3.1. Due to the orientation of the sources, the latter coincides with the x_2 -axis for both the dipole and the longitudinal quadrupole, which are characterised by a far-field noise pattern in a figure-of-eight shape. The lateral quadrupole has instead a four-leaved clover pattern, with four directions of maximum radiation at $0^\circ \pm 45^\circ$ and at $180^\circ \pm 45^\circ$ from the positive x_1 -axis.

The emission frequency of all four elementary sources is $f = 5.67$ kHz ($\lambda = 0.06$ m), and $N_T = 40$ points are used to discretise the period T of the acoustic waves. The FW-H surface is defined as a cube with side $a = 2\ell = 2\lambda$, centred at the origin of the

Cartesian axes. $N_\lambda = 20$ points per wavelength are used to provide an appropriate spatial discretization, as in Section 3.1.

The noise radiation directivity is reported in Figure D.1, for two values of the observers polar coordinate r_o , measured from the origin of the Cartesian reference system, *i.e.* $r_{o,1} = 10\lambda$ and $r_{o,2} = 20\lambda = 2r_{o,1}$. All the sound sources are placed at the origin of the reference system itself, so that r_o is also the acoustic radial distance source-observer $r = |\mathbf{x} - \mathbf{y}|$. The typical decay of the acoustic pressure fluctuation amplitude with the inverse of r is expected to be obtained for the acoustic pressure fluctuation in the far-field, that is $p' \propto 1/r$.

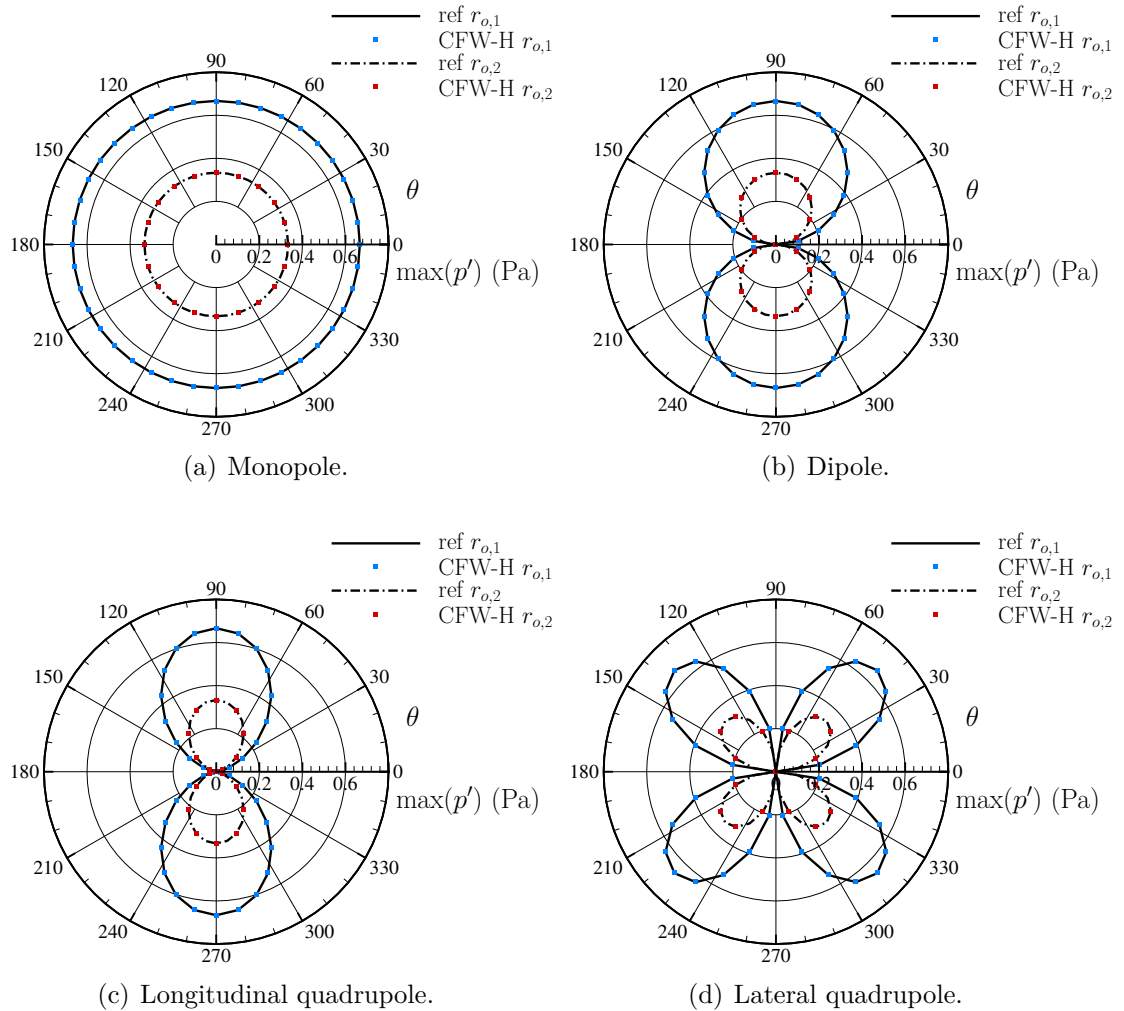
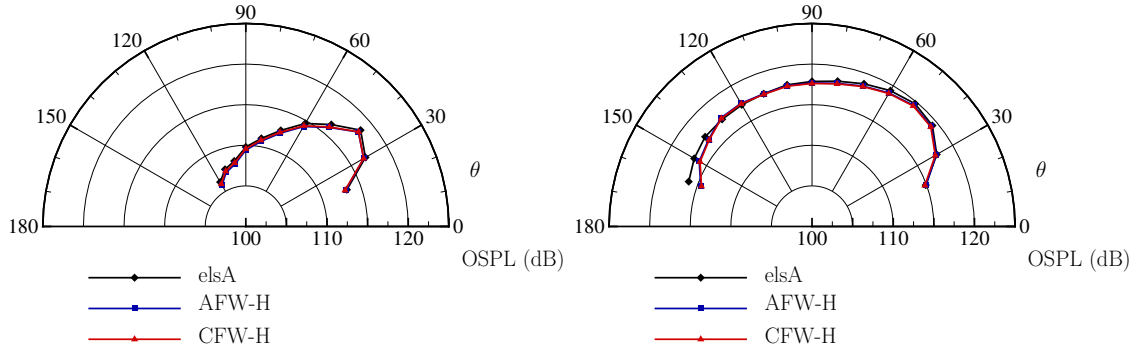


Figure D.1: Radiation in a stationary medium from elementary noise sources, located at the origin, to observers placed at radial distances $r_{o,1} = 10\lambda$ and $r_{o,2} = 20\lambda$ from the origin. $a = 2\lambda$, $\ell = \lambda$, $\lambda = 0.06$ m, $N_T = 40$, and $N_\lambda = 20$.

As shown from Figure D.1, the numerical prediction denoted by “CFW-H” closely

matches the analytical solution denoted by “ref” for all the sources considered, in terms of the acoustic pressure amplitude and directivity. The acoustic pressure amplitude decay with increasing radial distance r is also correctly captured, with a 0.5 ratio between the acoustic pressure amplitude at $r_{o,2} = 20\lambda$ and at $r_{o,1} = 10\lambda$. These results provide a sanity check on the correct implementation of the convective FW-H acoustic analogy formulation in the new Python CFW-H tool.



(a) Single-stream subsonic isothermal jet (Section 4.1.1). $M_j = 0.9$, $Re = 4 \times 10^5$, $r_o = 30D_e$. (b) Dual-stream under-expanded cold jet (Section 4.2). $M_{jp} = 0.89$, $M_{js} = 1.20$, $Re_p = 0.57 \times 10^6$, $Re_s = 1.66 \times 10^6$, $r_o = 30D_s$.

Figure D.2: Overall Sound Pressure Level (OSPL) vs polar angle θ from stationary ($M_0 = 0$) jets, modelled by LES.

The outcome from a second test on the implementation of the CFW-H acoustic analogy is shown in Figure D.2, where Overall Sound Pressure Levels (OSPLs) are reported for the acoustic pressure fluctuation emitted by the subsonic single-stream jet and by the under-expanded dual-stream jet, discussed respectively in Sections 4.1.1 and 4.2. Three curves are reported in Figure D.2 that are the two numerical predictions from the new Python AFW-H and CFW-H tools, and the numerical reference solution by elsA [130]. The latter is indicated by black diamond symbols, while blue squares and red deltas denote the results obtained respectively with the AFW-H and with the CFW-H tool applied to the LES prediction by Biolchini [135], for the single-stream jet (Figure D.2(a)), and by Pérez [16], for the dual-stream jet (Figure D.2(b)).

The three curves match very well and the two Python implementations predict overlapping OSPLs, for both the single-stream and the dual-stream jet. A good

match is obtained at all polar angles over the range $20^\circ \leq \theta \leq 120^\circ$ for the single-stream jet in Figure D.2(a) and over the range $20^\circ \leq \theta < 160^\circ$ for the dual-stream jet in Figure D.2(b). A noticeable difference is shown in Figure D.2(b) only at $\theta = 160^\circ$, where the discrepancy between the elsA reference solution and the numerical prediction by the new FW-H tools reaches 1.6 dB.

The good match obtained in Figures D.1 and D.2 is just a starting point in the process of validation of the CFW-H tool. It proves the equivalence between the stationary (Section 2.2.3) and the convective (Section 2.2.4) FW-H acoustic analogy formulations, when $M_0 = 0$. Tests with a uniformly moving flow are performed in Chapter 5, for both elementary sources (Section 5.1) and jet noise problems (Section 5.2), to provide further confidence in the new CFW-H tool at $M_0 > 0$.

References

- [1] M. J. Lighthill, “On sound generated aerodynamically I. General theory,” *Proceedings of the Royal Society of London*, vol. 211, no. 1107, pp. 564–587, 1952.
- [2] M. J. Lighthill, “Jet noise,” *AIAA Journal*, vol. 1, no. 7, pp. 1507–1517, 1963.
- [3] T. Tyler, “IATA Annual Review 2016.” IATA-2016, June 2016. 72nd Annual General Meeting of the International Air Transport Association (IATA), Dublin, Ireland.
- [4] C. K. W. Tam, “Jet noise: since 1952,” *Theoretical and Computational Fluid Dynamics*, vol. 10, no. 1–4, pp. 393–405, 1998.
- [5] M. L. Shur, P. R. Spalart, and M. K. Strelets, “Noise prediction for increasingly complex jets. Part I: Methods and tests,” *International Journal of Aeroacoustics*, vol. 4, no. 3, pp. 213–245, 2005.
- [6] S. W. Rienstra and A. Hirschberg, *An introduction to acoustics. Extended and revised edition*. Eindhoven University of Technology, 2003.
- [7] J. E. Ffowcs Williams, “The noise from turbulence convected at high speed,” *Philosophical Transactions of the Royal Society of London*, vol. 255, no. 1061, pp. 469–503, 1963.
- [8] B. Henderson, “Fifty years of fluidic injection for jet noise reduction,” *International Journal of Aeroacoustics*, vol. 9, no. 1–2, pp. 91–122, 2010.
- [9] R. Westley and G. M. Lilley, “An investigation of the noise field from a small jet and methods for its reduction,” Tech. Rep. 53, College of Aeronautics, Cranfield, UK, 1952.

- [10] M. Samimy, K. B. M. Q. Zaman, and M. F. Reeder, “Effect of tabs on the flow and noise field of an axisymmetric jet,” *AIAA Journal*, vol. 31, no. 4, pp. 609–619, 1993.
- [11] J. Bridges and C. A. Brown, “Parametric testing of chevrons on single flow hot jets,” in *10th AIAA/CEAS Aeroacoustics Conference*, (Manchester, UK), 10–12 May 2004. AIAA Paper 2004-2824.
- [12] A. Gomar, T. Léonard, *et al.*, “Antares: Python post-processing library, ver. 1.4.0.” [Online.] available: Antares, 2012. Cerfacs.
- [13] A. Rona, E. J. C. Hall, G. Puigt, R. Camussi, C. Schram, C. Airiau, M. Felli, and C.-H. Lai, “European doctoral training in aeroacoustics by a Marie Curie integrated training network,” in *24th International Congress on Sound and Vibration (ICSV24)*, (London, United Kingdom), July 2017.
- [14] K. Viswanathan, “Mechanisms of jet noise generation: classical theories and recent developments,” *International Journal of Aeroacoustics*, vol. 8, no. 4, pp. 355–407, 2009.
- [15] A. Mancini, *Detached eddy simulations of single and coaxial supersonic jets*. PhD thesis, Department of Engineering, University of Leicester, UK, 2018.
- [16] C. Pérez Arroyo, *Large eddy simulations of a dual stream jet with shock-cells and noise emission analysis*. PhD thesis, Institut National Polytechnique de Toulouse (INP Toulouse), 2016.
- [17] C. K. W. Tam, “Supersonic jet noise,” *Annual Review of Fluid Mechanics*, vol. 27, no. 1, pp. 17–43, 1995.
- [18] S. A. E. Miller and P. J. Morris, “The prediction of broadband shock-associated noise from dualstream and rectangular jets using RANS CFD,” in *16th AIAA/CEAS Aeroacoustics Conference*, (Stockholm, Sweden), 7–9 June 2010. AIAA Paper 2010-3730.
- [19] J. M. Seiner, J. C. Manning, and M. K. Ponton, “The preferred spatial mode of instability for a Mach 2 jet,” in *10th AIAA Aeroacoustics Conference*, (Seattle, Washington, U.S.A.), 9–11 July 1986. AIAA Paper 1986-1942.

- [20] C. K. W. Tam and L. Auriault, “Jet mixing noise from fine-scale turbulence,” *AIAA Journal*, vol. 37, no. 2, pp. 145–153, 1999.
- [21] C. K. W. Tam and L. Auriault, “Mean flow refraction effects on sound radiated from localized sources in a jet,” *Journal of Fluid Mechanics*, vol. 370, no. 2, pp. 149–174, 1998.
- [22] C. K. W. Tam and K. C. Chen, “A statistical model of turbulence in two-dimensional mixing layers,” *Journal of Fluid Mechanics*, vol. 92, no. 2, pp. 303–326, 1979.
- [23] C. K. W. Tam, M. Golebiowski, and J. M. Seiner, “On the two components of turbulent mixing noise from supersonic jets,” in *2nd AIAA Aeroacoustics Conference*, (State College, Pennsylvania, U.S.A.), 6–8 May 1996. AIAA Paper 1996-1716.
- [24] A. Powell, “On the mechanism of choked jet noise,” *Proceedings of the Physical Society*, vol. 66, no. 12, pp. 1039–1057, 1953.
- [25] C. K. W. Tam, J. M. Seiner, and J. C. Yu, “Proposed relationship between broadband shock associated noise and screech tones,” *Journal of Sound and Vibration*, vol. 110, no. 2, pp. 309–321, 1986.
- [26] J. Panda, “An experimental investigation of screech noise generation,” *Journal of Fluid Mechanics*, vol. 378, pp. 71–96, 1999.
- [27] T. A. Manning and S. K. Lele, “A numerical investigation of sound generation in supersonic jet screech,” in *6th Aeroacoustics Conference and Exhibit*, (Lahaina, Hawaii, U.S.A.), 12–14 June 2000. AIAA Paper 2000-2081.
- [28] T. Suzuki and S. K. Lele, “Shock leakage through an unsteady vortex-laden mixing layer: application to jet screech,” *Journal of Fluid Mechanics*, vol. 490, pp. 139–167, 2003.
- [29] T. D. Norum, “Screech suppression in supersonic jets,” *AIAA Journal*, vol. 21, no. 2, pp. 235–240, 1983.

- [30] C. K. W. Tam, “Computational aeroacoustics - Issues and methods,” *AIAA Journal*, vol. 33, no. 10, pp. 1788–1796, 1995.
- [31] P. L. Roe, “Technical prospects for computational aeroacoustics,” in *DGLR/AIAA 14th Aeroacoustics Conference*, (Aachen, Germany), 11–14 May 1992. AIAA Paper 1992-02-032.
- [32] H. K. Tanna, W. H. Brown, and C. K. W. Tam, “Shock associated noise of inverted-profile coannular jets, part I: Experiments,” *Journal of Sound and Vibration*, vol. 98, no. 1, pp. 95–113, 1985.
- [33] M. D. Dahl and P. J. Morris, “Noise from supersonic coaxial jets, part 1: Mean flow predictions, part 2: Normal velocity profile, part 3: Inverted velocity profile,” *Journal of Sound and Vibration*, vol. 200, no. 5, pp. 643–719, 1997.
- [34] K. Viswanathan, “Parametric study of noise from dual-stream nozzles,” *Journal of Fluid Mechanics*, vol. 521, pp. 35–68, 2004.
- [35] C. K. W. Tam and H. K. Tanna, “Shock associated noise of inverted-profile coannular jets, part II: Condition for minimum noise,” *Journal of Sound and Vibration*, vol. 98, no. 1, pp. 115–125, 1985.
- [36] C. K. W. Tam and H. K. Tanna, “Shock associated noise of supersonic jets from convergent-divergent nozzles,” *Journal of Sound and Vibration*, vol. 81, no. 3, pp. 337–358, 1982.
- [37] C. K. W. Tam and H. K. Tanna, “Shock associated noise of inverted-profile coannular jets, part III: Shock structure and noise characteristics,” *Journal of Sound and Vibration*, vol. 98, no. 1, pp. 127–145, 1985.
- [38] M. Harper Bourne and M. J. Fisher, “The noise from shock waves in supersonic jets,” Tech. Rep. cp-131, Agard, 1974.
- [39] C. K. W. Tam and D. E. Burton, “Sound generated by instability waves of supersonic flows, part 2: Axisymmetric jets,” *Journal of Fluid Mechanics*, vol. 138, pp. 273–295, 1984.

- [40] H. K. Tanna, “An experimental study of jet noise, part II: shock associated noise,” *Journal of Sound and Vibration*, vol. 50, no. 3, pp. 429–444, 1977.
- [41] C. K. W. Tam, N. N. Pastouchenko, and K. Viswanathan, “Broadband shock-cell noise from dual stream jets,” *Journal of Sound and Vibration*, vol. 324, no. 3, pp. 861–891, 2009.
- [42] C. K. W. Tam, N. N. Pastouchenko, and K. Viswanathan, “Computation of shock cell structure of dual-stream jets for noise prediction,” *AIAA Journal*, vol. 46, no. 11, pp. 2857–2867, 2008.
- [43] D. Guariglia, *Shock-cell noise investigation on a subsonic/supersonic coaxial jet*. PhD thesis, Von Karman Institute for fluid dynamics, Brussels, Belgium, February 2017. Partnership with University of Rome La Sapienza, Mechanical and Aerospace Engineering Department.
- [44] M. S. Howe, *Theory of vortex sound*, vol. 33. Cambridge Univ Press, 2003.
- [45] C. L. Morfey, *Dictionary of acoustics*. Academic Press, 2000.
- [46] M. J. Lighthill, *Waves in fluids*. Cambridge Univ Press, 2001.
- [47] A. D. Pierce *et al.*, *Acoustics: an introduction to its physical principles and applications*, vol. 20. New York, McGraw-Hill, 1981.
- [48] A. S. Lyrintzis, “Surface integral methods in computational aeroacoustics-From the (CFD) near-field to the (Acoustic) far-field,” *International Journal of Aeroacoustics*, vol. 2, no. 2, pp. 95–128, 2003.
- [49] K. A. Kurbatskii and R. R. Mankbadi, “Review of computational aeroacoustics algorithms,” *International Journal of Computational Fluid Dynamics*, vol. 18, no. 6, pp. 533–546, 2004.
- [50] X. M. Li, R. C. K. Leung, and R. M. C. So, “One-step aeroacoustics simulation using lattice Boltzmann method,” *AIAA Journal*, vol. 44, no. 1, pp. 78–89, 2006.
- [51] B. A. Singer, D. P. Lockard, and G. M. Lilley, “Hybrid acoustic predictions,” *Computers & Mathematics with Applications*, vol. 46, no. 4, pp. 647–669, 2003.

- [52] J. E. Ffowcs Williams and D. L. Hawkings, “Sound generation by turbulence and surfaces in arbitrary motion,” *Philosophical Transactions of the Royal Society of London*, vol. 264, no. 1151, pp. 321–342, 1969.
- [53] A. Rona, *Aerodynamic and aeroacoustic estimations of oscillatory supersonic flows*. PhD thesis, Department of Aeronautics and Astronautics, University of Southampton, UK, 1997.
- [54] D. Casalino, “An advanced time approach for acoustic analogy predictions,” *Journal of Sound and Vibration*, vol. 261, no. 4, pp. 583–612, 2003.
- [55] A. Najafi-Yazdi, G. A. Brès, and L. Mongeau, “An acoustic analogy formulation for moving sources in uniformly moving media,” *Proceedings of the Royal Society of London*, vol. 467, no. 2125, pp. 144–165, 2011.
- [56] G. M. Lilley, “On the noise from air jets,” Tech. Rep. cp-131, 13.1–13.12, Agard, 1973.
- [57] T. Colonius and S. K. Lele, “Computational aeroacoustics: progress on non-linear problems of sound generation,” *Progress in Aerospace Sciences*, vol. 40, no. 6, pp. 345–416, 2004.
- [58] G. J. Bennett, J. Kennedy, C. Meskell, M. Carley, P. Jordan, and H. Rice, “Aeroacoustics research in Europe: The CEAS-ASC report on 2013 highlights,” *Journal of Sound and Vibration*, vol. 340, pp. 39–60, 2015.
- [59] J. B. Freund, “Noise sources in a low-Reynolds-number turbulent jet at Mach 0.9,” *Journal of Fluid Mechanics*, vol. 438, pp. 277–305, 2001.
- [60] J. B. Freund, S. K. Lele, and P. Moin, “Numerical simulation of a Mach 1.92 turbulent jet and its sound field,” *AIAA Journal*, vol. 38, no. 11, pp. 2023–2031, 2000.
- [61] J. Taylor, *Jane's all the world's aircraft 1983–84*. Jane's Publishing Company Ltd., 238 City Road, London, England, 1983.
- [62] A. Rona, D. Di Stefano, A. Mancini, and E. J. C. Hall, “Time-dependent prediction of the unsteady pressure near-field from an under-expanded jet,” in

20th AIAA/CEAS Aeroacoustics Conference, (Atlanta, Georgia, U.S.A.), 16–20 June 2014. AIAA Paper 2014-2340.

- [63] R. R. Mankbadi, M. E. Hayder, and L. A. Povinelli, “Structure of supersonic jet flow and its radiated sound,” *AIAA Journal*, vol. 32, no. 5, pp. 897–906, 1994.
- [64] P. Di Francescantonio, “A new boundary integral formulation for the prediction of sound radiation,” *Journal of Sound and Vibration*, vol. 202, no. 4, pp. 491–509, 1997.
- [65] M. J. Lighthill, “On sound generated aerodynamically II. Turbulence as a source of sound,” *Proceedings of the Royal Society of London*, vol. 222, no. 1148, pp. 1–32, 1954.
- [66] M. J. Fisher, P. A. Lush, and M. Harper Bourne, “Jet noise,” *Journal of Sound and Vibration*, vol. 28, no. 3, pp. 563–585, 1973.
- [67] C. L. Morfey, “Amplification of aerodynamic noise by convected flow inhomogeneities,” *Journal of Sound and Vibration*, vol. 31, no. 4, pp. 391–397, 1973.
- [68] N. Curle, “The influence of solid boundaries upon aerodynamic sound,” *Proceedings of the Royal Society of London*, vol. 231, no. 1187, pp. 505–514, 1955.
- [69] S. C. Crow, “Aerodynamic sound emission as a singular perturbation problem,” *Studies in Applied Mathematics*, vol. 49, no. 1, pp. 21–46, 1970.
- [70] G. M. Lilley, “Jet noise classical theory and experiments,” in *Aeroacoustics of flight vehicles: theory and practice* (H. H. Hubbard, ed.), vol. 1, pp. 211–289, NASA RP-1258, 1991.
- [71] G. M. Lilley, “The radiated noise from isotropic turbulence with applications to the theory of jet noise,” *Journal of Sound and Vibration*, vol. 190, no. 3, pp. 463–476, 1996.
- [72] M. E. Goldstein, *Aeroacoustics*, vol. 1. New York, McGraw-Hill International Book Co., 1976.

- [73] M. E. Goldstein, “Noise from turbulent shear flows,” in *Aeroacoustics of flight vehicles: theory and practice* (H. H. Hubbard, ed.), vol. 1, pp. 291–310, NASA RP-1258, 1991.
- [74] O. M. Phillips, “On the generation of sound by supersonic turbulent shear layers,” *Journal of Fluid Mechanics*, vol. 9, no. 1, pp. 1–28, 1960.
- [75] H. S. Ribner, “The generation of sound by turbulent jets,” *Advances in Applied Mechanics*, vol. 8, pp. 103–182, 1964.
- [76] M. S. Howe, “Contributions to the theory of aerodynamic sound, with application to excess jet noise and the theory of the flute,” *Journal of Fluid Mechanics*, vol. 71, no. 4, pp. 625–673, 1975.
- [77] J. E. Yates and G. Sandri, “Bernoulli enthalpy: A fundamental concept in the theory of sound,” in *2nd AIAA Aeroacoustics Conference*, (Hampton, Virginia, U.S.A.), 24–26 March 1975. AIAA Paper 1975-439.
- [78] A. P. Dowling, J. E. Ffowcs Williams, and M. E. Goldstein, “Sound production in a moving stream,” *Philosophical Transactions of the Royal Society of London*, vol. 288, no. 1353, pp. 321–349, 1978.
- [79] M. E. Goldstein, “A generalized acoustic analogy,” *Journal of Fluid Mechanics*, vol. 488, pp. 315–333, 2003.
- [80] C. Bogey, C. Bailly, and D. Juvé, “Computation of flow noise using source terms in linearized Euler's equations,” *AIAA Journal*, vol. 40, no. 2, pp. 235–243, 2002.
- [81] R. Ewert, M. Meinke, and W. Schroeder, “Comparison of source term formulations for a hybrid CFD/CAA method,” in *7th AIAA/CEAS Aeroacoustics Conference and Exhibit*, (Maastricht, Netherlands), 28–30 May 2001. AIAA Paper 2001-2200.
- [82] M. E. Goldstein and S. J. Leib, “The role of instability waves in predicting jet noise,” *Journal of Fluid Mechanics*, vol. 525, pp. 37–72, 2005.

- [83] G. Kirchhoff, “Zur theorie der lichtstrahlen,” *Annalen der Physik*, vol. 254, no. 4, pp. 663–695, 1883.
- [84] A. S. Lyrintzis, “Review: the use of Kirchhoff's method in computational aeroacoustics,” *Journal of Fluids Engineering*, vol. 116, no. 4, pp. 665–676, 1994.
- [85] K. S. Brentner and F. Farassat, “Analytical comparison of the acoustic analogy and Kirchhoff formulation for moving surfaces,” *AIAA Journal*, vol. 36, no. 8, pp. 1379–1386, 1998.
- [86] W. R. Morgans, “XIV. The Kirchhoff formula extended to a moving surface,” *The London, Edinburgh, and Dublin Philosophical Magazine and Journal of Science*, vol. 9, no. 55, pp. 141–161, 1930.
- [87] D. L. Hawkings, “Noise generation by transonic open rotors,” in *Mechanics of Sound Generation in Flows*, vol. 1, pp. 294–300, 1979.
- [88] F. Farassat and M. K. Myers, “Extension of Kirchhoff's formula to radiation from moving surfaces,” *Journal of Sound and Vibration*, vol. 123, no. 3, pp. 451–460, 1988.
- [89] A. R. Pilon and A. S. Lyrintzis, “Development of an improved Kirchhoff method for jet aeroacoustics,” *AIAA Journal*, vol. 36, no. 5, pp. 783–790, 1998.
- [90] B. E. Mitchell, S. K. Lele, and P. Moin, “Direct computation of the sound generated by vortex pairing in an axisymmetric jet,” *Journal of Fluid Mechanics*, vol. 383, pp. 113–142, 1999.
- [91] P. J. Morris, L. N. Long, T. E. Scheidegger, Q. Wang, and A. R. Pilon, “High speed jet noise simulations,” in *4th AIAA/CEAS Aeroacoustics Conference*, (Toulouse, France), 2–4 June 1998. AIAA Paper 1998-2290.
- [92] A. S. Lyrintzis and R. R. Mankbadi, “Prediction of the far-field jet noise using Kirchhoff's formulation,” *AIAA Journal*, vol. 34, no. 2, pp. 413–416, 1996.
- [93] J. C. Hardin and D. S. Pope, “An acoustic/viscous splitting technique for computational aeroacoustics,” *Theoretical and Computational Fluid Dynamics*, vol. 6, no. 5, pp. 323–340, 1994.

- [94] J. C. Hardin and D. S. Pope, “Sound generation by flow over a two-dimensional cavity,” *AIAA Journal*, vol. 33, no. 3, pp. 407–412, 1995.
- [95] W. Z. Shen and J. N. Sørensen, “Comment on the aeroacoustic formulation of Hardin and Pope,” *AIAA Journal*, vol. 37, no. 1, pp. 141–143, 1999.
- [96] W. Z. Shen and J. N. Sørensen, “Aeroacoustic modelling of low-speed flows,” *Theoretical and Computational Fluid Dynamics*, vol. 13, no. 4, pp. 271–289, 1999.
- [97] W. Z. Shen and J. N. Sørensen, “Aeroacoustic modeling of turbulent airfoil flows,” *AIAA Journal*, vol. 39, no. 6, pp. 1057–1064, 2001.
- [98] R. Ewert and W. Schröder, “Acoustic perturbation equations based on flow decomposition via source filtering,” *Journal of Computational Physics*, vol. 188, no. 2, pp. 365–398, 2003.
- [99] C. Cheong, P. Joseph, Y. Park, and S. Lee, “Computation of aeolian tone from a circular cylinder using source models,” *Applied Acoustics*, vol. 69, no. 2, pp. 110–126, 2008.
- [100] W. De Roeck, M. Baelmans, and W. Desmet, “An aerodynamic/acoustic splitting technique for hybrid CAA applications,” in *13th AIAA/CEAS Aeroacoustics Conference*, (Rome, Italy), 21–23 May 2007. AIAA Paper 2007-3726.
- [101] S. A. Slimon, M. C. Soteriou, and D. W. Davis, “Computational aeroacoustics simulations using the expansion about incompressible flow approach,” *AIAA Journal*, vol. 37, no. 4, pp. 409–416, 1999.
- [102] A. Powell, “Theory of vortex sound,” *Journal of the Acoustical Society of America*, vol. 36, no. 1, pp. 177–195, 1964.
- [103] D. S. Jones, *Generalised functions*. London, McGraw-Hill, 1966.
- [104] F. Farassat, “Derivation of formulations 1 and 1A of Farassat,” Tech. Rep. 214853, NASA, 2007.
- [105] F. Farassat, “Introduction to generalized functions with applications in aerodynamics and aeroacoustics,” Tech. Rep. 3428, NASA, 1994.

- [106] F. Farassat, “Theory of noise generation from moving bodies with an application to helicopter rotors,” Tech. Rep. R-451, NASA, 1975.
- [107] K. S. Brentner and P. C. Holland, “An efficient and robust method for computing quadrupole noise,” *Journal of the American Helicopter Society*, vol. 42, no. 2, pp. 172–181, 1997.
- [108] K. S. Brentner and P. C. Holland, “An efficient and robust method for predicting helicopter rotor high-speed impulsive noise,” *Journal of Sound and Vibration*, vol. 203, no. 1, pp. 87–100, 1997.
- [109] F. Farassat, “Linear acoustic formulas for calculation of rotating blade noise,” *AIAA Journal*, vol. 19, no. 9, pp. 1122–1130, 1981.
- [110] F. Farassat and G. P. Succi, “A review of propeller discrete frequency noise prediction technology with emphasis on two current methods for time domain calculations,” *Journal of Sound and Vibration*, vol. 71, no. 3, pp. 399–419, 1980.
- [111] M. L. Shur, P. R. Spalart, and M. K. Strelets, “LES-based noise prediction for shocked jets in static and flight conditions,” in *16th AIAA/CEAS Aeroacoustics Conference*, (Stockholm, Sweden), 7–9 June 2010. AIAA Paper 2010-3840.
- [112] P. T. Lew, G. Blaisdell, and A. S. Lyrantzis, “Investigation of noise sources in turbulent hot jets using large eddy simulation data,” in *45th AIAA Aerospace Sciences Meeting and Exhibit*, (Reno, Nevada, U.S.A.), 8–11 January 2007. AIAA Paper 2007-16.
- [113] H. Xia, P. Tucker, and S. Eastwood, “Towards jet flow LES of conceptual nozzles for acoustics predictions,” in *46th AIAA Aerospace Sciences Meeting and Exhibit*, (Reno, Nevada, U.S.A.), 7–10 January 2008. AIAA Paper 2008-10.
- [114] A. Uzun and M. Y. Hussaini, “Prediction of noise generated by a round nozzle jet flow using computational aeroacoustics,” *Journal of Computational Acoustics*, vol. 19, no. 3, pp. 291–316, 2011.

- [115] A. Fosso Pouangué, M. Sanjosé, S. Moreau, G. Daviller, and H. Deniau, “Subsonic jet noise simulations using both structured and unstructured grids,” *AIAA Journal*, vol. 53, no. 1, pp. 55–69, 2014.
- [116] C. L. Morfey and M. C. M. Wright, “Extensions of Lighthill's acoustic analogy with application to computational aeroacoustics,” *Proceedings of the Royal Society of London*, vol. 463, no. 2085, pp. 2101–2127, 2007.
- [117] P. R. Spalart and M. L. Shur, “Variants of the Ffowcs Williams-Hawkings equation and their coupling with simulations of hot jets,” *International Journal of Aeroacoustics*, vol. 8, no. 5, pp. 477–491, 2009.
- [118] S. Mendez, M. Shoeybi, A. Sharma, S. K. Lele, and P. Moin, “Post-processing of large-eddy simulations for jet noise predictions,” *Center for Turbulence Research Annual Research Briefs*, 2009.
- [119] S. Mendez, M. Shoeybi, S. K. Lele, and P. Moin, “On the use of the Ffowcs Williams-Hawkings equation to predict far-field jet noise from large-eddy simulations,” *International Journal of Aeroacoustics*, vol. 12, no. 1-2, pp. 1–20, 2013.
- [120] G. Rahier, J. Prieur, F. Vuillot, N. Lupoglazoff, and A. Biancherin, “Investigation of integral surface formulations for acoustic post-processing of unsteady aerodynamic jet simulations,” *Aerospace Science and Technology*, vol. 8, no. 6, pp. 453–467, 2004.
- [121] A. Uzun, A. S. Lyrintzis, and G. A. Blaisdell, “Coupling of integral acoustics methods with LES for jet noise prediction,” *International Journal of Aeroacoustics*, vol. 3, no. 4, pp. 297–346, 2004.
- [122] D. P. Lockard and J. H. Casper, “Permeable surface corrections for Ffowcs Williams and Hawkings integrals,” in *11th AIAA/CEAS Aeroacoustics Conference*, (Monterey, California, U.S.A.), 23–25 May 2005. AIAA Paper 2005-2995.
- [123] T. Ikeda, S. Enomoto, K. Yamamoto, and K. Amemiya, “On the modification of the Ffowcs Williams-Hawkings integration for jet noise prediction,” in *19th*

- AIAA/CEAS Aeroacoustics Conference*, (Berlin, Germany), 27–29 May 2013. AIAA Paper 2013-2277.
- [124] F. Farassat and G. P. Succi, “The prediction of helicopter rotor discrete frequency noise,” *Vertica*, vol. 7, no. 4, pp. 309–320, 1983.
- [125] K. S. Brentner and F. Farassat, “Modeling aerodynamically generated sound of helicopter rotors,” *Progress in Aerospace Sciences*, vol. 39, no. 2, pp. 83–120, 2003.
- [126] J. G. Leishman, “Aeroacoustics of 2-D and 3-D blade vortex interaction using the indicial method,” in *52nd Annual Forum of the American Helicopter Society*, (Washington, D.C.), 4–6 June 1996.
- [127] Y. Ozyoruk and L. N. Long, “Computation of sound radiating from engine inlets,” *AIAA Journal*, vol. 34, no. 5, pp. 894–901, 1996.
- [128] G. A. Brès, K. S. Brentner, G. Perez, and H. E. Jones, “Maneuvering rotorcraft noise prediction,” *Journal of Sound and Vibration*, vol. 275, no. 3–5, pp. 719–738, 2004.
- [129] D. I. Blokhintsev, “Acoustics of a nonhomogeneous moving medium.,” Tech. Rep. 1399, National Advisory Committee for Aeronautics (NACA), (Washington, D.C.), 1956.
- [130] L. Cambier, S. Heib, and S. Plot, “The ONERA elsA CFD software: input from research and feedback from industry,” *Mechanics & Industry*, vol. 14, no. 3, pp. 159–174, 2013.
- [131] J. Prieur and G. Rahier, “Aeroacoustic integral methods, formulation and efficient numerical implementation,” *Aerospace Science and Technology*, vol. 5, no. 7, pp. 457–468, 2001.
- [132] A. Rona, A. Mancini, and E. J. C. Hall, “Modelling the unsteady flow and shock-associated noise from dual-stream turbulent jets,” in *24th International Congress on Sound and Vibration (ICSV24)*, (London, United Kingdom), July 2017.

- [133] C. Pérez Arroyo, G. Puigt, C. Airiau, and J. F. Boussuge, “Large Eddy Simulation of shock–cell noise from a dual stream jet,” in *22nd AIAA/CEAS Aeroacoustics Conference*, (Lyon, France), 30 May–1 June 2016. AIAA Paper 2016–2798.
- [134] R. Biolchini, C. Bailly, J. F. Boussuge, and R. Fernando, “Numerical study on the relation between hydrodynamic fluctuations and noise in hot jets at high Reynolds number,” in *22nd AIAA/CEAS Aeroacoustics Conference*, (Lyon, France), 30 May–1 June 2016. AIAA Paper 2016–3048.
- [135] R. Biolchini, *Étude des effets de température sur le bruit de jet subsonique par simulation des grandes échelles*. PhD thesis, École Centrale de Lyon, 2017. Personal communication.
- [136] P. Pineau, “Étude de l’effet du vol d’avancement sur le bruit d’un jet supersonique par simulation des grandes échelles.” École centrale de Lyon & Cerfacs, 2015. Rapport Final de Travail de Fin d’études.
- [137] C. Bogey and C. Bailly, “A family of low dispersive and low dissipative explicit schemes for flow and noise computations,” *Journal of Computational Physics*, vol. 194, no. 1, pp. 194–214, 2004.
- [138] T. Suzuki and T. Colonius, “Instability waves in a subsonic round jet detected using a near-field phased microphone array,” *Journal of Fluid Mechanics*, vol. 565, pp. 197–226, 2006.
- [139] P. A. Nelson, “Acoustics II, Student notes of M.Sc. course in sound and vibration studies,” student notes of M.Sc. course in sound and vibration studies, Institute of Sound and Vibration Research, 1991.
- [140] D. Di Stefano, A. Rona, E. J. C. Hall, and G. Puigt, “Implementing the Ffowcs Williams and Hawkings acoustic analogy in Antares,” in *22nd International Congress on Sound and Vibration (ICSV22)*, (Florence, Italy), 12–16 July 2015.
- [141] D. Di Stefano, A. Rona, E. J. C. Hall, C. L. Morfey, and G. Puigt, “Validating the Ffowcs Williams and Hawkings acoustic analogy implementation in Antares,”

- in *22nd AIAA/CEAS Aeroacoustics Conference*, (Lyon, France), 30 May–1 June 2016. AIAA Paper 2016–3059.
- [142] C. Bogey and C. Bailly, “Computation of a high Reynolds number jet and its radiated noise using large eddy simulation based on explicit filtering,” *Computers & Fluids*, vol. 35, no. 10, pp. 1344–1358, 2006.
- [143] B. André, *Étude expérimentale de l’effet du vol sur le bruit de choc de jets supersoniques sous-détendus*. PhD thesis, École Centrale de Lyon, Lyon, France, November 2012.
- [144] D. Di Stefano, A. Rona, E. J. C. Hall, and G. Puigt, “Modelling directional sound radiation in Antares by the Ffowcs Williams and Hawkings analogy,” in *23rd International Congress on Sound and Vibration (ICSV23)*, (Athens, Greece), 10–14 July 2016.
- [145] Y. Zhou, A. Praskovsky, and S. Oncley, “On the Lighthill relationship and sound generation from isotropic turbulence,” *Theoretical and Computational Fluid Dynamics*, vol. 7, no. 5, pp. 355–361, 1995.
- [146] P. Welch, “The use of fast Fourier transform for the estimation of power spectra: a method based on time averaging over short, modified periodograms,” *IEEE Transactions on audio and electroacoustics*, vol. 15, no. 2, pp. 70–73, 1967.
- [147] A. Savarese, P. Jordan, S. Girard, A. Royer, C. Fourment, E. Collin, Y. Gervais, and M. Porta, “Experimental study of shock-cell noise in underexpanded supersonic jets,” in *19th AIAA/CEAS Aeroacoustics Conference*, (Berlin, Germany), 27–29 May 2013. AIAA Paper 2013–2080.
- [148] K. Viswanathan, “Scaling laws and a method for identifying components of jet noise,” *AIAA Journal*, vol. 44, no. 10, pp. 2274–2285, 2006.
- [149] K. Viswanathan, “True farfield for dual-stream jet noise measurements,” *AIAA Journal*, vol. 49, no. 2, pp. 443–447, 2011.
- [150] G. M. Lilley, “On the noise from air jets,” Tech. Rep. 20376, Aeronautical Research Council, 1958.

- [151] K. Viswanathan, “Instrumentation considerations for accurate jet noise measurements,” *AIAA Journal*, vol. 44, no. 6, pp. 1137–1149, 2006.
- [152] K. Viswanathan, “Distributions of noise sources in heated and cold jets: are they different?,” *International Journal of Aeroacoustics*, vol. 9, no. 4-5, pp. 589–625, 2010.
- [153] D. P. Lockard, “A comparison of Ffowcs Williams-Hawkings solvers for airframe noise applications,” in *8th AIAA/CEAS Aeroacoustics Conference*, (Breckenridge, Colorado, U.S.A.), 17–19 June 2002. AIAA Paper 2002-2580.
- [154] A. P. Dowling and J. E. Ffowcs Williams, *Sound and sources of sound*. Horwood Publishing, Westergate, 1983.
- [155] H. K. Tanna and C. L. Morfey, “Sound radiation from point sources in circular motion,” *Journal of Sound and Vibration*, vol. 16, no. 3, pp. 337–348, 1971.
- [156] C. K. W. Tam, “Broadband shock-associated noise from supersonic jets in flight,” *Journal of Sound and Vibration*, vol. 151, no. 1, pp. 131–147, 1991.
- [157] T. D. Norum and J. G. Shearin, “Effects of simulated flight on the structure and noise of underexpanded jets,” Tech. Rep. 2308, NASA, 1984.
- [158] J. Huber, K. Britchford, E. Laurendeau, V. Fleury, J. Bulté, A. A. Sylla, and D. Long, “Understanding and reduction of cruise jet noise at model and full scale,” in *15th AIAA/CEAS Aeroacoustics Conference*, (Miami, Florida, U.S.A.), 11–13 May 2009. AIAA Paper 2009–3382.
- [159] B. André, T. Castelain, and C. Bailly, “Experimental study of flight effects on slightly underexpanded supersonic jets,” *AIAA Journal*, vol. 55, no. 1, pp. 57–67, 2017.
- [160] C. K. W. Tam, “Broadband shock associated noise from supersonic jets measured by a ground observer,” *AIAA Journal*, vol. 30, no. 10, pp. 2395–2401, 1992.
- [161] T. Ansaldi, *Compressible single and dual stream jet stability and adjoint-based sensitivity analysis in relationship with aeroacoustics*. PhD thesis, Institut de Mécanique des Fluides de Toulouse (IMFT), 2016.

- [162] T. Herbert, “Parabolized stability equations,” *Annual Review of Fluid Mechanics*, vol. 29, no. 1, pp. 245–283, 1997.
- [163] O. Léon and J. P. Brazier, “Application of the linear parabolized stability equations to a subsonic coaxial jet,” in *17th AIAA/CEAS Aeroacoustics Conference (32nd AIAA Aeroacoustics Conference)*, (Portland, Oregon, U.S.A.), 5–8 June 2011. AIAA Paper 2011–2839.
- [164] G. Rahier, M. Huet, and J. Prieur, “Additional terms for the use of Ffowcs Williams and Hawkings surface integrals in turbulent flows,” *Computers & Fluids*, vol. 120, pp. 158–172, 2015.
- [165] F. Farassat, K. S. Brentner, and M. Dunn, “Working with the wave equation in aeroacoustics- The pleasures of generalized functions,” in *13th AIAA/CEAS Aeroacoustics Conference*, (Rome, Italy), 21–23 May 2007. AIAA Paper 2007-3562.